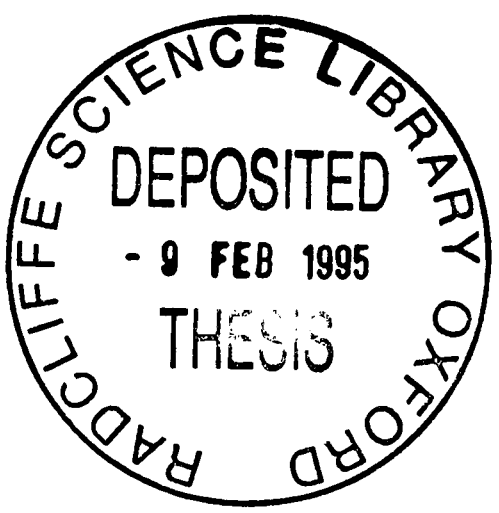
Many-Body Effects in Ionic Systems

Mark Wilson

Keble College, Oxford



A thesis submitted in partial fulfilment of the requirements for the degree of Doctor of Philosophy of the University of Oxford

Trinity Term 1994

Many-Body Effects in Ionic Systems

Mark Wilson

Keble College, Oxford

A thesis submitted in partial fulfilment of the requirements for the degree of Doctor of Philosophy of the University of Oxford

Trinity Term 1994

Many-Body Effects in Ionic Systems.

Mark Wilson
Keble College, University of Oxford

A thesis submitted in partial fulfilment of the requirements
for the degree of Doctor of Philosophy, Trinity Term 1994

Abstract

The electron density of an ion is strongly influenced by its environment in a condensed phase. When the environment changes, for example due to thermal motion, non-trivial changes in the electron density, and hence the interionic interactions occur. These interactions give rise to many-body effects in the potential. In order to represent this phenomenon in molecular dynamics (MD) simulations a method has been developed in which the environmentally-induced changes in the ionic properties are represented by extra dynamical variables. These extra variables are handled in an extended Lagrangian formalism by techniques analogous to those used in Car and Parrinello's *ab initio* MD method.

At its simplest level (the polarizable-ion model or PIM) induced dipoles are represented. With the PIM it has proven possible to quantitatively account for numerous properties of divalent metal halides, which had previously been attributed to unspecific "covalent" effects. In the solid-state the prevalence of layered crystal structures is explained. Analogous non-coulombic features in liquid structures, in particular network formation in "strong" liquids like $ZnCl_2$, have been studied as has network disruption by "modifiers" like RbCl. This work leads to an understanding of the relationship between the microscopic structure and anomalous peaks ("prepeaks") seen in diffraction data of such materials.

The PIM was extended to include induced quadrupoles and their effect studied in simulations of AgCl. In the solid-state it is found that the both are crucial in improving the phonon dispersion curves with respect to experiment. In the liquid-state polarization effects lower the melting point markedly.

For oxides the short-range energy has been further partitioned into overlap and rearrangement energies and electronic structure calculations are used to parameterize a model in which the radius of the anion is included as an additional degree of freedom. The B1 $\longrightarrow$ B2 phase transition is studied in MgO and CaO and the differences between the new model and a rigid-ion model are analysed.

To my parents.

Acknowledgments: Technical.

Many people have helped in various and varying capacities over the course of my D.Phil.

First and foremost immense thanks are due to my supervisor, Paul Madden, not only for the huge amount of help, encouragement and ideas, but also for never being phased by my ignoring his suggestion and doing something else.

I would like to thank Dr.John Harding (AEA, Harwell) for his help in formulating and developing the model in chapter 8. Thanks here are also due to Dr. Nick Pyper (Cambridge) for discussions and supplying electronic structure calculations prior to publication.

Many thanks are also due to Dr. Benedito Costa Cabral (Lisbon) for helpful discussions and many simulation results regarding the AgCl work in chapter 7.

Within the research group I would like to thank (in no particular order) Ian, Matt, Martin, Enrico, Stuart, Mike, Yolande and "Mykl" for various discussions and technical help over the years. I would like to single out Mike Foley for proving my code could be run by someone other than me.

Finally, thanks to RSRE Malvern for financial support for the last three years with no requirement to ever prove something was actually being done.

Acknowledgments: Personal.

SCENE: a glittering awards ceremony in London.

MC: And the awards for the members of the Madden/Logan groups are as follows:

Fumbles with envelope. It reads....

Most outrageous comment during a presentation

- Dr. P.A. Madden for "The shell model is, well, wrong".

Most unusual interpretation of *that* Koeman penalty

- Dr. Martin Van der Hoef.

Most excuses for poor tetris/spatial performances

- Dr. Martin Van der Hoef.

Most bizarre excuses for computer code failure

- Dr. Martin Van der Hoef.

Best serial killer beard

- Michael Foley (with a special mention for Stuart Watson).

Most "imaginative" use of AVS

- Michael Foley for the piece "box-sneeze".

Best "wind-up-merchant"

- Matt Eldridge (who else ?).

Most psychotic member of the group

- Stuart "Big Axe" Watson for "Do you need *all* those Rahman windows ?".

The Dr.Doom "keeping a job down" award

- Mike Tusch for his manly dive into the murky world of consultancy and Polish.

The person most suited to being sent to Pluto, third class.

- *This space is left intentionally blank*

and finally,

Best Pole, most cuddly goth,

- Guess who ?

The work described in this thesis has led to the following publications:

1. Chapters 2 and 3.

   - *Polarization Effects in Ionic Systems from First Principles*,
     Wilson, M and Madden, P.A,
     J. Phys: Condensed. Matter, **5**, 2687. 1993.

2. Chapter 4.

   - *On the Rationalization of* MX_2 *Crystal Structures based on an Ionic Model*,
     Wilson, M and Madden, P.A,
     J. Phys: Condensed. Matter, **6**, 159, 1994.

3. Chapter 5.

   - *Short and Intermediate Range Order in* MCl_2 *Melts: the Importance of Anionic Polarization*,
     Wilson, M and Madden, P.A,
     J. Phys: Condensed. Matter, **5**, 6833, 1993.

   - *Polarization Effects on the Structure and Dynamics of Ionic melts* ,
     Wilson, M and Madden, P.A,
     J. Phys: Condensed. Matter, **6**, A151, 1994.

   - *Boson peaks and slow relaxation in a simulation of a network-forming ionic melt* ,
     Foley, M, Wilson, M and Madden, P.A,
     Phil. Mag. B, *to be published.*

4. Chapter 6.

   - *"Prepeaks" and "First Sharp Diffraction Peaks" in Computer Simulations of Strong and Fragile Ionic Liquids* ,
     Wilson, M and Madden, P.A,
     Phys. Rev. Lett, **6**, 3033, 1994.

Contents

1 Introduction. **1**

1.1 "Covalent" Effects in Ionic Systems. 1

1.2 The Crystalline Environment. 4

1.3 The Rigid-ion Model. 8

1.4 Distorting the Crystal. 10

1.5 Including Induction Effects. 11

1.5.1 The Problem of Non-additivity. 11

1.5.2 The Shell Model. 13

1.5.3 Other Models. 15

1.6 Summary. 16

2 Simulation Methods. **17**

2.1 Deriving the Equations of Motion. 17

2.1.1 Dipolar Model. 18

2.1.2 Quadrupolar Model. 21

2.2 Simulation Techniques. 23

2.2.1 Integrating the Equations of Motion. 23

2.3 Application of the Car-Parrinello Method. 25

2.3.1 Methodology. 25

2.3.2 The Factors which Control Adiabaticity. 28

2.3.3 Choosing the Fictitious Masses. 29

2.3.4 Thermostating the Systems. 31

3 Parameterization of the Model. **36**

3.1 Short-range Interactions. 37

3.2 Dispersion. 38

3.3 Induction. 39

3.4 Comparing the PIM and Shell Models. 41
3.5 Alternative Means of Potential Derivation. 42
3.5.1 Induction. 43
3.5.2 Dispersion. 44
3.5.3 Short-range. 44

4 Rationalizing MX_2 Crystal Structures. 46
4.1 Introduction 46
4.2 Crystal Structures. 46
4.3 Predicted Structural Trends. 50
4.4 The Calculations. 52
4.4.1 Parameterization of the Model. 52
4.4.2 Perfect Crystal Energetics. 57
4.4.3 The Role of Anion Polarization. 64
4.4.4 Molecular Dynamics Simulations. 70
4.5 A More General Crystal Model. 72
4.6 Other MX_2 Systems. 74

5 MX_2 Liquids. 79
5.1 Experimental Work. 79
5.1.1 Neutron Scattering. 79
5.1.2 Raman Scattering. 84
5.2 Simulations and Theory. 84
5.2.1 Summary. 87
5.3 The Simulations. 88
5.3.1 Short Range Order. 88
5.3.2 Intermediate Range Order. 90
5.3.3 Liquid Structure. 94
5.4 The Role of Anion Polarization. 94
5.5 The Origin of the FSDP. 96
5.6 The Formation of MX_2 Molecules. 96
5.7 Constant NpT Simulations. 102
5.7.1 Performing constant-NpT Simulations in the RIM. . . . 102
5.7.2 Performing constant-NpT Simulations in the PIM. 103
5.7.3 The Simulations. 104

5.7.4 Results. 105

6 Network-Modified Systems. 109

6.1 Experimental Studies. 109
6.2 The Simulation Model. 110
6.3 Results. 112
6.3.1 Distribution Functions. 112
6.3.2 Molecular Graphics. 117
6.3.3 Structure Factors. 122
6.4 Raman Scattering. 127
6.5 The Origin of the FSDP. 128
6.6 Classifying the First Sharp Diffraction Peak. 129
6.6.1 Modelling the FSDP. 131
6.6.2 Summary: A Possible Classification of Prepeaks. 135

7 Cation Polarization and Induced Quadrupoles. 138

7.1 Crystalline LiF. 138
7.2 The "Anomalous" Behaviour of AgCl. 139
7.2.1 Crystal. 139
7.2.2 Melt. 140
7.3 Previous Silver Halide Simulations. 141
7.4 Parameterization of the AgCl model. 143
7.4.1 The Dipolar Model. 143
7.4.2 Including the Induced Quadrupoles. 143
7.5 Overview of the Simulations. 146
7.6 The Crystal. 147
7.6.1 Simulation Details. 147
7.6.2 Results. 149
7.6.3 Summary and Comments. 154
7.7 The Molten State. 155
7.7.1 Simulation Details. 155
7.8 The Role of Induced Quadrupoles in the Liquid. 168

8 Beyond the Polarizable-Ion Model. 170

8.1 Introduction: The Problems of Simulating Oxides. 170

8.2 Pressure-induced Phase Transitions. 170
8.3 The Anion Compression Model (ACM). 171
8.4 Electronic Structure Calculations. 174
8.5 Parameterization of the ACM. 174
8.5.1 Magnesium Oxide. 175
8.5.2 Calcium Oxide. 178
8.6 Deriving RIM Potentials. 178
8.7 Results. 180
8.7.1 Effect of Potential Terms. 180
8.7.2 System Size Effects. 181
8.7.3 Modelling Phase Transitions. 182
8.8 Behaviour of the Model. 192
8.9 Comparison with Other Oxides. 192
8.10 Closing Remarks. 194

A Multipole Interaction Tensors. 206
A.1 The Full Tensors. 206
A.2 The Interactions. 207
A.3 General. 207

B The Quadrupolar Model . 208
B.1 Derivation of the Dipole and Quadrupole Expressions. 208
B.2 Derivation of the Induction Energy. 209

1

Introduction.

1.1 "Covalent" Effects in Ionic Systems.

In the last decade much progress has been made in the field of computer simulation following the introduction of the Car-Parrinello (CP) method [1, 2], which allows for an explicit representation of the valence electron wavefunctions. The system is split into cores (the nuclei and non-valence electrons) and the valence electrons are treated by a standard density-functional or Hartree-Fock method. In the CP method the valence electronic state is automatically updated to the variationally optimum value as the cores undergo their thermal motion *without* repeated explicit energy minimizations. The advantage of this approach is that the behaviour of systems that involve itinerant electrons (e.g if chemical bonds are broken) may be correctly described. The need for effective interaction-potentials which include such effects is avoided. Such techniques can now produce results to within experimental accuracy for a (limited) number of systems. However, the greater generality of this model over an effective-interaction potential-based approach results in a large increase in computational expense. On one hand one would like to use this model generally. On the other hand a model utilizing effective potentials may be orders of magnitude faster and be the only realistic option for many problems of interest.

The question which then arises is for what systems will the generality of a CP-like approach be needed? It is well known that simple pair potentials describe the noble gases very well. This is because their valence electrons are in closed shell configurations which follow the nuclei without distortion; the "itinerancy" of their electrons is trivial. It is also known that the extension to model simple ionic alkali halides is relatively successful, but additional (polarization) effects are necessary in order to reproduce some of the more subtle experimental observations (see section 1.3). The most popular approach is to set up a *shell model* simulation (see section 1.5.2) which effectively reintroduces an aspect of

the electron itineracy; that is, the shell model formalism caricatures that aspect of the ion electronic response needed for these systems.

Away from the alkali halides, however, the ionic effective-interaction potentials seem to be an inappropriate starting point. In, for example, the alkaline-earth halides (MX_2 systems) "covalency" is often invoked to explain both solid- and liquid-state properties, though, on electronegativity grounds it would appear that these systems *ought* to be ionic.

The appeal to covalency can be appreciated on empirical grounds from the structure map for the MX_2 systems shown in figure 1.1, where M is a divalent metal cation and X is a halide anion. The anions are plotted along the x-axis with the smallest (F^-) on the left going to the largest (I^-) on the right. Similarly, along the y-axis the ions go from the smallest (Pd^{2+}) at the top to the largest (Ba^{2+}) at the bottom. The coloured areas show clear regions of crystal structures with the same basic structural type across the whole map. The precise details of these structures will be discussed in chapter 4. For the purpose of this discussion the crucial point is the change in basic structural type as one moves from the bottom left (large cation, small anion) to the top right (small cation, large anion). The compounds in the bottom left corner have a fluorite structure (see section 4.2 for details) in which the doubly charged cation-cation separation is larger with respect to the characteristic anion-anion correlations. This structure can be fully justified on *purely coulombic* grounds, that is, it is the structure formed by packing charges spheres of the appropriate radius. At the top right the compounds are *layered*; the cations are as close together as the anions meaning that this whole class of structures (29 out of 60 in figure 1.1) seems inappropriate on *purely* ionic grounds. There will always be more energetically favoured crystal structures for charged spheres of the appropriate radius.

Barnes and Enderby [3] define covalency as: "Interactions which change the charge distribution of the valence electrons relative to some conceptual extreme represented by the ionic model." In effect, this merely restates the problem - what non-trivial aspect of the electronic behaviour is to be invoked to account for such phenomena.

A full CP-like description of these systems is not desirable as:

- The closed-shell nature of the ions leaves a relatively large number of

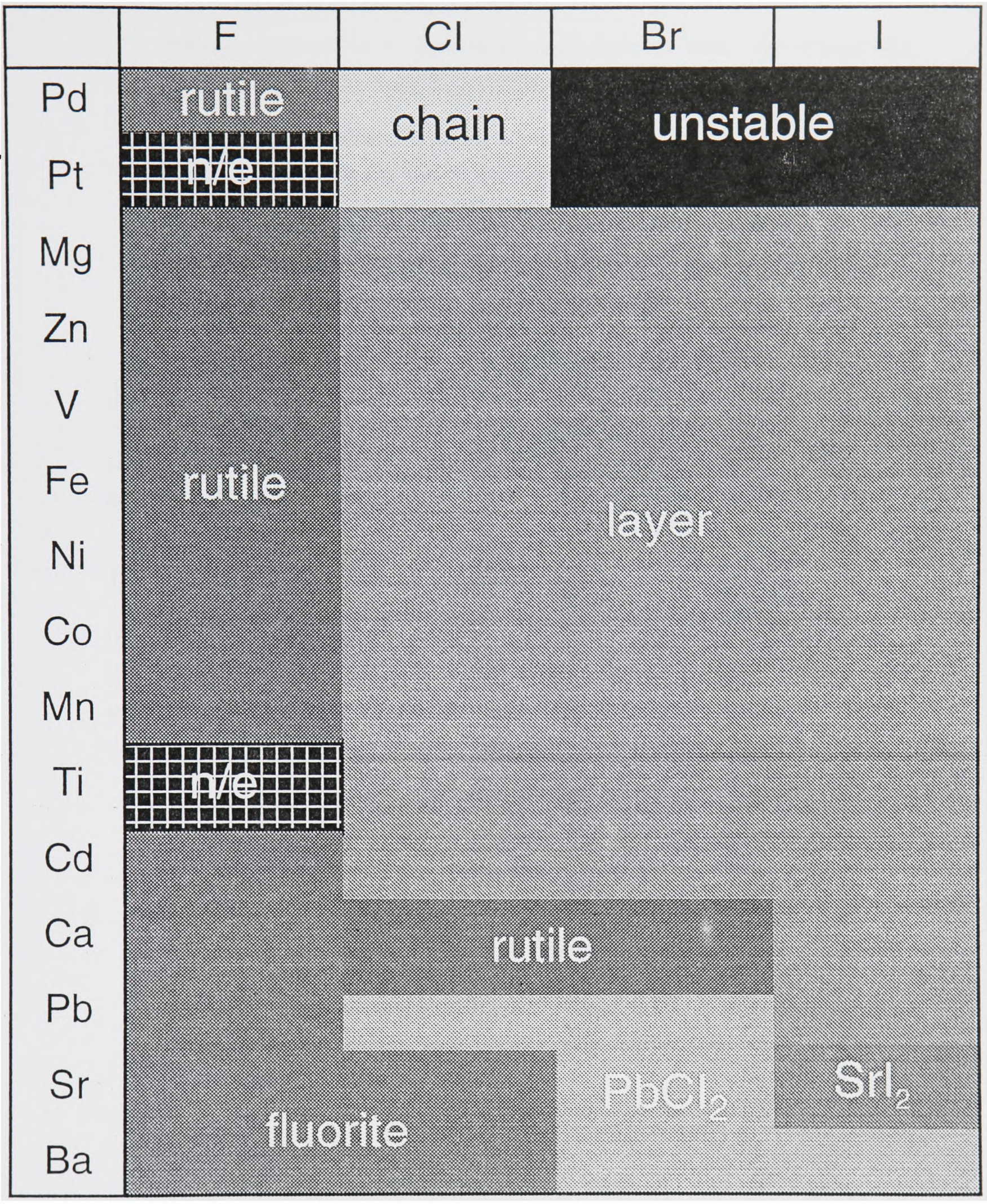


FIGURE 1.1: *Full structure map for the* MX_2 *systems.*

valence electrons to be described which interact with very strong core pseudopotentials because of the high effective nuclear charge.

- The repulsion between the ions is a non-bonding interaction between closed shells. Existing density functional methods are not optimized for describing such effects.

- Many of the properties of interest for this range of systems (such as glass transitions) require long timescale simulations.

The central aim of this thesis is to show how a representation of induction (polarization) effects at an *ab initio* level of accuracy can be included in a basically ionic model in a computationally tractable way. These models will allow an accurate description of the properties of the materials included in figure 1.1, including the crystal structures.

1.2 The Crystalline Environment.

In order to effectively model the electronic behaviour in condensed ionic systems it is necessary to understand the nature of the ionic environment. To this effect most attention has been paid to the *crystalline environment* and it is from this direction that the problem shall be approached in this thesis [4, 5]:

- *Crystal Field*: Consider the effect of surrounding an anion by a lattice of point charges. The potential felt by an electron in the immediate vicinity of ion i is the *Madelung potential* and can be written

$$V^i(\mathbf{r}) = -\sum_{i \neq j}^{\infty} \frac{Q^j}{\mid \mathbf{r} - \mathbf{r}^j \mid}, \tag{1.1}$$

where Q^j is a point charge in the lattice, and $\mathbf{r} - \mathbf{r}^j$ is the anion electron-point charge separation. In a perfect cubic crystal this can be written as an expansion in cubic harmonics,

$$V^i(\mathbf{r}) = V_0^i(r) + V_4^i(r)P_4(\hat{r}_z) + V_6^i(r)P_6(\hat{r}_z) + ..., \tag{1.2}$$

where P_m in the mth-order Legendre polynomial. The effect of this potential on the electronic state is dominated by the spherical (V_0) term for ions with an sp ground state (for example, in F^- 98% of the environmental

effect on the polarizability is attributed to this term [6]). The reason for this dominance is that, in the spherical geometry, the closed-shell ionic ground state is ^1S. Perturbation theory would suggest that the $l = 4$ potential could mix in terms of ^1G symmetry. For sp valence ions such terms will be remote in energetic terms, as the occupation of very high angular momentum orbitals would be required. Hence, the degree of this mixing is small. For transition metal ions this argument would need to be reconsidered (chapter 8) as, for ions possessing occupied d-orbitals, the V_4 term will act to *split* these orbitals. For the moment it is reasonable to assume that only the V_0 term makes a significant contribution.

Figure 1.2a shows the effect of the spherically averaged potential, due to the first cation shell, on the electrons of an anion sitting at the origin. The potential has a constant value, given by the Madelung constant, up to the position of the first cation shell at the lattice spacing, a_0 (the potential inside a charged sphere is constant). Thus, an electron sitting on the anion at the origin experiences a *confining* potential. This effectively binds the electron more tightly than in the free environment and hence *reduces* the anion polarizability.

- *Overlap compression.* In reality the ions surrounding the central anion are not point charges; they have a finite volume which further affects the central anion. Fowler and Madden [5, 7] have demonstrated this effect in a series of coupled-Hartree-Fock calculations. Mahan [4] has shown that this effect can be modelled by spherically averaged one-electron pseudopotentials giving a potential in the same form as equation 1.2. The potential can be considered as a spherical potential whose radius is smaller than the lattice spacing, effectively the anion radius, at which point the cation electron density becomes non-zero. Figure 1.2b shows this effect.

  Pyper [8] has shown how this is the combination of two effects:

  - an *attractive* term due to the interaction of the anion nucleus and the cation electrons.
  - a purely *repulsive* exchange term acting between electrons on neighbouring sites. The electrostatic repulsion is included in the first part.

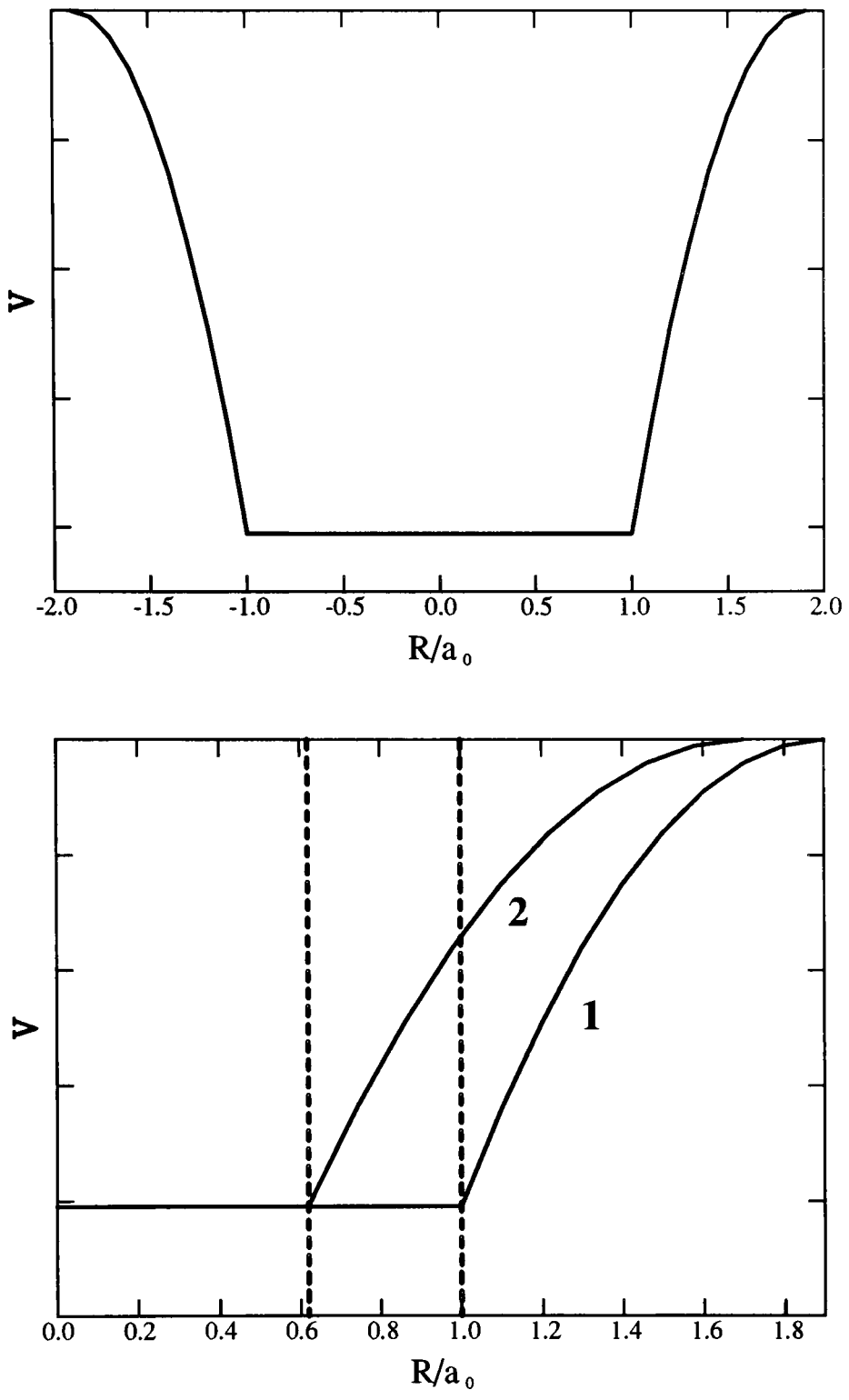


FIGURE 1.2: *Potential felt by an electron in an anion at the origin due to the crystalline environment. Top - due to point charges only, bottom - curve 1 - point charges only, 2 - with overlap terms.*

Anion	FREE	CRYS	CLUS
	(all in atomic units)		
F^-	10.654	7.300	6.18
Cl^-	31.468	26.655	20.232
O^{2-}	"∞"	21.177	12.32

TABLE 1.1: Ab initio *polarizabilities for anions in the free state (FREE) , in a lattice of point charges (CRYS), and with a fully described first cation shell (CLUS). From [6], [5] and [7] respectively.*

This extra (dominant) term arises from the increase in kinetic energy of the electrons in the regions where the electron density due to nearest-neighbours is non-zero due to the Exclusion Principle.

Overall, therefore, both the overlap and crystal field effects act to *compress* the anion electron density markedly. The effect can be seen in the reduction of the anion polarizability. Some examples from *ab initio* coupled-Hartree-Fock (CHF) calculations are given in table 1.1. The CRYS column contains the effect of the Madelung terms only whilst the CLUS column contains a full description of the first cation shell. The energy required to compress the free anion into the crystalline environment is termed the *self* (rearrangement) energy.

Thus, for the halides the effect of the confining potentials is to reduce the polarizability by around 40%. However, the nature of the counterion is relatively unimportant, that is, the alkali metal cations tend to reduce the halide polarizability by around the same amount (see table 4.7 in chapter 4).

The effect on O^{2-}, however, is much more dramatic. In the free state the doubly charged anion is *unstable* with respect to electron loss ($\Delta U^{affin}(O \rightarrow O^-)$ = -142kJmol^{-1}, $\Delta U^{affin}(O^- \rightarrow O^{2-})$ = +844 kJmol^{-1}), that is, the polarizability of the free O^{2-} is effectively infinite. Addition of the second electron can be stabilized, however, by the confining potential of the crystal giving finite polarizabilities [4, 7]. The fact that the anion is only stable at all due to the crystalline environment means that the variation in anion properties is much more dependent upon the precise nature of that environment. The implications of this will be discussed further when the proposed models are parameterized (chapters 3 and 8).

The same arguments also apply for a central *cation* surrounded by nearest-neighbour anions. Figure 1.3 shows the potential on the central cation. Thus, the effect of the neighbours in the point charge approximation is similar to that in the anion case but of the opposite sign due to the repulsive interaction between the cation electron density and the negatively charges point charges. Hence, this potential acts to *destabilize* the cation electrons with respect to the free state.

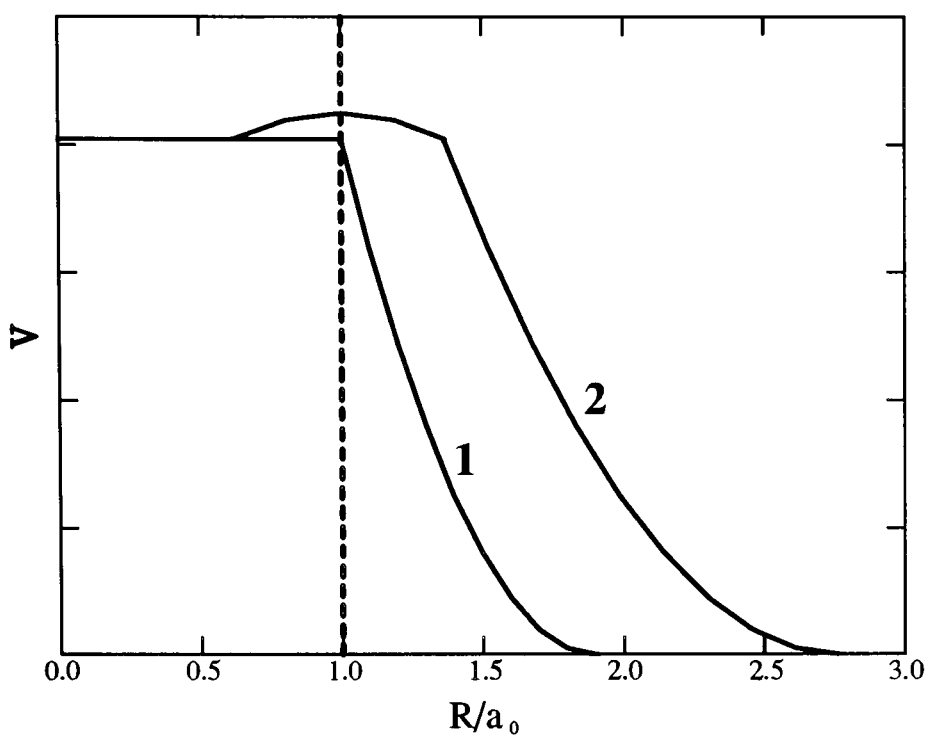


FIGURE 1.3: *Potential experienced by an electron in a cation at the origin in the crystalline environment. Curve labels as figure 1.2.*

Overall, therefore, the crystal field has very little effect on the cation properties, with respect to the free state, as the cation electrons tend to be more tightly bound with respect to those in the anions due to the excess of positive nuclear charge. Hence, the cation is relatively unperturbed by the crystalline environment. *Ab initio* calculations confirm the very small dependence of the cation polarizabilities on the crystalline environment [5].

1.3 The Rigid-ion Model.

In an *undeformed* crystal the system energetics can be effectively represented as a combination of the short-range (overlap), coulombic and dispersion effects. This is the *rigid-ion model* (RIM) and is the simplest simulation model for ionic

systems. The simplest potential available is of the Born-Mayer type [9] simply

$$U^{ij}(r^{ij}) = \underbrace{\frac{Q^i Q^j}{r^{ij}}}_{Coulombic} + \underbrace{B^{ij} e^{-a^{ij} r^{ij}}}_{Short-range} + \underbrace{\sum_{n=6,8,10\ldots} \frac{C_n^{ij}}{R^{ij\,n}} f_n^{ij}}_{Dispersion}, \tag{1.3}$$

that is, the sum of the coulombic and overlap interactions for the ion pair ij. The preexponent B^{ij} is governed by the sum of the ionic radii of i and j and a^{ij} is the "steepness" of the repulsive potential wall. Such potentials are usually augmented with pairwise additive dispersion terms shown as a summation in the above equation. The f_n function represents the effect of dispersion damping. These terms are usually cutoff at the C_6 (dipole-dipole) or C_8 (dipole-quadrupole) level. These potentials have been used with great success, mainly concentrating on the alkali halide series (see [10] for a review) and are usually parameterized by fitting to known experimental properties such as perfect crystal energetics and densities.

It has long been known, however, that the RI description is inadequate for describing even alkali halide behaviour when the crystal is *deformed.* Specifically;

- in crystals the *phonon dispersion curves* are poorly reproduced. In a primitive model the splitting at the Brillouin zone centre is given by the expression due to Lyddane, Sachs and Teller [11]

$$\frac{\omega_{LO}^2}{\omega_{TO}^2} = \frac{\epsilon_0}{\epsilon_\infty}, \tag{1.4}$$

  where ϵ_∞ is the high frequency dielectric permittivity and ϵ_0 is the static dielectric constant. For rigid (unpolarizable) ions ϵ_∞ is unity but is higher in reality (i.e $\epsilon_\infty = 2.2$ for NaCl and 4.0 for AgCl [12]). The result of the RI approximation is that the LO-TO splitting at the Brillouin zone centre is too great [13].

- in liquids the frequencies of the *charge density waves* (analogous to the crystalline optical phonons) are poorly described, whilst diffusion coefficients are often too small [13, 14].

A further problem lies in the model parameterization. For systems away from the alkali halides more complex RI potentials have had to be derived in order to reproduce the known experimental properties. For example, the potential of

Rahman, Vashishta and Parrinello (RVP) [15] has been very successful in modelling the various phase transitions that occur in crystalline AgI. This potential employs low ionic charges, extra-soft repulsive walls and additional pairwise additive r^{-4} terms which can be interpreted as modelling induction effects in a crude way. The crucial point is that, although such potentials have been successful in modelling specific properties they are often less reliable away from the statepoints on which they have been parameterized. They are not *transferable.* The inclusion of these effects in the correct manner should allow the derivation of potentials that are *transferable.*

1.4 Distorting the Crystal.

Having ascertained the effect of the perfect crystalline environment on both the anion and the cation it is important to now understand the effect of *distorting* the perfect lattice. It is anticipated that this scenario will be important in developing a model that will be effective in *both* the solid and liquid phases

Consider the anion in the perfect lattice site as in the previous section. Now consider the effect of moving a single cation from the first coordination shell outwards by a small displacement (figure 1.4) Fowler and Madden [16, 17] performed electronic structure calculations on these distorted crystals and noted two major effects:

- *Coulombic induction.* The outward displacement of the cation leaves a resultant electric field along the line of the displaced cation-anion inducing a dipole whose positive end will point at the displaced cation.

- *Overlap induction.* The displaced cation has effectively left a hole in the spherical pseudopotential. The compressing effect of the first shell has been effectively relaxed in the direction of the displaced cation. Thus, the anion electron density is pushed into this hole inducing a dipole that *opposes* that induced by the coulombic field.

Figure 1.5 shows the effect of this distortion of the potential felt by the anion. The coulombic field tends to restrict the anion electron motion towards the distortion whilst the overlap effect opposes this leading to the short-dashed potential in figure 1.5. The shape of this curve lead to its description as the

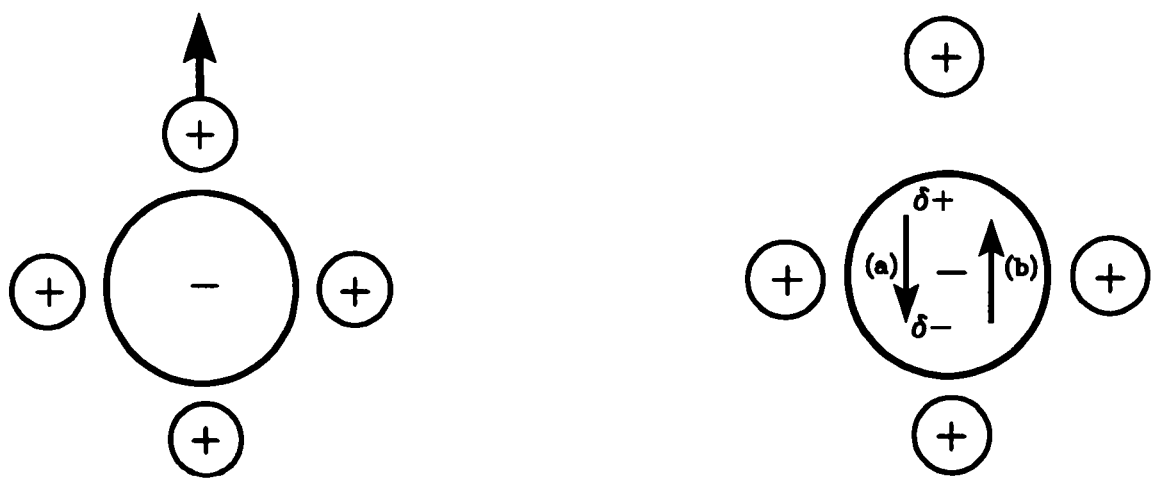


FIGURE 1.4: *Schematic showing the effect on an anion (right) of distorting the first cation shell as shown on the left. The result is a coulomb-field induced dipole (left) and an overlap-induced dipole (right).*

"dent-in-the-wall". Fowler and Madden showed that this effect is approximately additive for several ions.

An analogous analysis can be applied to a *quadrupolar* deformation of the type shown in figure 1.6 Again, the coulombic induced moment is opposed by that induced from overlap effects.

1.5 Including Induction Effects.

1.5.1 The Problem of Non-additivity.

The addition of induction effects to the RI model is a non-trivial problem. Within the *dipolar approximation* (DA) the dipole induced on an ion i by a permanent charge on j for the isolated pair ij is

$$\boldsymbol{\mu}^i = \alpha \mathbf{E}^{ij}, \tag{1.5}$$

where α is the *polarizability* of ion i and $\mathbf{E}^{ij}$ is the electric field on i due to j [18]. One might hope, therefore, that the dipole induced on i in a condensed system would be

$$\boldsymbol{\mu}^i = \alpha \sum_{i \neq j} \mathbf{E}^{ij}. \tag{1.6}$$

Sadly, the world rarely functions in such a trivial way and, indeed, the above equation is *wrong*. Consider figure 1.7 : On the left $\boldsymbol{\mu}^i$ is given by equation 1.5. On the right the same ion pair has been placed in a condensed environment.

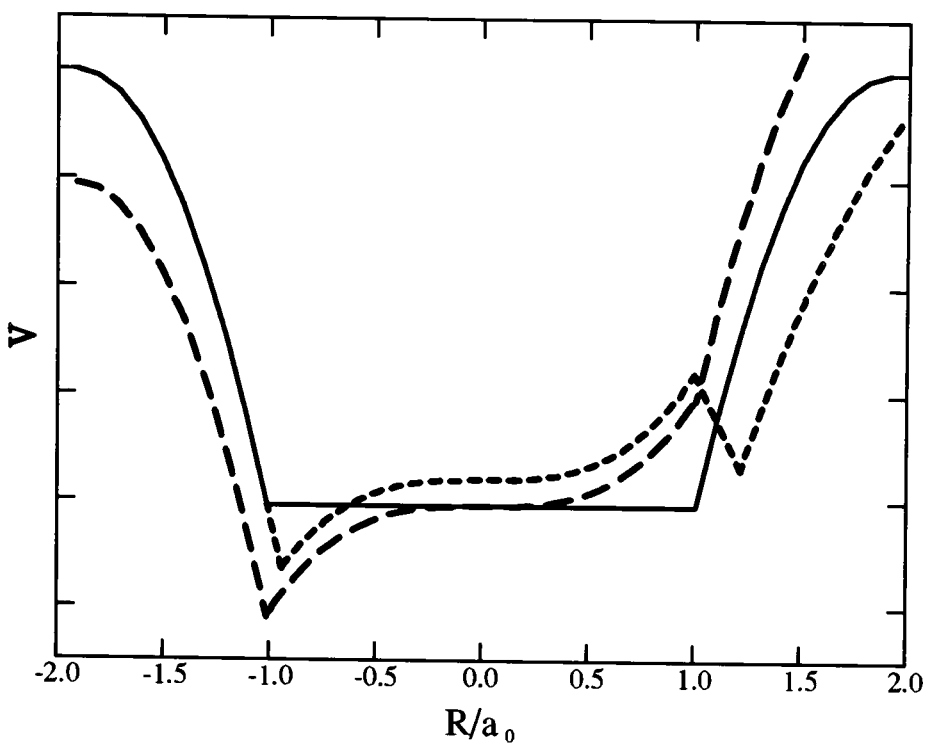


FIGURE 1.5: *The change in the potential felt by an anion at the origin as a cation in the first shell is distorted outwards by 1/10 of* a_0. *Key: solid line - undistorted potential, long-dashes - coulomb-field induced potential after distortion, short-dashes - total potential after distortion.*

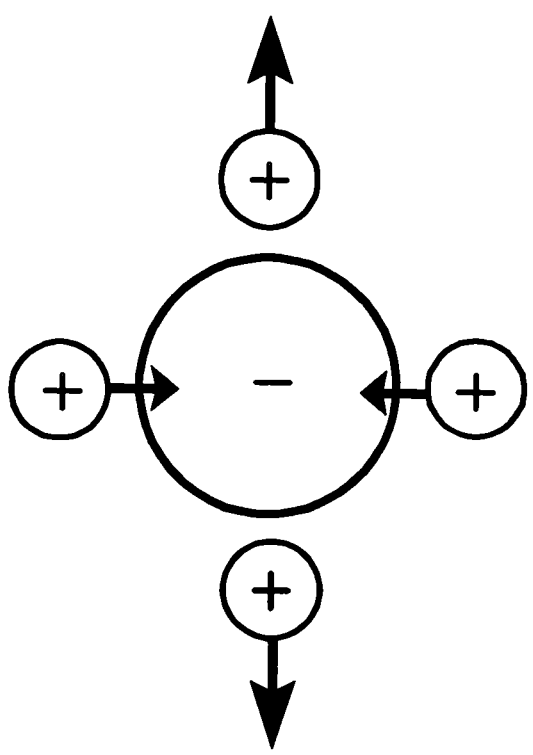


FIGURE 1.6: *Schematic quadrupolar distortion about an anion.*

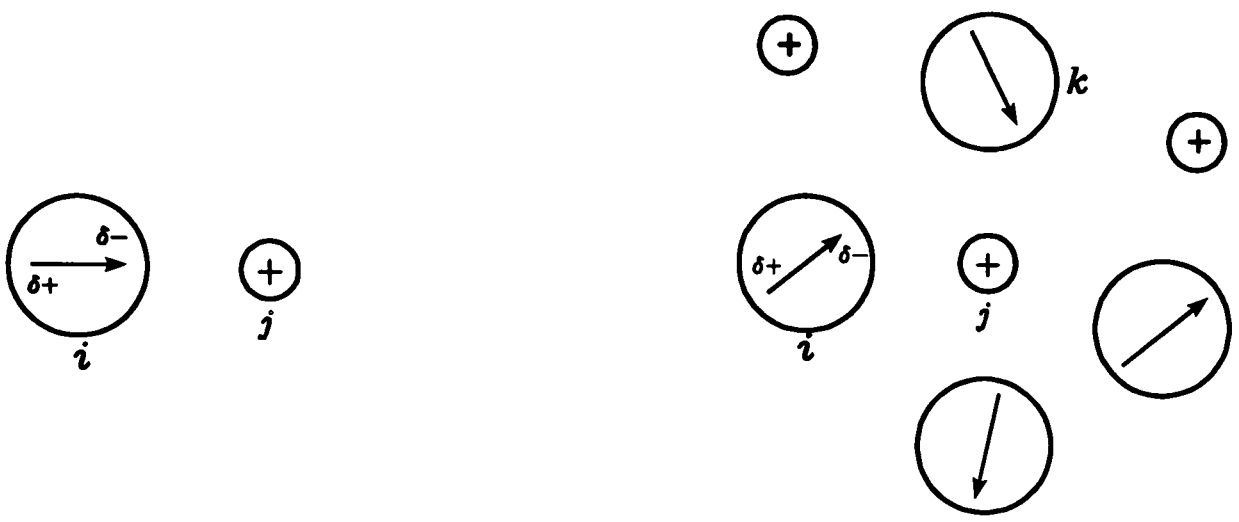


FIGURE 1.7: *Schematic ionic system illustrating the non-additivity of induction effects. Left - ion pair only, right - same ion pair in a condensed environment.*

Thus, the dipole induced on, for example, k by the charge on j will also influence the dipole on i which will, in turn, alter the dipole on k. Thus, the *self-consistent* dipoles on each site can only be obtained via the solution of the coupled equations [19]

$$\boldsymbol{\mu}^i = \alpha^i \left\{ \underbrace{\sum_{j \neq i} \frac{Q^j \mathbf{r}^{ij}}{r^{ij\,3}}}_{charge\ induced} - \underbrace{\sum_{j \neq i} \left[\frac{\boldsymbol{\mu}^i}{r^{ij\,3}} - \frac{3\mathbf{r}^{ij}(\mathbf{r}^{ij}.\boldsymbol{\mu}^{ij})}{r^{ij\,5}} \right]}_{dipole-dipole\ coupling} \right\}, \tag{1.7}$$

leading to the non-additivity. It is the presence of this non-additivity that has made simulation including these effects computationally expensive with respect to simple RI calculations. It should be stressed that, once the coupled equations have been solved, then the induced dipoles generated include *many-body* interactions up to and including the order of the number of polarizable ions in the simulation cell.

1.5.2 The Shell Model.

Polarization effects have traditionally been incorporated into simulations of ionic systems via the **shell model** (SM) (see i.e [10]). Figure 1.8 shows a typical setup in which an ion is represented by a core joined to a shell by a harmonic spring. The polarizability of the ion is parameterized by the shell charge (Y) and the spring force constant (k) with the overall ion charge (the sum of the shell and core charges) being the formal ionic charge (in the figure the ion has overall charge -1). The short range overlap interactions are considered to act

on the shells and so dipoles are induced both by the coulombic field *and* by short range interactions. The shell model was originally introduced in *lattice dynamics* (LD) calculations. A dynamical matrix can be obtained for the model and then diagonalized to produce phonon frequencies. The shell charge and spring constant were parameterized by empirical fitting to experimental data which included the low and high frequency dielectric permittivity and therefore information on the dipoles associated with lattice vibrations.

More recently molecular dynamics calculations have been done with the shell model. At each time step the shells must be relaxed into the self-consistent energy minimum by solving equation 1.7. This can be done via an iterative steepest descent method or, more recently, by a conjugate gradient method [20]. Recent progress has been made in applying a Car-Parrinello type algorithm [21] which eliminates with the need for the computationally expensive series of minimizations.

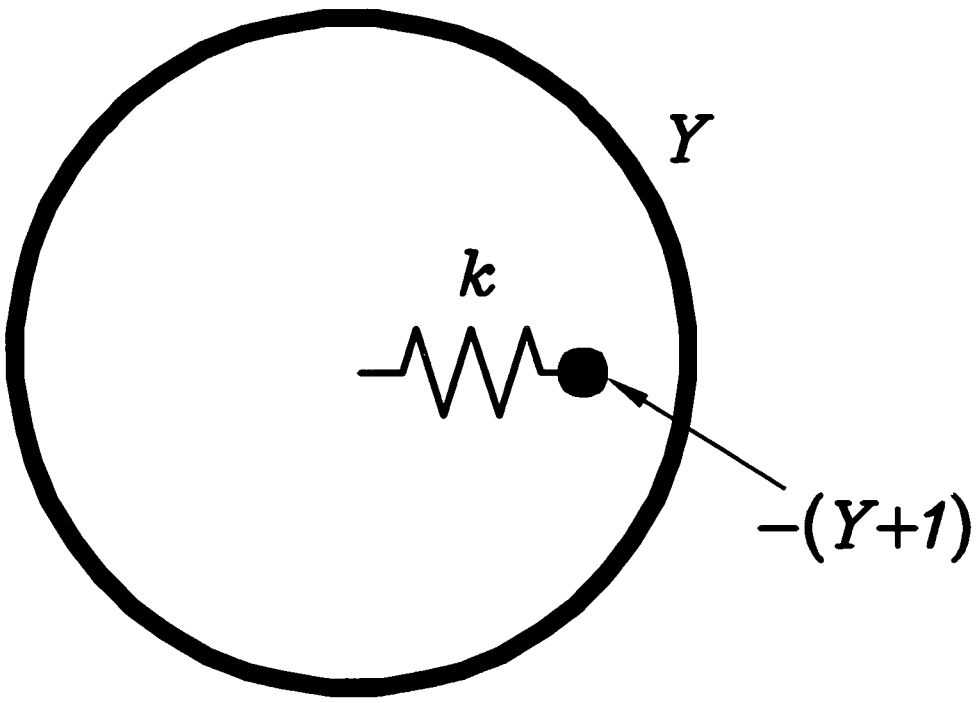


FIGURE 1.8: *The shell model for an anion of charge -1 consisting of a shell of charge Y, a core of charge -(Y+1), connected by a harmonic spring with force constant k.*

The notable success of the SM over the RIM is in improving the crystalline phonon dispersion curves of the alkali halides by allowing polarization effects. However these models do not give good agreement with experiment away from the MX stoichiometry, notably for the MX_2 systems with a small M^{2+} cation. Furthermore, difficulties with parameterization are encountered. For example,

positive shell charges may emerge, especially in systems with polarizable cations and, generally speaking, shell parameters do not enjoy a high degree of transferability. The original idea that the shell represents the displaced electron cloud is difficult to sustain in these circumstances.

The construct of allowing the short-range induced dipoles to be a result of the Born-Mayer interaction between shells seems to have no *a priori* justification. It does mean that relatively few parameters need to be determined empirically. However, *ab initio* investigations of induced dipoles (see chapter 3) show clear differences with the dipoles generated by the shell model. What is required is a computationally tractable model in which all aspects of polarization phenomena are represented and parameterized via *ab initio* calculations.

A further problem with the SM is the lack of natural progression to higher order multipoles. Breathing-shell models [22] contain these terms but their values tend not to be well controlled. Such deformations have been included (see i.e Fischer *et al* [23] and chapter 7) at a lattice dynamics level. MD simulations on condensed ionic systems with higher order induced moments are still lacking. This problem will be addressed in chapter 7.

The shell model indicates how additional degrees of freedom may be introduced into a simulation model which themselves interact in a simple way but allow for a representation of the complex, many-body, forces. It is of interest to develop a model of induction effects of this nature but to allow for a more flexible representation of the overlap induced moments than the shell model allows. This representation should be capable of accurately representing results of *ab initio* calculations.

1.5.3 Other Models.

Sabounghi *et al* [24] studied $NaAlCl_4$ with dipolar polarizable Cl^- anions, finding that the structure was greatly altered with respect to the RIM analogues. In this model the dipoles were induced purely by coulombic effects.

Sprik and Klein [25] used the same basic model type to study dipolar induction effects in water [25, 26, 27, 19] and the solvation of Cl^- [28, 19]. Instead of using point dipoles they chose to model both the induced *and* permanent dipoles in H_2O via a *tetrahedron* of four dynamic charges whose orientation is fixed with respect to the molecular frame of reference. The dimensions of the tetrahedron

are kept small in order that higher order multipoles are not problematic (a typical vertex-vertex separation being 0.28Å). Thus, the system Lagrangian was extended to contain these dynamical charges as additional degrees of freedom. In this model *short range* induction effects are included. As was shown in section 1.2 short-range induced moments are significant for nearest-neighbour interactions. In the Sprik-Klein model these effects are mimicked by representing the dynamic charges by Gaussian distributions,

$$g^{i\alpha}(\mathbf{r},t) = \frac{1}{(2\pi\xi^2)^{\frac{3}{2}}} q^{i\alpha}(t) exp\left\{\frac{-(\mathbf{r}-\mathbf{r}^{i\alpha}(t))^2}{2\xi^2}\right\}. \tag{1.8}$$

The width of the gaussian, ξ, is determined by optimization to the system energy, pressure and form of the O-O distribution function giving, a value of 0.7Å. Thus, at small separations the Gaussian nature of the dynamic charges will tend to damp down the coulombic induced dipole in the desired manner.

1.6 Summary.

The outline of this thesis is as follows. In chapter 2 models to allow for the simulation of condensed ionic systems including both induced dipoles and quadrupoles will be derived. In chapter 3 the theory behind, and the methods of, parameterization will be discussed.

The importance of anion polarization effects in determining the crystal properties of the alkaline-earth halides will be demonstrated in chapter 4. In chapter 5 the same model will be shown to similarly reproduce known liquid-state results, including the formation of networks such as in $ZnCl_2$. In chapter 6 the effect of adding network modifiers to $ZnCl_2$ will be considered along with the implications for the nature of the first sharp diffraction peak present in pure $ZnCl_2$ and some (but not all) of the network-modified systems.

In chapter 7 the roles of cation polarization at both a dipolar and quadrupolar level will be discussed in a study of the crystalline and molten state properties of AgCl.

Finally, in chapter 8, a model to simulate metallic oxides will be developed in which the size of the oxide anion is included as an additional variable dependent upon the crystalline environment. This model will be used to look at phase transitions in MgO and CaO.

2

Simulation Methods.

In standard molecular dynamics (MD) the classical equations of motion for a system of N molecules, with kinetic energy $\mathcal{T}$, interacting through a given potential $\mathcal{U}$ are solved. The Lagrange-Euler equation has the form

$$\frac{d}{dt}\frac{\partial \mathcal{L}}{\partial \dot{\mathbf{r}}^i} - \frac{\partial \mathcal{L}}{\partial \mathbf{r}^i} = 0, \tag{2.1}$$

where $\mathcal{L}(= \mathcal{T} - \mathcal{U})$ is the Lagrangian and $\mathbf{r}^i$ is the set of 3N coordinates, $\{\mathbf{r}^N\} - \{\mathbf{r}^i, i = 1, ..., N\}$ with momenta $\mathbf{p}^N$. For a set of spherical atoms the recognisable Newtonian equations are recovered,

$$\mathbf{F}^i = -\frac{\partial \mathcal{U}}{\partial \mathbf{r}^i} \tag{2.2}$$

$$\mathbf{p}^i = m^i \mathbf{v}^i = \frac{\partial \mathcal{T}}{\partial \dot{\mathbf{r}}^i}. \tag{2.3}$$

The conserved variable is the Hamiltonian, $\mathcal{H} = \mathcal{U} + \mathcal{T}$.

As discussed in the introduction, to express $\mathcal{U}$ simply in terms of the ionic coordinates leads to a very complex many-body interaction. To circumvent this, additional degrees of freedom are included to represent the changes in the ion's properties brought about by interaction with its neighbours. In the **polarizable-ion model** (PIM) these *additional* degrees of freedom are the components of the induced multipole moments on the ions. These induced moments are included in the total system Hamiltonian and the equations governing their time-evolution are generated via an *extended Lagrangian formalism.*

2.1 Deriving the Equations of Motion.

In this section equations of motion will be derived that govern the time-evolution of induced multipoles in ionic systems. Two models will be considered; firstly only induced dipoles will be included, and then the generalisation to both induced quadrupoles and dipoles will be made.

2.1.1 Dipolar Model.

In the simplest model only induced dipole moments (ion distortions due to the electric fields only) are included. This is the *dipolar approximation* (DA) in which the Hamiltonian has the form:

$$\mathcal{H} = \mathcal{U} + \mathcal{T} \tag{2.4}$$

$$\mathcal{U} = \sum_{i=1}^{N_t-1} \sum_{j=i+1}^{N_t} \{U^{sr}(r^{ij}) + T^{ij}Q^iQ^j + T^{ij}_{\alpha}(Q^j\mu^i_{\alpha} - Q^i\mu^j_{\alpha}) - T^{ij}_{\alpha\beta}\mu^i_{\alpha}\mu^j_{\beta}\}$$

$$+ k^{\mu}\sum_{i=1}^{N_t}\mu^{i2} \tag{2.5}$$

$$\mathcal{T} = \frac{1}{2}\sum_{i=1}^{N_t} m^i v^{i2} + \frac{1}{2}\sum_{i=1}^{N_t} m^i_{\mu}\dot{\mu^i}^2, \tag{2.6}$$

where r^{ij} represents the separation of ions i and j, U^{sr} is the short-range part of the potential, N_t is the total number of ions, $\boldsymbol{\mu}^i$ is the dipole induced on ion i (of which α labels an individual component xyz), and T^{ij}, T^{ij}_{α} and $T^{ij}_{\alpha\beta}$ are the components of the charge-charge, charge-dipole and dipole-dipole interaction tensors respectively. In general terms these are given by [18]:

$$T^{ij}_{\alpha\beta\gamma\delta....} = \nabla_{\alpha}\nabla_{\beta}\nabla_{\gamma}\nabla_{\delta}...\frac{1}{r^{ij}}. \tag{2.7}$$

These are written out explicitly in appendix A including the higher order tensors required to extend the model to include induced quadrupoles. Note that the Einstein summation convention is employed implying that repeated Greek indices are summed over. The k^{μ} term represents the energy required to polarize an ion.

The Lagrangian for this system has the form:

$$\mathcal{L} = \mathcal{T} - \mathcal{U}, \tag{2.8}$$

thus the equation of motion governing the ion positions now reads:

$$\frac{d}{dt}\frac{\partial \mathcal{L}}{\partial \dot{\mathbf{r}}^i} - \frac{\partial \mathcal{L}}{\partial \mathbf{r}^i} = 0 \tag{2.9}$$

$$m_i\ddot{\mathbf{r}}^i = -\nabla_{\mathbf{r}^i}\mathcal{U}. \tag{2.10}$$

Similarly equations of motion can be generated that govern the time evolution of the additional degrees of freedom. Thus, for a component α of the induced

dipole

$$\frac{d}{dt}\frac{\partial \mathcal{L}}{\partial \dot{\mu}^i_\alpha} - \frac{\partial \mathcal{L}}{\partial \mu^i_\alpha} = 0 \tag{2.11}$$

$$m^i_\mu \ddot{\mu}^i_\alpha = \sum_{j \neq i}^{N_t} \left\{ -T^{ij}_\alpha Q^j + T^{ij}_{\alpha\beta} \mu^j_\beta \right\} - 2k^\mu \mu^i_\alpha. \tag{2.12}$$

The additional degrees of freedom are at equilibrium, for a given ionic configuration, when $\ddot{\mu}^i_\alpha = 0$, i.e. there is no "force" acting to alter the induced moments. Thus, equation 2.12 gives

$$2k^\mu \mu^i_\alpha = \sum_{j \neq i}^{N_t} \left\{ -T^{ij}_\alpha Q^j + T^{ij}_{\alpha\beta} \mu^j_\beta \right\}. \tag{2.13}$$

The right-hand side of this equation is simply the total electric field, E^i_α on site i due to all other permanent charges Q^j and all other induced dipole components μ^j_β. Thus,

$$2k^\mu \mu^i_\alpha = E^i_\alpha. \tag{2.14}$$

Setting $k^\mu = \frac{1}{2\alpha}$, where α is the dipole polarizability, recovers the correct equation relating the induced dipole to the electric field, namely, $\mu^i_\alpha = \alpha E^i_\alpha$ [18]. Substitution back into equation 2.6 recovers the correct form of the induction energy,

$$U^i_{ind} = \sum_{j \neq i}^{N_t} \left\{ T^{ij}_\alpha Q^j \mu^i_\alpha - T^{ij}_{\alpha\beta} \mu^i_\alpha \mu^j_\beta \right\} + k^\mu {\mu^i_\alpha}^2 \tag{2.15}$$

$$= -E^i_\alpha \mu^i_\alpha + k^\mu {\mu^i_\alpha}^2, \tag{2.16}$$

and, substituting in $k^\mu = \frac{1}{2\alpha}$ and $\mu^i_\alpha = \alpha E^i_\alpha$ gives

$$U^i_{ind} = -\frac{1}{2} \alpha {E^i_\alpha}^2, \tag{2.17}$$

which is the correct induction energy within the dipolar approximation [29].

If *all* of the induced dipoles in the system obey the equilibrium or *adiabatic* condition then the electric field that they generate will include the full self-consistent (many-body) dipolar polarization effects. This field is denoted $\bar{\mathbf{E}}$ and termed the *adiabatic field.* If this condition is obeyed the full equation of motion for the ion translation now becomes

$$m^i \ddot{r}^i_\alpha = -\sum_{j \neq i}^{N_t} \left\{ \nabla_{r^i_\alpha} U^{sr}(r^{ij}) - Q^i \bar{E}^i_\alpha - \mu^i_\beta \bar{E}^i_{\alpha\beta} \right\}, \tag{2.18}$$

which is precisely the form expected for an ion carrying a charge Q^i and dipole $\boldsymbol{\mu}^i$ in the field $\mathbf{E}^i$. Consequently, the induced dipoles contribute to the induction forces on the ions in the correct way *provided that the adiabatic condition holds.*

Overlap-induced Dipoles.

The above analysis demonstrates how equations of motion obtained from a multipole expansion can readily be derived for dipoles induced by coulombic fields. In condensed ionic systems, however, there is another significant contribution to the induced moments due to *overlap effects.* It was shown in the introduction that these overlap effects *oppose* the coulombic dipole induced on an anion by a cation but *reinforce* that induced on the cation by the anion. In the shell model description of induction effects (see section 1.5.2) the short range part of the Fumi-Tosi potential [9] is taken to act on the *shells* effectively *damping* the coulombic dipoles at close anion-cation approach. This *ad hoc* procedure limits the magnitude of the overlap-induced dipoles to the interionic potential in an overly restrictive manner leading to the kind of extensive parameterization difficulties discussed in 1.5.2.

Fowler and Madden [16] have investigated the short-range induced dipole (i.e. the part of the dipole not induced by the coulomb field and its gradient) in a series of electronic structure calculations on distorted LiF crystals. They demonstrated that it could be viewed as the result of an additional potential (dubbed the "dent-in-the-wall" term) that was approximately additive (see section 1.4). This suggests that these dipoles can be incorporated into the present model by adding a term to the coulombic field, $\mathbf{E}^c$. Thus

$$\boldsymbol{\mu}^i = \alpha \mathbf{E}^c(\mathbf{r}^i) + \sum_{j \neq i}^{N_t} \alpha f(r^{ij}) \frac{Q^j \mathbf{r}^{ij}}{\mid r^{ij^3} \mid}, \tag{2.19}$$

where $f(r)$ is a suitable short-range function which will be chosen to go to a limiting value of -1 as $r \rightarrow 0$ and to reproduce the *ab initio* dipoles calculated by Fowler and Madden when r is in the range of nearest neighbour separations. A convenient form for $f(r)$ was introduced by Tang and Toennies [30] as a damping function for dispersion forces

$$f(r^{ij}) = -e^{-br^{ij}} \sum_{k=0}^{4} \frac{(br^{ij})^k}{k!}, \tag{2.20}$$

which has the limiting properties described above and which involves a *single parameter*, b, termed the *short range damping parameter* (SRDP).

The dipolar equation of motion (2.12) now becomes

$$m^i_\mu \ddot{\mu}^i_\alpha = -k^\mu \mu^i_\alpha + E^i_\alpha + \sum_{j \neq i}^{N_t} \frac{\mathbf{r}^{ij}}{\mid r^{ij^3} \mid} f(r^{ij}) Q^j, \tag{2.21}$$

whilst the full translational equation of motion becomes

$$m^i r^{ij}_\alpha = F^c_\alpha + \frac{\mu_\alpha f(r^{ij})}{\mid r^{ij^3} \mid} Q^j + \boldsymbol{\mu}^i . \mathbf{r}^{ij} \left\{ \frac{-3 r^i_\alpha f(r^{ij})}{\mid r^{ij^5} \mid} + \frac{r^i_\alpha}{\mid r^{ij^4} \mid} \frac{df(r^{ij})}{dr^{ij}} \right\}, \tag{2.22}$$

where F^c_α denotes the force given by equation 2.18. The extraction of the SRDP from *ab initio* calculations will be discussed in section 3.3.

2.1.2 Quadrupolar Model.

Within the *quadrupole approximation* (QA) all moments induced by the field and field gradient are included. In a spherical ion these moments are given by [18]:

$$\mu^i_\alpha = \alpha E^i_\alpha + \frac{1}{3} B E^i_\alpha E^i_{\beta\gamma} \tag{2.23}$$

$$\theta^i_{\alpha\beta} = \frac{1}{2} B E^i_\alpha E^i_\beta + C E^i_{\alpha\beta}, \tag{2.24}$$

where $E_{\beta\gamma}$ is a component of the field *gradient* and B and C are the dipole-dipole-quadrupole hyperpolarizability and the quadrupole polarizability respectively.

A Hamiltonian which allows for both contributions to the induced quadrupole has the form:

$$\begin{aligned}
\mathcal{H} &= \mathcal{U} + \mathcal{T} \qquad (2.25)\\
\mathcal{U} &= \sum_{i=1}^{N_t - 1} \sum_{j=i+1}^{N_t} \{ U^{sr}(r^{ij}) + T^{ij} Q^i Q^j + T^{ij}_\alpha (Q^j \mu^i_\alpha - Q^i \mu^j_\alpha) \\
&+ T^{ij}_{\alpha\beta} (-\mu^i_\alpha \mu^j_\beta + \frac{1}{3} Q^i \theta^j_{\alpha\beta} + \frac{1}{3} Q^j \theta^i_{\alpha\beta}) \\
&+ T^{ij}_{\alpha\beta\gamma} (\frac{1}{3} \mu^i_\alpha \theta^j_{\beta\gamma} - \frac{1}{3} \mu^j_\alpha \theta^i_{\beta\gamma}) \\
&+ T^{ij}_{\alpha\beta\gamma\delta} (\frac{1}{9} \theta^i_{\alpha\beta} \theta^j_{\gamma\delta}) \} \\
&+ k_1 \sum_{i=1}^{N_t} \mu^{i^2} + k_2 \sum_{i=1}^{N_t} \mu^i_\alpha \theta^i_{\alpha\beta} \mu^i_\beta
\end{aligned}$$

$$+ \quad k_3 \sum_{i=1}^{N_t} \theta^i_{\alpha\beta}\theta^i_{\alpha\beta} + k_4 \sum_{i=1}^{N_t} \mu^{i4} \tag{2.26}$$

$$\mathcal{T} = \frac{1}{2}\sum_{i=1}^{N_t} m^i v^{i2} + \frac{1}{2}\sum_{i=1}^{N_t} m^i_\mu \dot{\mu^i}^2_\alpha + \frac{1}{2}\sum_{i=1}^{N_t} m^i_\theta \dot{\theta^i}^2_{\alpha\beta}, \tag{2.27}$$

where the inclusion of the μ^4 term means that all terms up to and including those to the power four in the electron density which are allowed by the spherical symmetry of the ion are included. Thus, the equations of motion for the induced moment components now have the form:

$$\frac{d}{dt}\frac{\partial \mathcal{L}}{\partial \dot{\mu}^i_\alpha} - \frac{\partial \mathcal{L}}{\partial \mu^i_\alpha} = 0$$

$$\begin{aligned} m^i_\mu \ddot{\mu}^i_\alpha &= \sum_{j\neq i}^{N_t} \left\{ -T^{ij}_\alpha Q^j + T^{ij}_{\alpha\beta}\mu^j_\beta - \frac{1}{3}T^{ij}_{\alpha\beta\gamma}\theta^j_{\beta\gamma} \right\} \\ &- 2k_1\mu^i_\alpha - 2k_2\mu^i_\beta\theta^i_{\alpha\beta} - 4k_4\mu^i_\alpha\mu^{i2} \end{aligned} \tag{2.28}$$

and

$$\frac{d}{dt}\frac{\partial \mathcal{L}}{\partial \dot{\theta}^i_{\alpha\beta}} - \frac{\partial \mathcal{L}}{\partial \theta^i_{\alpha\beta}} = 0$$

$$\begin{aligned} m^i_\theta \ddot{\theta}^i_{\alpha\beta} &= \sum_{j\neq i}^{N_t} \left\{ -\frac{1}{3}T^{ij}_{\alpha\beta}Q^j + \frac{1}{3}T^{ij}_{\alpha\beta\gamma}\mu^j_\gamma - \frac{1}{9}T^{ij}_{\alpha\beta\gamma\delta}\theta^j_{\gamma\delta} \right\} \\ &- k_2\mu^i_\alpha\mu^i_\beta - 2k_3\theta^i_{\alpha\beta}. \end{aligned} \tag{2.29}$$

Again note that the sum of the T^{ij} terms in equation 2.28 is simply the component α of the total electric field at site i, E^i_α whilst in equation 2.29 this sum is $\frac{1}{3}E^i_{\alpha\beta}$ [18].

The definition of the induced quadrupole required is that it be traceless throughout [29]. Consideration of equation 2.29 demonstrates that the $k_2\mu^i_\alpha\mu^i_\beta$ term is the only that can lead to a trace. Hence, this term is *constrained* with an additional quantity which acts to remove the trace. Each k_2 term is replaced by

$$k_2\left(\mu^i_\alpha\mu^i_\beta - \frac{\delta_{\alpha\beta}\mu^{i2}}{3}\right), \tag{2.30}$$

which is, of course, traceless. Note that the use of Lagrangian mechanics lends itself easily to the use of such constraints.

Again, the system is in equilibrium when no forces are acting on the induced moments, that is, $\ddot{\mu}^i_\alpha = 0$ and $\ddot{\theta}^i_{\alpha\beta} = 0$. Thus, equating 2.28 and 2.29 to zero

and solving for μ^i_α and $\theta^i_{\alpha\beta}$ the relationships become

$$k_1 = \frac{1}{2\alpha} \tag{2.31}$$

$$k_2 = \frac{-B}{6\alpha^2 C} \tag{2.32}$$

$$k_3 = \frac{1}{6C} \tag{2.33}$$

$$k_4 = \frac{-B^2}{36\alpha^4 C}. \tag{2.34}$$

Substitution back into equation 2.24 yields the correct terms for both induced moments whilst substitution back into the original Hamiltonian (equation 2.27) gives the desired energy expression [18] (see Appendix B).

$$U^i_{ind} = -\frac{1}{2}\alpha {E^i_\alpha}^2 - \frac{1}{6}B E^{i2} E^i_{\alpha\beta} - \frac{1}{6}C {E^i_{\alpha\beta}}^2. \tag{2.35}$$

Thus, the full equation of motion within the QA now reads:

$$m^i \ddot{r}^i_\alpha = -\sum_{j\neq i}^{N_t} \left\{ \nabla_{r^i_\alpha} U^{sr}(r^{ij}) - Q^j \bar{E}^i_\alpha - \mu^j_\beta \bar{E}^i_{\alpha\beta} - \frac{1}{9}\theta^i_{\beta\gamma}\bar{E}^i_{\alpha\beta\gamma} \right\}, \tag{2.36}$$

where the bar notation again represents *adiabatic* fields and gradients.

2.2 Simulation Techniques.

2.2.1 Integrating the Equations of Motion.

In order to use the equations of motion within an MD simulation they must be solved with a *finite difference method.* All sets of equations of motion (i.e equations 2.18 and 2.12 for the dipolar model and equations 2.36, 2.28 and 2.29 for the quadrupoles) can be integrated using a standard **leapfrog algorithm** [31]. These equations can be derived as follows. Firstly the ion coordinates are Taylor expanded about $\mathbf{r}^i(t)$ giving

$$\mathbf{r}^i(t+\Delta t) = \mathbf{r}^i(t) + \mathbf{v}^i(t)\Delta t + \frac{1}{2}\mathbf{a}^i(t)\Delta t^2 .... + \mathcal{O}(\Delta t^3) \tag{2.37}$$

$$\mathbf{r}^i(t-\Delta t) = \mathbf{r}^i(t) - \mathbf{v}^i(t)\Delta t + \frac{1}{2}\mathbf{a}^i(t)\Delta t^2 .... + \mathcal{O}(\Delta t^3) \tag{2.38}$$

and

$$\mathbf{a}^i(t) = \frac{\mathbf{F}^i(t)}{m^i} = \frac{-\nabla_{\mathbf{r}^i}\mathcal{U}(t)}{m^i}. \tag{2.39}$$

where $\mathbf{r}^i(t)$ and $\mathbf{r}^i(t+\Delta t)$ represent the coordinates of ion i at time t and (t+Δt) respectively, $\mathbf{v}^i(t)$ is the velocity of ion i at the time t and $\mathbf{a}^i(t)$ is the acceleration on ion i at time t. The integration time step is Δt. Summing these leaves

$$\mathbf{r}^i(t+\Delta t) = 2\mathbf{r}^i(t) - \mathbf{r}^i(t-\Delta t) + \mathbf{a}^i(t)\Delta t^2 .... + \mathcal{O}(\Delta t^4). \tag{2.40}$$

This is the basic *Verlet algorithm* but is unsatisfactory as it involved subtracting a small $\mathcal{O}\Delta t^2$ term from a large difference of $\mathcal{O}\Delta t^0$ terms. A suitable modification is to calculate the velocities at the half time step

$$\mathbf{v}^i(t+\frac{1}{2}\Delta t) = \frac{\mathbf{r}^i(t+\Delta t) - \mathbf{r}^i(t)}{\Delta t}. \tag{2.41}$$

Substitution of equation 2.40 into 2.41 gives:

$$\mathbf{v}^i(t+\frac{1}{2}\Delta t) = \frac{\mathbf{r}^i(t) - \mathbf{r}^i(t-\Delta t) + \mathbf{a}^i(t)\Delta t^2}{\Delta t}, \tag{2.42}$$

giving the final equations as

$$\mathbf{r}^i(t+\Delta t) = \mathbf{r}^i(t) + \mathbf{v}^i(t+\frac{1}{2}\Delta t)\Delta t \tag{2.43}$$

$$\mathbf{v}^i(t+\frac{1}{2}\Delta t) = \mathbf{v}^i(t-\frac{1}{2}\Delta t) + \mathbf{a}^i(t)\Delta t, \tag{2.44}$$

which have no equivalent problems to those described for equation 2.40.

Analogous equations can be derived to integrate the additional degrees of freedom. For the induced dipoles

$$\boldsymbol{\mu}^i(t+\Delta t) = \boldsymbol{\mu}^i(t) + \dot{\boldsymbol{\mu}}^i(t+\frac{1}{2}\Delta t)\Delta t \tag{2.45}$$

$$\dot{\boldsymbol{\mu}}^i(t+\frac{1}{2}\Delta t) = \dot{\boldsymbol{\mu}}^i(t-\frac{1}{2}\Delta t) + \ddot{\boldsymbol{\mu}}^i(t)\Delta t, \tag{2.46}$$

where $\ddot{\boldsymbol{\mu}}^i(t)$ is given by equation 2.12. Similarly for the induced quadrupoles

$$\boldsymbol{\theta}^i(t+\Delta t) = \boldsymbol{\theta}^i(t) + \dot{\boldsymbol{\theta}}^i(t+\frac{1}{2}\Delta t)\Delta t \tag{2.47}$$

$$\dot{\boldsymbol{\theta}}^i(t+\frac{1}{2}\Delta t) = \dot{\boldsymbol{\theta}}^i(t-\frac{1}{2}\Delta t) + \ddot{\boldsymbol{\theta}}^i(t)\Delta t. \tag{2.48}$$

Thus, at the end of a molecular dynamics step the stored variables are the ion positions and the induced moments at time $t+\Delta t$ and the ion and induced moment velocities at the *half* time step. This means that care must be taken when calculating energies to ensure that the potential and kinetic terms are calculated at the same time step, using, for example

$$\dot{\boldsymbol{\theta}}^i(t) = \frac{\dot{\boldsymbol{\theta}}^i(t+\frac{1}{2}\Delta t) + \dot{\boldsymbol{\theta}}^i(t-\frac{1}{2}\Delta t)}{2} \tag{2.49}$$

to generate a velocity at the full time step.

2.3 Application of the Car-Parrinello Method.

2.3.1 Methodology.

The original methodology of Car and Parrinello [1] dealt with degrees of freedom which specified the ion wavefunctions as the additional variables. These variables were updated in parallel with the ionic equations of motion, the basic premise being that the additional variables would be automatically updated to their new positions on the *adiabatic surface* provided that they start from a self-consistent variable set. In the PIM the additional degrees of freedom describing the induced moments are envisaged as playing an analogous role to the electronic degrees of freedom of Car and Parrinello in the manner considered by Sprik [25] (see section 1.5.3). All equations of motion are integrated over *simultaneously* with the same time step. Note that the time step must be chosen as to be small enough to integrate over the equations of motion governing the time evolution of the fastest degrees of freedom. The induced moments will evolve more quickly than the ion motion and hence these simulations will require a smaller time step than might be used for a typical RI simulation.

Figure 2.1 shows the comparison of a dipole component induced on a selected anion calculated via the equation 2.12 with that calculated from the field on that anion (i.e $= \alpha E^i_\alpha$) in a simulation of liquid NaCl using the dipolar model. These two values should be equal if the additional variables are obeying the adiabatic condition. Figure 2.1 leads to two major conclusions:

- As the runtime increases the value of the dipole component generated from the equations of motion (the light grey curve) oscillates more and more vigorously about the desired value.

- As the run progresses the high frequency oscillations, characteristic of the additional degrees of freedom, are seen to filter through to the required value curve (black line). This oscillatory character reflects the loss of adiabaticity of nearby anions.

Another way of monitoring the adiabaticity as the CP dynamics progresses is to look at the fictitious kinetic energy (fke) (the term in $\dot{\mu}^2$ in equation 2.6)

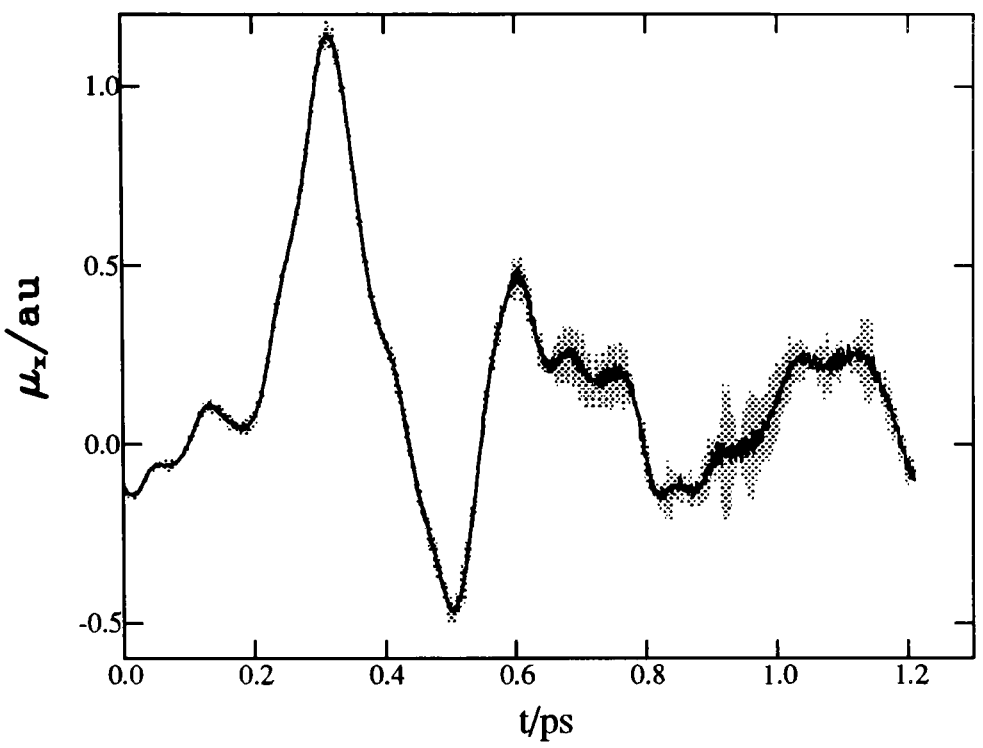


FIGURE 2.1: *Evolution of the x-component of the induced dipole on a single selected anion. The black line represents the value of the dipole required by the field and the grey line the value obtained by performing CP dynamics using the derived equations of motion to govern the time evolution of the induced dipoles.*

or the kinetic temperature associated with it, namely

$$T_{fke} = \frac{\sum_{i=1}^{N_t} m_\mu^i \dot{\mu^i}^2}{g k_B}, \tag{2.50}$$

where g is the number of degrees of freedom associated with the additional system and k_B is the Boltzmann constant. For the dynamics of the additional degrees of freedom to follow the adiabatic surface this temperature is required to remain small (ideally orders of magnitude less than the real temperature). This requirement arises from the fact that the only motion required of the additional variables is to update their values to the new adiabatic surface given by the updated ion coordinates. Hence, a two level *metastable* state with high and low temperature variables is set up [32]. Further "heating" of the additional variables accompanies a departure from the adiabatic surface. This behaviour is illustrated in figure 2.2 for the same simulation as figure 2.1. Thus, the increase in amplitude of the high frequency oscillations in figure 2.1 is accompanied by a slow, linear, heating of the additional variables. This heating arises from the *ergodic* nature of the total system (i.e. the ions plus the additional degrees of freedom) which acts to equilibrate the ionic degrees of freedom with the much

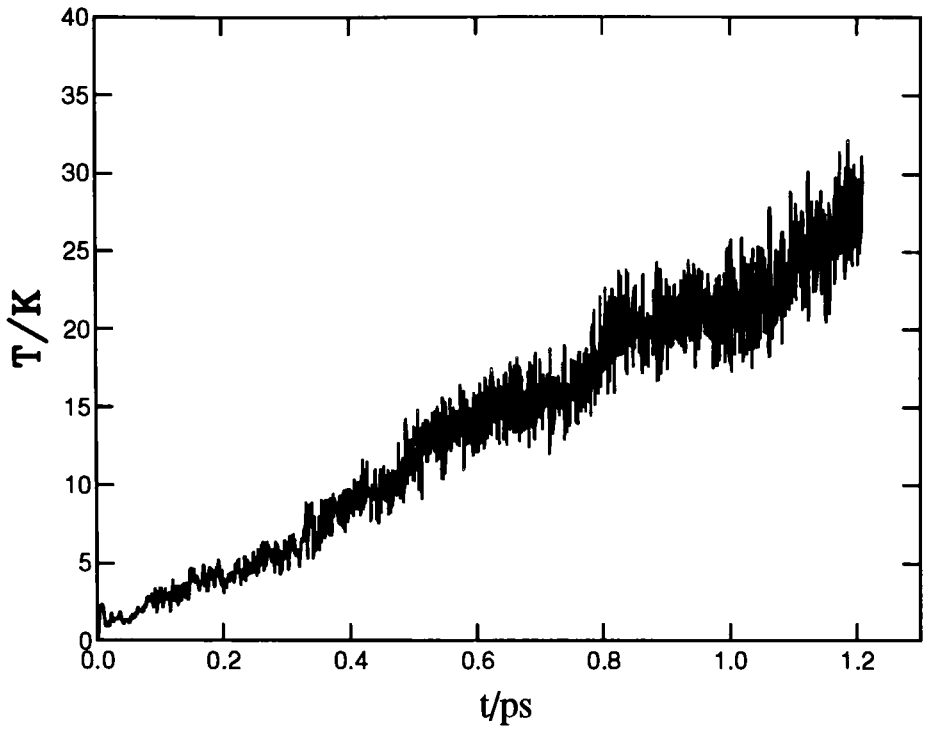


FIGURE 2.2: *Time evolution of the kinetic "temperature" of the dipolar degrees of freedom for the same simulation run as in figure 2.1.*

cooler additional degrees.

In order to demonstrate why this heating of the additional variables occurs it is revealing to refer back to the wealth of electronic CP simulations performed in the past decade. Pastore *et al* [32] have carefully analysed the circumstances under which the electronic CP scheme can maintain the adiabatic condition for long periods. If the character of the equations of motion of the additional variables is oscillatory, and if the range of oscillation frequencies does not overlap the density of states of the translational degrees of freedom of the system studied, then energy transfer between the translational and additional degrees of freedom is slow and adiabaticity is maintained for long periods. In the electronic case, these favourable circumstances arise if there is an appreciable energy gap between the occupied and unoccupied electronic orbitals and if the fictitious inertia parameters are chosen sufficiently small. The converse occurs in metals, where there is no band gap. However, it has been shown [26, 33, 34] that in such cases a modified CP procedure, in which the excess heat transferred to the additional degrees of freedom is removed by adding "thermostats" to the equations of motion, can maintain adiabaticity during long runs.

2.3.2 The Factors which Control Adiabaticity.

Consider the first MD time step. Starting from the energy minimum (i.e with all the induced moments self-consistent) the ions are updated to their new positions governed by the ionic equations of motion. The changed system topology shifts the energy minimum causing the induced moments to experience *restoring forces* [32] causing them to move towards the *new* energy minimum. The small masses associated with the additional degrees of freedom cause this motion to be rapid. Hence high frequency oscillations arise in the induced moments corresponding to the moments moving about the energy minimum. Referring back to the original Hamiltonians there is a mix of slow (ionic) and fast (induced moment) variables. Using the "Averaging method" [35, 36] this type of Hamiltonian can be approximated to one containing the slow variables plus an *averaged* component obtained by averaging over the fast variables in the original Hamiltonian. Thus, if the fast motion arises due to oscillations about the Born-Oppenheimer (BO) surface the induced moments will be expected to remain close to that surface.

Again, considering the first MD step, the additional variables now experience a restoring force. Within the DA, for small deviations ($\Delta\mu$) from the BO surface ($\mu = \bar{\mu}$), $\frac{\partial^2 \Delta\mu}{\partial t^2}$ can be approximated as being linear in $\Delta\mu$, giving

$$\frac{\partial^2 \Delta\mu}{\partial t^2} = -\left(\frac{\partial}{\partial\mu}\left(\frac{\partial U}{\partial\mu}\right)\right)_{\mu=\bar{\mu}} \Delta\mu. \tag{2.51}$$

The equations of motion tell us that the induced dipoles will harmonically oscillate about the BO surface with a characteristic frequency [37]

$$\omega_\mu = \sqrt{\frac{\frac{\partial}{\partial\mu}\left(\frac{\partial U}{\partial\mu}\right)}{m_\mu}}. \tag{2.52}$$

The rate of energy transfer between the ionic and induced moment subsystems depends upon the frequency ω_μ and the characteristic frequencies of the ionic motion. If there is appreciable overlap then the rate of energy transfer will be large leading to a rapid equilibration of the subsystems. If the frequencies are well separated the metastable two level system should be stable for an appreciable finite time period. Figure 2.3 shows a Fourier transform of the real ion kinetic energy for a simulation of crystalline AgCl within the DA. The low frequency modes are from the real ionic motion whereas the much higher frequency

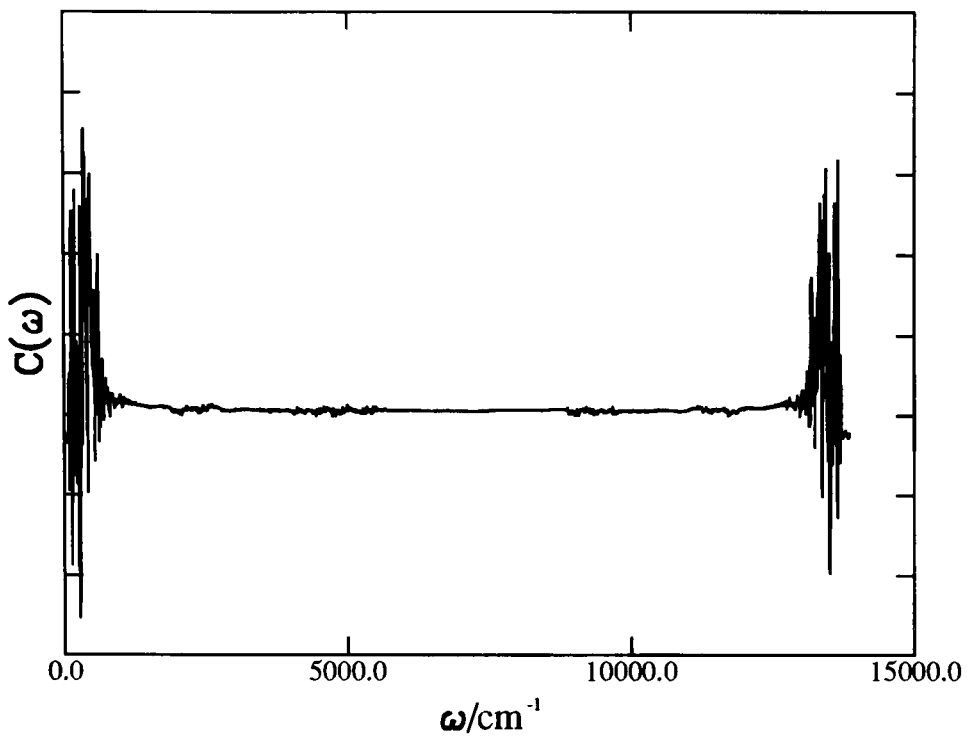


FIGURE 2.3: *Fourier transformation of the ion kinetic energy for a simulation of crystalline AgCl. The low frequency peaks correspond to the real ionic modes whilst the high frequency peaks correspond to the rapid oscillations of the induced moments due to the application of the CP method.*

($> 10000\text{cm}^{-1}$) modes are a result of the oscillations in the induced moments brought about by the application of the CP method. Thus, the large difference in frequencies shows that the energy transfer between these systems is *relatively* inefficient. However, figure 2.2 shows that the heating of the additional variables *is* significant over the time period of a typical MD simulation and so strategies must be developed to overcome this. Note though that the additional variables in figure 2.2 rise to $\sim$ 20K in 1ps with the ionic variables at 1000K, i.e in 1ps the additional subsystem has reached only 2% of the real system temperature indicating the *inefficient* nature of this energy transfer.

2.3.3 Choosing the Fictitious Masses.

The use of Lagrangian mechanics to generate Newtonian equations of motion generates *fictitious masses* (m_μ in equations 2.12 and 2.28 governing the induced dipole motion and m_θ in equation 2.29 controlling the quadrupoles). In this section the factors affecting the choice of these masses will be considered.

The smaller the characteristic fictitious masses the quicker the additional variables will be able to react to changes brought about by the real ion motion.

Too large a mass will result in more sluggish motion which may make adhesion to the BO surface impossible.

Our desire to calculate system averages over as long a real time as possible requires the time step, Δt, to be as large as possible. However, the maximum size of Δt is governed by the most rapidly changing subsystem in real time. In the PIM the most rapidly changing systems are always those concerned with the induction effects. Hence the choice of fictitious masses and time step are *directly* linked (Δt scales as $\sqrt{m}$ via equation 2.52); the smaller the fictitious mass the larger the induced moment accelerations ($\ddot{\boldsymbol{\mu}}$ and $\ddot{\boldsymbol{\theta}}$) at each time step, and hence the smaller the time step that is required to integrate the equations of motion accurately.

Thus, there is a clear conflict of interests implying that only a narrow range of acceptable mass/time step sets will satisfy both our criteria. The factors that will affect this parameter choice will be:

- *Ion masses* - the smaller the ion mass the greater the accelerations for a given force leading to a larger change in the electric field (and gradients) for a given time step. Thus a small fictitious mass set is required to allow the additional degrees of freedom to adapt to the rapidly changing system topology.

- *System Temperature* - the higher the real system temperature the larger the changes in fields for a given time step.

- *Polarizabilities* - the larger the system polarizabilities the greater the changes in the induced moments for a given change in field (gradient) requiring a smaller mass and/or smaller time step to effectively integrate these equations of motion. Δt scales as $\sqrt{\alpha^{-1}}$ from equation 2.52.

Typical suitable dipole masses are of the order of 500au. It should again be stressed that this is *not* a real mass and, indeed, does not have the dimensions of real mass.

In a system working within the quadrupolar approximation it is found that $m_{\boldsymbol{\theta}}$ has to be around an order of magnitude less than $m_{\boldsymbol{\mu}}$ in order to keep both the dipolar and quadrupolar subsystems on their respective BO surfaces. For a given distortion of the ionic electron density the change in the quadrupole moment goes as the *square* of the electron density change whereas the dipole moment is

linear. Hence, the magnitude of the quadrupole moment varies more than that of the dipole, requiring a smaller fictitious mass to integrate the quadrupolar equations of motion.

2.3.4 Thermostating the Systems.

In the previous section it was shown that the additional degrees of freedom behave in a manner analogous to electronic CP simulations on metals [34, 33, 26], in that there is significant energy transfer with the real ionic system. In keeping with previous electronic CP [33, 26] the motion of the additional variables can be kept under control via the application of *Nosé-Hoover thermostats* [38, 39].

Briefly, Nosé proposed coupling the real systems to an additional variable s which acts to scale the particle velocities by coupling them to a constant temperature heat reservoir. The variable s has conjugate momentum p_s giving a total system Hamiltonian as

$$H^N = \phi(r) + \sum_{i=1}^{N_t} \frac{p^{i2}}{2m^i s^2} + (g+1)k_B T ln(s) + \frac{p_s^2}{2Q}, \tag{2.53}$$

where $\phi(r)$ is the potential, g is the total number of degrees of freedom of the system being thermostated and Q relates to the rate at which the thermostat acts on the real system. Lagrangian mechanics leads to the equations of motion

$$\ddot{\mathbf{r}}^i = \frac{\mathbf{F}^i}{ms^2} - \frac{2\dot{s}\dot{\mathbf{r}}^i}{s} \tag{2.54}$$

$$Q\ddot{s} = \sum_{i=1}^{N_t} m\mathbf{r}^{i2}s - \frac{(g+1)k_B T}{s}. \tag{2.55}$$

Hoover further developed this by eliminating the scaling variable. The Nosé-Hoover (NH) equations of motion become simply

$$\dot{\mathbf{r}}^i = \frac{\mathbf{p}^i}{m^i} \tag{2.56}$$

$$\dot{\mathbf{p}}^i = \mathbf{F}^i - \zeta \mathbf{p}^i, \tag{2.57}$$

where ζ is a *friction parameter* given by

$$\dot{\zeta} = \frac{\sum_{i=1}^{N_t} \frac{p^{i2}}{m^i} - gk_B T}{Q}. \tag{2.58}$$

Here $Q = gk_BT\tau^2$ with T the desired system temperature and τ the *characteristic thermostat relaxation time* [40] which governs the speed of response of the thermostats to a move from the desired temperature.

In section 2.2.1 it was shown how a standard leapfrog algorithm could be employed to update the induced moments in an analogous way to the ion coordinates. Toxvaerd [40] describes how the Nosé-Hoover thermostats may be applied using various finite difference techniques. For the standard leapfrog algorithm the basic equations become

$$\mathbf{r}^i(t+\Delta t) = \mathbf{r}^i(t) + \mathbf{v}^i(t+\frac{1}{2}\Delta t)\Delta t \tag{2.59}$$

$$\mathbf{v}^i(t+\frac{1}{2}\Delta t) = \mathbf{v}^i(t-\frac{1}{2}\Delta t) + \mathbf{a}^i(t)\Delta t - \xi(t)\mathbf{v}^i(t). \tag{2.60}$$

Since only the velocities, $\mathbf{v}^i$ at the *half* time step are stored in the simulation the relationship

$$\mathbf{v}^i(t) = \frac{\mathbf{v}^i(t+\frac{1}{2}\Delta t) + \mathbf{v}^i(t-\frac{1}{2}\Delta t)}{2} \tag{2.61}$$

is substituted into equation 2.60. Taking all the $\mathbf{v}^i(t+\frac{1}{2}\Delta t)$ terms to the left-hand side gives

$$\mathbf{v}^i(t+\frac{1}{2}\Delta t) = \frac{\mathbf{v}^i(t-\frac{1}{2}\Delta t)\{1-\frac{\xi(t)\Delta t}{2}\} + \mathbf{a}^i(t)\Delta t}{\{1+\frac{\xi(t)\Delta t}{2}\}}. \tag{2.62}$$

Considering equation 2.62 there are two special cases worthy of comment:

- if $\xi(t) = \frac{-2}{\Delta t}$ the algorithm catastrophically fails due to the denominator becoming infinite.
- if $\xi(t) = \frac{2}{\Delta t}$ the algorithm describes the *steepest descent* method [41]. As noted by Fois *et al* [33] such a values for $\xi(t)$ will only return the variables to the adiabatic surface if the ions remain *stationary*.

These thermostats are employed on all subsystems. For example, within the DA the ion equation of motion now becomes

$$m^i\ddot{r}^i_\alpha = -\sum_{j\neq i}^{N_t}\left\{\nabla_{r^i_\alpha}U^{sr}(r^{ij}) - Q^j\bar{E}^i_\alpha - \mu^j_\beta\bar{E}^i_{\alpha\beta}\right\} - \zeta_{ion}m^i\dot{r}^i_\alpha, \tag{2.63}$$

whilst the dipolar equation of motion becomes

$$m^i_\mu\ddot{\mu}^i_\alpha = \sum_{j\neq i}^{N_t}\left\{-T^{ij}_\alpha Q^j + T^{ij}_{\alpha\beta}\mu^j_\beta\right\} - 2k^\mu\mu^i_\alpha - \zeta_\mu m_\mu\dot{\mu}^i_\alpha, \tag{2.64}$$

where the subscripts on the ζ represent the ionic and dipolar subsystems respectively. Rearrangement of 2.58 gives

$$\dot{\zeta}_{sys} = \frac{\frac{T_{kin,sys}}{T_{sys}} - 1}{\tau_{sys}^2}, \tag{2.65}$$

where the *sys* subscript labels each subsystem (i.e ionic, dipolar or quadrupolar). $T_{kin,sys}$ is the kinetic temperature of the *sys*-subsystem, T_{sys} is the thermostat target temperature and τ_{sys} is the characteristic thermostat relaxation time. The τ_{sys} parameter set is chosen so as to provide acceptable temperature control whilst not allowing the equations of motion to become too stiff. The target temperatures of the induced moment subsystems are taken to be much smaller than that of the ionic motion. A target temperature of zero is *not* desirable as this would leave ζ as positive definite resulting in its acting to reduce the velocities of the additional degrees of freedom. This leads to the additional variables being unable to keep up with the motion of the ions. Thus, a small but non-zero target temperature must be set to allow for the *adiabatic motion* appropriate to the motion of the ions. Following Fois *et al* [33] approximate temperatures are chosen via

$$T_{fke}^{target} = f\frac{m_\mu}{m^i}T_{ions}^{target}. \tag{2.66}$$

Thus, the target temperatures are dependent upon the masses and the system temperature as would be expected. However, this relationship is not exact (f was found to be between 0.05 and 0.35 for different electronic CP simulations [33]), but it does allow an estimate to be made of the desired temperature. A short simulation run allows these to be tested. Too small a target temperature will result in the thermostats permanently removing energy from the additional variables (until an algorithm breakdown) whilst too large a temperature will result in large oscillations with a frequency characteristic of the thermostat relaxation time. It should be stressed that neither the target temperatures nor the thermostat relaxation times have been found to be critical in making the additional variables stay on the BO surface. The algorithm appears much more robust than the full electronic CP counterparts.

Figure 2.4 shows the evolution of the *thermostated* temperature for a run equivalent to that shown in figure 2.2. The temperature of the additional degrees of freedom now oscillates about the fixed value of 2K. Figure 2.5 shows

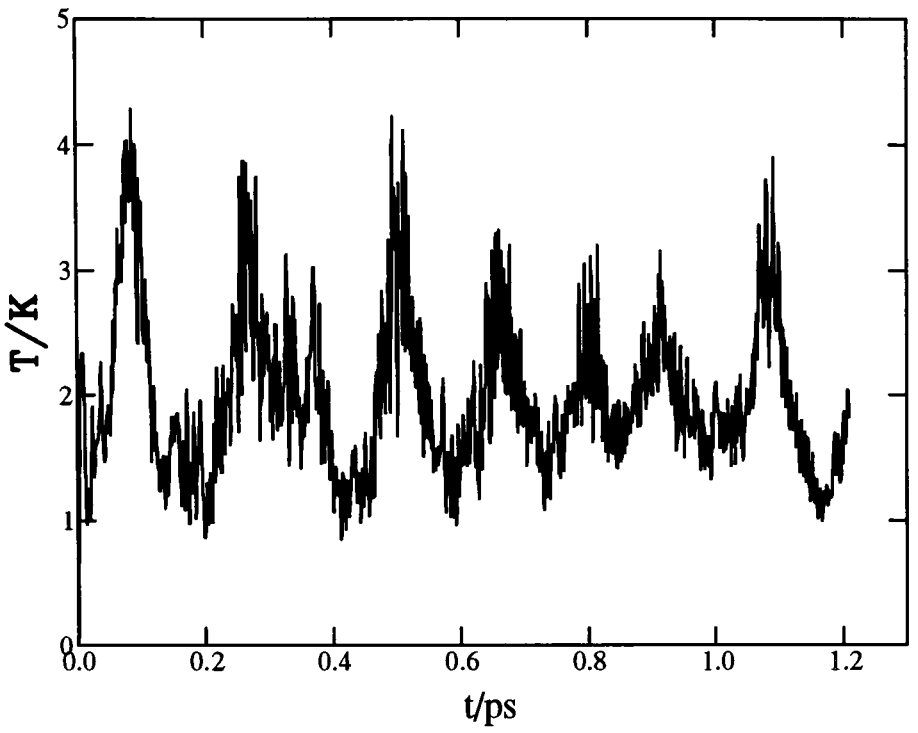


FIGURE 2.4: *Evolution of the temperature of the dipolar subsystem for the thermostated simulation.*

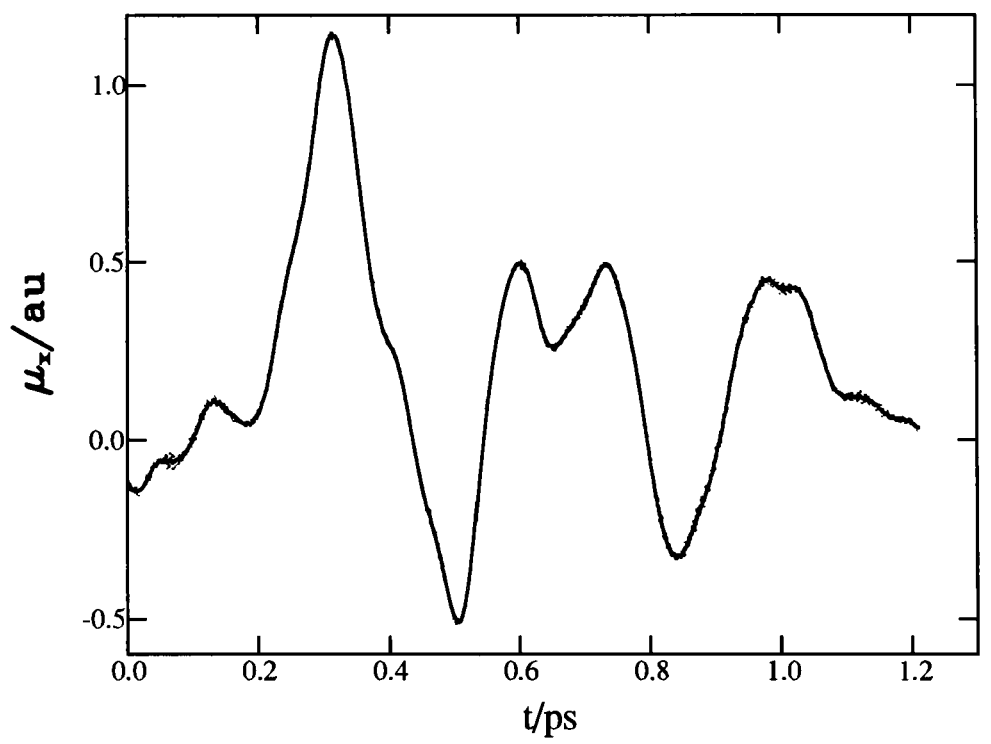


FIGURE 2.5: *Evolution of the same dipole component as in figure 2.4 but with thermostating.*

the evolution of the same component of an induced dipole as in figure 2.1. The induced dipole from the CP algorithm now adheres very closely to the required value over the whole simulation run. Figure 2.4 shows no heating of the additional variables. There are two characteristic sets of oscillations in figure 2.4:

- the high frequency oscillations - these are again due to the rapid motion of the additional variables about the BO surface.

- the low frequency oscillations - these are characteristic of the thermostat relaxation time, τ, that is, the rate at which the thermostat responds to the move away from the required temperature. These oscillations may be suppressed via *chain thermostating* techniques [42], that is, by thermostating the thermostats. However, the robust nature of the simulation algorithm with respect to *electronic CP* means that such developments are not mandatory for the overall success of the simulations.

3

Parameterization of the Model.

As expressed in the introduction, the objective of this thesis is to examine the scope of an *ionic model* to represent a range of condensed systems. The essential feature of this model is that the system can be regarded as an assembly of ionic entities which retain their integrity. The properties of these entities determine the macroscopic system properties whilst the interactions between these entities determine the system energetics. The appropriateness of the ionic description can, therefore, be tested by its ability to reproduce experimental properties in both the liquid and solid phases.

It seems intrinsic to this description that the ions should carry the charges predicted by their oxidation state and, as a result, have closed shells [43]. Within this model one might hope to be able to partition the total energy into the following contributions,

$$U^{tot} = \underbrace{U^{sr}}_{short-range} + \underbrace{U^{coul}}_{coulombic} + \underbrace{U^{disp}}_{dispersion} + \underbrace{U^{ind}}_{induction} + \underbrace{U^{self}}_{self(rearrangement)}, \qquad (3.1)$$

where U^{coul} is the coulombic energy (see section 1.2), U^{sr} is the short-range repulsion energy, U^{disp} the dispersion energy, U^{ind} the induction energy, and U^{self} the ion rearrangement energy. These should be obtained *independently* from calculations concentrating on different aspects of the interaction between the ionic entities. Note that this partition will only have a significance if there is no electron transfer; that is, the ionic entities must retain their integrity throughout.

The definition of the entity which underlies most of the work in this thesis is that its electronic properties are those of the ion embedded in a *spherical* pseudopotential which represents the potential felt by the electrons of the ion. This pseudopotential will contain both crystal field and overlap effects (see section 1.2). Note that only the spherical part of this potential is included in the definition of the ion. In highly asymmetric environments non-spherical components

will be produced. However, as discussed in section 1.2 these are expected to be dominated by the spherical term in many of the systems of interest. The ionic entity as defined here should, therefore, be very close to the true ionic species which exists in the high symmetry crystal.

3.1 Short-range Interactions.

Let us now consider how to set about first obtaining the U^{sr} contribution to the energy of a perfect cubic crystal. For a given lattice parameter the electron densities and properties of the individual ionic entities would be calculated as above. U^{sr} would then be obtained by calculating the energy due to the overlap between these electron densities when the ions are assembled in the crystal in the appropriate way.

In order to understand how the short-range terms in the energy partition behave, it is instructive to think about how they will vary as the lattice parameter is reduced (as the crystal is put under pressure). Firstly, the overlap between neighbouring ions will be increased. For a relatively small degree of overlap the overlap will be additive and the interaction can be approximated as a sum of pair terms

$$U^{sr} \sim \sum_{i=2}^{N_t} \sum_{j=1}^{i-1} U^{sr}(r^{ij}), \tag{3.2}$$

as in the RIM (section 1.3).

However, the reduction of the lattice parameter may lead to a further, more subtle, effect. As the lattice parameter is reduced so does the width of the spherical potential used to define the ionic entity (see figure 1.2). If the ionic entity were particularly sensitive to this change, over the range of lattice parameters in question, then it will become more *compressed* by the reduction in the lattice parameter. Thus, the self-energy (rearrangement energy) of the ion will be increased due to the increased electron density compression. Opposing this effect there will be a *reduction* in the overlap interaction between the neighbours with respect to that predicted if the ions had not been compressed.

There are two cases to consider.

- The ionic entity may be relatively insensitive to the compression caused by a reduction in lattice parameter. In this case U^{self} may be taken as

constant over the range of lattice parameter studied, and so be effectively absorbed into U^{sr}, usually represented by a Born-Mayer function of the form

$$U^{sr} = \sum_{i=2}^{N_t} \sum_{j=1}^{i-1} B^{ij} e^{-a^{ij} r^{ij}}. \tag{3.3}$$

- In the second case U^{self} will have a dependence upon the ionic coordinates and, as a result, U^{sr} will acquire a many-body character. For example, one might consider still keeping a Born-Mayer type of function to represent U^{sr} but allow the parameters which express the properties of the ionic entities (the ionic radii and the "wall hardness", a^{ij}) to depend upon the lattice parameter or, more generally, on the coordinates of the other ions.

For the majority of the work in this thesis, concentrating on the halide systems, the first approximation will be assumed appropriate. However, the sensitivity of the oxide ion to its environment is well known (see section 1.2) and so a model will be developed in the final chapter that is appropriate to this kind of entity.

Ideally, the properties of the ionic entities will be determined by *ab initio* calculations on the idealised ion in the spherical pseudopotential followed by a separate calculation of the interactions between the charge densities. If, however, such calculations are not available, one might hope to be able to learn about the interactions from total energy crystal calculations or, indeed, from experiment. Note that, even with information from cubic crystals, such as energies or compressibilities, and assuming that dispersion interactions can be represented from independent sources of information, U^{sr} can only be obtained if U^{self} can be taken as constant over the range of lattice parameters in question.

3.2 Dispersion.

U^{disp} would be obtained by calculating the total inter-ion correlation energy between the closed-shell species. In practice the dominant term is the pairwise additive term in equation 1.3 where the dispersion coefficients are given by the Casimir-Polder formula [44],

$$C_6^{MX} = \frac{3}{\pi} \int \alpha_M(i\omega)\alpha_X(i\omega)d\omega, \tag{3.4}$$

where $\alpha_{M(X)}(i\omega)$ is the polarizability of species M(X) at imaginary frequency $i\omega$.

Additionally, the contributions to U^{disp} arising from the overlap of the wavefunctions of the (nearest-neighbour) ions must also be calculated [8]. Jacobi and Csanak [45] have shown how the *total* dispersive interaction can be derived by expanding the interaction Hamiltonian using spherical Bessel functions. This produces a single parameter dispersion damping function for each ion-pair for a given dispersion interaction.

3.3 Induction.

From the discussion on the role of the non-spherical parts of the potential (section 1.4), the ionic entity only represents the "in-crystal" ion accurately in crystals in which the ion is in a site of octahedral symmetry. In lower symmetry crystals, or in distorted crystals, the ion density will become distorted. These distortions will give rise to energy contributions that should be identified with U^{ind}. Without further information it will not possible to separately determine how a total energy should be partitioned into short-range and induction terms.

The degree to which an ion is distorted in a given environment is governed by two contributions, the polarizability, giving the asymptotic contribution, and the short-range (overlap) effect (see section 1.4). The suitable polarizability will be that which corresponds to the ionic entity in the perfect crystal. Note that, for cations, the much smaller dependence of the species on the crystalline environment will mean that the free ion value will often be appropriate.

"In-crystal" values are available for a variety of anions from Fowler and Madden [5], Pyper [8] and Mahan [4], the first two using coupled Hartree-Fock methods, and the latter density functional methods to model the overlap.

In section 2.1.1 it was shown how the damping effect on the anion induced anion dipole could be modelled using a simple function. A function in the same form as that used for the dispersion damping is used (equation 2.20).

In order to parameterize this function electronic structure calculations are again used. Fowler and Madden [16] have calculated the effect on the anion properties of distorting the first shell of cations in the LiF crystal. In these calculations the central anion and the first shell of cations are treated at the CHF level, whilst the longer range crystal interactions are modelled by embedding this

cluster in an array of point charges. In a perfect crystal the inherent symmetry means that the induced dipole on the anion is zero. However, a small distortion of the first cation shell around a given anion will act to destroy this symmetry distorting the anion and resulting in a non-zero induced moment (see section 1.4). The magnitude and type of this moment will depend upon the type of distortion performed on the crystal.

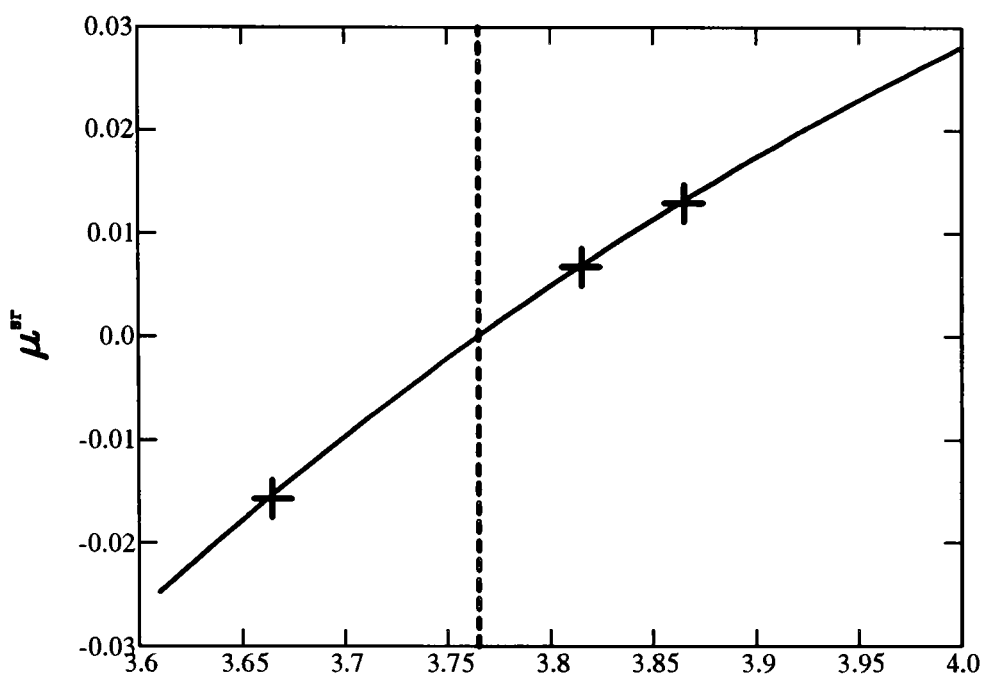


FIGURE 3.1: *Short-range contributions to the induced dipole moment in distorted crystalline environments. r is the anion-cation separation relating to the distorted cation.*

In modelling the *dipole* induction damping the distortion of interest involves moving a single cation from the first coordination sphere inwards or outwards, in a line with the central anion. Fowler and Madden [16, 17] present three such distortions from which the calculated total induced dipole moment is decomposed into a configurational, a coulombic and short-range effect, the first two of which can be calculated analytically. Hence, the latter can then be fitted to the Tang-Toennies function. Table 3.1 gives this decomposition and figure 3.1 shows the *ab initio* dipole moments along with the fitted function. For LiF the SRDP is found to be 1.0835au

$\Delta z/au$	$\mu^{sr}/10^2 au$
0.1	-1.57
-0.05	0.67
-0.1	1.29

TABLE 3.1: *Short-range contributions to the induced dipole on a fluoride anion caused by the distortion of the first coordination shell of cations.*

3.4 Comparing the PIM and Shell Models.

It is of interest to compare the induced dipoles predicted by the PIM parameterized from the *ab initio* data, with those due to the shell model of [10]. Figure 3.2 gives this comparison showing the dipole induced dipole upon a fluoride anion at the origin in an LiF crystal as a cation in the first coordination shell is distorted. The three curves represent the moment induced from a purely coulombic field, that predicted from the SM, and that predicted by the PIM with the *ab initio* SRDP. At large anion-cation separations both the SM and PIM curves tend to the purely coulombic limit, that is, the overlap effects are relatively *insignificant* beyond the first coordination shell. (Careful analysis of figure 3.2 shows that the PIM and SM curves tend to different values. This is purely a manifestation of the polarizabilities used in each case. In the PIM, $\alpha = 6.18au$, in the SM $\alpha = 6.90au$).

At the separation corresponding to the first coordination shell the coulombic induced dipole is *damped* in both the PIM and SM. However, the magnitude of this effect is very different in the two models, the *ab initio* dipole moment being less than half that in the SM. Similarly, at shorter separations, there are further dissimilarities. As discussed in section 2.1.1 the nature of the Tang-Toennies SR damping function causes the total induced to tend to zero at zero separation. In the SM the *ad hoc* procedure of allowing the Born-Mayer short-range forces to act on the shells not only damps the induced dipole but actually *reverses* its sign at short separations. Separations of this magnitude could well be sampled at higher temperatures in the liquid phase and so this behaviour is obviously important.

It should be stressed that the only requirement for choosing the damping function is to fit the *ab initio* distorted crystal data. It is conceivable, of course,

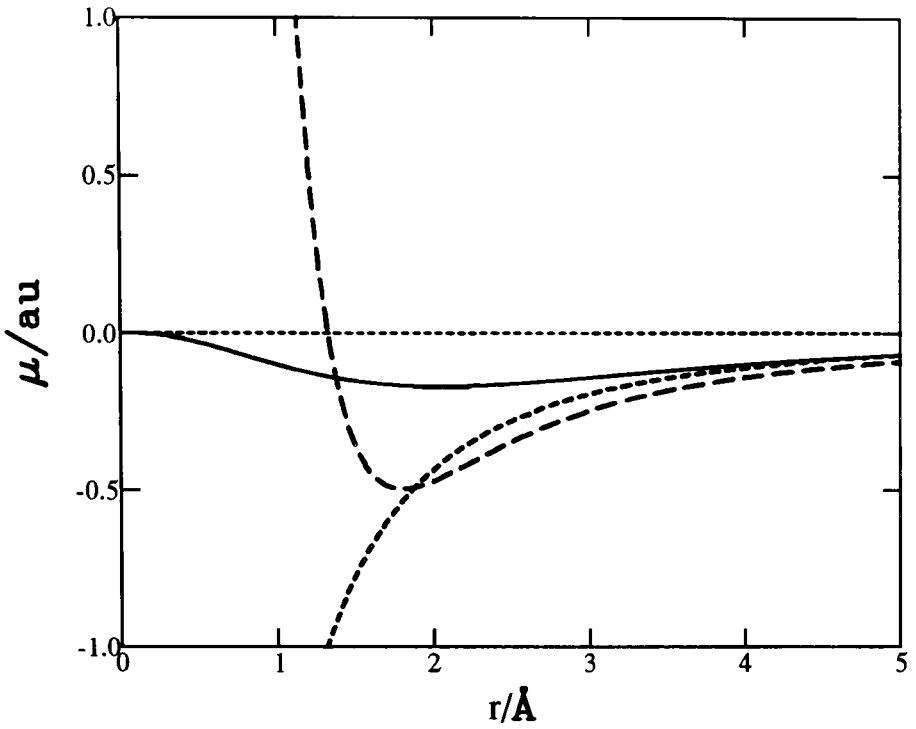


FIGURE 3.2: *Total induced dipole on a fluoride anion as a cation from the first coordination shell is moved. Key: solid-lines - PIM, long-dashed - shell model, short-dashes - purely coulombic dipole.*

that the function used does not describe correctly the induced dipoles on a separation smaller than the shortest range distortion. However, it is certainly true that the SM does not reproduce the correct *ab initio* dipole at any anion-cation separation where overlap effects are significant highlighting the *ad hoc* nature of the shell model parameterization. Hence, the overestimation of the dipole at longer range coupled with the underestimation at shorter range appear to be balancing each other to give a model that can produce the desired properties. It is also worth noting that the *ab initio* calculations predict an overlap contribution of the second cation coordination shell of $\sim 2\%$ that of the first shell. The chosen function gives the same magnitude of effect despite only having been fitted on distortions of the first shell. Hence, it is our belief that the chosen function is well-grounded.

3.5 Alternative Means of Potential Derivation.

In the earlier sections in this chapter the use of *ab initio* calculations to parameterize each term in equation 3.1 *independently* has been highlighted. However, in the absence of a wide body of such calculations it is of interest to consider

alternative, more approximate, methods.

Again, let us consider each term in turn:

3.5.1 Induction.

Refractive index measurements [46] provide information regarding the *total* crystal polarizability. For a given crystal the Clausius-Mossotti relationship [29], extrapolated to infinite frequency, gives the molar polarizability, α^{tot}. For s-different species in a crystal

$$\frac{\epsilon - 1}{\epsilon + 2} = \frac{4\pi}{3} \sum_s n_s \alpha_s, \tag{3.5}$$

where α_s is the polarizability of species s, and n_s is the number of ions of s per formula unit. Thus, for a simple MX_n crystal,

$$\alpha^{tot} = \alpha_M + n\alpha_X. \tag{3.6}$$

Thus, if the *ab initio* polarizability is available for the *free* cation, and if this value is also appropriate to the crystalline environment, then the anion polarizabilities can be deduced.

Fowler and Pyper [46] have shown how the anion polarizability can be expressed as a function of the nearest-neighbour anion-cation separation, R, via the empirical relationship

$$\log_{10}\alpha = A + \frac{B}{R^2} + \frac{C}{R^4}. \tag{3.7}$$

For the halides this is found to be *independent* of the crystal structure (for example, F^- in LiF and MgF_2 has the same polarizability, despite the differing crystal structures, as R is nearly identical). For the oxides and chalcogenides the same expression can be used but is not transferable between systems with different crystal structures. Again, this highlights the greater dependence of the properties of the oxide and chalcogenide ions on the nature of the crystalline environment.

The SRDPs for a given ion-pair, ij, may reasonably be related to the inverse of the sum of the ionic radii,

$$b^{sr} = \frac{\kappa}{\sigma^i + \sigma^j}, \tag{3.8}$$

where κ can be calculated from known *ab initio* SRDPs. This kind of relationship appears reasonable as one would expect smaller damping effects, at a given ion separation, for smaller ionic radii pairs. The smaller the sum of the ionic radii, the larger the SRDP, the shorter-ranged is the effect of equation 2.20.

3.5.2 Dispersion.

Semi-empirical methods can be used to determine both C_6 and C_8 from known polarizabilities [46]. For C_6 the Slater-Kirkwood approximation [47] gives

$$C_6^{ij} = \frac{3\alpha^i\alpha^j}{2\left\{\left(\frac{\alpha^i}{P^i}\right)^{1/2} + \left(\frac{\alpha^j}{P^j}\right)^{1/2}\right\}}, \tag{3.9}$$

where $P^{i(j)}$ are the "electron-numbers" and are derived by fitting to known rare gas systems [48].

Higher order terms can be introduced by an analogous method [49] or by using the Starkschall-Gordon formula relating C_8 to C_6 [8, 49].

Dispersion damping effects are also required. The Jacobi-Csanak [45] expressions are too complex to be readily used in MD simulations. Tang and Toennies [30] have shown how a function of the form introduced in section 2.1.1 can be used to model the dispersion damping between noble gas atom pairs. Thus, it seems reasonable to analytically fit this simpler function to the more complex exact expression and use the simpler function in the simulations themselves.

3.5.3 Short-range.

Let us assume a Fumi-Tosi [9] form for this interaction. For a given ion-pair ij,

$$U^{sr}(r^{ij}) = B^{ij}e^{-a^{ij}r^{ij}}, \tag{3.10}$$

where a^{ij} is the "hardness" of the repulsive wall, and B^{ij} is related to the ionic radii (σ) of i and j via

$$B^{ij} = Ae^{a^{ij}(\sigma^i+\sigma^j)}, \tag{3.11}$$

where A is a constant [9].

A large set of empirical $\{a, B\}$ parameter sets are available (see, for example, [10] for the alkali halides or [50] for the alkaline earth halides). These parameters

System	a^{--}/au	B^{--}/aeu
NaCl	1.67	128.2
$SrCl_2$	1.11	20.6

TABLE 3.2: *Short-range Born-Mayer terms for NaCl and $SrCl_2$.*

are useful as they are generally derived from bulk crystal properties and so cannot include any pseudo-induction effects as these are cancelled by the inherent crystal symmetry.

An approximation often made in order to reduce the parameter set is to assume that each ion pair interacts with the same repulsive wall "hardness", a^{ij}. In the alkali halides this is possible as the short-range interaction between the anions and cations dominates the short-range energetics and the elastic properties of the crystal. Hence, both the anion-anion and cation-cation interactions can be parameterized with the same repulsive wall hardness, whilst barely affecting the quality of the model.

Away from the MX stoichiometry the position is less clear. For example, in the MX_2 systems the anion-anion interactions are found to be as important energetically as the anion-cation [51, 52]. It is, therefore, much more important to consider this interaction more carefully than in the alkali halides.

The "hardness" of the repulsive wall depends upon the rate of decay of the ion (valence) electron density as one moves outwards from the core. Thus, the anion-anion interaction is expected to extend over a longer range than the other two. An example is to compare the Cl-Cl potential in a typical alkali halide, NaCl [10], where $a^{--} = a^{+-}$, with the same ion-ion potential in $SrCl_2$ [50], where a^{--} is independent of a^{+-}. It is anticipated that the $SrCl_2$ interaction will better reflect the longer ranged nature of this interaction as it is relatively important to the successful simulation of this system unlike in the NaCl. These numbers are given in table 3.2.

4

Rationalizing MX_2 Crystal Structures.

4.1 Introduction

In the introduction it was shown how the MX_2 systems (where M^{2+} is a divalent cation and X^- is a monovalent halide anion) went from having crystal structures that could be described by a purely ionic model to structures previously described as having inherent "covalent" effects. In this chapter the polarizable-ion model developed in the previous chapter will be applied to this series, demonstrating how the structural trends can be reproduced by the inclusion of induction (many-body) effects.

4.2 Crystal Structures.

The structure map of figure 1.1 shows four major structures. These are:

- **Fluorite**. The space group is *Fm3m* with each cation surrounded by eight anions ([8:4] coordination) [53]. The cations are in a face-centred cubic (fcc) lattice with the anions occupying *all* of the tetrahedral holes. The unit cell coordinates, given in terms of the lattice parameter, a_0, are:

$$\begin{pmatrix} 0.0 & 0.0 & 0.0 \\ 0.5 & 0.5 & 0.0 \\ 0.0 & 0.5 & 0.5 \\ 0.5 & 0.0 & 0.5 \end{pmatrix} \qquad \begin{pmatrix} 0.25 & 0.25 & 0.25 \\ 0.75 & 0.25 & 0.25 \\ 0.25 & 0.75 & 0.75 \\ 0.25 & 0.25 & 0.75 \\ 0.25 & 0.75 & 0.25 \\ 0.75 & 0.75 & 0.25 \\ 0.75 & 0.25 & 0.75 \\ 0.75 & 0.75 & 0.75 \end{pmatrix} \tag{4.1}$$

$$\text{Cations} \qquad\qquad \text{Anions} \tag{4.2}$$

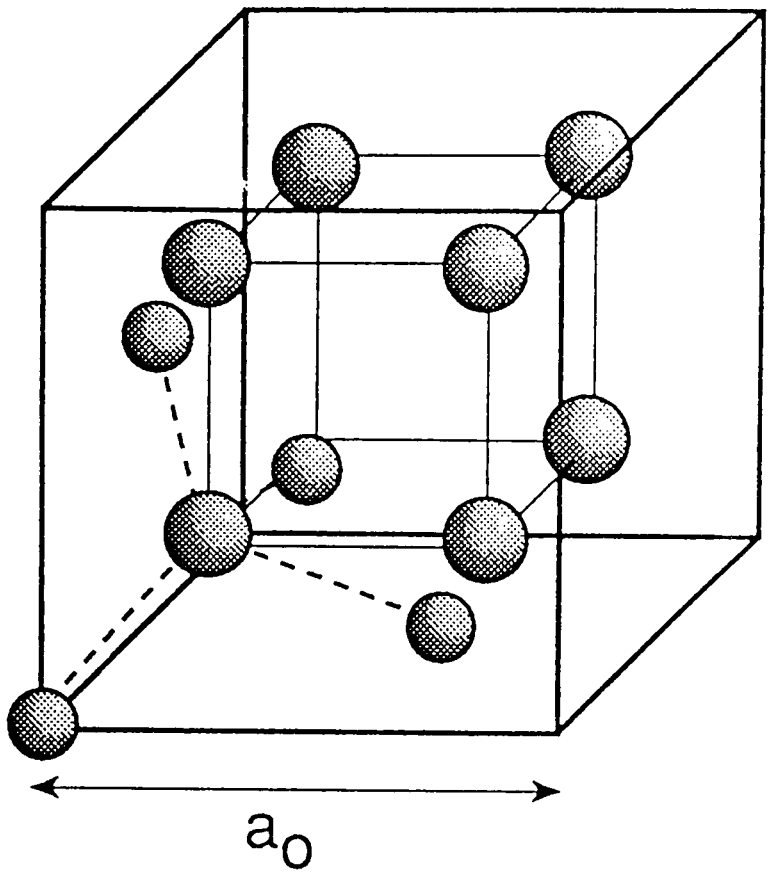


FIGURE 4.1: *The fluorite crystal unit cell. Key: small spheres - cations, large spheres - anions.*

and the structure is shown in figure 4.1.

If r_{AA} is assigned as the closest anion-anion distance and r_{CC} as the cation analogue then $r_{CC} = \sqrt{2} r_{AA}$. Thus, assigning full ionic charges to the species shows that the singly charged anions are closer together than the cations; that is, the structure is such that is keeps the more highly charged species as far apart as possible whilst maximising the anion-cation interactions. Systems that obey this property will be referred to as *charge-ordered*. The concept of a system being charge-ordered will arise in both the solid and liquid states and is a central theme of this chapter. It is clear from figure 4.1 that the anions sit in a symmetric environment leading to no electric field at the anion site and hence no induced dipoles.

The doubly charged nature of the cations means that the larger coulombic cation-cation repulsions tend to keep the fcc cation sublattice more rigid than the anion lattice. This lead to the *superionic conduction* behaviour characteristic of systems with this structure (see for example [54] and references therein). Here the anions diffuse in a liquid-like manner through the still crystalline cation sublattice at temperatures below the melting point. This kind of behaviour has important implications for the freezing properties of the molten salts that crystallize with this structure [55, 56].

- **Rutile**. The space group is $P4/mnm$, [6:3] coordination. The anions are in a distorted close-packed environment [53] with cations occupying the octahedral holes. Each cation has six nearest neighbour anions with $r_{CC} \simeq 1.45 r_{AA}$. The general rutile structure has the unit cell:

$$\begin{pmatrix} 0.0 & 0.0 & 0.0 \\ 0.5 & 0.5 & 0.5 \end{pmatrix} \qquad \begin{pmatrix} u & u & 0.0 \\ 1-u & 1-u & 0.0 \\ 0.5+u & 0.5-u & 0.5 \\ 0.5-u & 0.5+u & 0.5 \end{pmatrix} \tag{4.3}$$

$$\text{Cations} \qquad\qquad \text{Anions} \tag{4.4}$$

where $u = 0.31$ for the mineral rutile (TiO_2). This is shown in figure 4.2. The anions are sitting in an asymmetric environment leading to non-zero

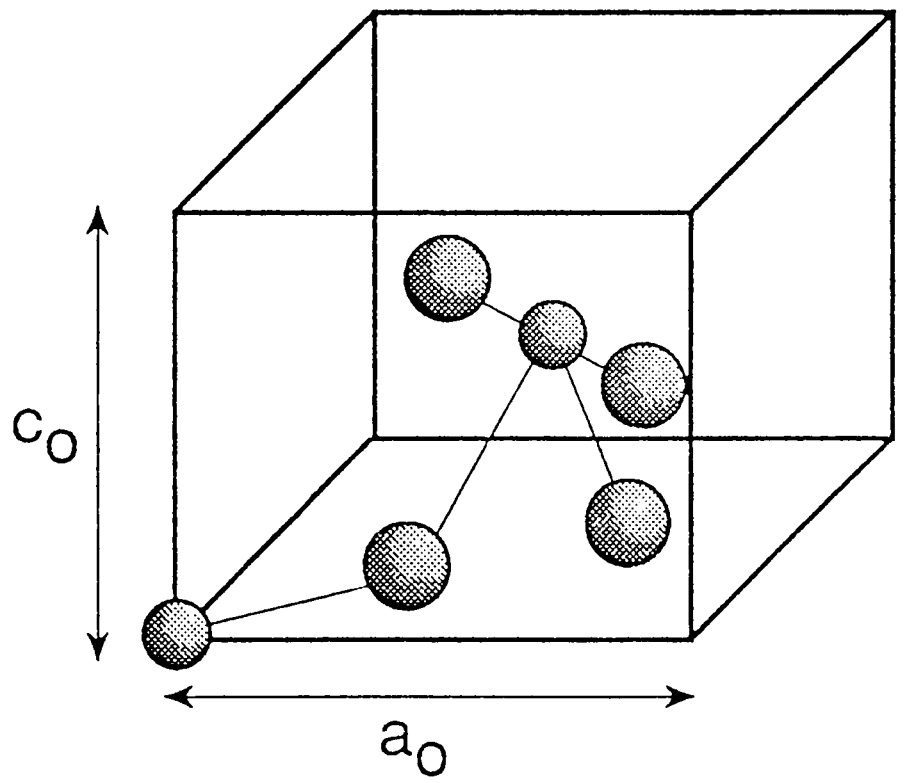


FIGURE 4.2: *The rutile crystal unit cell. Key: large spheres - anions, small spheres - cations.*

induced dipoles. Many compounds exist as subtle distortions of the basic rutile structure; for example, $CaCl_2$ has the space group $Pnnm$ [53].

- $PbCl_2$. Here the space group is $Pbnm$ and there are twelve ions in the unit cell [53]. Each anion again sits in an asymmetric environment with each cation surrounded by 7 anions at a distance of between 2.85 to 3.08Å in

$PbCl_2$ itself with $r_{CC} \simeq 1.34 r_{AA}$. The unit cell is:

$$\pm \begin{pmatrix} u & v & 0.25 \\ 0.5-u & 0.5+v & 0.25 \end{pmatrix} \tag{4.5}$$

where $u_{Pb} = 0.0956, v_{Pb} = 0.2617, u^1_{Cl} = 0.0742, v^1_{Cl} = 0.8610, u^2_{Cl} = 0.8370$ and $v^2_{Cl} = 0.4768$. The twelve-ion unit cell is formed by taking all the combinations of u_{Cl} and v_{Cl} with the pair of Pb coordinates.

- **Layered**. The term layered is used to cover 3 main structures, namely $CdCl_2$, CdI_2 and $ZnCl_2$. These structures will be described below but are grouped together as they share the same important structural feature, namely the characteristic alternate layers of filled/unfilled cation sites. Figure 4.3 shows a schematic representation of this ordering. The

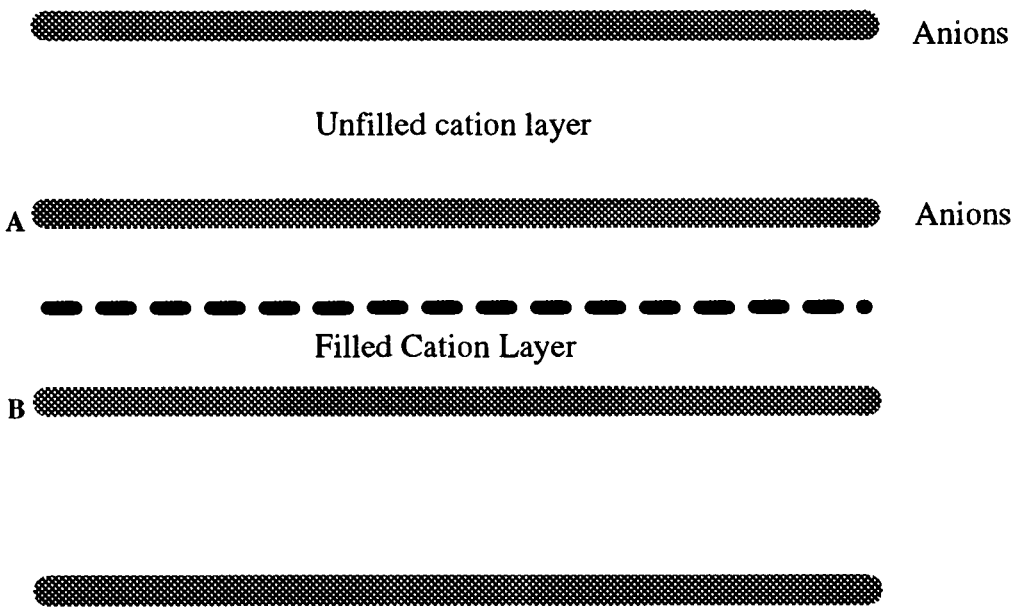


FIGURE 4.3: *Schematic representation of the general layered structure. The thick grey lines represent layers of anions with the dashed line a filled cation layer. The filled layer has an unfilled layer on either side in the c_0 direction leading to a large resultant electric field on the anions.*

filled/unfilled arrangement means that $r_{CC} = r_{AA}$, that is, the doubly charges cations are as close together as the singly charged anions. This type of arrangement is impossible to justify on coulombic grounds in that the MX_2 stoichiometry means that there will always be an energetically more favourable structure in which the cations are kept further apart within the RIM.

Thus, each anion sits in a symmetric potential along two directions (a_0, b_0) but in a highly asymmetric potential perpendicular to the cation planes (the c_0 direction) due to each anion having a filled cation layer as nearest neighbours along one side but an unfilled layer symmetrically opposite. This inherent asymmetry leads us to predict an important role for induction effects.

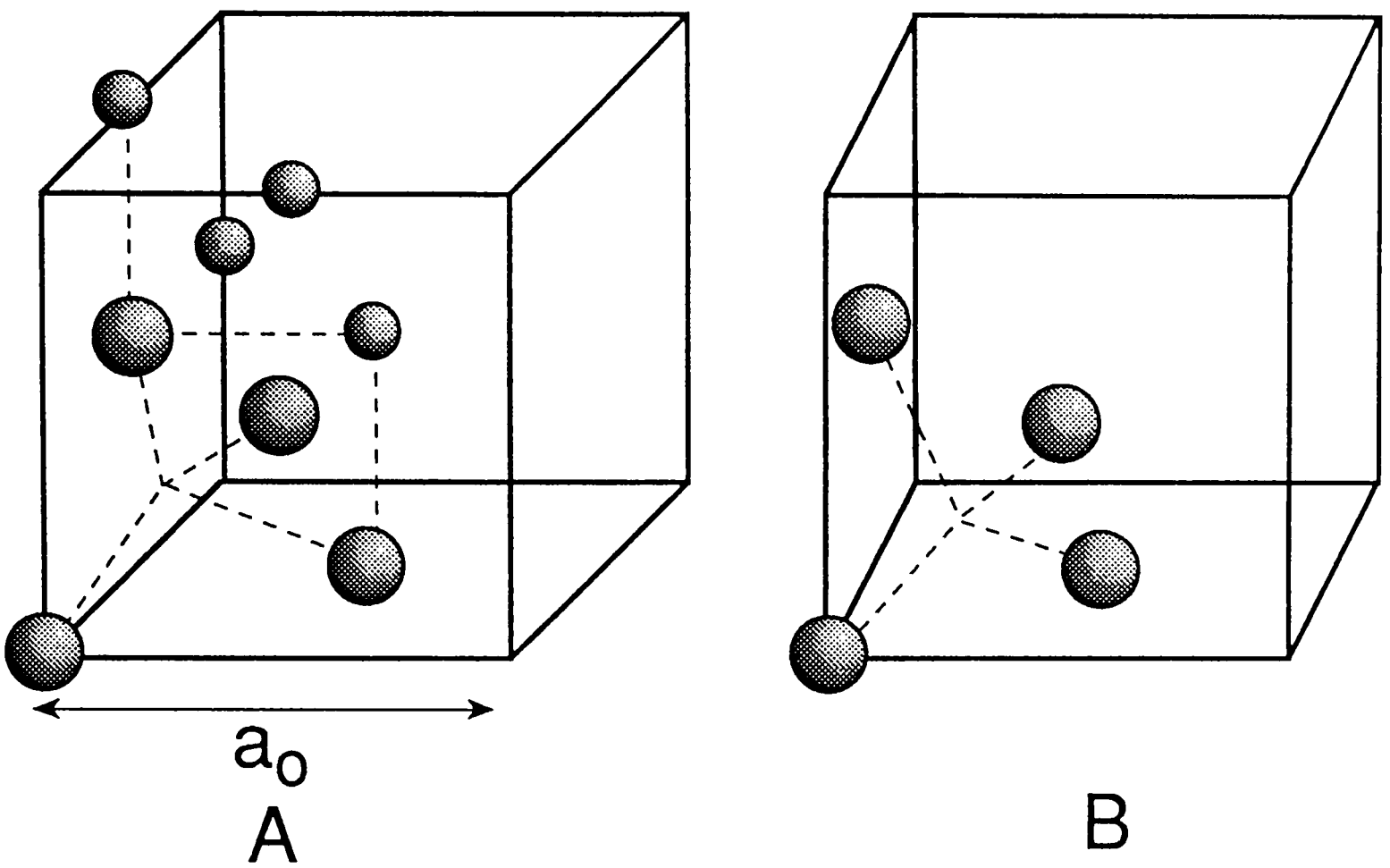
The three major structures are:

- $CdCl_2$. Symmetry group $R\bar{3}m$. The anions are in an fcc arrangement with cations occupying alternate layers of octahedral holes (thus each cation has six nearest neighbour anions). This structure can be constructed using the two basic building blocks in figure 4.4a to form the "supercell" of figure 4.4b. The alternate layers of filled/unfilled cation sites are evidently aligned along the (111) direction.
- CdI_2. Symmetry group $C\bar{3}m$. This differs from the $CdCl_2$ structure only in the packing of the anions. Here they are hexagonal- close packed (hcp) as opposed to fcc. The cations again sit in alternate layers of octahedral holes.
- $ZnCl_2$. As in CdI_2 the anions are in an hcp structure. Here, however, the cations sit in alternate layers of *tetrahedral* holes [57]. Figure 4.5 shows how this leads to a set of vertex sharing $ZnCl_4$ tetrahedra.

It is desirable to group these structures together to demonstrate how the induction effects stabilize a generic layered structure.

4.3 Predicted Structural Trends.

It is interesting to consider how the experimental structural trends in figure 1.1 compare with those predicted on the basis of *radius-ratio rules*, that is, the structures given by a simple charged sphere packing analysis. Simple geometrical analysis leads to the symmetries predicted in table 4.1 [58]. Figure 4.6a shows a reduced structure map for six sets of divalent cation halides predicted by the radius-ratio rules. The transition from high cation coordination for large cation/small anion combinations to low cation coordination for the reverse scenario is clear. Figure 4.6b shows the *experimental* structures for the same



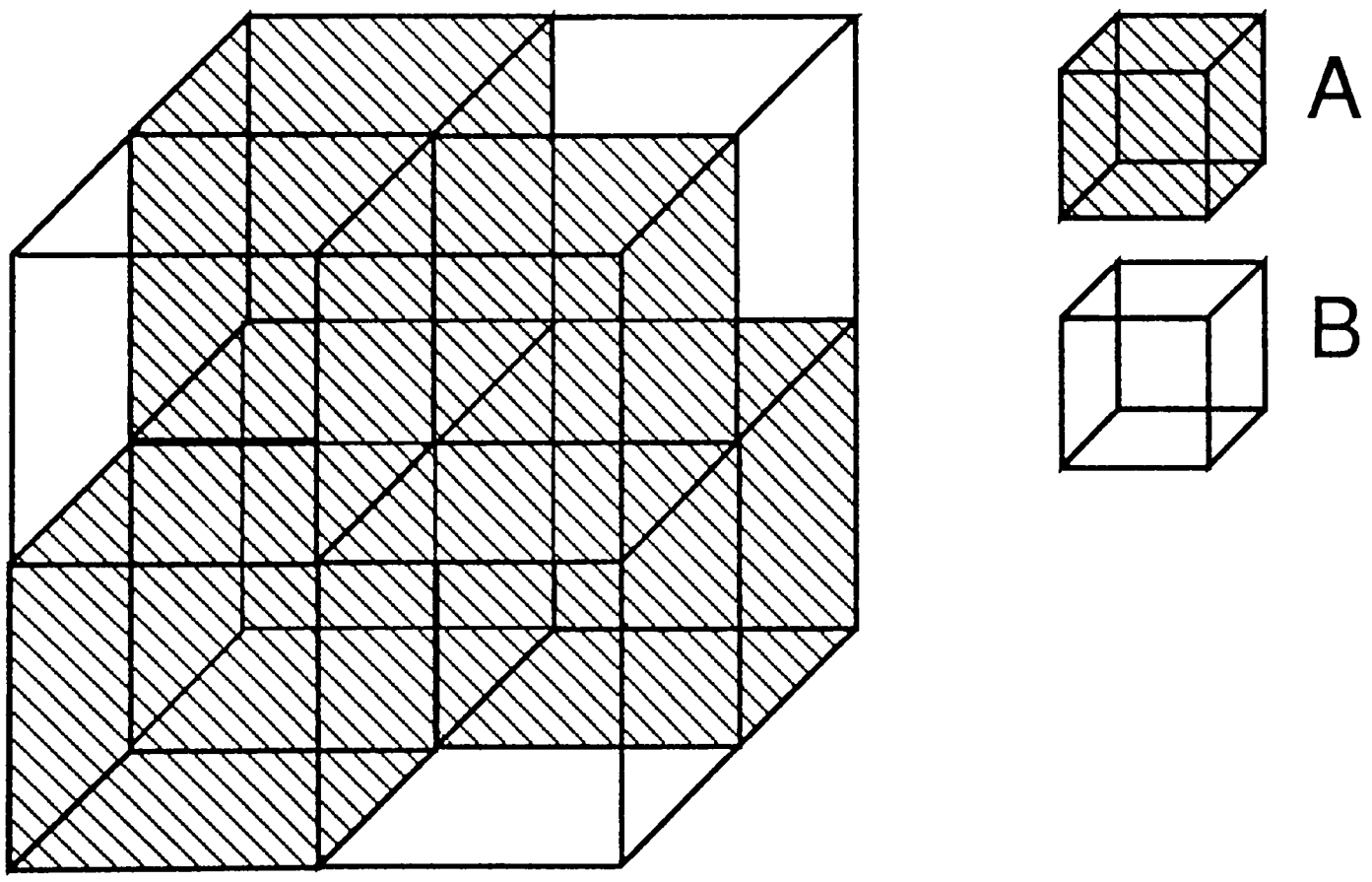


FIGURE 4.4: *The $CdCl_2$ layered crystal structure. Cells A and B are arranged as in the larger cube to form a cell with cation layers in the 111-direction.*

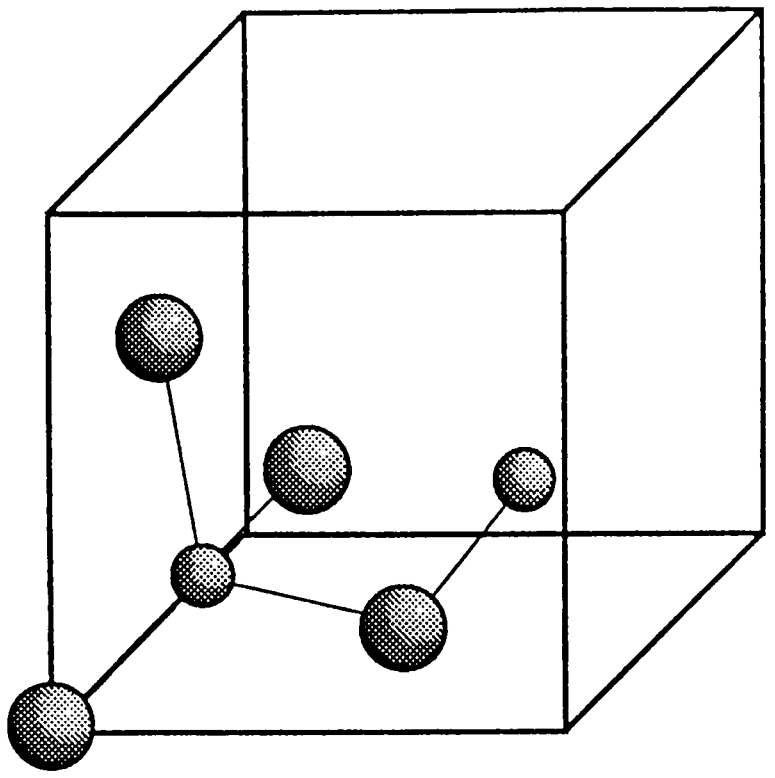


FIGURE 4.5: *The $ZnCl_2$ crystal unit cell. Key: large spheres - anions, small spheres - cations.*

$\frac{\sigma_-}{\sigma_+}$	Coordination number	Structural Type
1-1.37	8	Fluorite
1.37-2.44	6	Rutile
> 2.44	4	Cristobalite

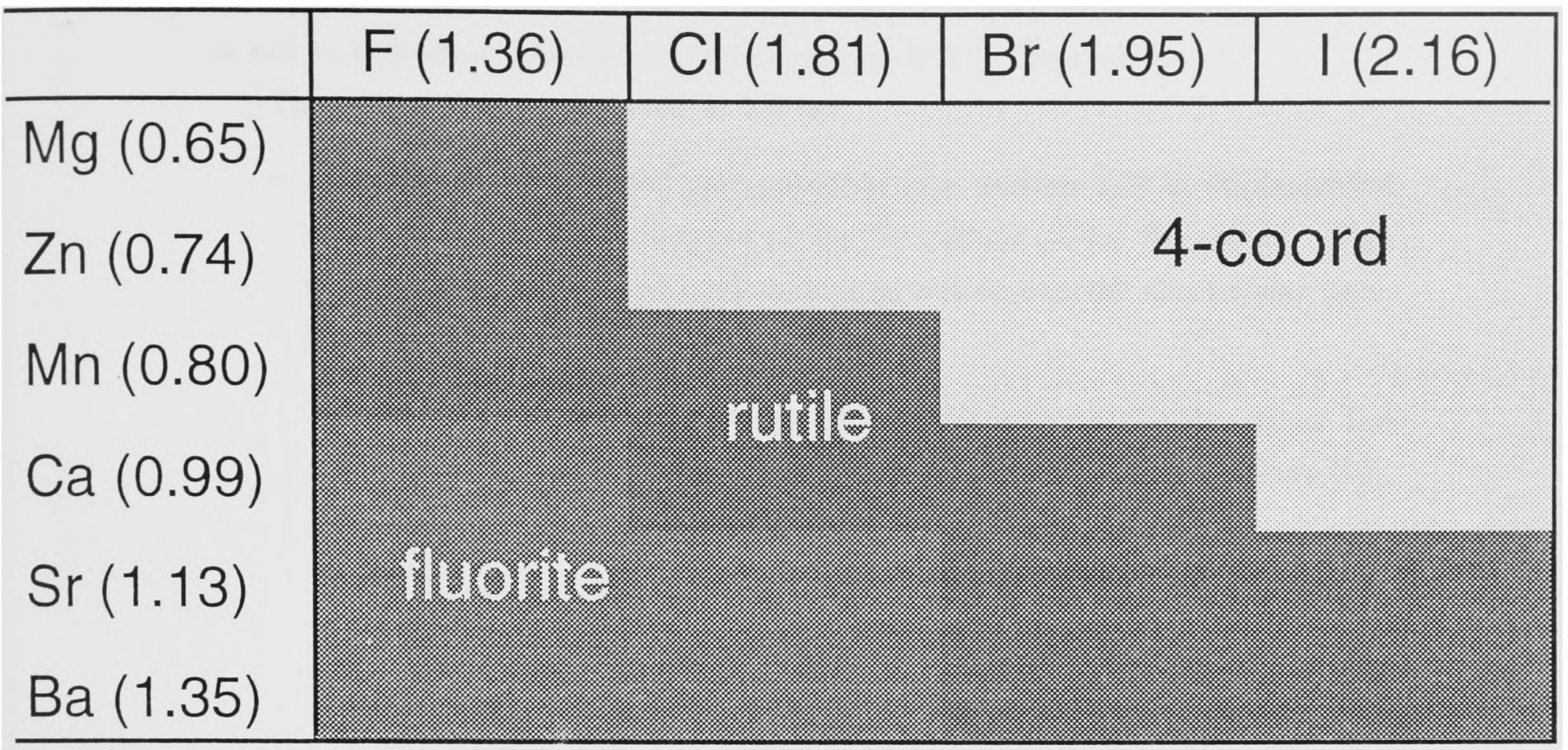
TABLE 4.1: *Predicted MX_2 structures from radius-ratio rules.*

compound set. Thus, the radius-ratio rules are only partially successful in that they predict the fluorite $\longrightarrow$ rutile/$PbCl_2$ transition but fail to account for the presence of the largely six-coordinated layered structures predicting instead four coordinated systems with the ideal-cristobalite structure (keeping the cations as far apart as possible in line with their greater coulombic repulsion).

4.4 The Calculations.

4.4.1 Parameterization of the Model.

In order to examine the role of induction effects a simple potential model with as few parameters as possible is required. In order to focus on the subtle structural effects which arise from the interplay of the induction effects and the short-range forces any contributions which do not influence the structure are neglected, that



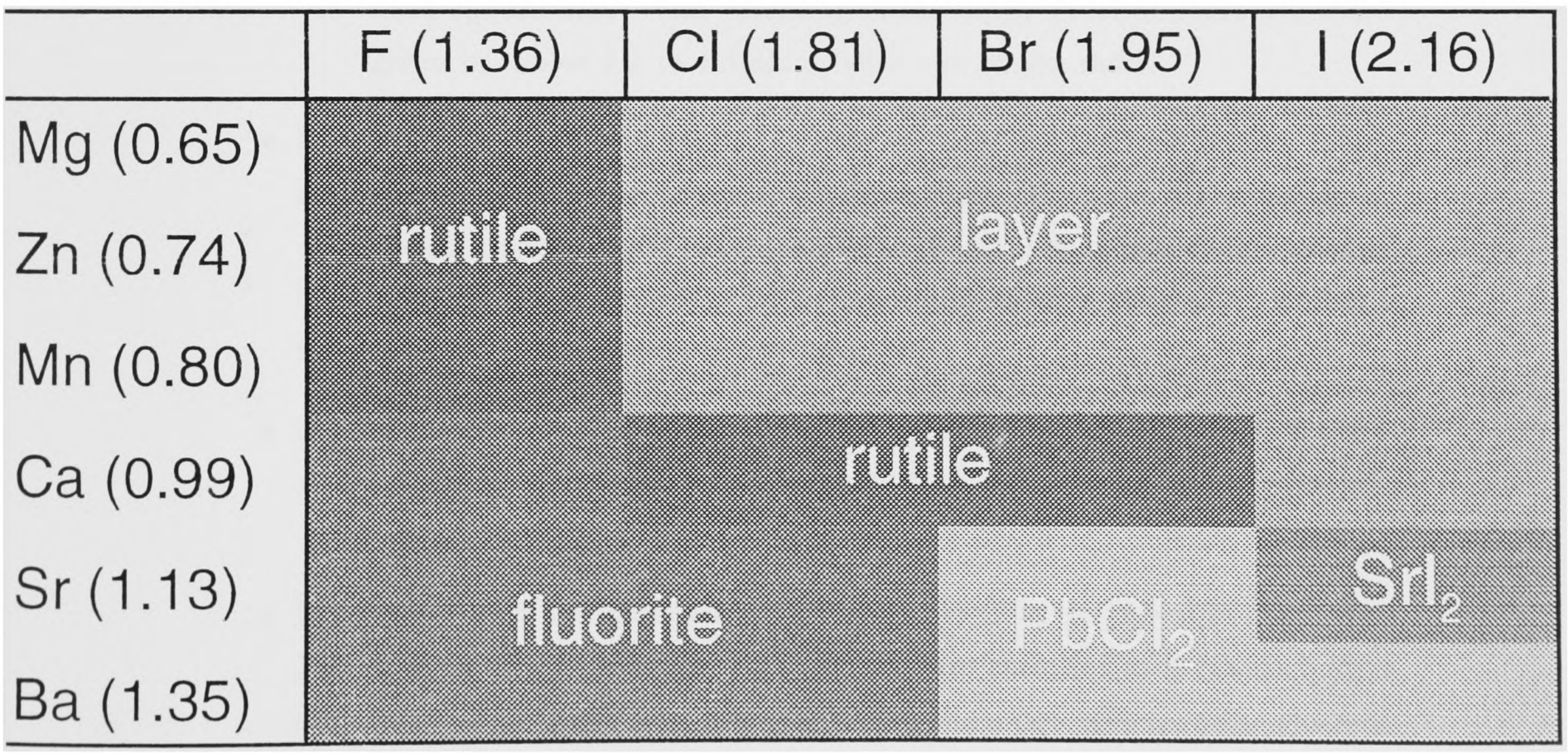


FIGURE 4.6: *Structure maps for a more limited set of cations. Top - from radius-ratio rules, bottom - from experiment. The numbers in brackets are the ionic radii in* Å.

is, extensive use of Occam's razor is advocated. The purpose of these calculations is not to reproduce *absolute* crystal energetics but to focus on *trends.*

The potential is constructed as follows:

- A standard Born-Mayer pair potential (see section 1.3) is implemented with full formal ionic charges (+2 for the cations, -1 for the anions). This includes both the ion-ion coulombic interactions and the short-range overlap effects.

  - The anion-anion interactions are taken as constant for all cations, the parameters being taken from previous alkali-halide simulations [10]. These are given in table 4.5.
  - The cation-cation short-range interaction is taken to be negligible as this is dominated by the large coulombic repulsion.
  - The anion-cation short-range interaction is derived by varying only the cation radius, σ_+, which is taken from standard tables [59]. The amplitude, A_{+-} and range, a_{+-}, of the short-range repulsion are taken as being constant at 7.75x10^{-3} au [10] and 1.6 au (3.02Å^{-1}) respectively reflecting the belief that it is the shape of the *anion* electron density that governs this interaction, the cations being more hard-sphere-like. The resulting short-range preexponents B_{+-} are given in tables 4.2 to 4.4 along with the cation radii.

- Dipole-dipole dispersion terms (C_6) are included for the anion-anion interactions only (C_6^{--}) and are cation-independent. They are estimated from *ab initio* electronic structure calculations [5, 8]. The cation-cation contribution would be expected to be considerably smaller than C_6^{--} whilst a full set of C_6^{+-} parameters is not available.

- Dipole-quadrupole dispersion terms are excluded as reliable values are not available from electronic structure calculations for a wide range of systems.

- Induction forces are included at the dipolar level as described in chapter 2. The possible effects of cation polarizability are excluded as it is anticipated that this will be much less important than the anion effects in the systems under study for the following reasons:

Cation	σ_+/Å	d_{+-}/Å	B_{+-}/aeu
Mg	0.65	2.46	13.1741
Zn	0.74	2.55	17.2942
Mn	0.80	2.61	20.7342
Ca	0.99	2.80	36.8281
Sr	1.13	2.94	56.2362
Pb	1.20	3.01	69.4919
Ba	1.35	3.16	109.3709

TABLE 4.2: *MCl_2 short-range M-Cl potential parameters. σ_+ is the cation radius, d_{+-} the sum of the anion and cation radii, and B_{+-} is the resulting Born-Mayer preexponent.*

Cation	σ_+/Å	d_{+-}/Å	B_{+-}/aeu
Mg	0.65	2.60	20.1167
Zn	0.74	2.69	26.4081
Mn	0.80	2.75	31.6610
Ca	0.99	2.94	56.2362
Sr	1.13	3.08	85.8722
Pb	1.20	3.15	106.1135
Ba	1.35	3.30	167.0083

TABLE 4.3: *MBr_2 short-range M-Br potential parameters.*

– The induction energy of the cation charge with anion polarizability is given by

$$U_-^{ind} = -\frac{1}{2}\alpha_- \left(\frac{Q_+}{r^2}\right)^2, \tag{4.6}$$

(see section 2.1.1). Similarly, the induction energy for a cation will be proportional to $\alpha_+ Q_-^2$. Thus, even if $\alpha_- = \alpha_+$ then U_-^{ind} would still be four times U_+^{ind} due to the magnitude of the formal ionic charges.

– Table 4.6 shows some typical cation polarizabilities from the electronic structure calculations of Pyper [8]. Even for the largest cation, Ba^{2+}, the polarizability is still only around half that of the chloride anion. Pb^{2+} is unique in the cation set chosen in having electrons in f-orbitals giving a large polarizability. This may account for some

Cation	σ_+/Å	d_{+-}/Å	B_{+-}/aeu
Mg	0.65	2.81	37.9587
Zn	0.74	2.90	49.8301
Mn	0.80	2.96	59.7418
Ca	0.99	3.15	106.1135
Sr	1.13	3.29	162.0343
Pb	1.20	3.36	200.2282
Ba	1.35	3.51	315.1321

TABLE 4.4: *MI_2 short-range M-I potential parameters.*

Anion	σ_-/Å	a_{--}/au	B_{--}/aeu	C_{--}/au	α_-/au
Cl	1.81	1.67	128.24	200.0	20.0
Br	1.95	1.56	140.63	350.0	30.0
I	2.16	1.37	113.83	600.0	45.0

TABLE 4.5: *Anion-anion short-range potential parameters.*

anomalies that occur for the lead systems considered.

- The cations tend to sit in symmetric or near-symmetric sites even in the layered structures where the anions are in their most asymmetric environment. This inherent symmetry lead to zero, or near-zero electric fields at the cation sites.

- The anion polarizabilities given in table 4.5 are taken from the "in-crystal" calculations due to Fowler and Madden [5] as described in 1.2. In reality they are known to be dependent upon the actual crystal but for present purposes are taken as constant. For example, table 4.7 gives the electronic structure calculation values for the polarizability of the chloride anion in the alkali halide series. These show an increase in the polarizability with lattice parameter for the reasons discussed in section 1.2.

- The induction damping parameter, b, is tied to the sum of the anion-cation ionic radii, setting

$$b = \frac{c}{\sigma_+ + \sigma_-}. \tag{4.7}$$

Cation	α_+/au
Be^{2+}	0.052
Mg^{2+}	0.486
Ca^{2+}	3.193
Sr^{2+}	5.20
Pb^{2+}	17.9
Ba^{2+}	10.1

TABLE 4.6: *The available* ab initio *divalent cation polarizabilities from ref. [8].*

Crystal	α_-/au	C_{--}/au
LiCl	19.412	158.5
NaCl	21.153	180.3
CsCl	24.421	223.7

TABLE 4.7: *The variation of the polarizability of the chloride anion and the chloride-chloride dipole-dipole dispersion term in different crystalline environments from ref. [8].*

As b increases the range of the exponential term decreases corresponding to decrease in overlap, that is, a decrease in the sum of the ionic radii for the ion pair involved. The choice of equation 4.7 leaves a single parameter (c) to be determined. It is found that the structural trends can be described by setting $b_{MgCl} = 1.0au$. All other b parameters are determined from this b (giving $c = 4.6487au$).

4.4.2 Perfect Crystal Energetics.

For each potential parameter set the minimum crystal energy for the four main crystal structure types in figure 4.6, namely fluorite, rutile, $PbCl_2$ and $CdCl_2$ is calculated (this layered structure is chosen for the relative simplicity of its underlying cubic symmetry). These four exemplify the major type of anion coordination across the whole MX_2 spectrum. Other structures exist but are generally subtle modifications of one of the above.

For each ion pair the lattice parameter, a_0, is calculated so as to minimize the crystal energy for each crystal structure. The procedure is simple; the crystal

energy is calculated as a function of the lattice parameter and fitted to a parabola in order to locate a_0 and the crystal energy U^{crys}. In the case of the fluorite structure the symmetrical nature of the anion site leads to no overall electric field and so no induced dipole. Hence, RI calculations are sufficient. In the remaining three structures we need to calculate the self-consistent values of the induced dipoles by iteratively solving equation 1.7.

Fluorite Structures.

Calculations were carried out on systems containing 108 molecules (324 ions) equivalent to 27 unit cells (three along each side of the cubic simulation cell). Figure 4.7 shows the crystal energy at the sets of lattice parameters studied for the five chlorides under consideration along with the parabolic fits of the form

$$U(r) = ar^2 + br + c. \tag{4.8}$$

Tables 4.8 to 4.10 gives the values of the fitting parameters in equation 4.8 along with the lattice parameter and crystal energy at the energy minimum of all 21 halides covered.

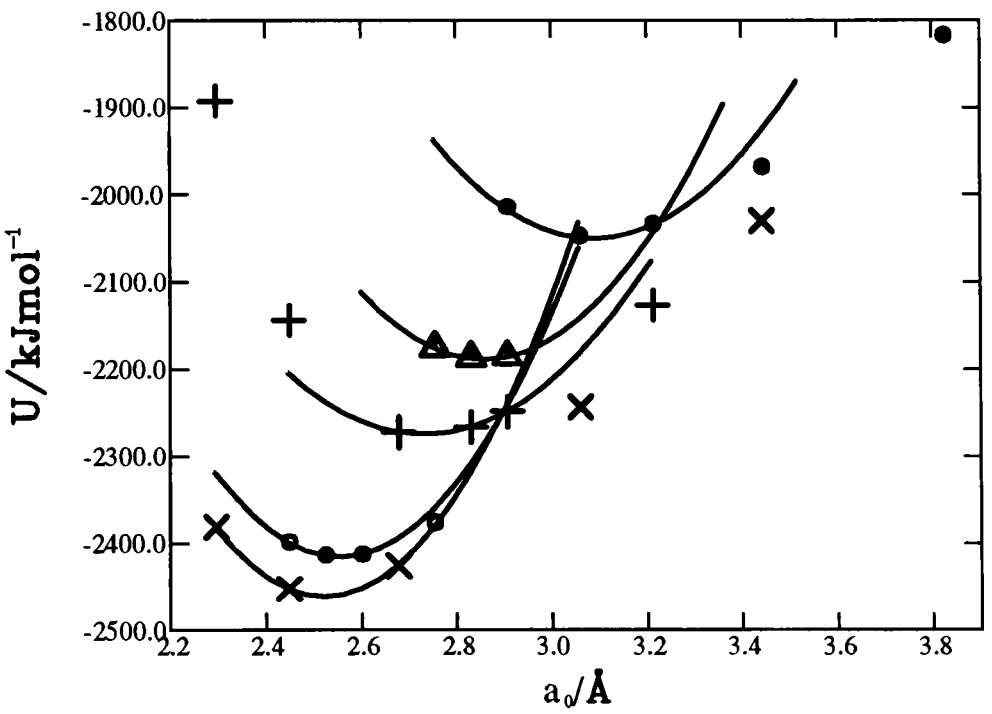


FIGURE 4.7: *MCl_2 fluorite crystal energies of five of the chlorides studied with varying lattice parameter. The solid lines are the parabolic fits to the points nearest the minimum. Key* - × - *$MgCl_2$*, ○ - *$ZnCl_2$*, + - *$CaCl_2$*, △ - *$SrCl_2$ and* • - *$BaCl_2$*.

Cation	a/au	b/au	c/au	a_0^{min}/Å	$U^{crys,min}/kJmol^{-1}$
Mg	0.360809	-23.8146	291.726	2.521	-2460.992
Zn	0.337979	-22.5977	278.367	2.553	-2415.396
Mn	0.316536	-21.5234	267.789	2.601	-2384.598
Ca	0.208652	-14.9141	172.923	2.730	-2275.046
Sr	0.275549	-20.6055	295.188	2.856	-2188.596
Pb	0.164819	-12.6203	153.556	2.929	-2139.993
Ba	0.238504	-19.2832	305.532	3.088	-2047.681

TABLE 4.8: *MCl_2 fluorite structure crystal energetics. a,b and c are the fitting parameters for equation 4.8, a_0^{min} is the lattice parameter at the energy minimum and $U^{crys,min}$ is the energy at this minimum. Note that 1Å $\equiv$1.8897au and 1 atomic energy unit $\equiv$ 4.3597$\times 10^{-18}J$*

Cation	a/au	b/au	c/au	a_0^{min}/Å	$U^{crys,min}/kJmol^{-1}$
Mg	0.274241	-18.9453	227.685	2.638	-2419.150
Zn	0.287731	-20.2500	258.569	2.688	-2375.565
Mn	0.354916	-25.3151	354.886	2.728	-2346.558
Ca	0.265847	-19.9583	282.757	2.867	-2232.451
Sr	0.217116	-17.0375	246.387	2.997	-2135.719
Pb	0.239518	-19.1895	298.324	3.064	-2091.281
Ba	0.165649	-14.0802	217.268	3.246	-1991.868

TABLE 4.9: *MBr_2 fluorite structure crystal energetics.*

Thus, as the cation size decreases for a given halide, the minimum energy becomes more negative and the lattice parameter decreases.

Layer Structures.

The relatively large nature of the unit cell described in section 4.2 limits the choice of system size to only 128 molecules (384 ions), being both large enough for a reliable calculation and small enough for realistic runtimes. The energies of an *idealised* layered structure, with the anions in a perfect fcc lattice and the cations in the alternate layers of octahedral holes, are calculated. In reality, there will be a certain amount of structural relaxation which will tend to pull

Cation	a/au	b/au	c/au	a_0^{min}/Å	$U^{crys,min}/kJmol^{-1}$
Mg	0.198223	-15.4036	209.238	2.960	-2169.843
Zn	0.204052	-16.0254	226.581	2.999	-2140.749
Mn	0.226717	-18.0381	271.658	3.043	-2118.107
Ca	0.190390	-15.7812	243.409	3.166	-2032.641
Sr	0.201910	-17.3203	290.693	3.276	-1963.061
Pb	0.158654	-13.9276	226.525	3.358	-1923.796
Ba	0.168009	-15.3516	274.705	3.490	-1846.950

TABLE 4.10: *MI_2 fluorite structure crystal energetics.*

Cation	a/au	b/au	c/au	a_0^{min}/Å	$U^{crys,min}/kJmol^{-1}$
Mg	0.194415	-13.6193	111.807	2.317	-2600.641
Zn	0.371957	-27.0951	370.445	2.409	-2522.616
Mn	0.258039	-19.1891	236.204	2.460	-2462.292
Ca	0.223601	-17.6504	236.700	2.611	-2289.442
Sr	0.182150	-15.1156	208.107	2.745	-2163.605
Pb	0.232766	-19.8953	322.515	2.827	-2104.780
Ba	0.215114	-19.4547	343.358	2.991	-1979.500

TABLE 4.11: *MCl_2 layered structure energetics.*

together layers of anions sandwiching a filled cation layer at the expense of layers sandwiching an unfilled layer [60, 61]. Approximating the structure to an idealized layered arrangement will mean that the crystal energies for these systems will be *too positive* although these effects should be small in comparison with the lattice energies. Again, an idealized calculation is performed in order to focus on the role of the induction forces and to simplify the calculation in computational terms.

Figure 4.8 shows the crystal energies for five chlorides considered with tables 4.11 to 4.13 listing the minimum energy lattice parameters and energies of all 21 systems studied.

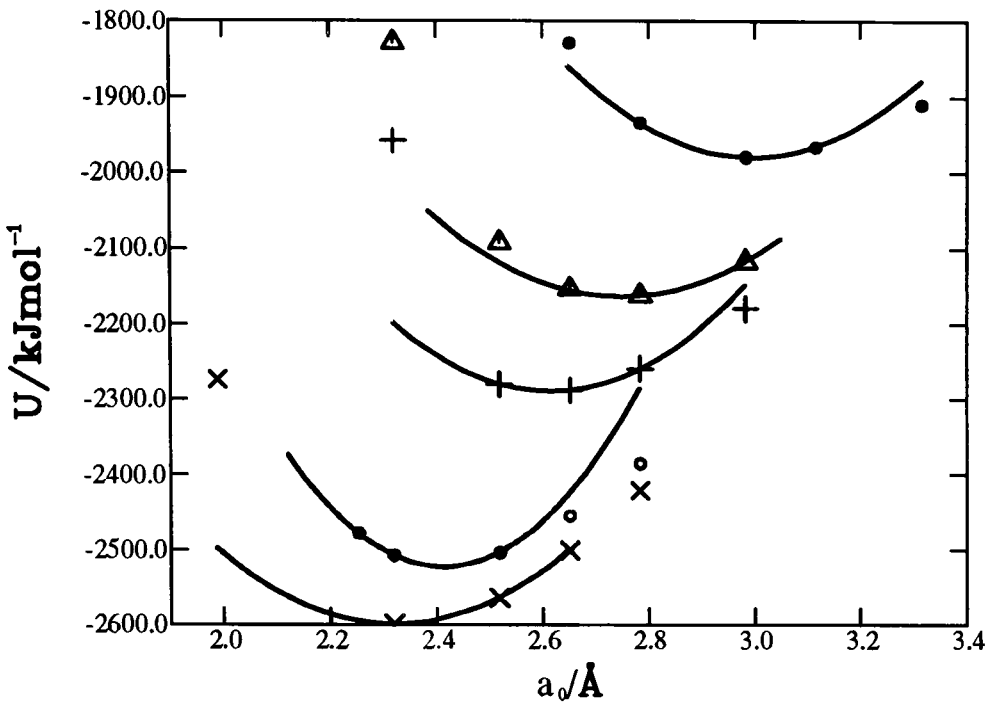


FIGURE 4.8: *MCl_2 layer crystal energies of five of the chlorides studied with varying lattice parameter. The solid lines are the parabolic fits to the points nearest the minimum. The symbols as as for figure 4.7.*

Rutile Structures.

The simulation cell contained 128 molecules (64 unit cells). The literature values for the ionic coordinates are used [53] where available, otherwise those for $CaCl_2$ are taken.

Cation	a/au	b/au	c/au	a_0^{min}/Å	$U^{crys,min}/kJmol^{-1}$
Mg	0.326654	-24.2828	324.902	2.459	-2592.273
Zn	0.382207	-29.0755	430.695	2.516	-2507.889
Mn	0.230473	-17.8036	224.820	2.555	-2440.939
Ca	0.701675	-57.6010	1071.71	2.715	-2264.726
Sr	0.285275	-24.7792	434.435	2.873	-2125.999
Pb	0.203893	-18.2542	308.190	2.961	-2058.832
Ba	0.179159	-16.9859	308.320	3.136	-1933.945

TABLE 4.12: *MBr_2 layered structure energetics.*

Cation	a/au	b/au	c/au	a_0^{min}/Å	$U^{crys,min}/kJmol^{-1}$
Mg	0.216855	-17.9797	257.381	2.742	-2364.904
Zn	0.303492	-26.1594	454.084	2.851	-2302.303
Mn	0.287932	-24.8234	425.350	2.851	-2249.609
Ca	0.276211	-25.4099	483.902	3.043	-2115.153
Sr	0.382147	-36.7818	787.933	3.183	-1992.271
Pb	0.144598	-14.1302	251.154	3.232	-1929.083
Ba	0.126154	-12.9583	243.888	3.397	-1822.996

TABLE 4.13: *MI_2 layered structure energetics.*

$PbCl_2$ Structures.

The simulation cell contained 108 molecules (27 unit cells). Again, experimental coordinates were used where available else the unit cell of $PbCl_2$ was taken as the standard.

Comparison of the Crystal Energetics.

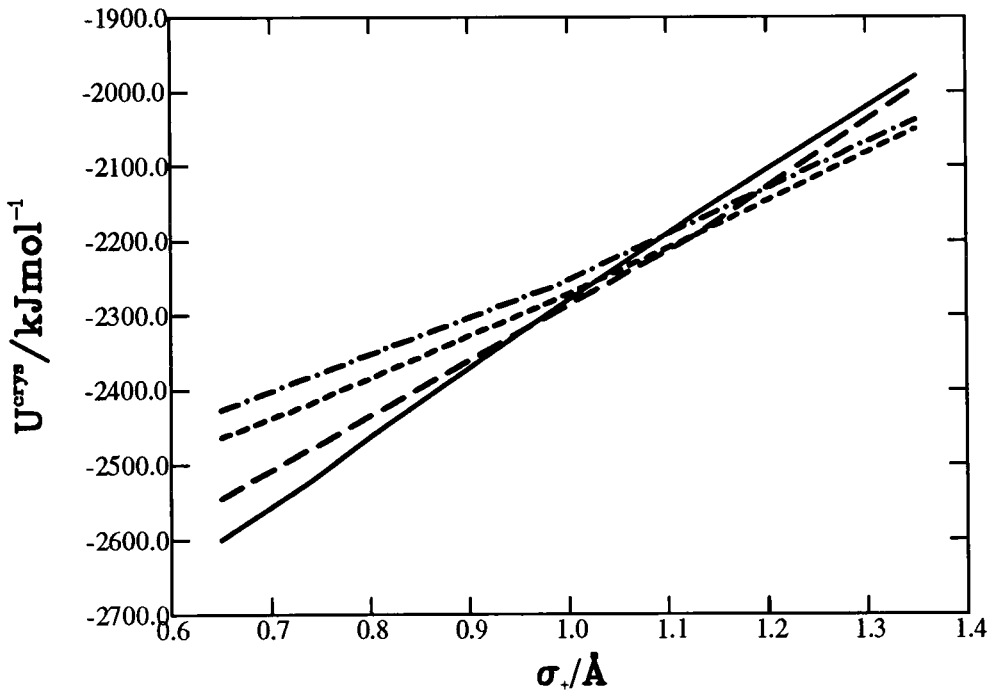


FIGURE 4.9: *MCl_2 crystal energies of the four main crystal structures with cation radius. Key: full line - layered, long dashes - rutile, short dashes - fluorite, dash-dot - $PbCl_2$.*

Figure 4.9 shows the crystal energies for the MCl_2 systems plotted against the cation radius of M^{2+}. Moving from small to large cation radius (i.e along the

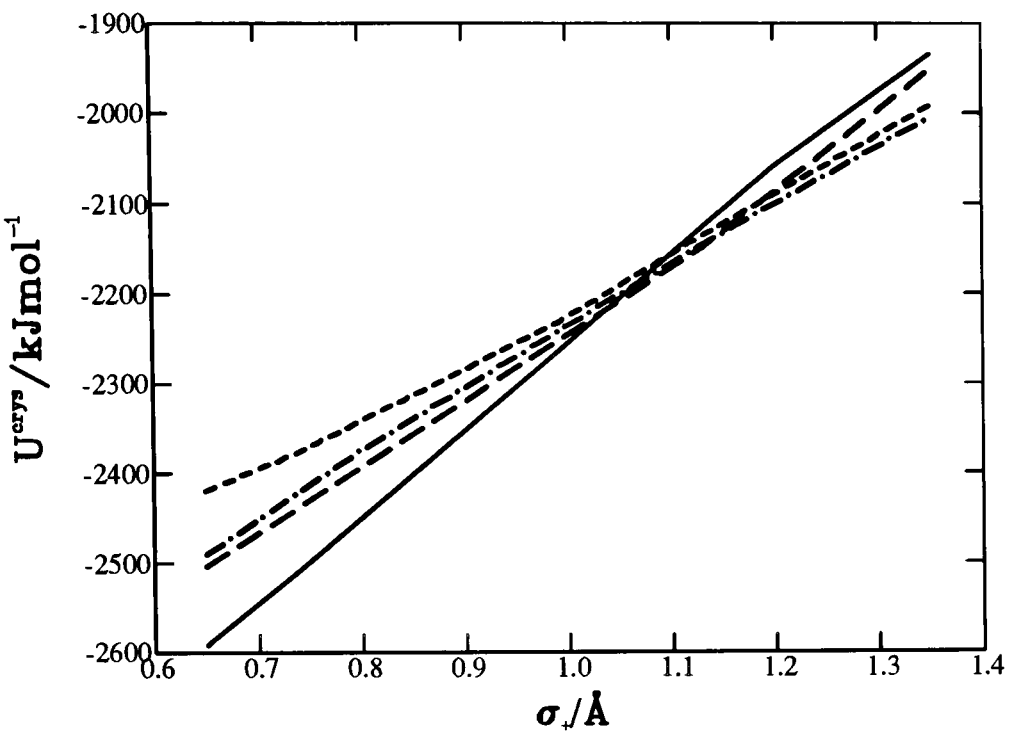


FIGURE 4.10: *MBr_2 crystal energies of the four main crystal structures with cation radius. Line styles as as for figure 4.9.*

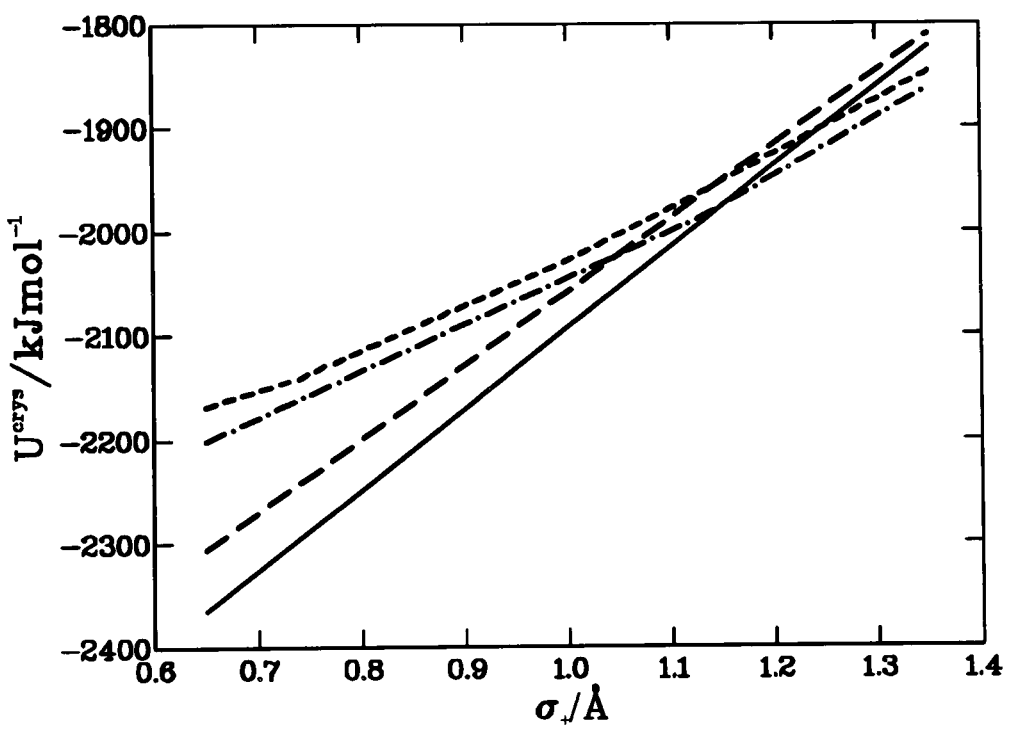


FIGURE 4.11: *MI_2 crystal energies of the four main crystal structures with cation radius. Line styles as as for figure 4.9.*

x-axis) the observed structural trend is layer $\longrightarrow$ rutile $\longrightarrow$ fluorite. Comparison with the reduced structure map of figure 4.6b confirms this as the experimentally observed trend with the exception that the emergence of the $PbCl_2$ structure is not predicted. This is not entirely surprising as this structure is only predicted to be stable for the lead cation itself amongst the chlorides and the lead systems are expected to be somewhat anomalous owing to the post-transitional nature of the cation. "Transition" cation radii of 0.95Å and 1.11Å respectively are predicted, i.e between Mn and Ca for layer $\longrightarrow$ rutile and between Ca and Sr for rutile $\longrightarrow$ fluorite.

Figure 4.10 shows the same properties for MBr_2. The trend of layer $\longrightarrow$ rutile $\longrightarrow$ $PbCl_2$ is consistent with the structure map. Note that, towards the larger cation radii, the fluorite structure is close to becoming energetically favoured; that is, if a larger cation could be found a fluorite structure bromide would become feasible. The radius ratio rules indicate that a cation radius of at least 1.42Å is required implying some type of molecular cation, e.g. NR_4^+ where R is an alkyl group, might yield a fluorite bromide.

Finally, figure 4.11 shows the same information for the diiodides. Again, the layer $\longrightarrow$ $PbCl_2$ is consistent with experiment. The fluorite structure is much less energetically favoured over the cation radius range studied.

4.4.3 The Role of Anion Polarization.

Clearly the anion polarization affects the crystal energetics markedly with the largest induced dipoles arising in the layered structures. Figure 4.12 shows a layered structure in which the negative ends of the induced dipoles are represented by the smallest white spheres. The effect of the induced dipole is to place a region of negative charge *between* adjacent cations thus effectively *screening* the coulombic repulsion between the cations. It is this screening effect that allows the cation-cation separation to equal the anion-anion in the energetically favoured structure. Similarly, the positive end of the dipole points towards a layer of anions resulting in a further stabilization acting against the direct coulombic repulsion between anion layers. The induced dipole-dipole interactions, however, supply an additional repulsive force. Careful consideration of the system geometry can reveal the relative importance of these effects. Figure 4.13 shows a small section of the layered structure including the induced dipoles. The

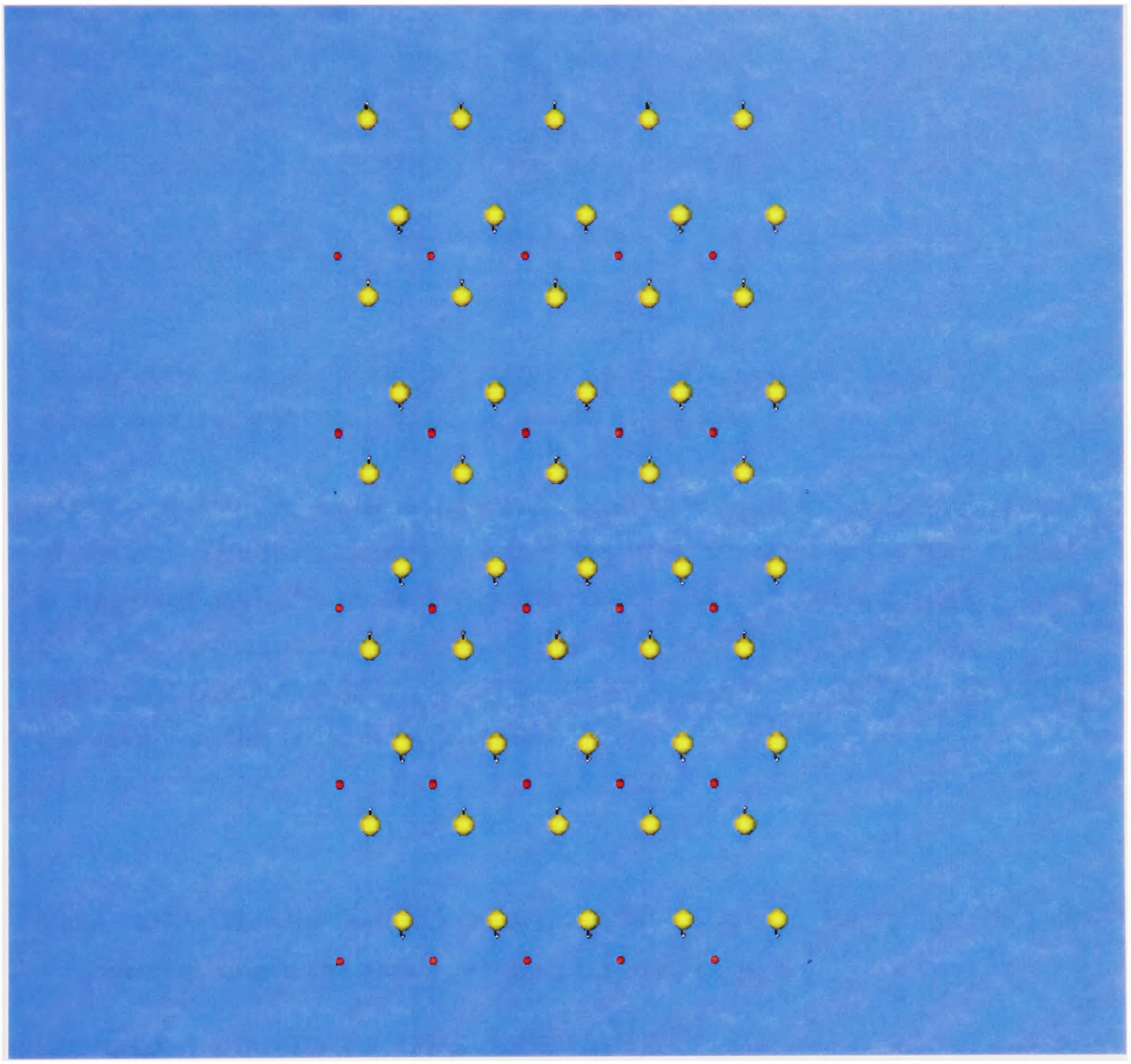


FIGURE 4.12: *AVS plot of a $CdCl_2$ startup. Yellow spheres - anions, red spheres - cations both drawn at 30% of their full ionic radius for clarity. The small white spheres represent the negative ends of the induced anion dipoles.*

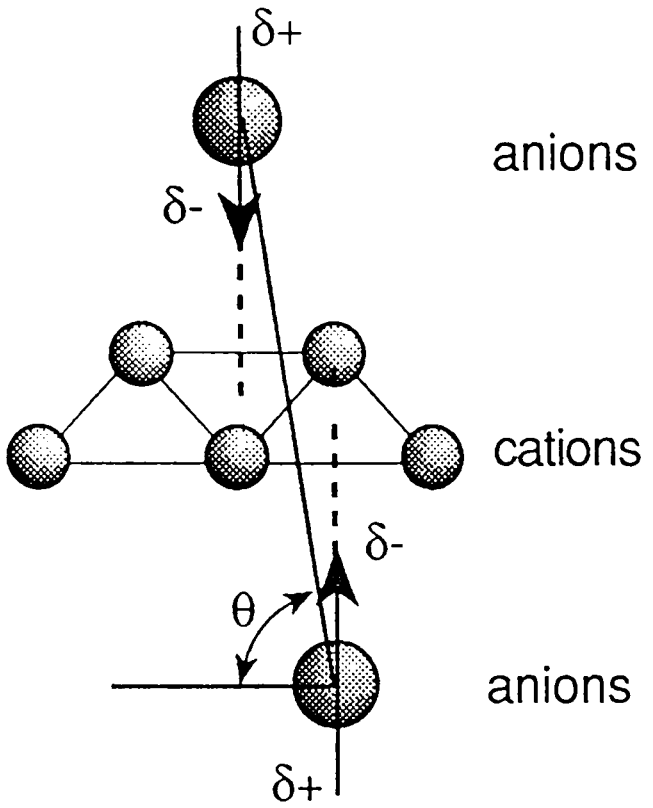


FIGURE 4.13: *A small section of the layered structure indicating the relative positions of dipoles induced in anion layers above and below a cation plane.*

negative end of the dipole points towards the centre of an equilateral triangle of cations. The fcc nature means that the layer of anions below that triangle is staggered with the anion layer above and so the dipoles induced above do not point *directly* at those induced below but instead point to the centre of an equilateral triangle of anions. Considering the two induced dipoles in figure 4.13 the energy of this interaction is given by

$$U^{\mu\mu} = -\sum_{j\neq i}^{N_t} \boldsymbol{\mu}^i . \mathbf{T}^{ij} . \boldsymbol{\mu}^j, \tag{4.9}$$

where $\mathbf{T}^{ij}$ is the dipole-dipole interaction tensor (see section 2.1.1). For the arrangement shown the only non-vanishing component is

$$U = \frac{\mu^i \mu^j \{1 - 3sin^2\theta\}}{r^3}, \tag{4.10}$$

and so the energy of interaction becomes zero when $\sin\theta = \frac{1}{\sqrt{3}}$, that is, $\theta = 35.3^o$. Below this *magic angle* the dipole-dipole interaction becomes attractive. In the layered structure this angle is above the magic angle confirming the assertion that this interaction destabilizes the structure. However, it is not as great a repulsive interaction as one might think from looking at figure 4.12. Similarly, there is an additional repulsive interaction between dipoles induced in the same

a_0/Å	$U^{\mu Q}$	$U^{\mu\mu}$	U^{pol}	$\mid \mu \mid$
	(all in atomic units)			
1.988	-11.8017	0.5387	-0.3859	0.2450
2.319	-15.1313	1.0332	-1.1742	0.4275
2.518	-15.6594	1.2013	-1.7470	0.5225
2.650	-15.5415	1.2455	-2.1123	0.5750
2.783	-15.1435	1.2416	-2.4374	0.6125

TABLE 4.14: *The variation of the dipole-charge ($U^{\mu Q}$), dipole-dipole ($U^{\mu\mu}$) and polarization energies (U^{pol}) for the $MgCl_2$ system, along with the magnitude of the self consistent induced dipole with lattice parameter.*

anion plane. Between two given dipoles this has the form

$$U^{\mu\mu} = \frac{2\mu^i\mu^j}{r^3}. \tag{4.11}$$

To summarize, the layered structure is *destabilized* by the cation-cation repulsions and both the *in-plane* and *trans-plane* dipole-dipole interactions but is *stabilized* by the charge-dipole interactions. Thus, the total energy can be written as

$$U^{crys} = \sum_{i=1}^{N_t-1}\sum_{j=i+1}^{N_t}\{\underbrace{\frac{Q^iQ^j}{r^{ij}}}_{Attractive} + \overbrace{U_{sr}^{ij}(r^{ij})}^{Repulsive} + \underbrace{T_\alpha^{ij}(\mu_\alpha^iQ^j - \mu_\alpha^jQ^i)}_{Attractive} + \overbrace{\mu_\alpha^iT_{\alpha\beta}^{ij}\mu_\beta^j}^{Repulsive}\}. \tag{4.12}$$

Tables 4.14 to 4.16 show the relative energies of interaction for three chosen systems $MgCl_2$, $PbBr_2$ and BaI_2 at various lattice parameters spanning the energy minimum. In these tables $U^{\mu Q} = \mu_\alpha^iT_\alpha^{ij}Q^j$, $U^{\mu\mu} = \mu_\alpha^iT_{\alpha\beta}^{ij}\mu_\beta^j$ and $U^{pol} = -\frac{1}{2}\alpha\sum_{i=1}^{N_t}E^{i^2}$. $\mid \mu \mid$ is the magnitude of the dipole induced on each anion site. This is constant for each anion in the system with half the dipole vectors opposing the other half. Thus, as the lattice parameter is lowered, the magnitude of the dipole induced is *reduced* via the increased overlap effects. This results in a fall in $U^{\mu Q}$, $U^{\mu\mu}$, U^{pol} and $\mid \mu \mid$. Note that $U^{\mu\mu}$ is typically an order of magnitude less than $U^{\mu Q}$ in line with our discussion above regarding the stabilization/destabilization of these structures. These relative energies will be considered more closely in the following section.

To illustrate the balance of these effects two sets of additional energy calculations are performed on the layered systems:

a_0/Å	$U^{\mu Q}$	$U^{\mu\mu}$	U^{pol}	$\mid \mu \mid$
	(all in atomic units)			
2.451	-7.1955	0.2470	-0.2210	0.2275
2.650	-8.6161	0.3828	-0.4328	0.3225
2.783	-9.2728	0.4655	-0.6093	0.3775
2.981	-9.8313	0.5607	-0.9024	0.4600
3.114	-9.9632	0.6014	-1.1027	0.5075

TABLE 4.15: *The variation of the dipole-charge, dipole-dipole and polarization energies for the $PbBr_2$ system, along with the magnitude of the induced dipole with lattice parameter.*

a_0/Å	$U^{\mu Q}$	$U^{\mu\mu}$	U^{pol}	$\mid \mu \mid$
	(all in atomic units)			
2.981	-8.2058	0.3906	-0.4191	0.3825
3.114	-8.7454	0.4634	-0.5664	0.4450
3.313	-9.2456	0.5509	-0.8108	0.5350
3.445	-9.3950	0.5916	-0.9793	0.5875
3.644	-9.3908	0.6252	-1.2244	0.6550

TABLE 4.16: *The variation of the dipole-charge, dipole-dipole and polarization energies for the BaI_2 system, along with the magnitude of the induced dipole with lattice parameter.*

- RI energies (i.e. the first two terms in equation 4.12).
- *maximum induction* energies are calculated by allowing for no overlap effects on the induced dipoles, that is, the dipoles are induced by *purely coulombic* interactions.

Table 4.17 shows the various energy terms for the set of dibromides with no overlap induced dipoles. Comparison with table 4.18 demonstrates the effect of the overlap on the values of the induced dipoles and hence on the energetics. Tables 4.19 to 4.21 gives the total crystal energies for all the systems studied for the RIM and the PIM with and without overlap induced dipoles. Figures 4.14 shows the energies of the layered structure for the three models along with that of the fluorite structure for comparison. The large overlap effect is evident. In the dibromide, for example, the induction energy is around 12.5% of the total

Cation	$U^{\mu Q}$	$U^{\mu\mu}$	U^{pol}	$\mid \mu \mid$
	(all in atomic units)			
Mg	-53.9732	13.8956	-12.437	1.7075
Zn	-50.6440	12.5647	-12.181	1.6875
Mn	-47.8200	11.1127	-11.991	1.6750
Ca	-41.8730	9.2670	-11.282	1.6250
Sr	-39.3016	8.3628	-10.945	1.6000
Pb	-32.5918	6.1616	-9.917	1.5250
Ba	-28.8045	5.0265	-9.217	1.4700

TABLE 4.17: *MBr_2 layered structure energetics with no overlap induced dipoles.*

crystal energy with overlap and a massive 40% without overlap. Figure 4.15 also clearly demonstrates how the layered structure is never favoured over the fluorite within the framework of the RIM. It is made favourable by the inclusion of the induction effects. The experimental trends are *not* observed with the RIM.

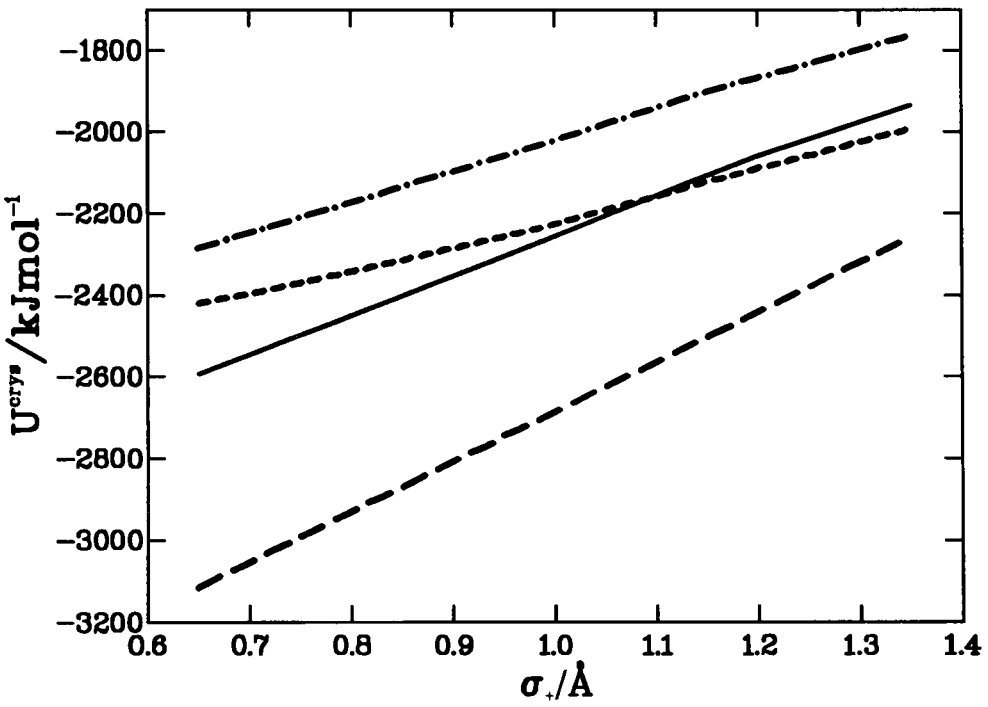


FIGURE 4.14: *MBr_2 Crystal energies for the three layered models considered. Long-dashes - no overlap effects, solid line - with overlap and dash-dotted line - RIM. The short dashed line is the energy of the fluorite structure for comparison.*

Careful analysis of figures 4.9 to 4.11 indicate non-zero induced dipoles in both the rutile and $PbCl_2$ structures. However, these dipoles are typically an

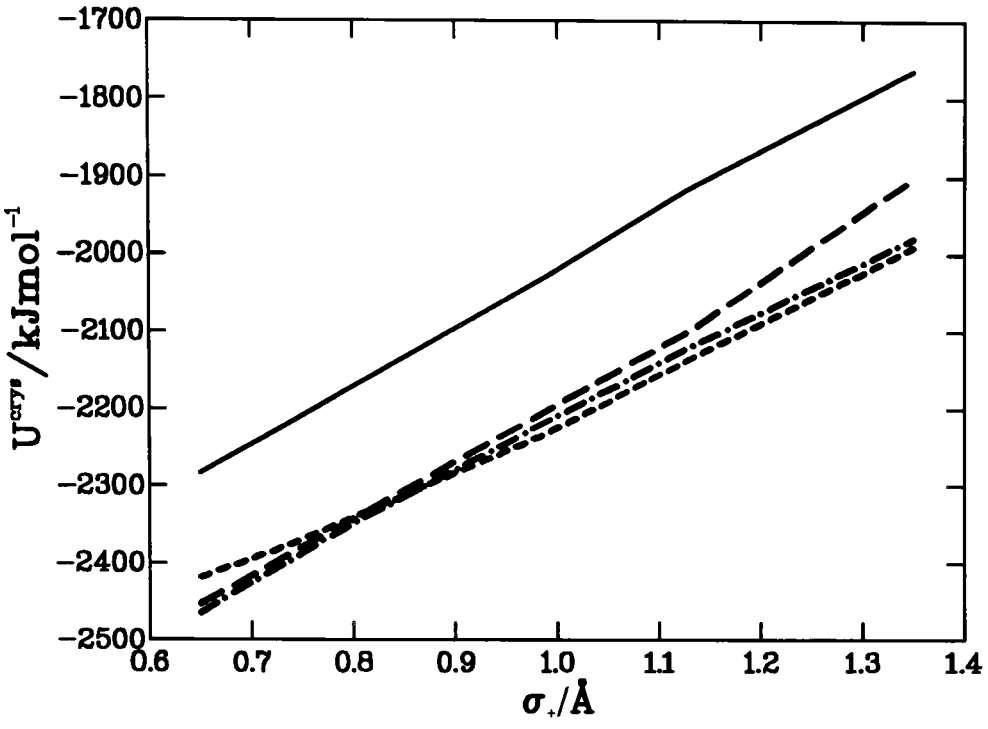


FIGURE 4.15: *MBr_2 crystal energies for the four main crystal types using a RIM. Line styles as as for figure 4.9.*

order of magnitude smaller than in the layered structures as the anions are in a near-symmetric site leading to effective cancellation of these fields. The magnitudes of the dipoles induced in these structures depend upon the exact ion coordinates and the relative dimensions of the unit cell. It is not our intention here to concentrate on these dipoles too closely as they are represent a much less significant effect than in the layered structures. This accounts for the success of a simple charged hard sphere model in predicting the transitions between these structures and the fluorite structure.

4.4.4 Molecular Dynamics Simulations.

All of the calculations described above are 0K energy minimizations. It is important, therefore, to demonstrate that the layered structures anticipated to be stable on purely energetic grounds are also stable during the course of an MD simulation. Simulations in the canonical (constant NVT) ensemble are performed on 384 ions (8 unit cells) using the $MgCl_2$ parameters at a temperature of 800K (the melting point of $MgCl_2$ is 987K). To monitor the stability of the layered structure the Bragg peak associated with the scattering from successive

Cation	$U^{\mu Q}$	$U^{\mu\mu}$	U^{pol}	$\mid \mu \mid$
	(all in atomic units)			
Mg	-16.0749	1.2326	-1.1032	0.5100
Zn	-14.2941	0.9746	-0.8723	0.4525
Mn	-13.1814	0.8288	-0.7418	0.4175
Ca	-11.8605	0.7616	-0.9968	0.4825
Sr	-10.5712	0.7216	-0.9524	0.4735
Pb	-9.8313	0.5607	-0.9024	0.4600
Ba	-8.6849	0.4861	-1.0731	0.5025

TABLE 4.18: *MBr_2 energetics including full overlap induced dipoles.*

layers of cations is monitored. This is

$$S_{++}(k) = \frac{1}{N_+} < A_+^*(k) A_+(k) >, \tag{4.13}$$

where N_+ is the number of cations and $A_\alpha(k)$ is the *scattering amplitude* of the cations given by

$$A_+(k) = \sum_{i=1}^{N_+} e^{i\mathbf{k}.\mathbf{r}^i}. \tag{4.14}$$

In the simulation cell chosen the relevant k-vector is at $\frac{2\pi}{L}(222)$ where L is the equilibrium simulation cell size (18.54Å).

Figure 4.16 shows the value of S(k) at this vector evolving in real time for a pair of simulations carried out with and without induction effects. This figure clearly shows the collapse of the layered structure in the RIM simulation whilst the analogous PIM simulation gives a stable structure on this timescale.

Figures 4.17a and 4.17b demonstrate this even more dramatically using molecular graphics to show a snapshot of the simulation cell after 1ps of the respective simulations. In the PIM simulation the layered nature of the structure is still evident with the ions performing small amplitude oscillations about their equilibrium coordinates. In stark contrast the RIM simulation cell is completely amorphous after the same simulation time period. The explanation is simple: in the PIM the induced dipoles stabilize the relatively close cation-cation separation via the screening mechanism described above. In the RIM no such stabilization exists and so the cations try to move as far apart as possible acting

Cation	U^{rim}	U^{pim}_{nodamp}	U^{pim}_{damp}
	(all in $kJmol^{-1}$)		
Mg	-2307.102	-3166.428	-2600.600
Zn	-2254.086	-3054.655	-2522.601
Mn	-2212.432	-2980.158	-2462.292
Ca	-2080.529	-2855.997	-2289.442
Sr	-1980.341	-2570.427	-2163.602
Pb	-1932.601	-2483.542	-2105.023
Ba	-1830.300	-2297.300	-1979.510

TABLE 4.19: *Crystal energies for the MCl_2 systems for the RIM (U^{rim}), PIM without overlap induced dipoles (U^{pim}_{nodamp}) and PIM with overlap induced dipoles (U^{pim}_{damp}).*

under the large coulombic repulsion. This leads to the catastrophic breakdown of the crystal structure resulting in the *charge-ordered* amorphous system.

4.5 A More General Crystal Model.

In the previous sections the calculations have concentrated on showing how the real, experimentally observed, crystal structural trends can be explained by the inclusion of induction effects. However, a clear conceptual illustration of these effects will allow the conclusions drawn from the previous calculations to be further clarified.

Consider the fcc anion unit cell in figure 4.18 along with the eight available cation tetrahedral holes numbered $1-8$ (note that if we swap the anions and cations and fill up all of the tetrahedral sites then the fluorite structure of figure 4.1 is recovered). To build an MX_2 system two tetrahedral holes must be filled leaving three choices:

- {1,7} (and three equivalent pairs). This arrangement gives $r_{CC} = \sqrt{3} r_{AA}$ and is the *charge-ordered* option.

- {1,3} (and eleven equivalent pairs). Here $r_{CC} = r_{AA}$ giving a layered structure that can be stabilized with respect to the first option by the anionic induced dipoles.

Cation	U^{rim}	U^{pim}_{nodamp}	U^{pim}_{damp}
	(all in $kJmol^{-1}$)		
Mg	-2283.344	-3113.832	-2572.273
Zn	-2219.804	-3009.085	-2487.889
Mn	-2171.479	-2936.023	-2420.939
Ca	-2028.180	-2704.655	-2244.726
Sr	-1915.517	-2557.338	-2105.999
Pb	-1867.184	-2414.285	-2058.832
Ba	-1763.677	-2257.366	-1913.945

TABLE 4.20: *Crystal energies for the MBr_2 systems for the RIM, PIM without overlap induced dipoles and PIM with overlap induced dipoles.*

- {1,2} (and eleven equivalent pairs). $r_{CC} = \frac{r_{AA}}{\sqrt{2}}$ allowing potentially larger induction effects with respect to option two but at the expense of greater cation-cation coulombic repulsion.

The first type of arrangement corresponds to an ideal-cristobalite structure, subtle modifications of which are formed by, for example, silica. The second structure corresponds to the $ZnCl_2$ unit cell (see figure 4.5) and consists of *vertex* sharing tetrahedra. The third option is equivalent to the *edge* sharing tetrahedral structures of, for example, $\{Pd,Pt\}Cl_2$ and $\{Si\}\{S,Se\}_2$. The final two options correspond to crystal structures of dimensionality three and one respectively [62].

Finally, it is worth going back to consider MX structures within this framework. These structure can be well predicted by RI models. However, induction effects could be important for crystal structure in extreme cases. Again, considering figure 4.18 (and noting that filling sites {1,3,6,8} recovers the NaCl structure sites) {1,2,3,4} (or {5,6,7,8}) could be filled leaving $r_{CC} = \frac{r_{AA}}{\sqrt{2}}$ but allowing induced dipoles to form. To our knowledge only CuTe [3] has such a structure. This falls into the general classification as it is clearly a combination of a small cation and an *extremely* polarizable anion.

Cation	U^{rim}	U^{pim}_{nodamp}	U^{pim}_{damp}
	(all in $kJmol^{-1}$)		
Mg	-2055.497	-2816.295	-2364.904
Zn	-1993.479	-2726.587	-2302.303
Mn	-1952.132	-2666.782	-2249.609
Ca	-1821.148	-2477.413	-2115.113
Sr	-1750.690	-2337.855	-1992.271
Pb	-1715.683	-2268.083	-1971.412
Ba	-1640.412	-2118.115	-1821.991

TABLE 4.21: *Crystal energies for the MI_2 systems for the RIM, PIM without overlap induced dipoles and PIM with overlap induced dipoles.*

4.6 Other MX_2 Systems.

For completeness it is worth considering the only other major series with this stoichiometry, namely the oxides and chalcogenides of the four-valent cations. Energy minimization calculations will not be performed on these systems for the following reasons:

- The instability of the free doubly charged anion with respect to electron loss results in the polarizabilities of these species being very dependent upon the specific crystalline environment (see the introduction and chapter 8).

- The spectre of polyanions (X_n^{m-}) formed by S, Se and Te systems arises. This is a chemical effect which cannot be reproduced within such a simple model.

It is, however, generally interesting to consider these structures to see if the same structural trends of the types associated with the halides can be identified. Figure 4.19 shows the full structure map for these systems plotted using the same rules as figure 1.1 (with data from [53] and [63]). It is apparent that the same *general* principles apply to the oxides and chalcogenides as to the halides. It should be noted that the term "layered" now applies to a wider range of structures with chemical effects distorting the more simple structures [63].

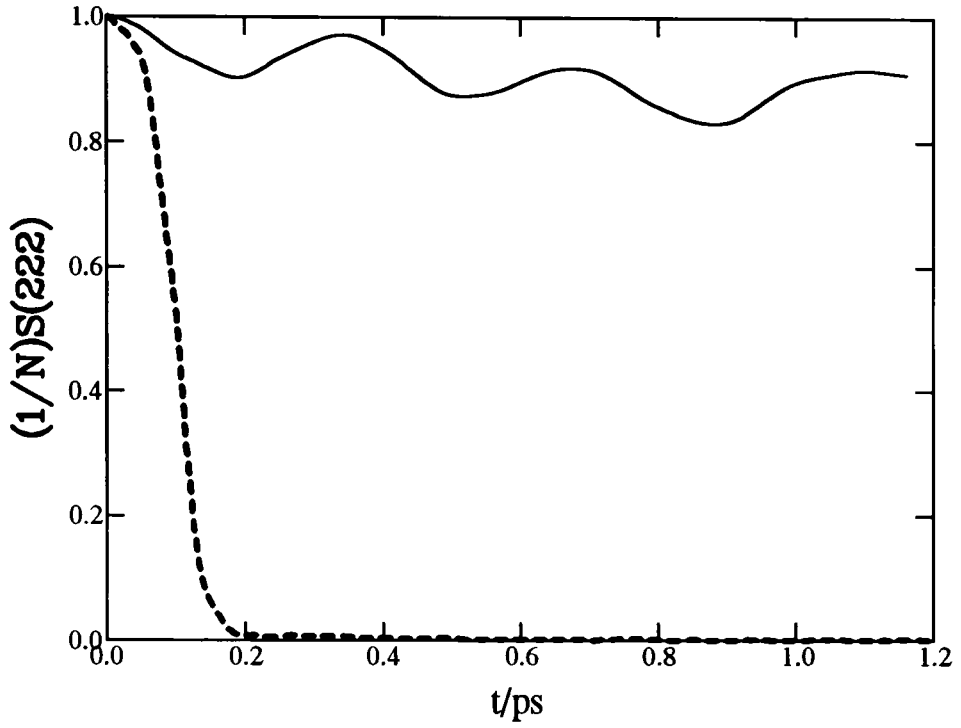


FIGURE 4.16: *The height of the Bragg peak corresponding to the interlayer cation correlations normalised to unity at* $t = 0$. *Solid line - PIM, dashed line - RIM.*

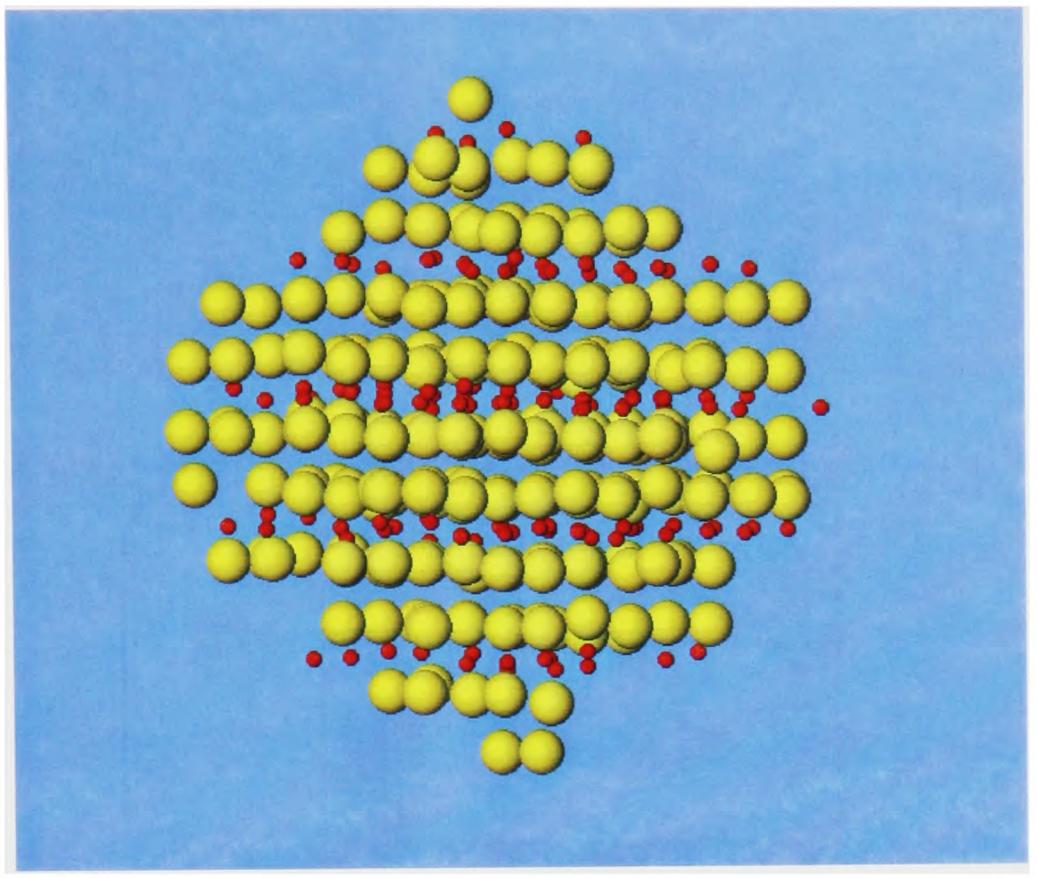


FIGURE 4.17: *AVS "snapshot" of the MD simulation cell after 1ps of a run with a layered $CdCl_2$ startup using the PIM (top) and RIM (bottom).*

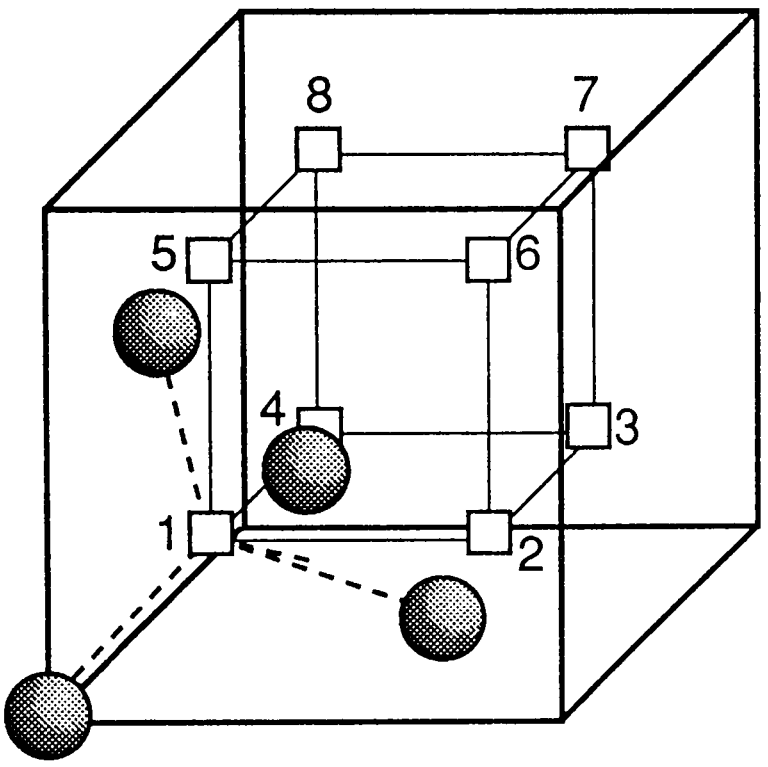


FIGURE 4.18: *An FCC anion unit cell with the eight tetrahedral sites (squares) labelled 1-8.*

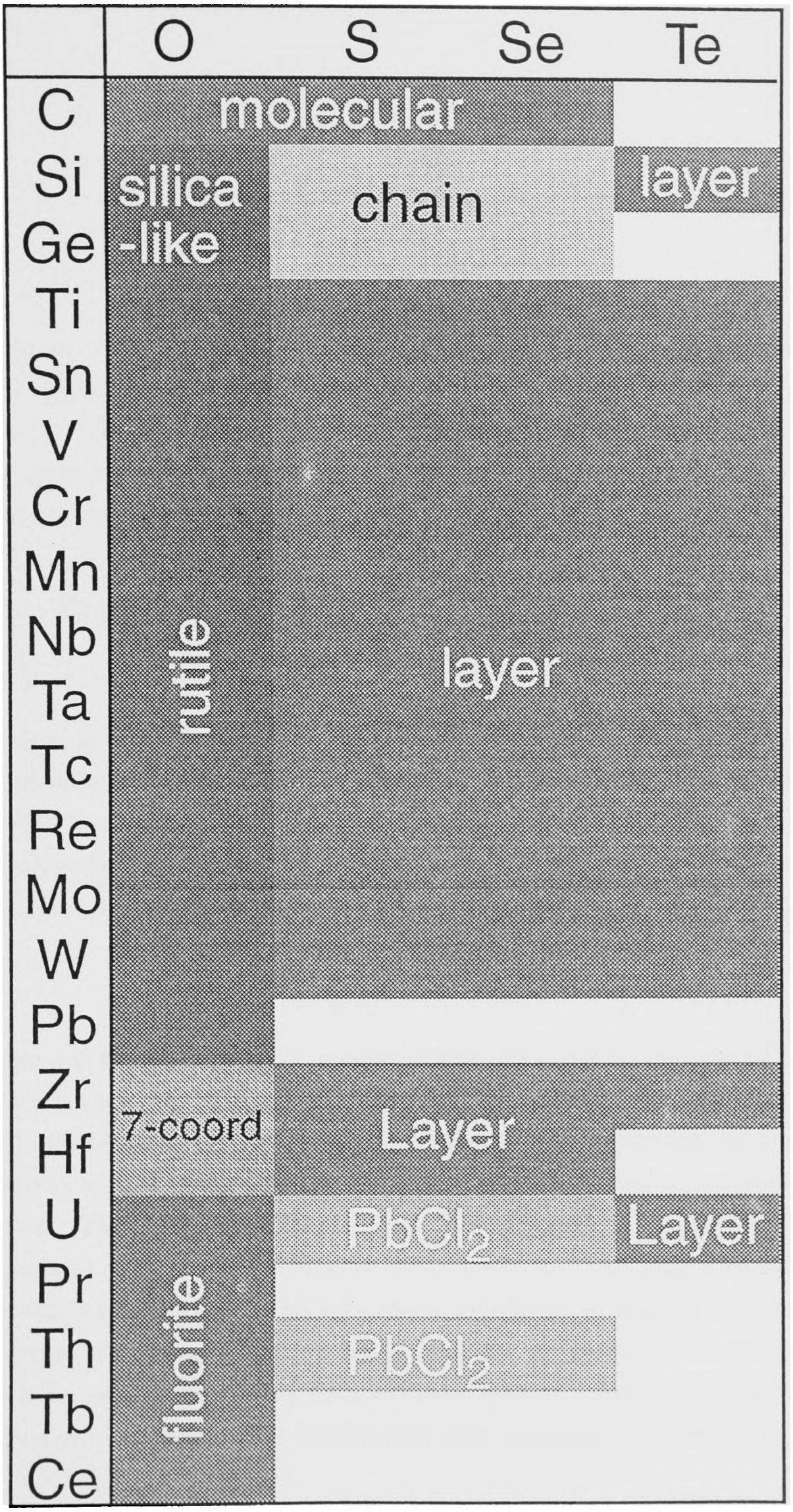


FIGURE 4.19: *Structure map for the metal oxides and chalcogenides.*

5

MX_2 Liquids.

In the previous chapter it was demonstrated how the experimentally observed MX_2 crystal structures can be reproduced by a simple, systematic model that includes induction effects. The next logical step is to demonstrate that the same principles apply to the liquid state, for which structural information is available from neutron scattering experiments.

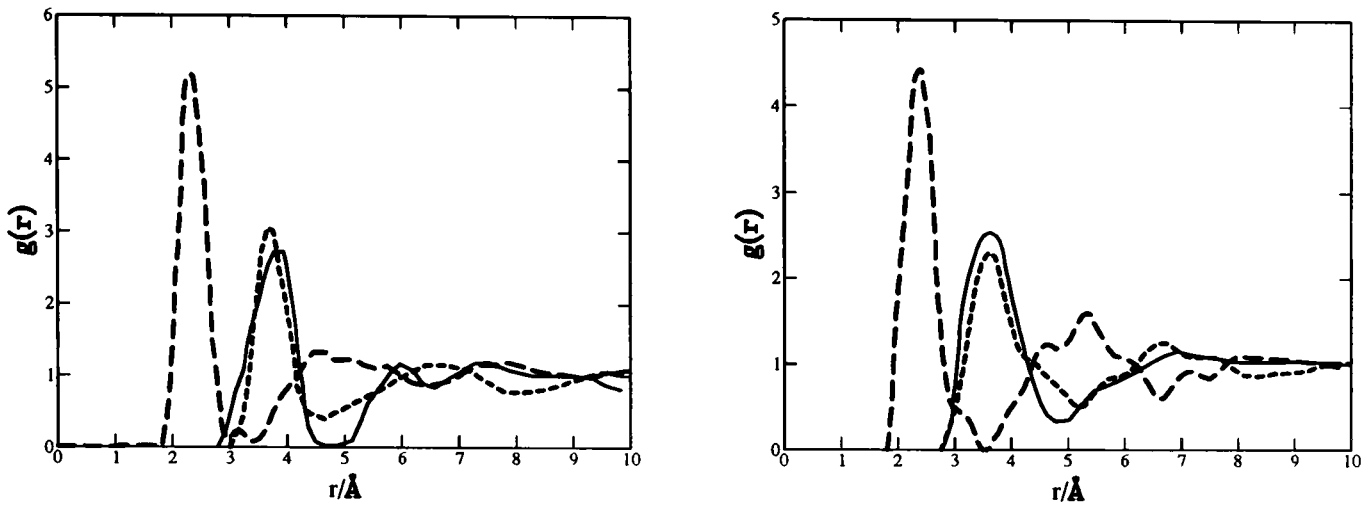
5.1 Experimental Work.

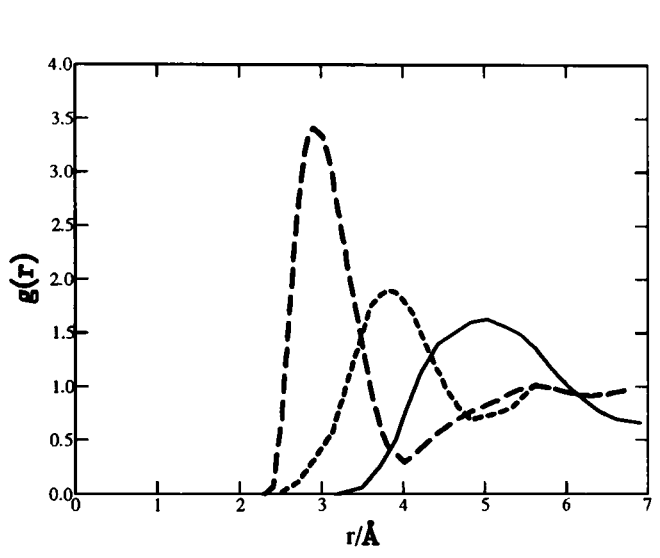
5.1.1 Neutron Scattering.

Neutron diffraction has, over the last two decades, become the primary source of information for probing the structure of ionic liquids. Using the *isotopic substitution* method [64] total scattering intensities can be resolved into *partial* structure factors. Fourier transformation of these partial structure factors, $S_{\alpha\beta}$, leads to a set of partial radial distribution functions, $g_{\alpha\beta}$, (prdf)

$$g_{\alpha\beta}(r) = \frac{1}{2\pi^2\rho}\int_0^\infty dk k^2 \frac{sin(kr)}{kr}(S_{\alpha\beta}(k) - 1), \tag{5.1}$$

where ρ is the ion-pair ($\alpha\beta$) number density, which gives the spatial correlations between each ion pair $\alpha\beta$ in real space. In general, for a system containing N chemically distinct species, N(N+1) scattering experiments on samples with different isotopic compositions are required to determine the partial structure factors. Thus, for the MX_2 systems, three experiments are required. This requirement can become prohibitive when there are more than two species in the system (e.g in the $ZnCl_2$/MCl mixtures considered in chapter 6) requiring large amounts of expensive neutron beam time. Hence, many of the systems of interest have neutron scattering data available only at a total structure factor level. This gives relatively little insight into the correlations between the individual





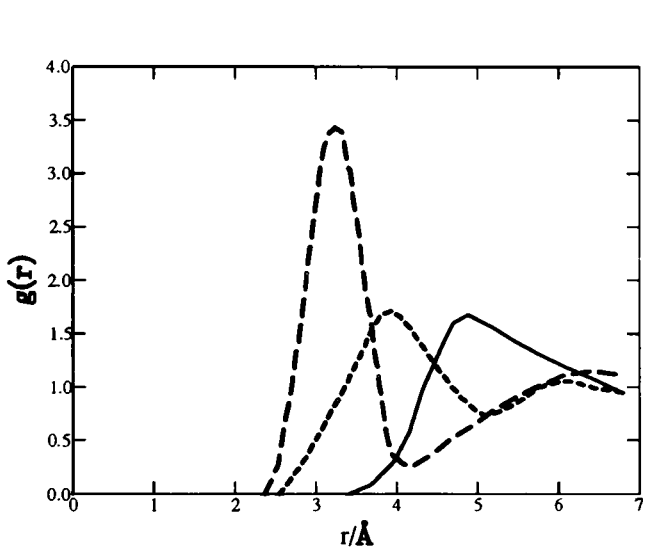


FIGURE 5.1: *Experimental partial radial distribution functions for the MCl_2 systems. Full line - $g_{MM}(r)$, short dashes - $g_{ClCl}(r)$, long dashes - $g_{MCl}(r)$. Top left - $ZnCl_2$, top right - $MgCl_2$, bottom left - $SrCl_2$, bottom right - $BaCl_2$.*

species and so a general computer simulation model should be of considerable use.

Figures 5.1a-d show the experimentally determined partial rdfs for $MgCl_2$ [65], $ZnCl_2$ [66, 67], $SrCl_2$ [68] and $BaCl_2$ [69] respectively. These represent an appreciable range of cation radii in the MCl_2 systems which have been resolved to the partial structure factor level by experiment. $NiCl_2$ [70] and $CaCl_2$ [71, 72] have also been resolved to this level. The chlorides are a popular choice for neutron scattering experiments of this kind due to the existence of two stable and abundant isotopes ^{35}Cl and ^{37}Cl. The other halide systems investigated, $NiBr_2$ and NiI_2 [73, 74], utilize the availability of two stable *metal* isotopes (^{60}Ni and ^{62}Ni). For completeness it is noted that $MnCl_2$ [65] and $CoCl_2$ [75] have been studied at the total scattering intensity level.

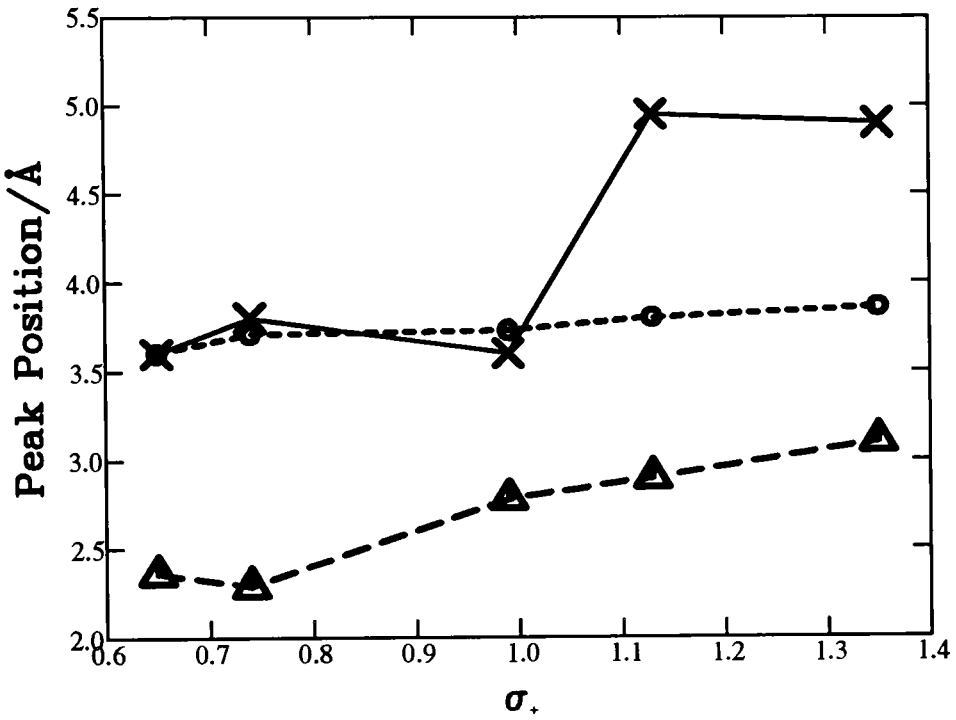


FIGURE 5.2: *Experimental positions of the first peaks in the radial distribution functions with respect to the cation radius (σ_+ in Å).* × *- cation-cation,* ○ *- anion-anion,* △ *- anion-cation.*

Considering the three ion-ion correlations in turn. Figure 5.2 shows the experimental first peak positions against cation radii. The essential characteristics can be summed up as follows:

- **M-Cl**: The peak position moves out with increasing cation radius and broadens - corresponding to a less tightly bound first coordination shell.
- **Cl-Cl**: The peak position is approximately constant across the cation

Cation	Coordination number
Mg	4.3
Zn	4.3
Ni	4.7
Ca	5.4
Sr	6.9
Ba	7.7

TABLE 5.1: *Experimental MCl_2 cation-anion coordination numbers.*

radius range. The minor differences in peak position and shape reflect the different temperatures at which the experiments were carried out. For example, the lower melting point of $ZnCl_2$ allows these experiments to be carried out at lower temperatures.

- M-M: Figure 5.2 indicates the existence of two regimes. For cation radii less than and including Ca^{2+} ($\sigma_{Ca^{2+}} = 0.99$Å) the position of $g_{MM}(r)$ is approximately equal to that in $g_{ClCl}(r)$ whilst for the larger Sr^{2+} and Ba^{2+} cations the cation-cation correlation is at longer range. On purely coulombic grounds this latter behaviour would be expected allowing the more highly charged cations to stay further away from each other with respect to the anions. Following the analysis of the crystalline systems these systems are termed *charge-ordered.* It is worth drawing attention at this early stage to the clear similarity between this liquid state behaviour and the solid state behaviour discussed in section 4.4.3.

Additional information arises from integrating over the first rdf peaks yielding the coordination numbers. Table 5.1 shows cation-anion coordination numbers

$$N_{+-} = 4\pi n_0 \int_0^{r_{min}} g_{+-}(r) r^2 dr, \tag{5.2}$$

where r_{min} is the first rdf local minimum and n_0 is the number density. The largest cation in this series, Ba^{2+}, is surrounded by the most anions, 7.7 on average (compared with 8 in the fluorite crystal structure), whilst the smallest cations have around 4 nearest anion neighbours *suggesting* tetrahedral coordination. This decrease in coordination number with cation radius is a simple *packing*

effect; that is, the smaller the cation the smaller the number of anions that can physically surround it. This behaviour can be (and has been) reproduced from a simple RIM; it is generating the experimental cation-cation correlations that is problematic.

The radial distribution functions represent the averaged real-space correlations between the species. There is, however, important structure evident in the reciprocal space structure factors that is hard to extract from the transformed functions. Let us consider partial structure factors for systems from either end of the range covered, namely $ZnCl_2$ and $BaCl_2$. Both the $S_{MCl}(k)$ and $S_{ClCl}(k)$ show typical ionic behaviour with the negative principal peak of the S_{MCl} function lying below the positive peak in S_{ClCl}. This demonstrates the charge-ordered (anions surrounded by cations) nature of these systems. The major difference, again, lies in the cation-cation correlations. The Zn-Zn function shows a clear feature at $\simeq 1\text{Å}^{-1}$, that is, at around half the value of the principal peak. This feature is not evident in the Ba-Ba function. The position of this peak corresponds to inherent order in the system of the range $5-10$Å [76], that is, longer ranged than the first coordination sphere, and so this is referred to as *intermediate range order* (IRO). The low k peak itself is termed the "prepeak" [66] (reflecting the fact that it appears at lower k than the principal peak) or the *first sharp diffraction peak* (FSDP) (reflecting the peak's relative sharpness). The FSDP is one of the most important and studied aspects of these systems and part of this, and the following, chapter will be devoted to considering its origins. An FSDP appears in the $S_{MM}(k)$ of the chlorides of Mg, Zn, Ni and Ca and to a much lesser extent in $S_{MCl}(k)$.

Day and McGreevy [72] have suggested that liquid $CaCl_2$ undergoes a change in its inherent structure between 1083 and 1223K. They suggest that the structure evolves from having the relatively close cation correlations at the lower temperature to being isomorphous with $BaCl_2$ at the higher temperature. However, although the Raman scattering indicates some sort of change and indeed Ca^{2+} is intermediate between the small and large cations, it is not clear that the change in total structure factor is consistent with such a transition. Specifically there seems to be no change in the total scattering intensity in the low k-vector region that would be characteristic of such a structural rearrangement.

5.1.2 Raman Scattering.

The Raman spectra of both the chlorides [77, 78] and bromides [79] have been measured. The low and high frequency behaviour is similar to the alkali halide melts [76]. In the intermediate cation radii range an additional shoulder is found that develops into a full blown peak in $MgCl_2$ [77], $ZnCl_2$ [80] and $MgBr_2$ [79]. This feature appears in only the polarized spectrum implying a symmetrical nature to the mode responsible. It has been attributed to the symmetric breathing of the tetrahedral units in the system [81].

5.2 Simulations and Theory.

Computer simulation has proved a major success in the analysis of molten alkali halide properties (see e.g [10] for a review). However, the seemingly natural progression to the simulation of the alkaline earth halides has been largely unsuccessful resulting in relatively few published works.

The most comprehensive body of work to date is by de Leeuw on $SrCl_2$ [51, 82, 83]. Born-Mayer potentials were derived by Busing [50] from self-consistent field calculations and vibrational spectra, with the subsequent parameters then adjusted to fit the lattice constants and crystal energies. These were used by de Leeuw to look at both the structural [51] and dynamic [82] properties. The anion-anion and cation-anion distribution functions were in good agreement with experiment [68] although the cation-cation function was less satisfactory being too high, too sharp, and peaking at slightly too large a separation. The relative peak positions show that the simulated system is charge-ordered. It is worth comparing the dispersion terms derived by Busing with those of Pyper [8] from electronic structure calculations. Busing gives C_6^{SrSr} as 207.9au compared with the Pyper value of 24.04au. Similarly the SrCl and ClCl terms appear high although there are no direct electronic structure calculations with which to compare them. Busing gives C_6^{ClCl} as 679.0au compared with the typical alkali halide values of table 4.7 which are a factor of $3-4$ less. An alternative potential due to Dixon and Gillan [84], calculated from an electron gas model with additional adjustments to fit defect energies, was used to look at the solid-state fast-ion conduction properties. Table 5.2 gives the parameter sets for the two models. The large differences between the two parameter sets supports the as-

sertion that empirical models tend to fit to a relatively narrow range of available data. It is impossible to reach a satisfying conclusion regarding the accuracy of such potentials away from the actual fitting conditions.

Ion Pair	a^{ij}/au		B^{ij}/au		C^{ij}/au	
	I	II	I	II	I	II
+ +	2.8145	0.0000	32776.4	0.00000	207.867	0.0000
− −	1.1117	1.6465	20.6123	45.0984	678.963	2.8283
+ −	1.5939	1.3590	150.771	28.4489	376.041	0.0000

TABLE 5.2: *The $SrCl_2$ parameters of Busing [50] (I) and Dixon and Gillan [84] (II).*

The only other MCl_2 system that has received serious attention is $ZnCl_2$ mainly due to its behaviour as a *glass former* of *intermediate strength* (Angell's classification [85]). Indeed, the first simulation of $ZnCl_2$ by Woodcock, Angell and Cheeseman (WAC) [86] was combined with a study of BeF_2 and SiO_2, both strong glass formers (see section 5.7 where these models will be used). The WAC potential generated the correct short range order with chloride tetrahedra surrounding central zinc cations. However, the liquid remained stubbornly charge-ordered. This was confirmed by the later studies of Gardner and Heyes [87] who studied four different potentials in which both the ion radii and the formal charges (of course retaining charge neutrality) were varied. These studies confirmed that the charge-ordered nature of the simulation liquid is a result of having a mixture containing charges in a ratio of 2:1 rather than depending upon the charge magnitude itself. Kumta, Deymier and Risbud (KDR) [88] successfully reproduced the position of all three partial distribution functions (although the lack of a y-axis scale in the original work prevents critical analysis of the peak heights). The method used, however, is worthy of serious critical comment. The Born-Mayer potential relating to cation-cation interactions can be written as

$$U^{++}(r^{ij}) = \frac{Q^{+2}}{r^{ij}} + B^{++}e^{-\alpha^{++}r^{ij}} - \frac{C_6^{++}}{r^{ij6}}, \tag{5.3}$$

where only the dipole-dipole dispersion term is included. Therefore, the only attractive term (and therefore the only term that can reduce the characteristic cation-cation correlation length) is the C_6^{++} dispersion term. In fact the doubly charged nature of the cations makes the Born-Mayer short range exponential

Cation	C_6^{++}/au
Mg	0.536
Ca	10.57
Sr	24.04
Ba	67.67
Pb	91.86
Zn	7207.5

TABLE 5.3: Ab initio *cation-cation dipole-dipole dispersion coefficients from ref. [8]. Also shown is the empirical Zn-Zn parameter used in the KDR potential.*

virtually redundant leading some authors to set $B^{++} = 0$ thus reducing the parameter set. The strategy of Kumta *et al* is to take the basic RIM but choose a C_6^{++} term large enough to partially overcome the coulombic repulsion thus bringing the $g_{ZnZn}(r)$ peak into agreement with experiment. They find that a value of 7207.5au fits this requirement. At this point a direct comparison with *ab initio* derived dispersion coefficients of the kind discussed in chapter 3 would be desirable. Unfortunately, the large number of valence electrons in the Zn^{2+} cation places such calculations out of the range of the great majority of current computational facilities. Table 5.3 lists all available *ab initio* values [8] for doubly charged cations along with the KDR value for comparison. The fitted C_6^{ZnZn} is found to be two orders of magnitude greater than the *ab initio* value for Pb^{2+} .This leads to three comments:

- The KDR C_6^{++} value, although allowing for the reproduction of the experimental distributions, is *not physically reasonable.*
- Since the C_6^{++} is the *only* attractive term pertaining to the cation-cation part of the potential, then there must be some inherent physics *missing* from the usual RIM.
- The "missing" force required to lower the range of the cation-cation distribution must be large, hence the large empirical C_6^{ZnZn}.

The observation of departures from idealised ionic model behaviour led to a theoretical assault on these systems by Ballone *et al* for $SrCl_2$ [89] and Pastore *et al* for $ZnCl_2$ [90].

For $ZnCl_2$ the authors demonstrate how the Zn-Zn spatial correlations can be accounted for as long as their mutual coulombic repulsion is *screened*, in this case using a *dielectric function* of the form

$$\epsilon_{\alpha\beta}(r) = 1 + (\epsilon_\infty - 1)\{1 - exp(-r/{\lambda_{\alpha\beta}}^2)\}, \tag{5.4}$$

where ϵ_∞ is the dielectric constant characteristic for the induced polarization, r is the cation-cation separation, and $\lambda_{\alpha\beta}$ is the cation-cation screening length chosen to be of the order of the mean anion-cation separation. $\epsilon_{\alpha\beta}$ is estimated to be 2.8 from solid-state refractive index data [90]. Thus, by this parameterization, $r > \lambda_{\alpha\beta}$ leading to an effective screening of the cation-cation repulsion. Note also that in the RI limit $\epsilon_\infty = 1$, leaving $\epsilon_{\alpha\beta}(r)$ at unity which results in the charge-ordered system.

In the $SrCl_2$ work the authors show how the experimental cation-cation distribution can be reproduced via a simple one-component plasma (OCP) model [91] in which the divalent cations sit in a smeared-out uniform neutralizing background representing the anions. By calculating the *plasma parameter* from the experimental density they find $\Gamma = 4e^2/ak_BT \simeq 200$, where a is the characteristic interionic separation, they reproduce the *simulated* $g_{Sr_rSr}(r)$ of de Leeuw. If Γ is reduced to $\simeq 73$ (consistent with a background dielectric constant of 2.72, as obtained from solid-state measurements [92]) a curve close to that observed experimentally is obtained.

5.2.1 Summary.

As the cation radius of M^{2+} is decreased:

- the M-M spatial correlation changes from a *next-nearest* neighbour to a *nearest* neighbour length scale.
- the cation-anion coordination number decreases in line with a simple charged sphere-packing analysis.
- A low k-vector feature (the "prepeak" or "first sharp diffraction peak") is present in $S_{MM}(k)$ (and to a much lesser extent in $S_{MCl}(k)$) in the smaller cation systems with M={Mg,Zn,Ni,Ca} but not M={Sr,Ba}. This is characteristic of *intermediate range order* on the length scale $5 - 10$Å.

- RI simulations can model the charge-ordered systems effectively but fail to account for the cation-cation distributions in the small cation systems unless *unphysical* dispersion terms are invoked.

- Analytical study demonstrates how screening the cation-cation interactions can greatly improve the agreement with experiment.

- A clear peak can be resolved in the polarized Raman spectrum at intermediate frequencies. This is distinct from typical molten alkali halide behaviour.

5.3 The Simulations.

The first objective is to apply the same simplified model described in chapter 4 to the liquid state. The simulation details specific to the liquid state are as follows:

- The simulation system contains 108 MCl_2 molecules (324 ions in total).

- The number density is kept constant for all cations using a box length, L, of 42au ($\equiv$ 22.3Å) corresponding to a number density of $0.00979 \text{molecules} \text{Å}^{-3}$.

- Each run begins from the an ion coordinate file, generated by melting a fluorite crystal at high temperature and gradually reducing to 1200K.

- Each run consists of 10000 steps at a time step of 20au ($\equiv 4.8ps$ total runtime) of equilibration from the molten state startup file followed by production runs of another 10000 steps.

Three systems spanning the physical range of cation radii, namely $ZnCl_2$, $SrCl_2$ and $BaCl_2$, were studied.

5.3.1 Short Range Order.

Figures 5.3a-c show the partial radial distribution functions for the three systems. It is clear from these that the trend in the cation-cation distribution *is* reproduced. Similarly the increased sharpness and the reduction in coordination number are also reproduced (see table 5.4). The shapes of $g_{++}(r)$ and $g_{--}(r)$ are not in as impressive agreement with experiment as the peak positions but this is

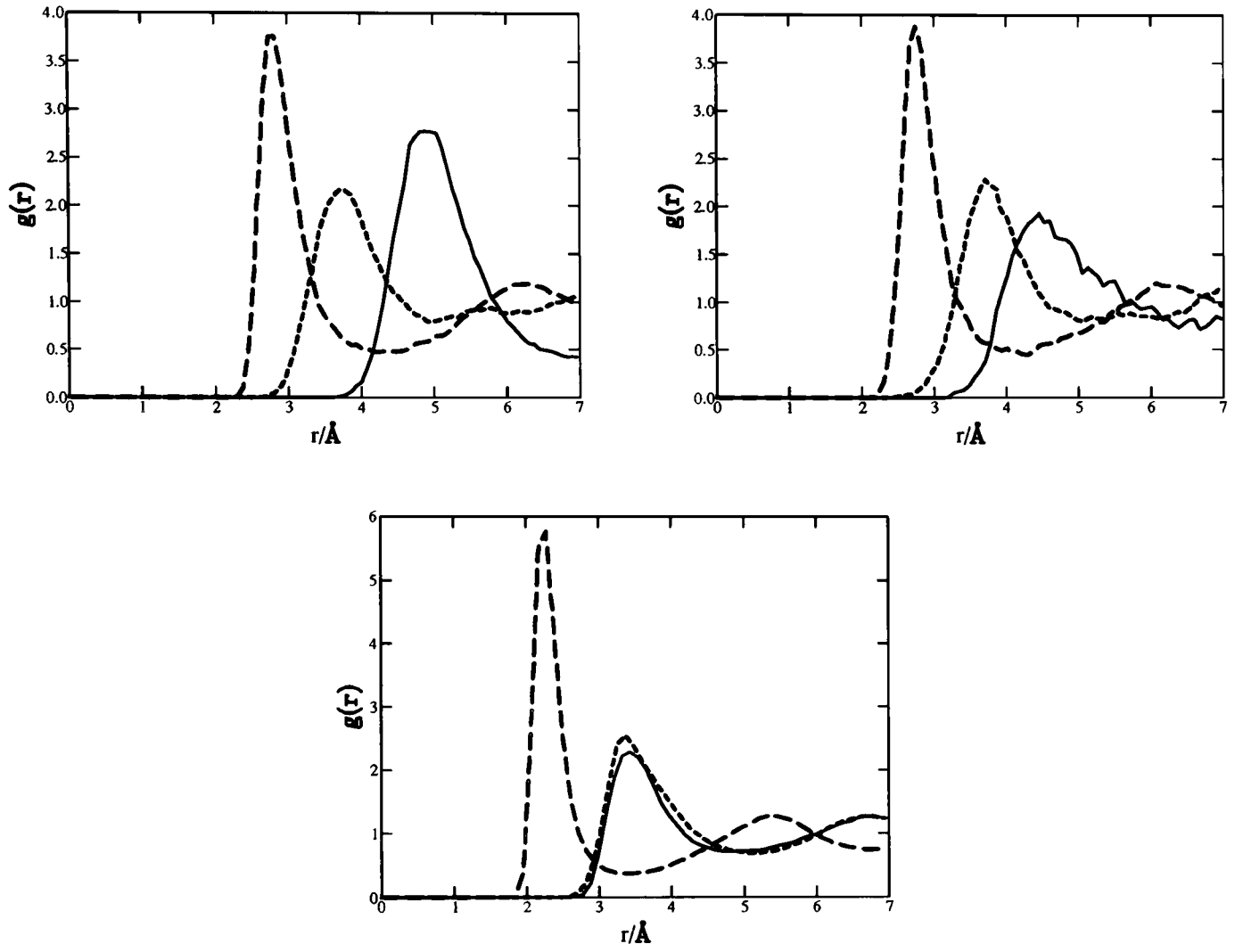


FIGURE 5.3: *Radial distribution functions for MCl_2 from the PIM. Line styles as in figure 5.1. Top left - $BaCl_2$, top right - $SrCl_2$, bottom - $ZnCl_2$.*

Cation	Coordination Number
Mg	4.22
Ca	5.45
Sr	6.20
Ba	6.63

TABLE 5.4: *MCl_2 M-Cl coordination numbers over the range of cation radii studied.*

largely a result of the high simulation temperature with respect to experiment. However, bearing in mind the simple generalizations invoked in order to generate *transferable* potentials, and considering the failure of previous RI simulations, the overall agreement with experiment must be considered to be excellent.

In order to identify the role of the induction forces another set of simulations of the same runtime and from the same startup file are performed using the RIM. Figures 5.4a-c show the three partial rdfs from these simulations. In agreement with previous RIM simulations [51, 87] these simulation cells are *charge-ordered* irrespective of the cation radius. *This comparison indicates that the evolution of the cation-cation structure with decreasing cation radius is directly attributable to the inclusion of induction forces caused by allowing for anionic polarization* [93]. The sharpness and reduction of the coordination number are also present in the RIM indicating that this is a simple *packing effect.*

Section 5.3.3 will deal with the characteristic changes in liquid structure more closely.

5.3.2 Intermediate Range Order.

A crucial test of the PIM is to see if an FSDP can be generated. The finite system size means that spurious features from truncation errors appear if the structure factors are generated via Fourier transformation of the rdfs (equation 5.1). Hence equation 4.13 is used to calculate $S_{\alpha\beta}(k)$ *directly.* Wavevectors are chosen so as to be commensurate with the periodic boundary conditions, i.e of the form $k = \frac{2\pi}{L}(m, n, p)$ where (m,n,p) are integers and L is the simulation cell length. The $S_{\alpha\beta}(k)$ functions are then generated by averaging over k-vectors of equal length. k-vectors are selected in order to focus on the low k region. The

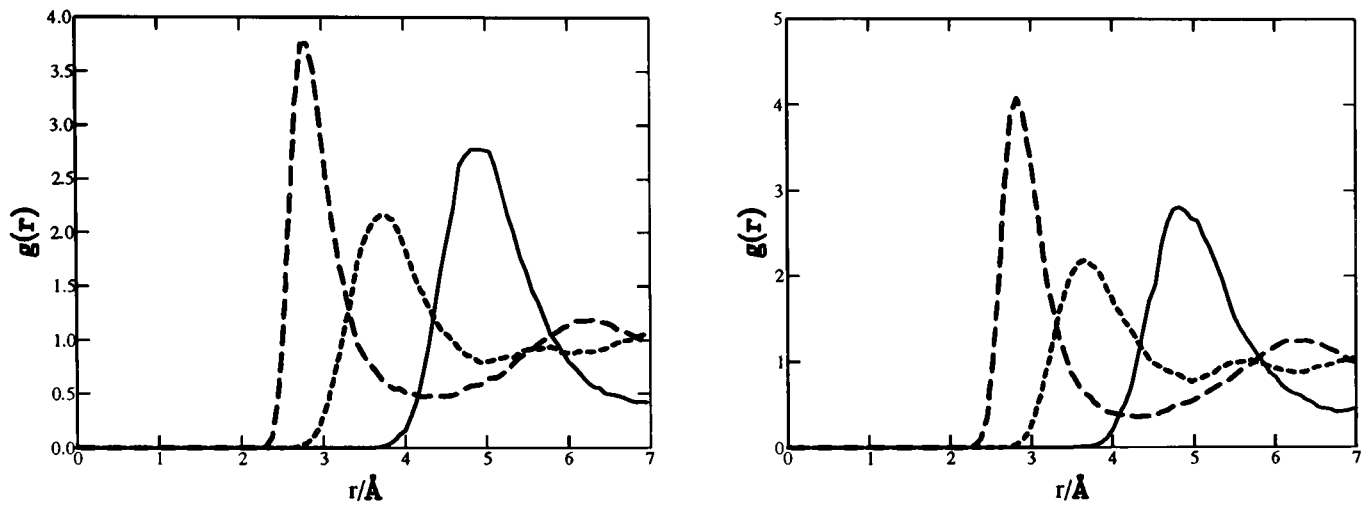


FIGURE 5.4: *Radial distribution functions for MCl_2 from the RIM. Line styles as in figure 5.1. Top left - $BaCl_2$, top right - $SrCl_2$, bottom - $ZnCl_2$.*

basic vectors are:

$$\begin{array}{c} x \\ y \\ z \end{array} \left(\begin{array}{cccccccccccccccccc} 1 & 0 & 0 & 1 & 1 & 0 & 1 & 1 & 1 & 1 & 1 & 0 & 1 & 1 & 0 & 2 & 2 & 0 \\ 0 & 1 & 0 & 1 & 0 & 1 & 1 & 1 & -1 & 2 & 0 & 1 & 3 & 0 & 1 & 3 & 0 & 2 \\ 0 & 0 & 1 & 0 & 1 & 1 & 1 & -1 & 1 & 0 & 2 & 2 & 0 & 3 & 3 & 0 & 3 & 3 \end{array} \right) \tag{5.5}$$

Each basic vector is taken to order 10, ie (1,0,0) $\longrightarrow$ (10,0,0) and (1,1,0) $\longrightarrow$ (10,10,0) giving 180 vectors overall.

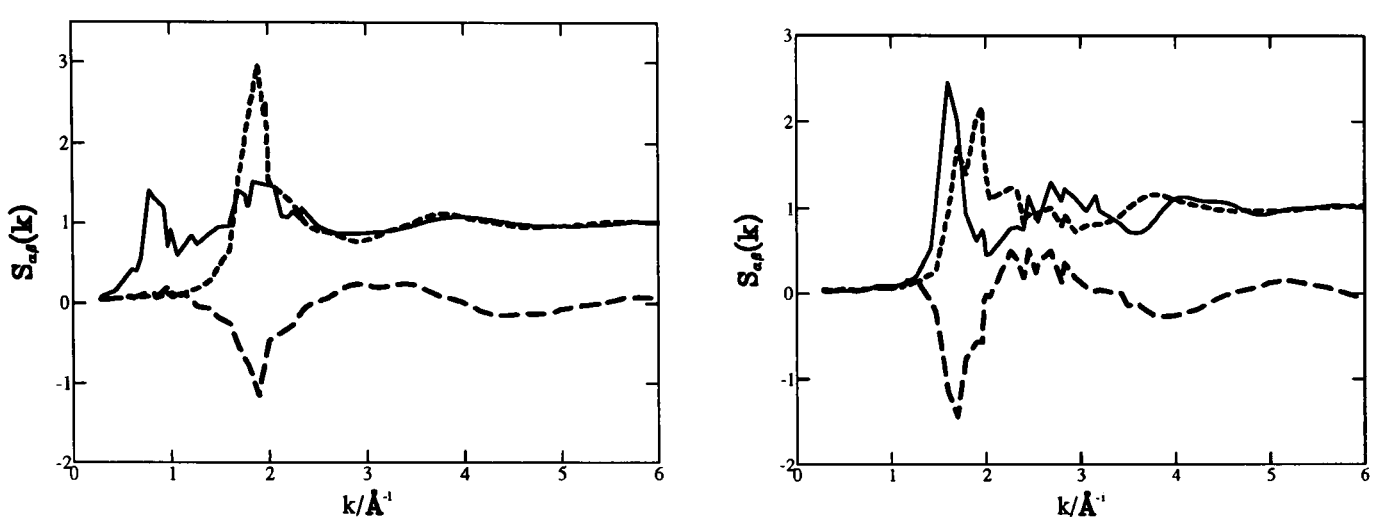


FIGURE 5.5: *Partial structure factors for $ZnCl_2$ using the (left) PIM and (right) RIM. Solid line - $S_{++}(k)$, long dashes - $S_{+-}(k)$, short dashes - $S_{--}(k)$.*

Figure 5.5a shows the three partial structure factors for the $ZnCl_2$ PIM. An FSDP is clearly visible in $S_{++}(k)$ with a small corresponding feature in $S_{+-}(k)$. This figure should be contrasted with figure 5.5b which shows the same functions for the same simulation parameter set but using the RIM. An FSDP is no longer apparent. Figure 5.6 focuses on the $S_{++}(k)$ functions by plotting the RIM and PIM structure factors on the same axis. The arrows on the x-axis indicate the location of the k-vectors sampled. In figure 5.5b (RIM) the principal peak in $S_{++}(k)$ is at lower k than in $S_{--}(k)$ corresponding to the cation-cation rdf peak being of longer range than the anion-anion, indicative of charge-ordering. However, in figure 5.5a (PIM) the principal peaks of $S_{++}(k)$ and $S_{--}(k)$ are at the *same* k-vector indicating the similarity in the nearest neighbour separation in real space. This shift in the position of the principal peak is associated with the emergence of the FSDP; that is, as the induction forces are included, the $S_{++}(k)$ principal peak in the RIM simulation "splits" into an FSDP at lower k and a new principal peak at higher k. For completeness figure 5.7 shows the

three partial structure factors for the $BaCl_2$ PIM simulation. No FSDP is seen in agreement with experiment [69] *despite* the inclusion of induction forces.

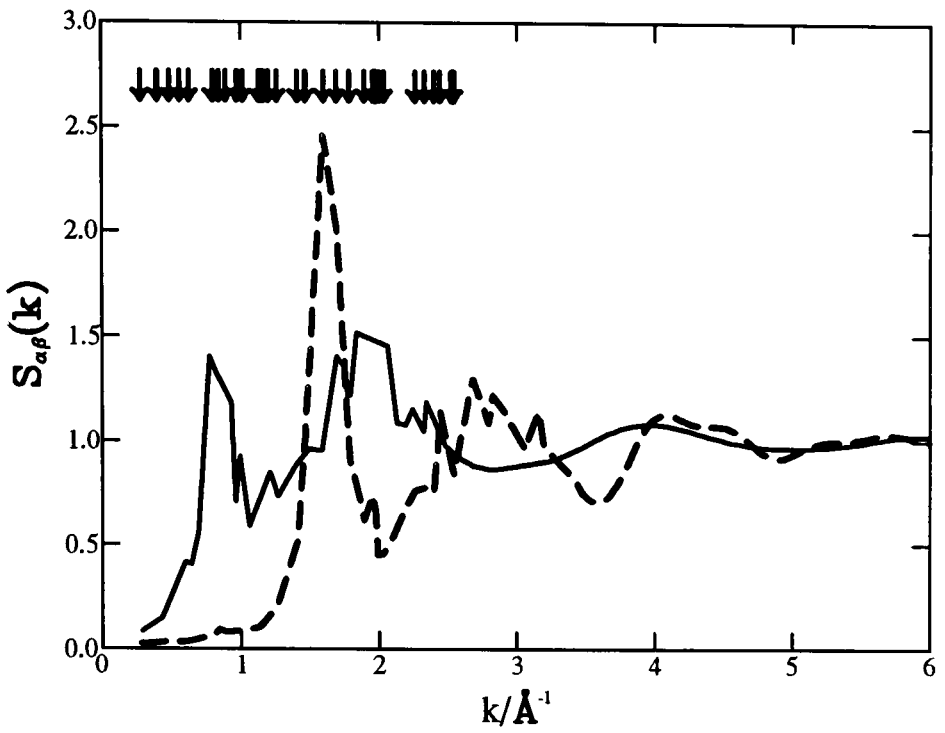


FIGURE 5.6: *Comparison of the cation-cation structure factors from the PIM and RIM simulations. Solid line - PIM, dashed line - RIM. The arrows indicate the allowed k-moduli in the low to medium k-vector range.*

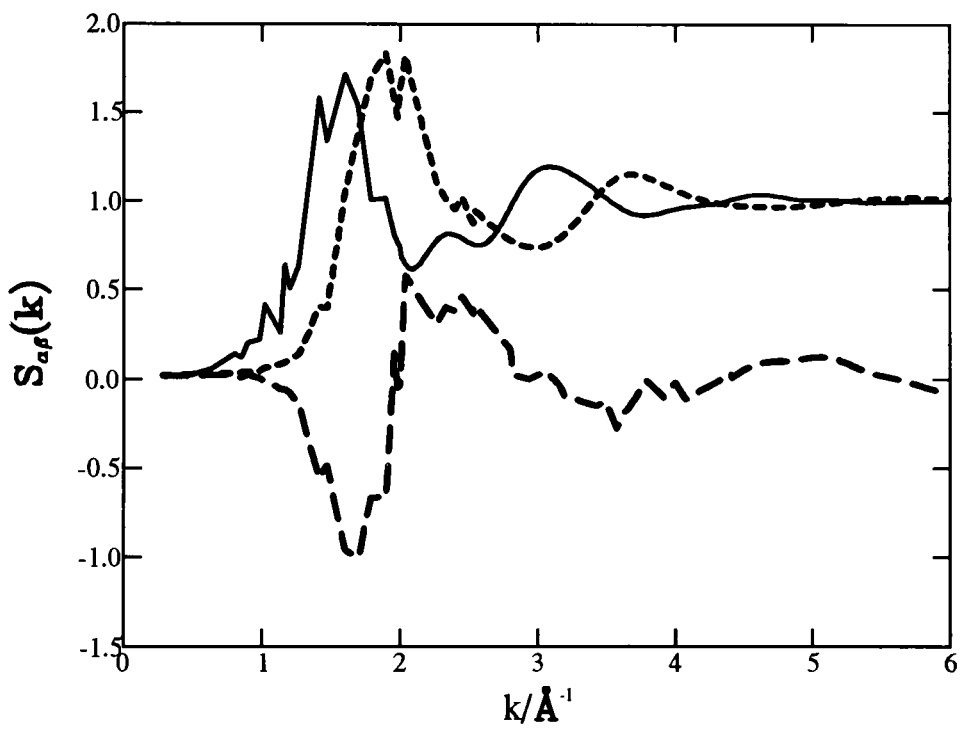


FIGURE 5.7: *Partial structure factors for $BaCl_2$ using the PIM. Line styles as in figure 5.5.*

5.3.3 Liquid Structure.

The radial distribution functions give information regarding the *pairwise, averaged* structure between species. As yet no clear information giving an indication of *directionality* has been shown associated with possible "covalent" effects discussed in the introduction. Three-dimensional structural information can be obtained using **molecular graphics** techniques [94].

For a charge-ordered MX_2 liquid the molecular graphics yields very little extra information - the structure is *typically ionic.* The opposite is true for the small cation systems. Figure 5.8a shows a "snapshot" from a simulation of $ZnCl_2$. The spheres are shown at 30% of their correct crystal ionic radius to allow the inherent liquid structure to become more clear. Anion-cation pairs separated by less than 6.8au (3.6Å), the position of the first minimum in $g_{+-}(r)$, are joined by a "bond". The figure raises the following points:

- The local tetrahedral coordination around each cation is clear.
- These tetrahedra form a *network* which extends across the whole simulation cell. The individual $ZnCl_4^{2-}$ tetrahedra share a *common corner*, forming sets of Zn-Cl-Zn triplets which have a *"bent bond"* (i.e $\theta_{Zn-Cl-Zn} \ll 180^o$). These chlorides are termed *bridging anions.*
- The origin of the FSDP in the cation-cation structure factor is not immediately apparent.

5.4 The Role of Anion Polarization.

Figure 5.8a shows the corner-linked $ZnCl_4$ tetrahedra forming a network spanning over the entire simulation cell. Figure 5.8b shows a smaller section of the network with the negative end of the induced dipole represented as a small white sphere displaced from the anion possessing that dipole along the dipole vector. The induced dipole on a bridging anion acts to introduce negative charge *in between* the two cations to which it is "bonded", effectively *screening* the coulombic repulsion between this cation pair. Note that this dipole can only form if the Zn-Cl-Zn bond is bent. It is the screening and bond-bending that allows the nearest-neighbour cation-cation and anion-anion separations to become equal.

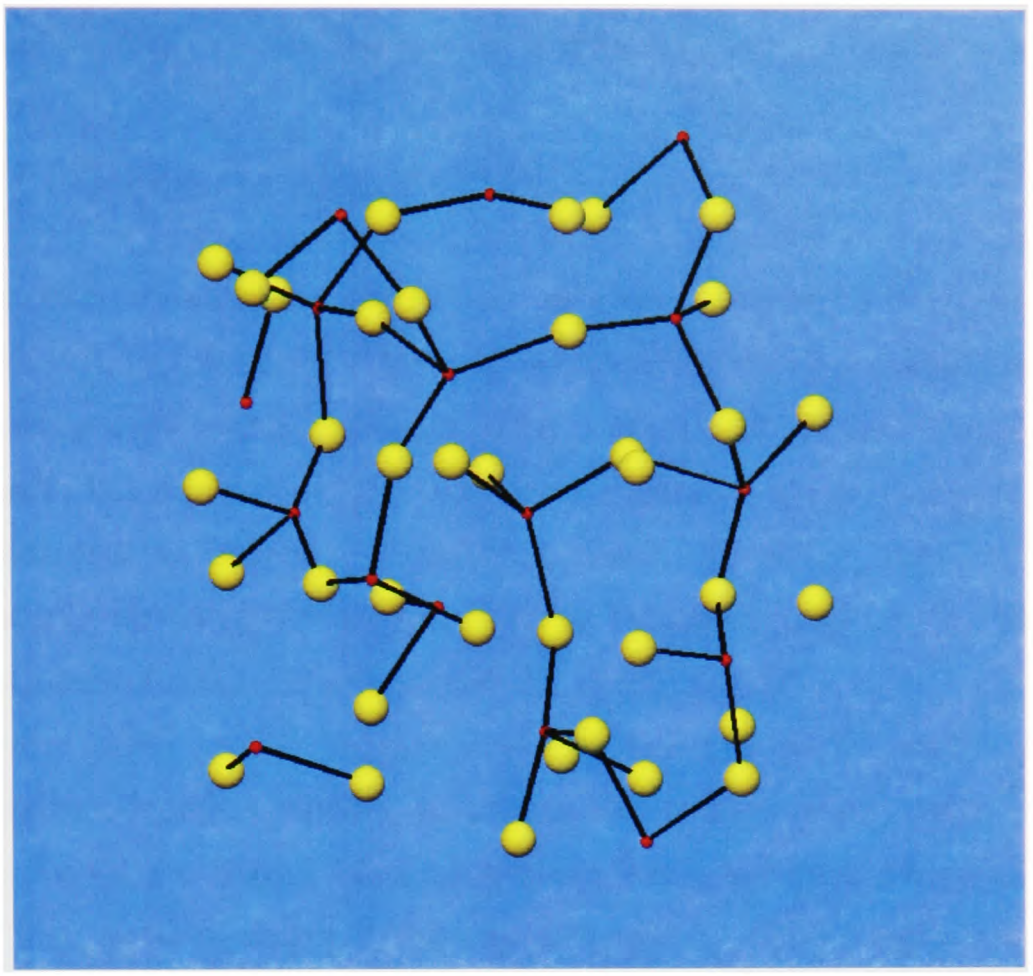


FIGURE 5.8: *AVS snapshot of the $ZnCl_2$ simulation cell. Yellow spheres - anions, red spheres - cations. Both are drawn at 30% of their crystal ionic radii for clarity. Anion-cation pairs within 6.8au are joined by a bond. Top - section through the cell, bottom - a smaller section with the negative end of the anion dipole as a small white sphere.*

There is a clear similarity between this analysis of the liquid structure and the analysis of the stability of the layered crystalline structures given in section 4.4.3.

5.5 The Origin of the FSDP.

The introduction of anion polarization effects allows an FSDP to develop in $S_{MM}(k)$ (and to a much lesser extent in $S_{MCl}(k)$) for the network-forming liquids (i.e the systems with small cations). The partial rdfs imply that this FSDP is associated with the cation-cation peak being shifted to lower r with respect to the position predicted on purely coulombic grounds. However, molecular graphics, although clearly showing the vertex-sharing tetrahedral network, fails to give a clear indication as to the structural origin of the FSDP.

As was discussed in the previous section the role of the anion polarization is to allow induced anion dipoles to *screen* the cation-cation interactions. This leads to the Zn-Cl-Zn triplet becoming more bent, bringing these cations closer together. Thus, doubly charged cations are now as close together as the singly charged anions. This results in an *excess* of local positive charge and a *depletion* of cation density on an *intermediate* length scale (i.e at the *next-nearest* neighbour level). It is this modulation in cation density that is the origin of the FSDP in $ZnCl_2$ and systems with similar network characteristics.

5.6 The Formation of MX_2 Molecules.

One of the benefits of computer simulation is the ability to "go that one stage further". The lowering of the cation radius within a simple PIM reduces the MX_2 system from a charge-ordered to a network. The question arises: **what happens if the cation radius is reduced yet further ?**

Figure 5.9 shows the partial radial distribution functions for a simulation run with the same parameter set as the previous runs but corresponding to a cation radius of 0.6Å Comparison with the $ZnCl_2$ rdfs shows that the ClCl peak is unchanged but the MM peak has shifted even further to low r, now actually *inside* the anion-anion distribution. Figure 5.10a shows a molecular graphics snapshot of this system. Clearly visible are *edge sharing* tetrahedral units in which a cation is connected to a neighbouring cation by *two* anion bridges. The formation of the second bridge is favoured by the further stabilization of the cation

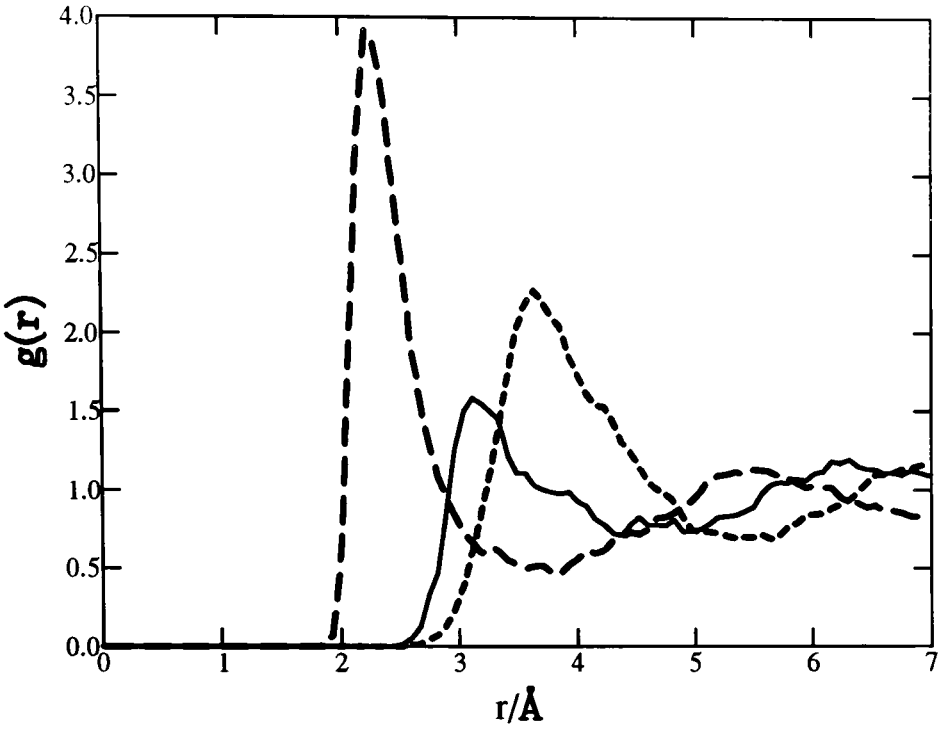


FIGURE 5.9: *Radial distribution functions for an idealized cation of radius 0.60Å. Line styles as figure 5.1*

subsystem by the increased induction effect at the expense of a lowering in the range of the cation-cation distribution giving larger coulombic repulsion effects. This type of structural unit is reminiscent of the chain-like crystal structures shown by the small cation radius halides (see section 4.5).

Figure 5.10b shows a molecular graphics snapshot of a system with a cation radius of 0.50Å The result is the dramatic formation of MX_2 "molecules" with non-linear MXM "bonds". Figure 5.10b also shows the negative end of the induced anion dipoles as a small white sphere. The dipole clearly points almost directly at the parent cation. The quantity

$$J = \frac{< \boldsymbol{\mu}^i . \mathbf{r}^{ij} >}{\mid \boldsymbol{\mu}^i \mid\mid \mathbf{r}^{ij} \mid}, \tag{5.6}$$

where i is the anion and j is the parent cation, within the range of the first rdf peak, has a value of 0.988 which indicates that the induced dipoles are almost entirely parallel to the anion-cation "bond".

Figure 5.11 shows the corresponding distribution functions. Again, the anion-anion correlations are essentially unchanged, and, although $g_{MM}(r)$ has not been pulled to lower r, it has become flat and featureless in that the characteristic ionic peaks and troughs of previous functions have vanished. It is worth noting that such a featureless cation-cation distribution is characteristic of the

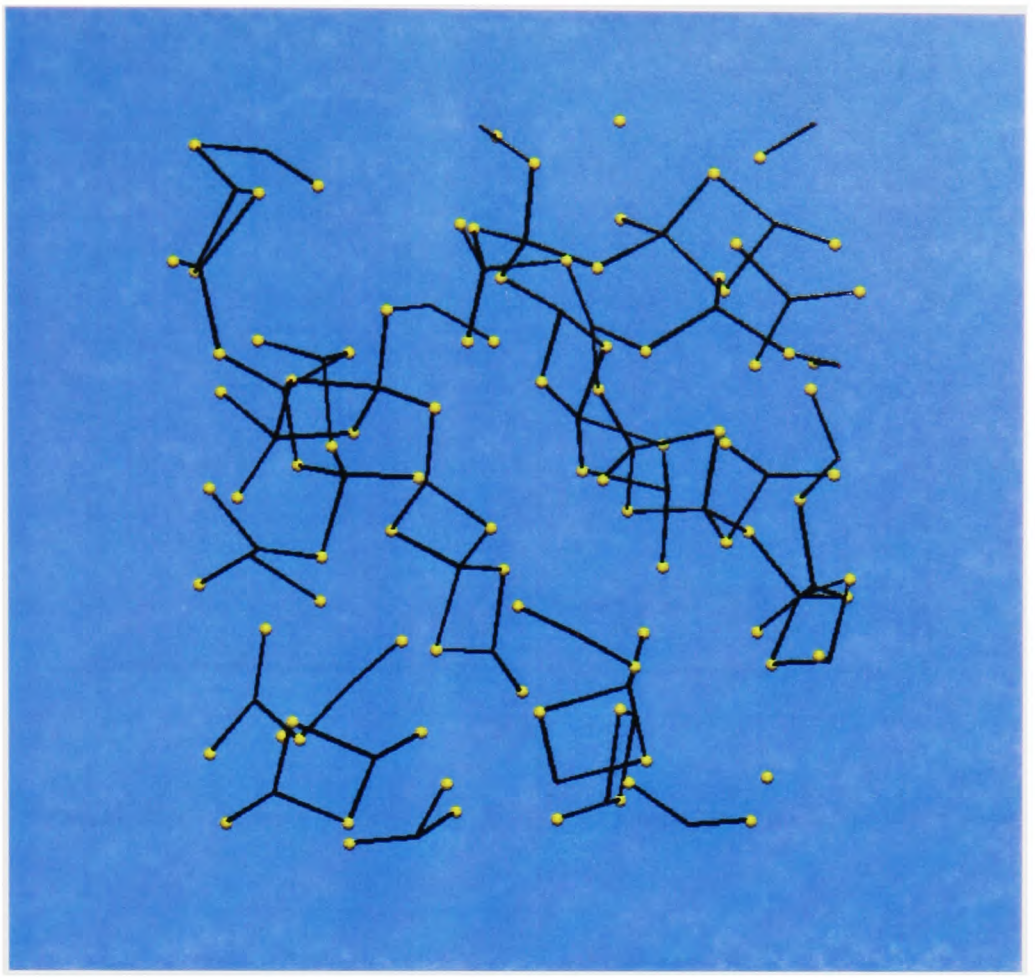


FIGURE 5.10: *AVS snapshot of the MCl_2 simulation cell. Yellow spheres - anions, red spheres - cations. Top - cation radius 0.60Å - spheres are drawn at 20% of their crystal ionic radii to emphasize the network, bottom - cation radius 0.50Å - the small white sphere again represents the dipole..*

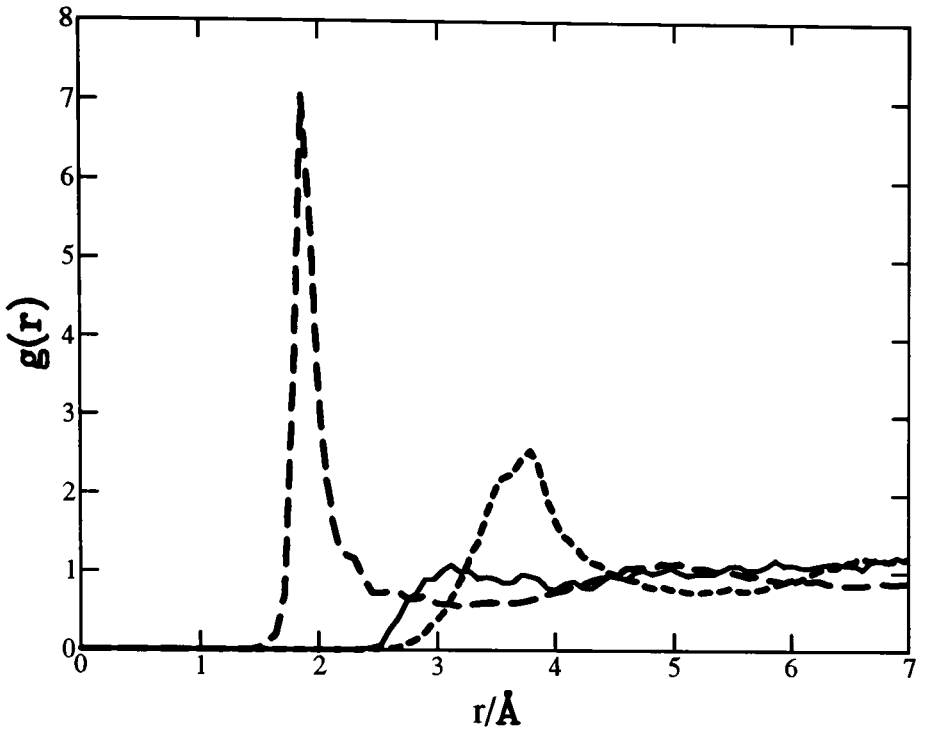


FIGURE 5.11: *Radial distribution functions for an idealised cation of radius 0.50Å. Line styles as figure 5.1.*

NiI_2 system [74, 73], i.e a system with a combination of a small cation and a highly polarizable anion. Thus, the combination of a smaller cation but with a less polarizable anion can produce qualitatively the same effects. Similarly, the first peak in $g_{MCl}(r)$ has become much higher and sharper and integrates to give a coordination number of two, in support of the graphical evidence of figure 5.10b.

Figure 5.12 shows the XMX bond angle distribution for the $ZnCl_2$ and the "molecular" systems. The $ZnCl_2$ distribution shows a clear tetrahedral peak whilst the "molecular" system has a peak at a higher angle.

It is essential to understand why each structural type is favoured for a particular cation radius. Perhaps the simplest way to do this is to perform a thought experiment considering the effect of reducing the cation radius *in situ* during a simulation.

From an initial ionic, charge-ordered, system the first effect of lowering the cation radius is to favour tetrahedral anion-cation coordination (a packing effect) and reduce the cation-cation separation (an induction effect) giving *vertex sharing* units. A further reduction of the cation radius favours the formation of *edge sharing* tetrahedra and yet more reduction leads to the "molecules".

Figures 5.13A-E show a schematic proposal for these processes. Considering

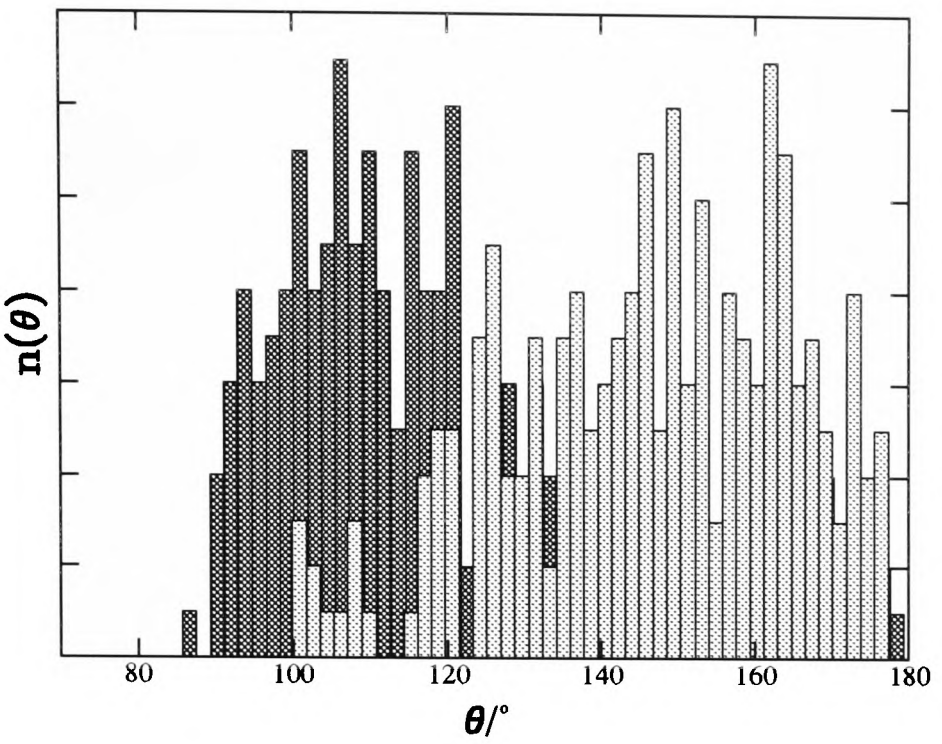
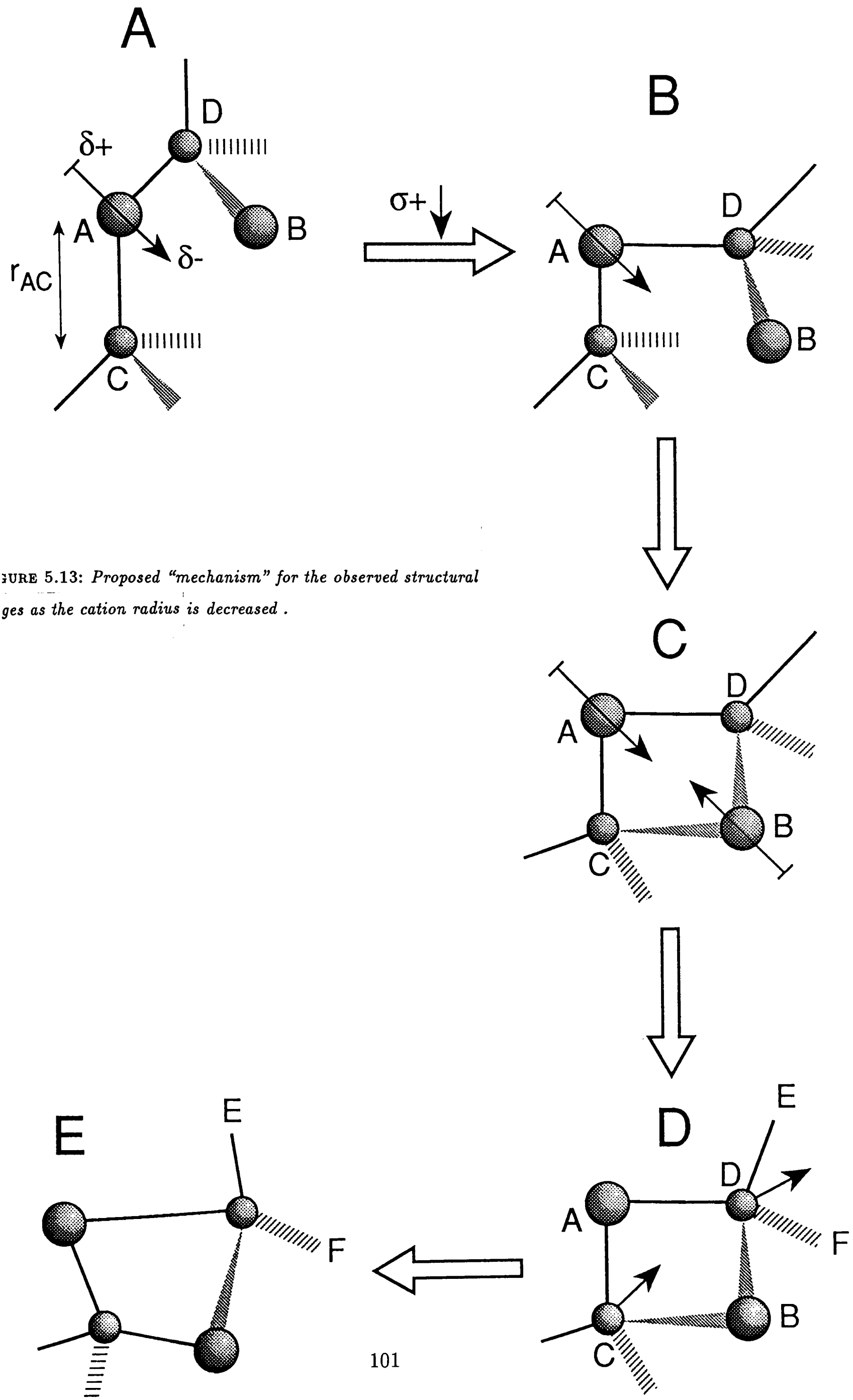


FIGURE 5.12: *XMX bond angle distributions for the $ZnCl_2$ (dark shading) and the smallest idealized cation (light) PIM simulations.*

A-C first, frame A corresponding to the vertex sharing network (i.e $ZnCl_2$-like). As the cation radius is reduced (frames A $\longrightarrow$ B) the separation r_{AC} falls and causes the induced dipole on anion A to increase in size. This in turn causes a reduction in the separation between cations C and D via the greater cation-dipole interactions. This leads to anion B approaching cation C, coming more within that cation's "sphere of influence". Hence the dipole induced on B tends to reflect more the presence of the cation C than it did in frame A. A further reduction in the cation radius (frames B $\longrightarrow$ C) completes the vertex- $\longrightarrow$ edge-sharing process by bringing B close enough to cation C as as to be considered "bonded". A chloride anion becomes detached from this unit during this process.

Frames C-E show the proposed mechanism for the final transition to the molecular structure. Reduction of the cation radius from frame C causes r_{AC} to become yet smaller. However, the cation is now so small as to effectively be allowed to "rattle" in the tetrahedral hole. This allows the cation to move towards a particular edge. This displacement is correlated for the cations as the movement of one cation towards a particular tetrahedral vertex will influence the motion of a neighbouring cation via the large coulombic repulsion. Hence, in figure 5.13 cation C moves to vertex AB and D goes to EF leaving two "molecules", ACB and EDF respectively. This change is consistent with that



URE 5.13: *Proposed "mechanism" for the observed structural ges as the cation radius is decreased .*

shown in the rdfs of figures 5.9 and 5.11 in that the peak in $g_{MM}(r)$ has not shifted to lower r. It is also consistent with the XMX bond angle distributions (figure 5.12). Hence, although figure 5.10 shows clear molecule-like structure, it is evident that the cations are still in tetrahedral holes in the anion sublattice but are small enough to become biased towards a particular vertex driven by the induction forces. Thus, in figure 5.13E there are two molecules but also two "stretched bonds" for each cation, completing the tetrahedron.

5.7 Constant NpT Simulations.

All of the liquid state simulations described previously have been performed in the constant NVT ensemble. The discussions regarding the macroscopic network structures of the $ZnCl_2$ system demonstrates the important role of anionic polarization effects. Thus, it is important to see how the imposition of a constant box volumes affects the formation of the network. That is, is the network held in some metastable state by the rigid simulation cell ?

5.7.1 Performing constant-NpT Simulations in the RIM.

Isobaric MD has been performed in a variety of ways following Andersen [95], who included the volume as an additional degree of freedom and extended the Lagrangian accordingly. The simulation cell volume was varied to keep the system pressure at the desired value. Parrinello and Rahman [96] introduced a more general extended-Lagrangian method by allowing the cell *shape* as well as volume to change, the three vectors defining the cell edges being treated as the additional variables. Other variants on these themes are due to Ray and Rahman [97], Berendsen [98] and Nosé and Hoover [38, 39].

All of these methods require the calculation of (at least) the scalar pressure and, in the case of the variable cell methods, the whole pressure tensor must be evaluated. The usual way of calculating the pressure within the RIM is via the **virial theorem** [99], leading to [10, 100]

$$p = \langle \rho k_B T \rangle - \frac{2}{V} \left\langle \sum_{i=2}^{N_t} \sum_{j=1}^{i-1} r^{ij} \frac{d\phi^{ij}(r)}{dr} \right\rangle, \tag{5.7}$$

where the first term is the kinetic pressure. This only applies, however, if the interionic potential, $\phi^{ij}(r)$ is expressible in terms of pairwise additive terms. The

inclusion of the induction effects in a self-consistent way, however, leads to the introduction of *many-body* forces and a direct calculation of the pressure in the presence of these forces has not been possible.

A method is required that is based upon the ability to calculate pressures *indirectly* from a knowledge of the internal system energy at a variety of densities [100].

5.7.2 Performing constant-NpT Simulations in the PIM.

Abraham [101] applied the isobaric constraint via a clever mix of MD and Monte-Carlo (MC) techniques. An attempt is made to vary the volume of the simulation cell every z MD time steps by a random amount ΔV. The total change in energy is given by

$$\Delta W = \Delta U + p\Delta V - Nk_BT\left(\frac{V+\Delta V}{V}\right), \tag{5.8}$$

where ΔU is the change in the internal energy of the system with the volume change and p is the target pressure. In the PIM the need to calculate ΔU means that the induced moments must be reannealed at each attempted cell volume move. This gives the full energy change *including* the many-body effects. A standard Metropolis algorithm [102] is employed; if ΔW is negative then the move is accepted, if positive it is accepted with a probability of $e^{\frac{-\Delta W}{k_BT}}$. The effect of the set pressure is now clear; making the pressure more positive favours negative volume changes via equation 5.8. Thus, the larger the pressure set the smaller the equilibrium cell volume.

Testing the procedure with the PIM is difficult as the pressure cannot as yet be simply calculated directly. However, the same procedure can be applied within a standard RIM and compared to the pressures calculated via equation 5.7. Figure 5.14 shows the time evolution of the pressure for two different set pressures in a simulation of molten AgCl (see chapter 7 for simulation details). The straight lines are the set pressures of 0.0 and 0.0001au ($\simeq$ 3GPa) and the dashed lines represent the *direct* pressure. Thus, although the initial call is not at the correct density for this statepoint, the MC procedure acts to change the cell volume to give the desired pressure about which the real pressure oscillates.

The maximum size of the volume change, ΔV^{max}, is varied to keep the ratio of accepted to attempted moves at 40% [31]. The larger the volume change at each step, the less likely a move is to be accepted. To maintain the desired acceptance

ratio (AR) the *actual* ratio is calculated after each attempted move with ΔV^{max} being increased if too many moves are being accepted or decreased it if too few are being accepted. The very simple nature of the algorithm requires that the initial $\Delta V^{max}(t = 0)$ is similar to that for the desired AR, otherwise ΔV^{max} will fluctuate too wildly and result in a computationally inefficient algorithm in which the desired AR is maintained via a series of oscillating large ΔV^{max} (low AR) and small ΔV^{max} (high AR).

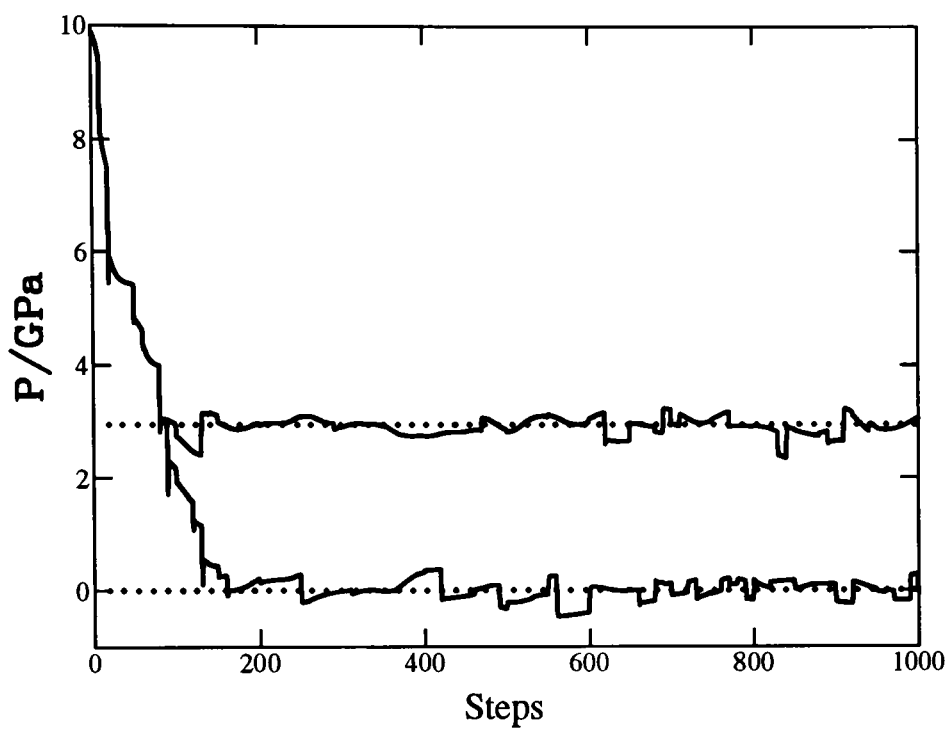


FIGURE 5.14: *Direct pressure from a RIM simulation (solid line) of molten AgCl compared with that required by the MC pressure algorithm (dotted line). Two simulations are shown with target pressures of 0 and ~3GPa respectively.*

5.7.3 The Simulations.

The NpT simulations were directed to investigate network structures in the intermediate to strong systems BeF_2, $ZnCl_2$ and SiO_2, respectively. To retain objectivity the original RI potentials of Woodcock, Angell and Cheeseman [86] (table 5.5) are used without modification with the dipolar induction effects included in the manner described in chapter 2. The dipole polarizabilities of Cl^- and F^- are taken as 20.0 and 6.2au respectively following electronic structure calculations [5, 8]. The oxide polarizability is chosen via extrapolation from a wide range of *empirical* values due to Lewis and Catlow [103]. Figure 5.15 shows the empirical values against cation radius. From this a value of 13.6au is

Ion pair,ij	B^{ij}_{ZnCl}	B^{ij}_{BeF}	B^{ij}_{SiO}
M-M	19.6099	49.7112	151.0509
X-X	63.4770	12.3842	16.6374
M-X	35.5311	16.3817	79.4403

TABLE 5.5: *The potential parameters of Woodcock, Angell and Cheeseman [86] for $ZnCl_2$, BeF_2 and SiO_2. The repulsive "hardness" parameters, a, are 1.8247au for BeF_2 and SiO_2 and 1.5564au for $ZnCl_2$ respectively.*

obtained for the oxide in SiO_2. Damping parameters are chosen empirically so

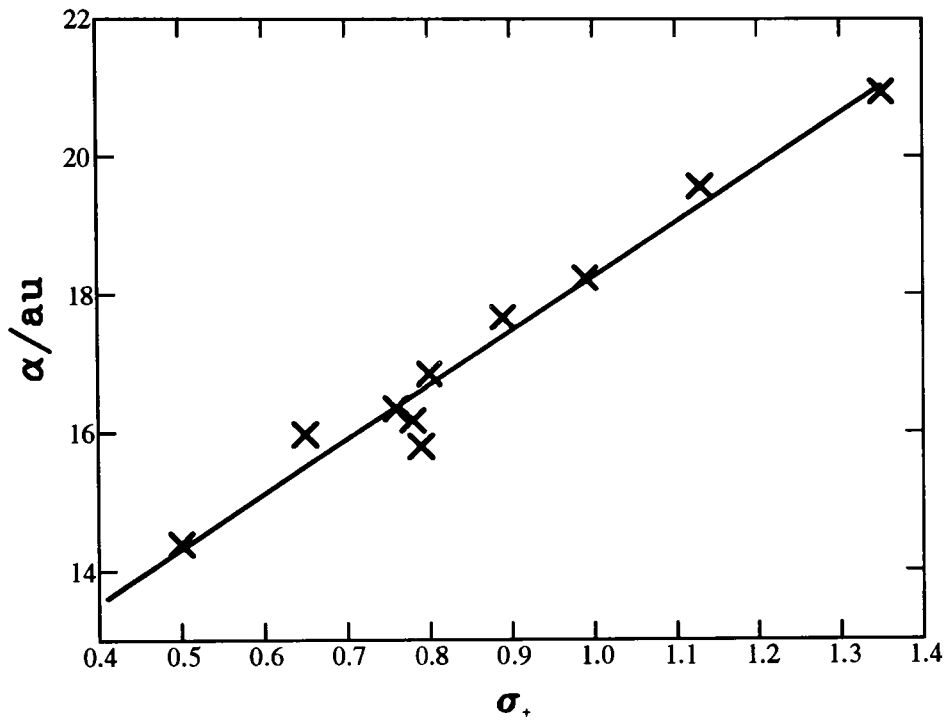


FIGURE 5.15: *Empirical oxide polarizabilities from ref.[103] against cation radius (in Å). The straight line represents a least squares fit.*

as to fit the experimental distribution functions. They are 1.55 for both BeF_2 and $ZnCl_2$, and 1.5 for SiO_2. Some specific problems of simulating oxides will be discussed in chapter 8.

5.7.4 Results.

Experimental neutron diffraction [57, 104] (and NMR for silica [105]) give useful information regarding the *three body* interactions - the triplet *bond angle distributions*. Of particular interest is the MXM triplet. The bond angle distributions are calculated by identifying the required triplets by summing over each centre

System	θ^{expt}	θ^{RIM}	θ^{PIM}	$\Delta\theta$
BeF_2	156	155	150	5
$ZnCl_2$	105	130	110	20
SiO_2	142-152	160	130	30

TABLE 5.6: *Peak positions in the MXM bond angle distributions from experiment and from both RIM and PIM simulations.* $\Delta\theta = \theta^{RIM} - \theta^{PIM}$.

ion and looking for pairs of counterions within a specified cutoff radius (usually the first minimum in $g_{+-}(r)$).

Figures 5.16a-c give the bond angle distributions for the MXM triplet in the NpT simulations using both the RIM and PIM for BeF_2 , $ZnCl_2$ and SiO_2 at 600K, 1000K and 2500K respectively. The effect of introducing the anion polarization is to shift the MXM distribution peak to lower angle, that is, pushing the cations together. In section 5.4 it was shown how the induced dipoles cause this effect. Table 5.6 lists the positions of the MXM peaks in the RIM and PIM along with the experimental values. Also listed is the change in bond angle, $\Delta\theta$, in going from the RIM to PIM. Overall, the PIM brings the distribution peak into excellent agreement with experiment. Three factors that affect the magnitude of this shift can be readily identified:

- the anion polarizability.
- the anion to cation radius ratio.
- the polarizing power of the cation (its formal charge).

Thus, $\Delta\theta$ is smallest for BeF_2 which has the least polarizable anion but is comparable for $ZnCl_2$ and SiO_2 as the larger polarizing power of the silicon cation combined with the oxide polarizability is approximately equivalent to the effect of the less polarizing zinc cation with the more polarizable chloride anion.

Table 5.7 gives the equilibrium box lengths for each model in the RIM and PIM. The effect of including the induction effects is to *lower* the box volume with respect to the RIM. This a direct result of the network contracting as the dipoles induced lower the MXM bond angles. Note that all three potentials fail to give the experimental density even in the RIM. This is indicative of a failing of the pair-potentials. Future work, therefore, requires a rethink of the potential

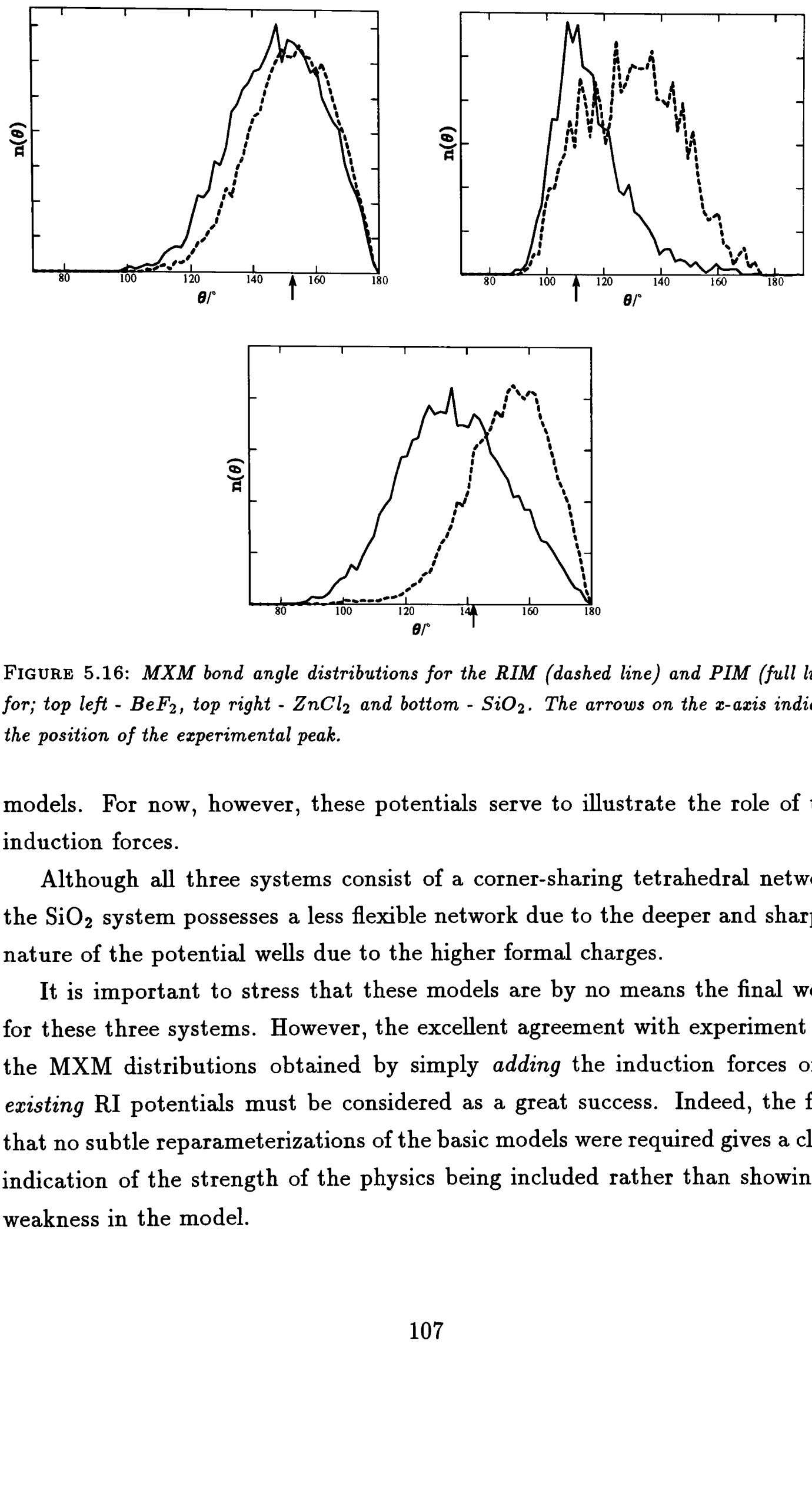


FIGURE 5.16: *MXM bond angle distributions for the RIM (dashed line) and PIM (full line) for; top left - BeF_2, top right - $ZnCl_2$ and bottom - SiO_2. The arrows on the x-axis indicate the position of the experimental peak.*

models. For now, however, these potentials serve to illustrate the role of the induction forces.

Although all three systems consist of a corner-sharing tetrahedral network the SiO_2 system possesses a less flexible network due to the deeper and sharper nature of the potential wells due to the higher formal charges.

It is important to stress that these models are by no means the final word for these three systems. However, the excellent agreement with experiment for the MXM distributions obtained by simply *adding* the induction forces onto *existing* RI potentials must be considered as a great success. Indeed, the fact that no subtle reparameterizations of the basic models were required gives a clear indication of the strength of the physics being included rather than showing a weakness in the model.

System	Box length/au		
	RIM	PIM	Experiment
BeF_2	31.9085	31.3582	30.4790
$ZnCl_2$	37.9683	36.1691	40.1180
SiO_2	33.7596	30.6098	32.0429

TABLE 5.7: *Equilibrium box lengths for the three systems studied in the RIM and PIM compared with experiment.*

6

Network-Modified Systems.

In the preceding chapter the linked tetrahedral network structures of three glass-formers (two strong - BeF_2 and SiO_2 and one intermediate - $ZnCl_2$) were reproduced using existing pair-potentials supplemented with anion polarization effects to a dipolar approximation. Having constructed the networks, therefore, a natural progression is to study the effect of adding different *network breaking* modifiers.

The most widely used network breaker is Na_2O in common window glass. The added *modifier* acts to reduce the viscosity of the silica melt allowing the molten glass to be easily worked. A typical stoichiometry is $SiO_2.Na_2O$. Similarly, alkali halides can be added to $ZnCl_2$ to alter the system characteristics and these have been studied experimentally. Within the framework of this thesis the modified zinc chloride systems are the natural ones to study.

6.1 Experimental Studies.

Neutron scattering experiments have been recently carried out by Howe and coworkers on $ZnCl_2KCl$, [106] , $NiCl_2LiCl$, $NiCl_2KCl$ and $ZnCl_2LiCl$ [107]. The major finding of these studies is the different degree of persistence of the FSDP in the total scattering function, F(k) in the LiCl and KCl modified systems. With added KCl the FSDP persists up to at least 67% modifier (certainly there is a very distinctive peak at 67% but no more than a weak shoulder at 81%, the next highest concentration studied). In the LiCl modified system, however, the intensity of the FSDP falls with added modifier. Badyal and Howe [107] show that the F(k) at a given LiCl concentration, can be reproduced by combining the partial structure factors of the *pure* components ($ZnCl_2$ from Biggin and Enderby [66] and LiCl from McGreevy and Howe [108]).

In the pure systems the only major FSDP is in S_{ZnZn}. The LiCl modified data is consistent with the loss of intensity of this peak as a result of the decreasing

mole fraction of $ZnCl_2$ as modifier is added. This analysis fails for the KCl modified system where the FSDP is much higher than that predicted from the pure $ZnCl_2$ S_{ZnZn} peak only. Allen *et al* [67] have suggested a model in which the K^+ ions fit into the $ZnCl_2$ network forming an FSDP in S_{KK} in the same manner as S_{ZnZn}. This, however, is inconsistent with the Raman scattering evidence [109] which suggests the formation of discrete $ZnCl_4^{2-}$ tetrahedral molecular ions, that is, the original $ZnCl_2$ network is completely destroyed. Badyal and Howe [107] have speculated that the polyatomic anions are somehow arranged to give an enhanced S_{ZnZn} FSDP along with additional contributions from both S_{KK} and S_{KZn}. However, due to the need to perform six separate experiments, these systems have not been resolved into the partial structure factors and so these ideas remain speculative. A properly constructed computer simulation model could give vital insight into the individual *partial* structure factor contributions to the experimentally observed *total* structure factor.

6.2 The Simulation Model.

Three mixtures will be studied; $ZnCl_2$LiCl, $ZnCl_2$KCl and $ZnCl_2$RbCl. The first two are chosen because of the availability of experimental data and the RbCl modified system is an extreme example of a large cation modified system.

The standard WAC $ZnCl_2$ pair-potential (see section 5.7.3) is used throughout for the Cl-Cl, Zn-Cl and Zn-Zn interactions. The M-M and M-Cl interactions are taken from previous pure alkali halide simulations [10]. The only remaining term, therefore, is the M-Zn potential which is derived from the M-M and Zn-Zn potentials using mixing rules [19]. It should again be noted that that only the Zn-Cl and M-Cl short-range terms are significant, with the Cl-Cl and M-M interactions of much lesser importance and the Zn-Zn and M-Zn short range terms being virtually negligible (these terms being dominated by the coulombic repulsion). The WAC parameters were given in table 5.5 and the remaining parameters appear in tables 6.1 to 6.3. The anion polarizability and damping parameter are those used in the pure $ZnCl_2$ simulations.

The configurations are generated from the existing pure amorphous $ZnCl_2$ files containing 324 ions by selecting a zinc cation at random, replacing it with an M^+, and simultaneously removing an anion. This configuration is then used as the basic startup file and requires several thousand steps of equilibration. Table

Ion pair	a	B^{ij}	C^{ij}
	(all in atomic units)		
Li-Cl	1.5473	8.6782	2.0891
Li-Li	1.5473	1.1450	0.07625
Li-Zn	1.5473	4.7385	1.7464

TABLE 6.1: *Additional $ZnCl_2/LiCl$ potential parameters.*

Ion pair	a	B^{ij}	C^{ij}
	(all in atomic units)		
K-Cl	1.5701	65.6207	67.6166
K-K	1.5701	57.1142	22.86
K-Zn	1.5701	33.0000	30.2390

TABLE 6.2: *Additional $ZnCl_2/KCl$ potential parameters.*

Ion pair	a	B^{ij}	C^{ij}
	(all in atomic units)		
Rb-Cl	1.6643	166.7404	82.5201
Rb-Rb	1.6643	165.7983	62.0468
Rb-Zn	1.6643	57.3627	49.8184

TABLE 6.3: *Additional $ZnCl_2/RbCl$ potential parameters.*

6.4 lists the number of ions at each composition along with the cpu time per step required (IBM 320H RISC system). The densities are taken from the neutron

%MCl	N^t	N^M	N^{Zn}	N^{Cl}	CPU time (s/step)
20	302	22	86	194	7.3
33	288	36	72	180	6.4
50	270	54	54	162	6.0
67	252	72	36	144	5.6
81	237	87	21	129	3.9

TABLE 6.4: *Simulation cell composition for each percentage of added modifier and cpu time required for each time step.*

scattering experiments for the KCl system [106] and from standard tables for the other two [110].

6.3 Results.

6.3.1 Distribution Functions.

Figures 6.1-6.3 show the full sets of partial rdfs at the compositions studied for the three modifiers (note that the pure $ZnCl_2$ partials were shown in figure 5.5). In order to extract the essential information from these figures, the position of the first peaks in each partial distribution function is plotted against the mole fraction of added modifier in figures 6.4a-c. The pure peak positions from neutron scattering experiments ($ZnCl_2$ [66], LiCl [108], KCl [111] and RbCl [112]) are also included. These show a fundamental difference between the LiCl modified system and the other two. In the LiCl case the peak positions do not vary appreciably across the composition range, whereas, for the larger cations there is a distinctive movement of the M-M, M-Zn and Cl-Cl peaks. Integration over the first peaks of g_{ZnCl} and g_{LiCl} shows both cations to be four coordinated at all compositions as are both pure liquids [66, 108]. Table 6.5 gives the coordination numbers over the composition range.

The implication is that the Li^+ cations can progressively replace the Zn^{2+} *and* fill the empty cation "sites" in the $ZnCl_2$ network, leading eventually to the

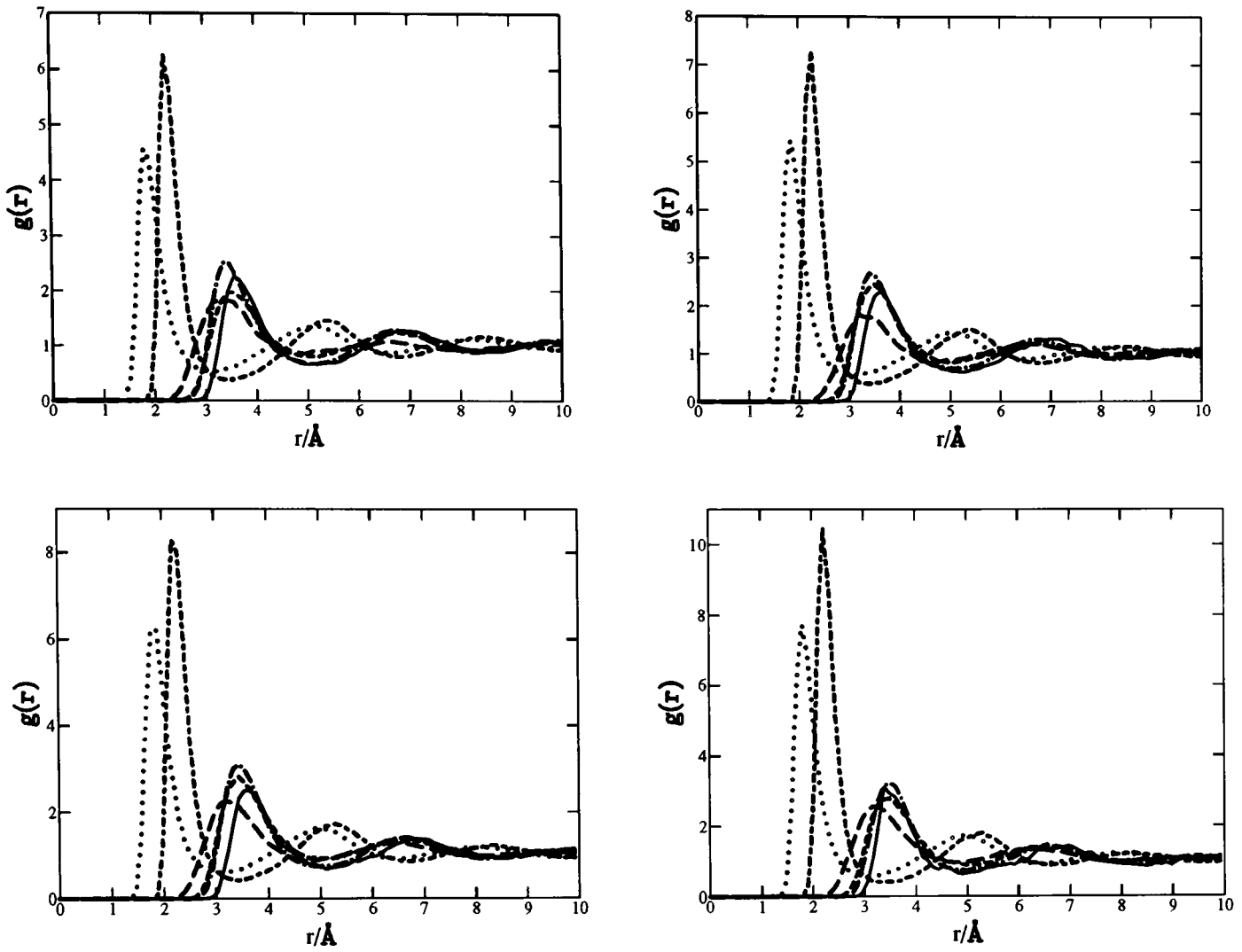


FIGURE 6.1: *Radial distribution functions for the $ZnCl_2LiCl$ system with, (a) top left - 33%, (b) top right - 50%, (c) bottom left - 67% and (d) bottom right - 81% LiCl modifier. Key: Solid line - g_{ZnZn}, long-dashes - g_{LiLi} , short-dashes - g_{LiZn}, dots - g_{LiCl}, dot-long-dashes - g_{ClCl}, dot-short-dashes - g_{ZnCl} .*

%LiCl	N_{ZnCl}	N_{LiCl}
20	3.92	3.81
33	4.13	4.01
50	3.73	3.86
67	3.92	3.91

TABLE 6.5: *Cation-anion coordination numbers for the LiCl modified system with increasing modifier.*

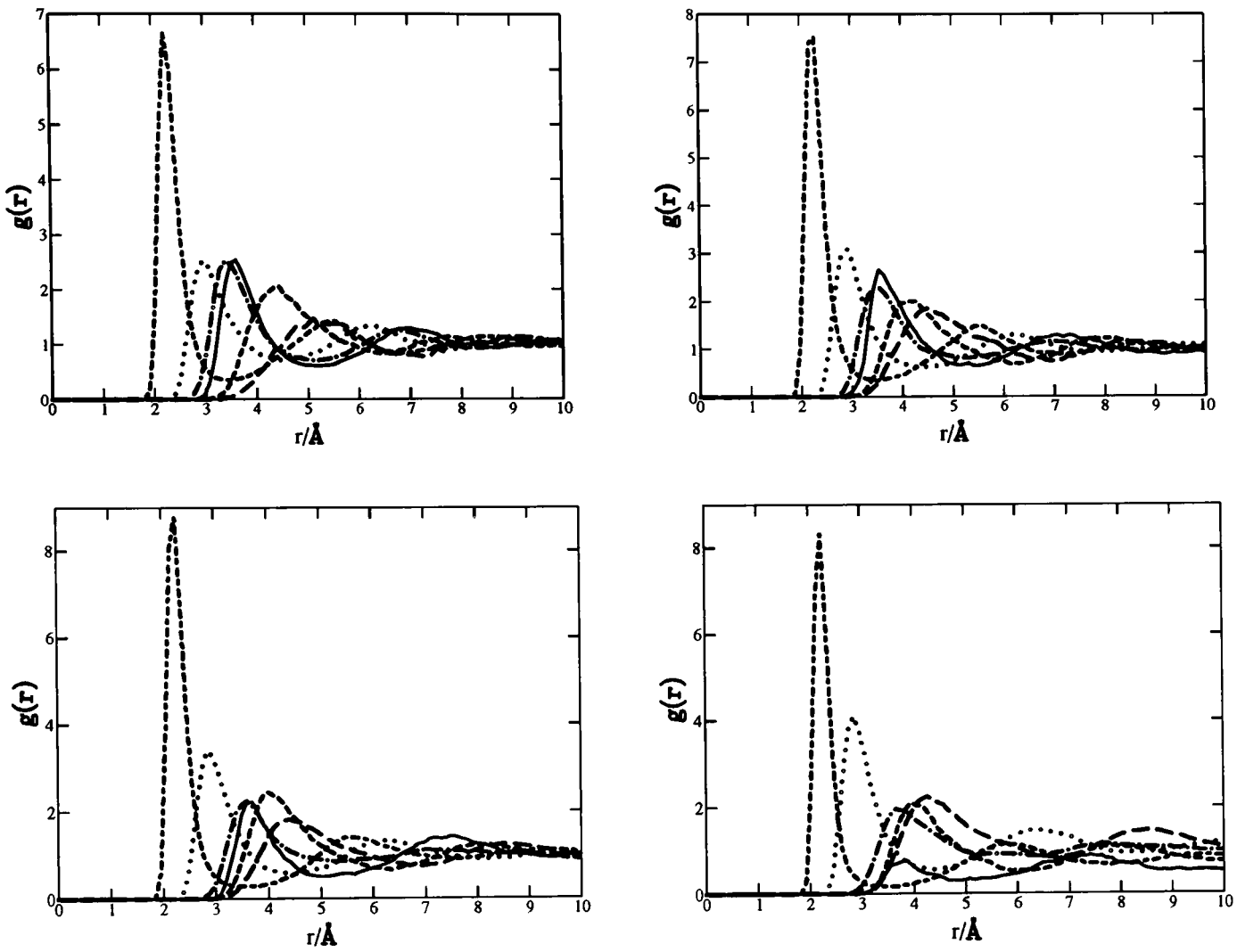


FIGURE 6.2: *Radial distribution functions for the $ZnCl_2KCl$ system with, (a) top left - 20%, (b) top right - 50%, (c) bottom left - 67% and bottom right - (d) 81% KCl modifier. Key: as figure 6.1.*

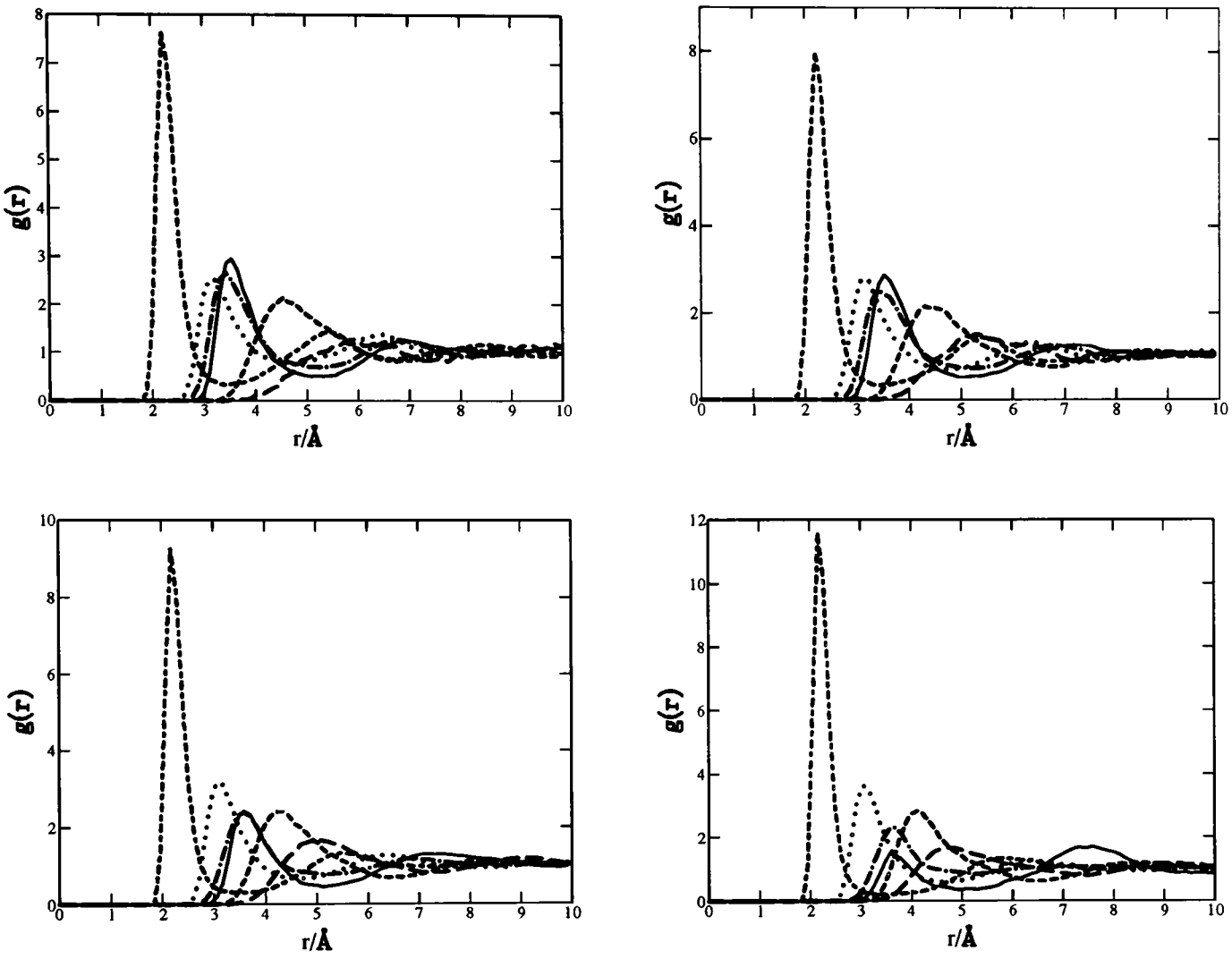


FIGURE 6.3: *Radial distribution functions for the $ZnCl_2RbCl$ system with, (a) top left 20%, (b) top right 33%, (c) bottom left 50% and (d) bottom right 67% RbCl modifier. Key: as figure 6.1.*

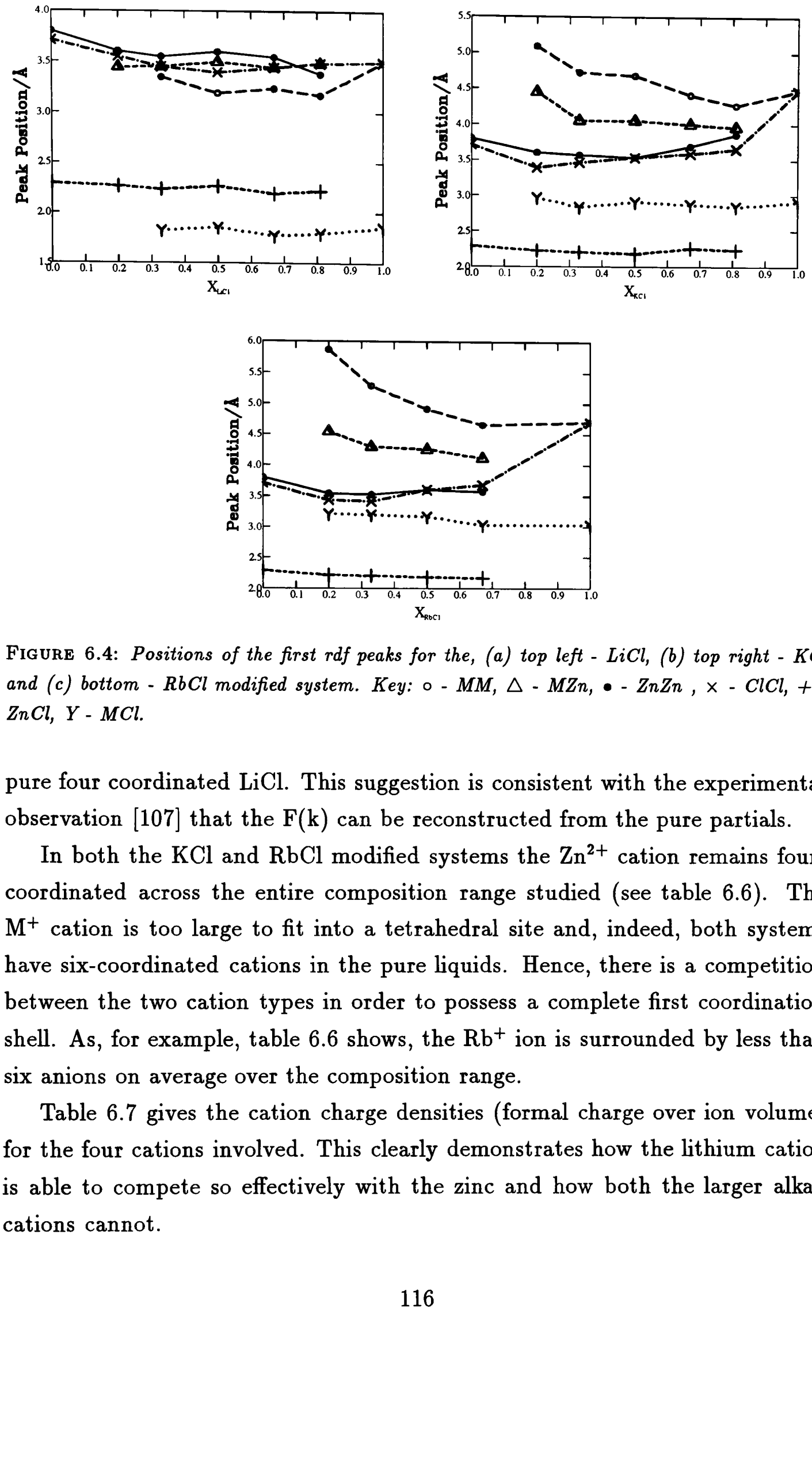


FIGURE 6.4: *Positions of the first rdf peaks for the, (a) top left - LiCl, (b) top right - KCl and (c) bottom - RbCl modified system. Key:* ○ *- MM,* △ *- MZn,* ● *- ZnZn ,* × *- ClCl, + - ZnCl, Y - MCl.*

pure four coordinated LiCl. This suggestion is consistent with the experimental observation [107] that the F(k) can be reconstructed from the pure partials.

In both the KCl and RbCl modified systems the Zn^{2+} cation remains four-coordinated across the entire composition range studied (see table 6.6). The M^{+} cation is too large to fit into a tetrahedral site and, indeed, both systems have six-coordinated cations in the pure liquids. Hence, there is a competition between the two cation types in order to possess a complete first coordination shell. As, for example, table 6.6 shows, the Rb^{+} ion is surrounded by less than six anions on average over the composition range.

Table 6.7 gives the cation charge densities (formal charge over ion volume) for the four cations involved. This clearly demonstrates how the lithium cation is able to compete so effectively with the zinc and how both the larger alkali cations cannot.

%RbCl	N_{ZnCl}	N_{RbCl}
20	4.16	4.81
33	3.96	4.98
50	3.85	5.47
67	4.03	5.73

TABLE 6.6: *Cation-anion coordination numbers for the RbCl modified system with increasing modifier.*

Cation	ρ^Q/chargeÅ^{-3}
Zn^{2+}	1.1783
Li^+	1.1052
K^+	0.1015
Rb^+	0.0736

TABLE 6.7: *Charge densities for the four cations in the modified network simulations.*

At low RbCl concentrations the Rb-Rb separation is greater than in the pure salt as the integrity of the $ZnCl_2$ network is being maintained on a localised level. As the concentration of modifier increases the Rb-Rb separation is reduced as the network breaks into smaller polyions. The zinc retains its four-coordinated first coordination shell owing to its much higher positive charge density eventually giving discrete $ZnCl_4^{2-}$ tetrahedral molecular ions at 67% added modifier ($\equiv ZnCl_2.2RbCl$ or Rb_2ZnCl_4). The peak position behaviour of the Cl-Cl distribution supports this suggestion. It remains approximately constant at less than that in pure RbCl across the whole composition range. The chlorides are kept at this separation by being tightly bound to the zinc cation.

6.3.2 Molecular Graphics.

Figure 5.8 showed the vertex-sharing tetrahedral network of pure $ZnCl_2$. Figure 6.5 shows a snapshot of the simulation cell with 33% added RbCl modifier. The network appears to be largely intact although some isolated units are visible. Figure 6.6 corresponds to the 50% modified system. The isolated $ZnCl_4^{2-}$ and larger polyanions (e.g. $Zn_2Cl_7^{3-}$) are now evident. Note that there is now

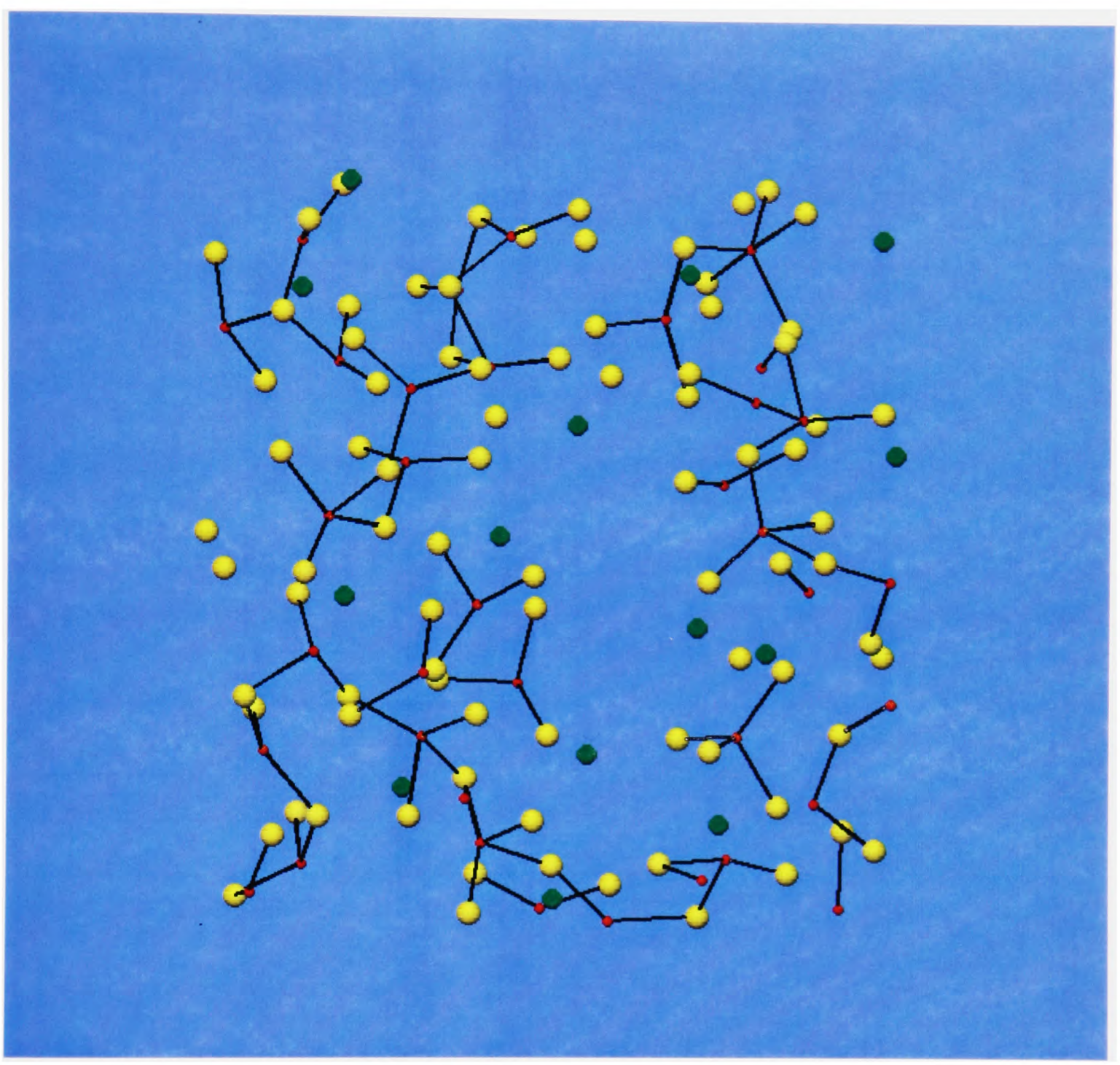


FIGURE 6.5: *AVS plot of a section through the simulation cell for the 33% RbCl modified system. Yellow spheres - anions, red spheres - zinc, green spheres - rubidium. All are drawn at 30% of their crystal ionic radius for clarity.*

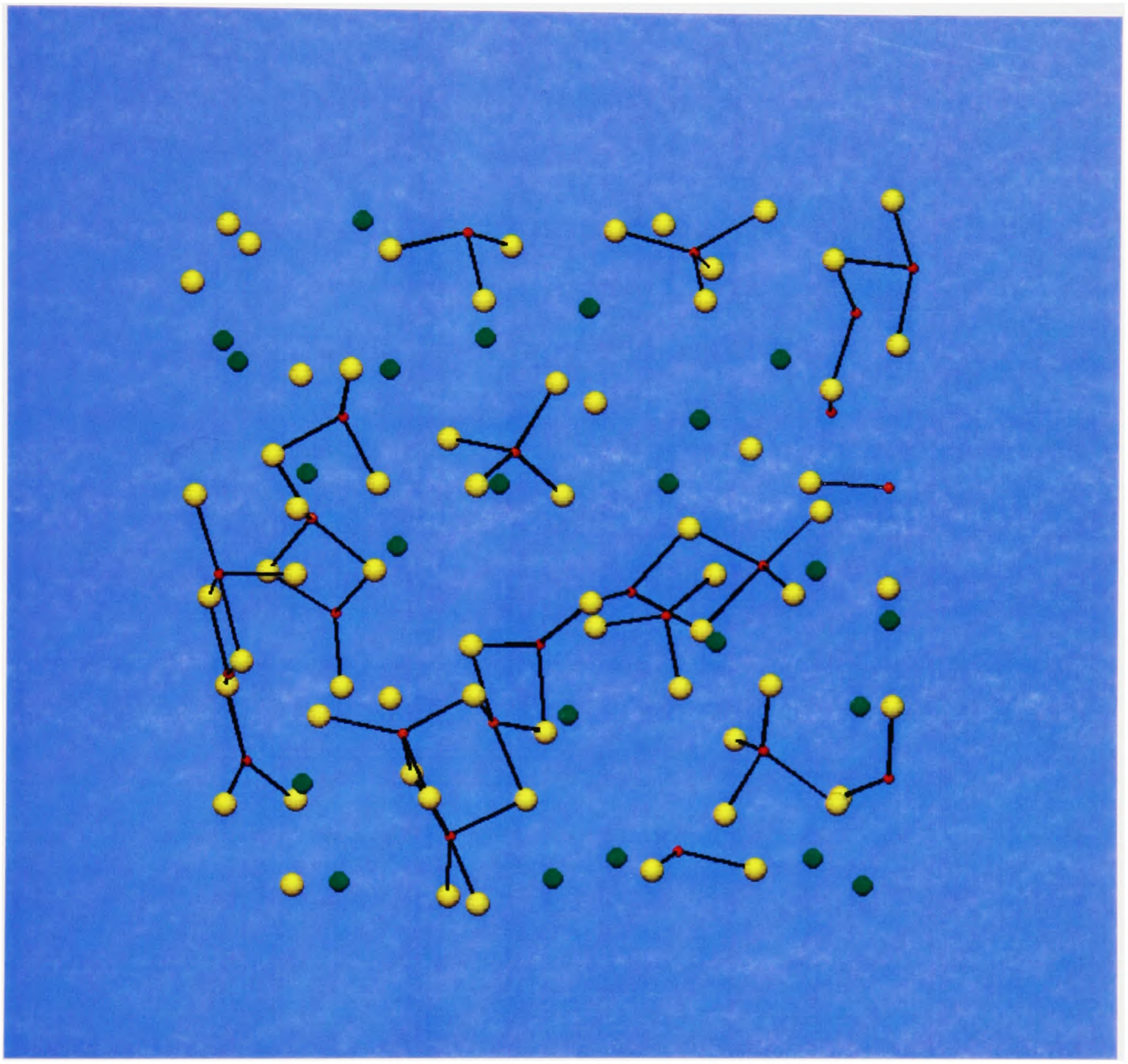


FIGURE 6.6: *AVS plot of a section through the simulation cell for the* 50% *RbCl modified system. The spheres are as for figure 6.5..*

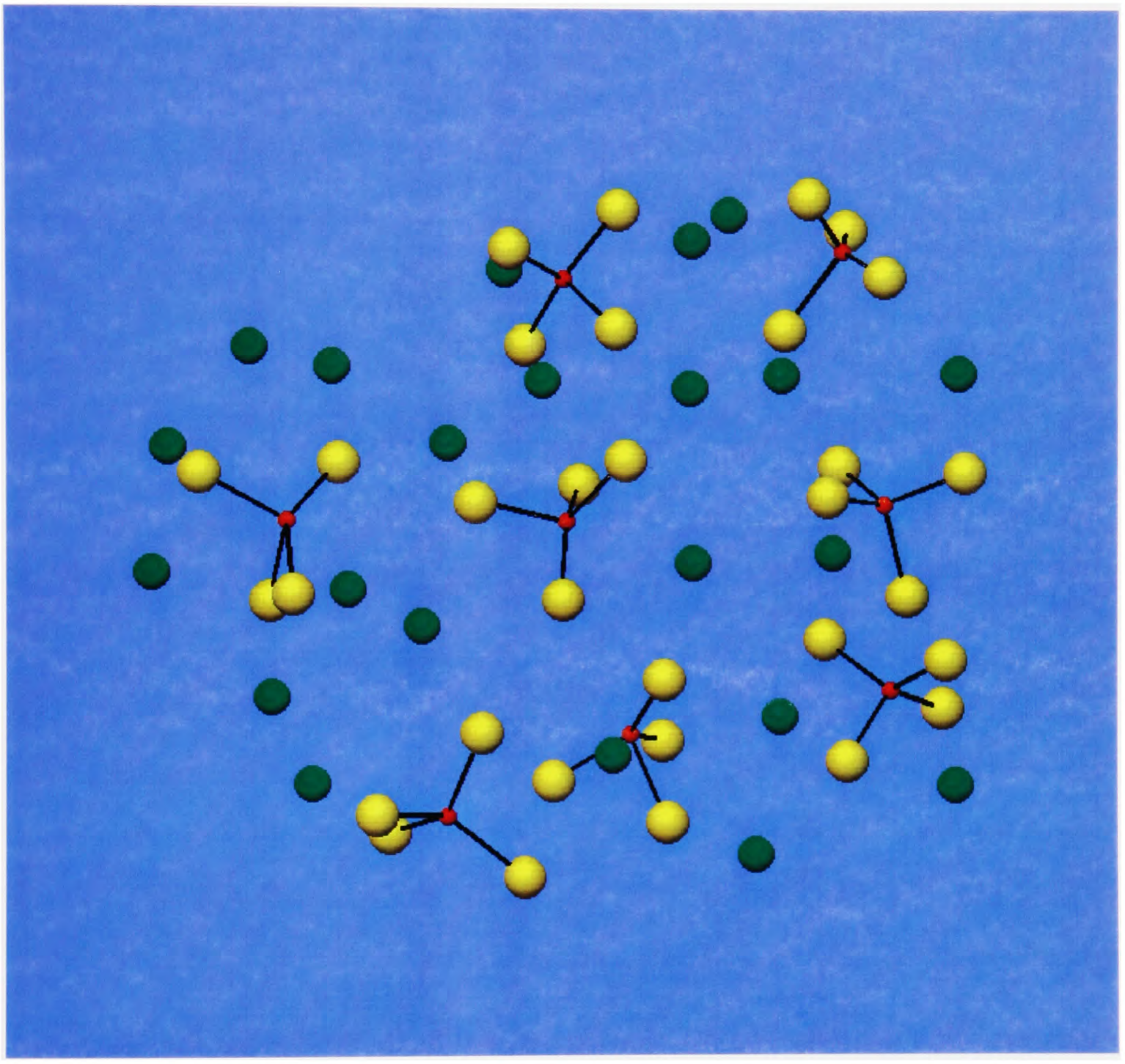


FIGURE 6.7: *AVS plot of a section through the simulation cell for the 67% RbCl modified system. The spheres are as for figure 6.5..*

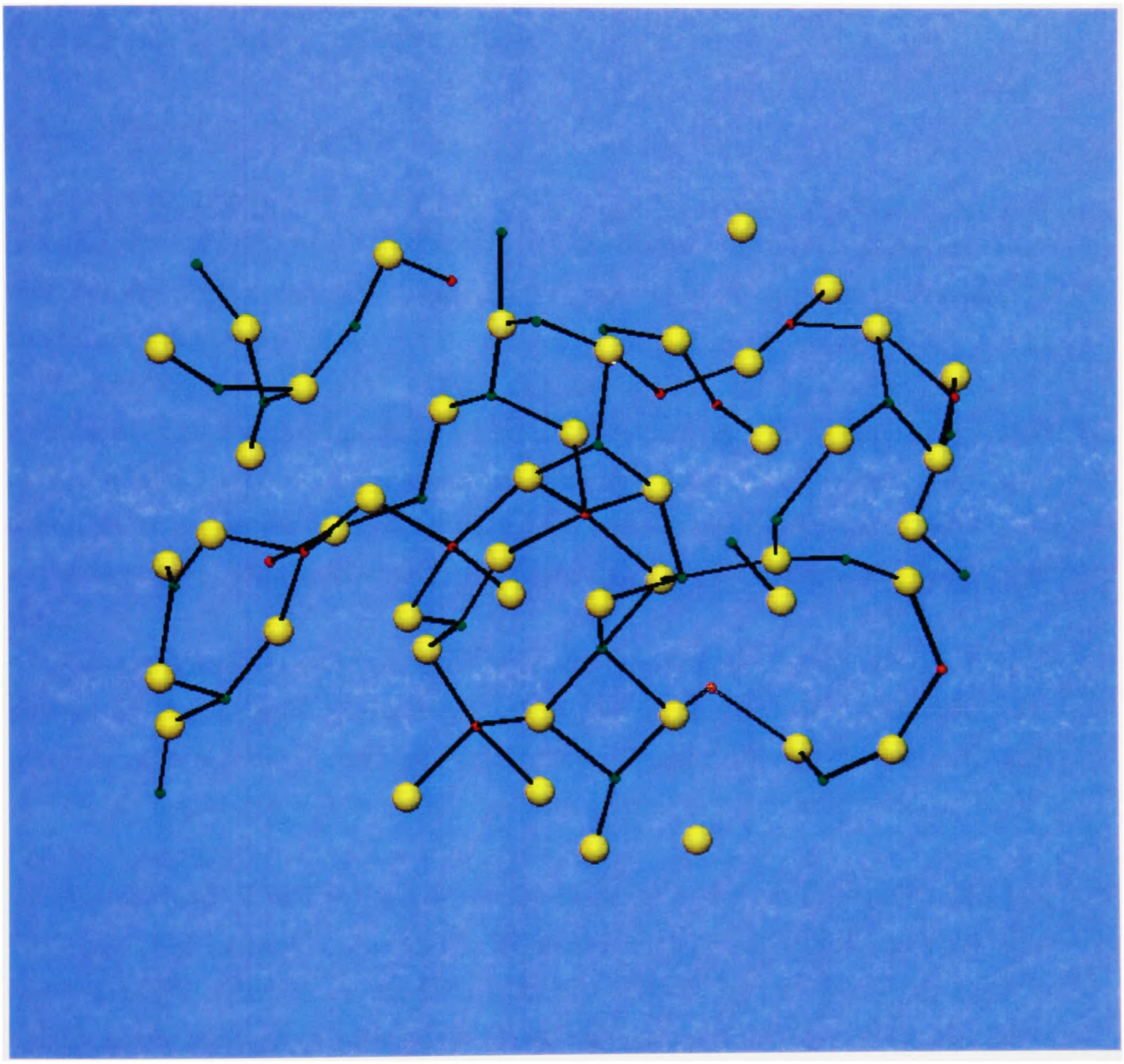


FIGURE 6.8: *AVS plot of a section through the simulation cell for the 67% LiCl modified system. The spheres are as for figure 6.5 except that the green spheres are now* Li^+..

a tendency for *edge* sharing in the surviving network in contradiction to the behaviour in the unmodified system. Figure 6.7 shows the simulation cell with 67% added RbCl modifier. The breaking up of the $ZnCl_2$ network into isolated $ZnCl_4^{2-}$ units is now complete. Contrasting this with figure 6.8 for the 67% LiCl analogue, it is clear that a network with zinc and lithium centred tetrahedra is still present at this concentration. This confirms the essential difference between the LiCl and the larger cation modifiers.

6.3.3 Structure Factors.

As molecular graphics clearly shows, the $ZnCl_2$ tetrahedral network is affected in different ways by the LiCl and $\{Rb, K\}$ modifiers. However, these real space pictures are not immediately suggestive of the origin of the enhanced FSDP in the larger adduct mixtures.

In keeping with the pure molten salt simulations the structure factors are calculated directly via equation 4.13. The method of calculation means that only the 33%, 50% and 67% added modifier mixtures will be considered. The other, more extreme, systems contain too few of a particular ion to allow the gathering of reasonable statistics for all partials in a finite amount of computer time.

Figures 6.9a-f show all six partial structure factors for the LiCl modified system at the three concentrations. The partials appear approximately independent of composition (subject to a certain amount of statistical error) with the FSDP appearing in the S_{ZnZn} function alone. Hence, the individual $F(k)$'s can be reconstructed from the pure partials.

Figures 6.10a-f and 6.11a-f show the same sets of partials for the KCl and RbCl modified systems respectively. These are qualitatively similar to each other but markedly different to the LiCl systems. The FSDP in S_{ZnZn} *increases* in height as the modifier is added. This is accompanied by an increase in the size of the negative peak in S_{MZn} and smaller FSDP features in *all* the other partials.

The previous analysis indicates that the enhancement in the magnitude of S_{ZnZn} may be related to the formation of the molecular ions. To test this hypothesis the molecular ions in the 67% added RbCl system are replaced by a doubly charged anion, T^{2-} of radius 3.7Å, giving the system "Rb_2T". Table 6.8 gives the pair-potential parameters for this model. The "hardness" parameter

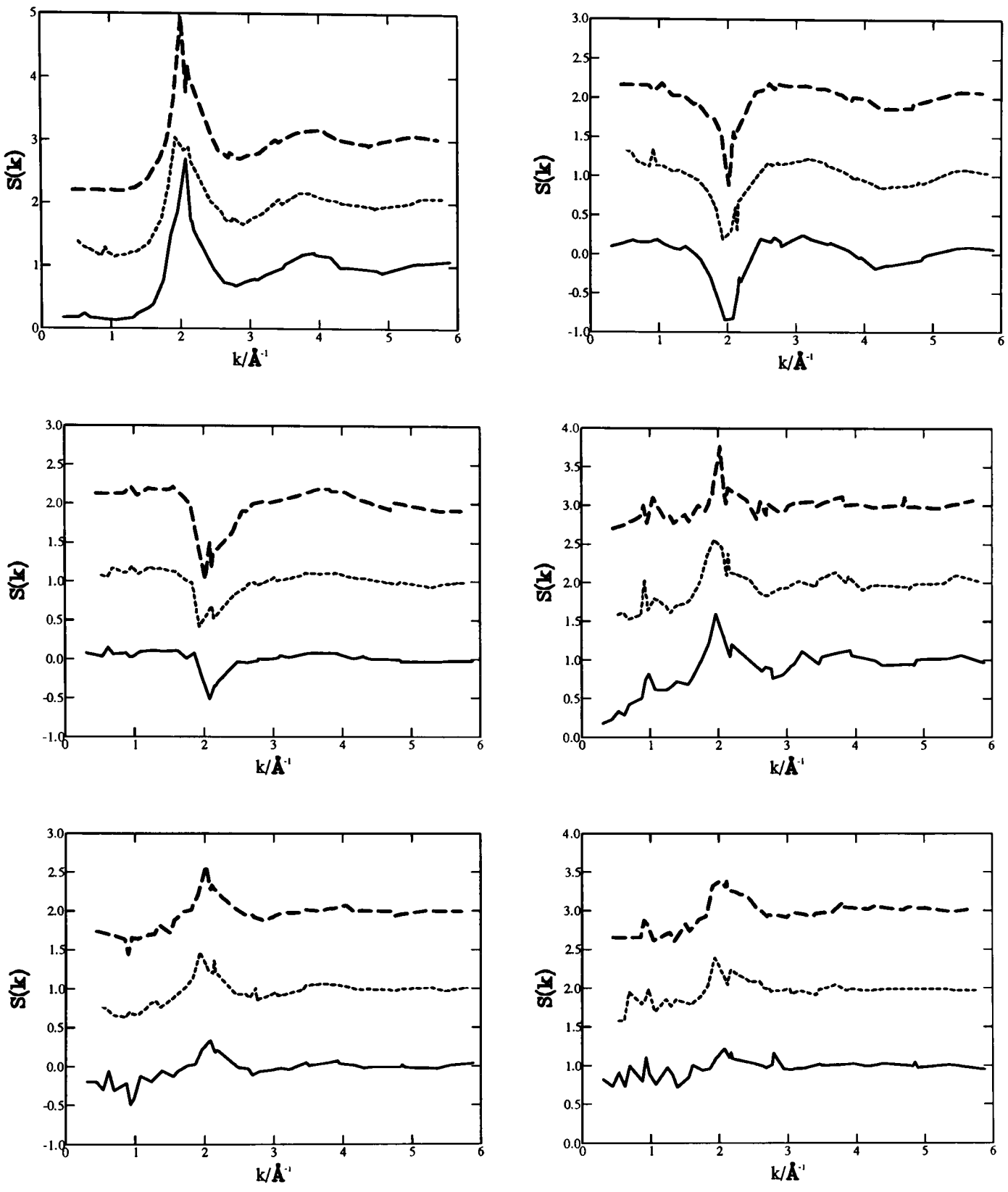


FIGURE 6.9: *Static structure factors for the $ZnCl_2LiCl$ system. (a) Top left - $S_{ClCl}(k)$, (b) Top right - $S_{ZnCl}(k)$, (c) centre left - $S_{LiCl}(k)$, (d) centre right - $S_{ZnZn}(k)$, (e) bottom left - $S_{LiZn}(k)$ and (f) bottom right - $S_{LiLi}(k)$. Key: Solid line - 33% modifier, short dashes - 50%, long dashes - 67%.*

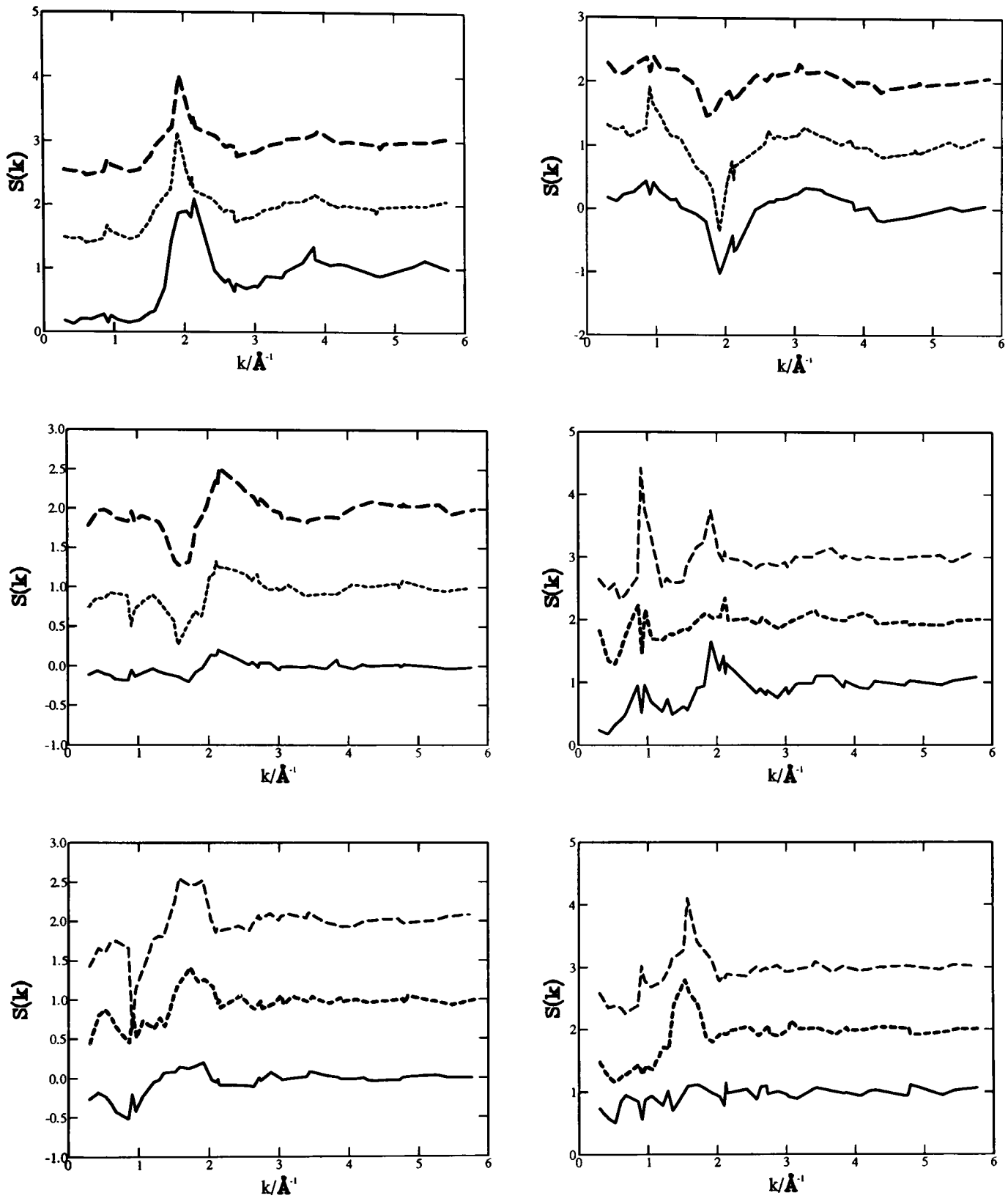


FIGURE 6.10: *Static structure factors for the $ZnCl_2KCl$ (a) Top left - $S_{ClCl}(k)$, (b) top right - $S_{ZnCl}(k)$, (c) centre left - $S_{KCl}(k)$, (d) centre right - $S_{ZnZn}(k)$, (e) bottom left - $S_{KZn}(k)$ and (f) bottom right - $S_{KK}(k)$. Key: as figure 6.9.*

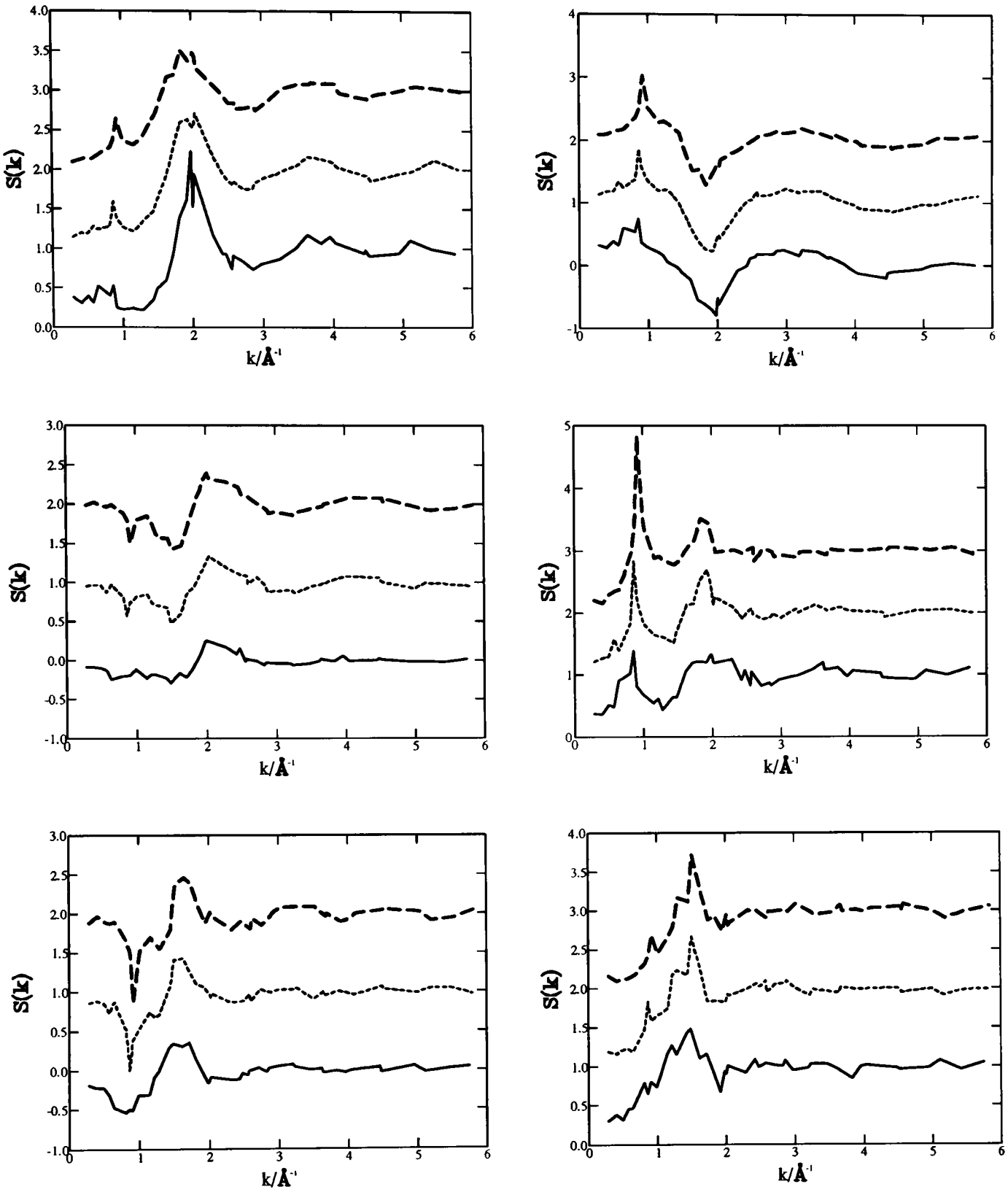


FIGURE 6.11: *Static structure factors for the $ZnCl_2RbCl$ (a) Top left - $S_{ClCl}(k)$, (b) top right - $S_{ZnCl}(k)$, (c) centre left - $S_{RbCl}(k)$, (d) centre right - $S_{ZnZn}(k)$, (e) bottom left - $S_{RbZn}(k)$ and (f) bottom right - $S_{RbRb}(k)$. Key: as figure 6.9.*

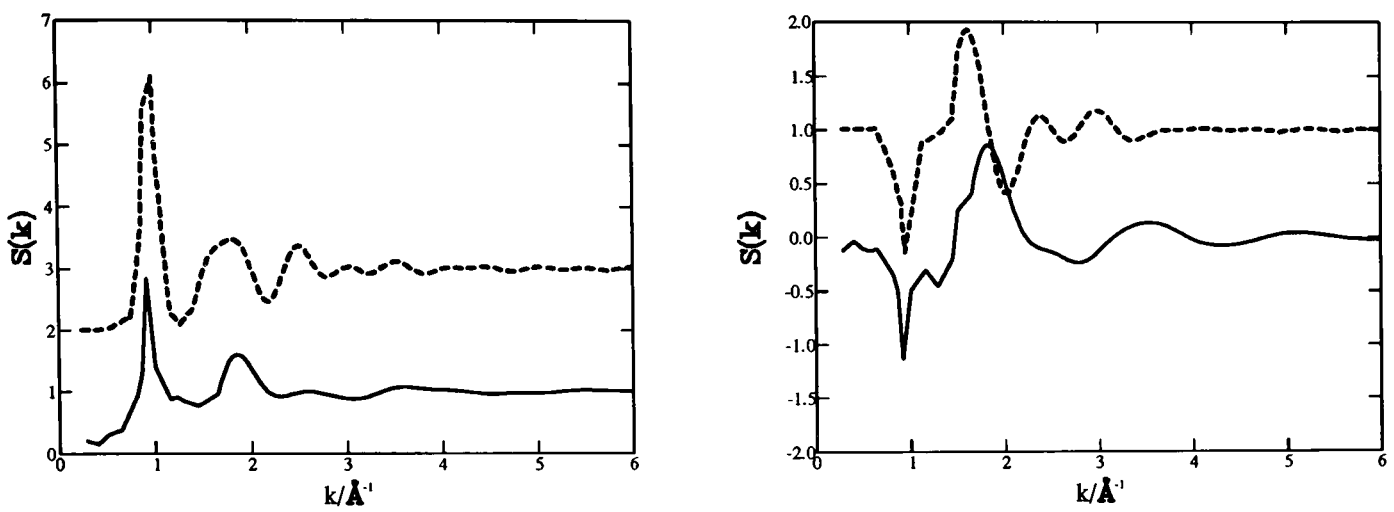


FIGURE 6.12: *Static structure factor for the 67% RbCl modified $ZnCl_2$ system compared with the Rb_2T model. Left - $S_{ZnZn}(k)$, $S_{TT}(k)$, right - $S_{RbZn}(k), S_{RbT}(k)$. Key: solid line - full PIM, dashed line - Rb_2T model.*

Ion pair	B^{ij}/au
RbRb	167.7983
RbT	93605.70
TT	0.0

TABLE 6.8: *Rb_2T potential parameters. The "a" term is 1.6643au.*

(a^{ij}) is from the model for pure RbCl [10] as is the B^{++} term. The resulting system contains 108 ions in total (72 Rb^+, 36 T^{2-}) on which a simple RI simulation is performed of length 30ps in real time. Figures 6.12a and b shows the S_{ZnZn} and S_{RbZn} functions across the whole composition range with the simple Rb_2T model for comparison. There is a marked similarity between the 67% added RbCl system and the simple model system. This confirms the assertion that the FSDP feature in the mixture is a direct result of the formation of the molecular ions. The FSDP in the mixture is simply caused by the charge-ordering in the simple Rb_2T molten salt.

6.4 Raman Scattering.

The formation of molecular ions in the modified-network fluids has been examined by Raman scattering. The primary interest is in the high frequency vibrational modes that involve bond stretching rather than bond bending. Thus, a *group bond correlation function* (GBCF) is calculated, following Boulard *et al* [113]. Each group of ions consists of a central cation surrounded by x anions within a chosen cutoff distance. A property $C^j_\alpha(t)$ which measures the bond stretching around a given ion j is defined as

$$C^j(t) = \sum_{i=1}^{N^i} \left\{ v^i_\alpha(t) - v^j_\alpha(t) \right\} r^{ij}_\alpha(t) \tag{6.1}$$

$$C(t) = \left\langle C^j(0) C^j(t) \right\rangle, \tag{6.2}$$

where v^i_α is the α component of the velocity of ion i, and then averaged over all the ion i's in the group associated with ion j. The group (the sum over i) refers to a local $ZnCl_4$ tetrahedral unit whether it is in a network or a discrete ion.

Figure 6.13 shows the calculated spectra for the KCl modified system. The main peak is shifted from $\sim$ 245cm^{-1} in the pure zinc salt to $\sim$ 260cm^{-1} in the 81% added modifier system. The shift is not as large as that observed experimentally [109] but is qualitatively correct. Furthermore, the emergence of features at $\sim$ 150cm^{-1} is consistent with experiment [81] attributed to a Cl-Zn-Cl *deformation* mode - i.e it is directly associated with the emergence of the discrete molecular ions.

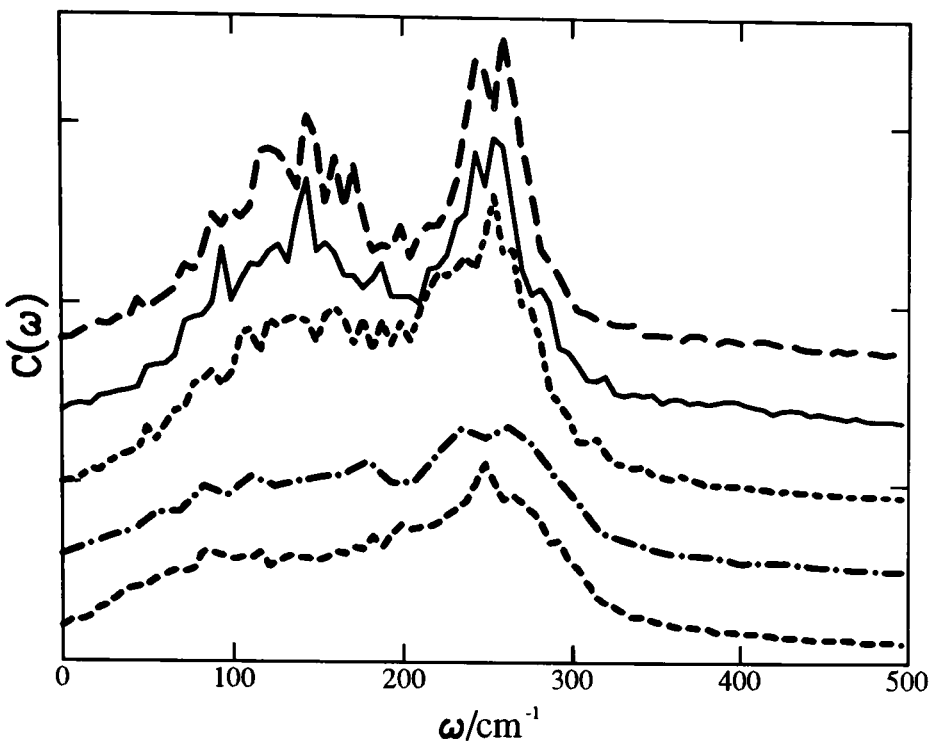


FIGURE 6.13: *Calculated Raman spectra for the KCl modified $ZnCl_2$. Key: short-dashes - pure $ZnCl_2$, long-dashes-dots - 33% KCl, short-dashes-dots - 50% KCl, solid line - 67% KCl, and long-dashes - 81% KCl.*

6.5 The Origin of the FSDP.

It is clear, therefore, that the FSDP in the M_2ZnCl_4 (M=K,Rb) originates in a different manner to that in the pure $ZnCl_2$. In the latter the network structure of the system is crucial. In the former, however, this "infinite" network has been totally destroyed leaving the discrete molecular anion units.

The origin of the FDSP in the M_2ZnCl_4 can be attributed to the size of the molecular anions. Iyetomi and Vashishta [114] have shown how an FSDP can appear in simple RIM simulations over a suitable range of the size ratio (R) of the cation to the anion. This will be discussed more fully in the following section. For the moment the essential point is that an FSDP appears at small R (i.e. small cation-large anion).

Although the work does not go as far as R=2.5 (the expected ratio between a Rb^+ and the $ZnCl_4^{2-}$ unit) it is reasonable to assume that the same principles apply; that is, the FSDP appears due to a *size ratio mechanism.* Thus, the low k feature, although termed an FSDP, in fact the *principal peak* due to the anion-anion correlations. Hence the system can be modelled effectively with a large charged sphere mimicking the $ZnCl_4^{2-}$ anion.

Assuming this origin for the FSDP let us consider each partial structure factor in turn:

- $S_{ZnZn}(k)$ has a large FSDP corresponding to the T-T peak. This is a result of the zinc species being at the centre of the molecular anion corresponding to the T-T correlations which centre on the charged anion sphere. This FSDP is actually the T-T principal peak.

- $S_{RbZn}(k)$ has a large negative FSDP corresponding to the negative principal peak observed in the anion-cation correlations of all ionic (charge-ordered) systems.

- *The rest* contain smaller low-k features (positive in S_{ClCl}, S_{ZnCl} and S_{RbRb} but negative in S_{RbCl}). These small features are simply *excluded-volume* effects caused by the presence of a large anion tending to push species apart causing intermediate range density fluctuations.

This mechanism of FSDP formation will be expanded upon in the following section.

6.6 Classifying the First Sharp Diffraction Peak.

In sections 5.5 and 6.5 explanations have been presented for the origin of the FSDP in pure $ZnCl_2$ and M_2ZnCl_4 (M=K,Rb). Although the low k feature appears in *both* systems it originates from a different mechanism in each. As a great many systems possess such a feature it is of interest to attempt to classify these in terms of the "mechanism" by which the FSDPs may be formed.

Recently, Elliott [115] has attempted to clarify what is meant by the terms "prepeak" and FSDP. A prepeak is defined as *any* diffraction peak that appears at a lower k than the principal peak. An FSDP is defined as a prepeak that behaves in an anomalous manner (with respect to the principal peak) in terms of response to temperature and pressure. Consider each of these in turn:

- **Temperature**. In general, the FSDP intensity *increases* with increasing temperature. The opposite behaviour of the principal peak arises from the standard Debye-Waller dependence.

- **Pressure**. The FSDP intensity *decreases* with increasing pressure.

Elliott [115] has shown how this anomalous behaviour can be decomposed into contributions from different system partial derivatives. For the variation with temperature the peak intensity, I, varies as

$$\left(\frac{\partial I}{\partial T}\right)_p = \left(\frac{\partial I}{\partial T}\right)_\rho + \left(\frac{\partial I}{\partial \rho}\right)_T \left(\frac{\partial \rho}{\partial T}\right)_p . \tag{6.3}$$

The first term on the right-hand side of this equation is negative - a standard Debye-Waller effect. The third term, the *thermal expansivity*, is also usually negative. The difference in behaviour between the principal peak and the FSDP lies in the nature of the second term. For the principal peak this term is small and positive whilst for the FSDP it is larger and negative. Hence, for the FSDP, $\left(\frac{\partial I}{\partial T}\right)_p$ depends upon a *balance* between the usual Debye-Waller effect and the second and third terms on the right-hand side of equation 6.3. For the principal peak the first term dominates resulting in the standard Debye-Waller behaviour. For the FSDP the second and third terms usually dominate resulting in the observed anomalous behaviour.

Salmon [116] describes the physical origin of these effects as a balance between the thermal vibrations (the Debye-Waller effect) and the *relaxation* of the network as the temperature is raised. The basic premise is that, as the temperature is raised, the network is allowed to relax more due to the thermal expansion. This leads to $\left(\frac{\partial I}{\partial \rho}\right)_T$ being negative corresponding to the observed *increase* in FSDP intensity. This phenomenon has been observed in MD simulations for $GeSe_2$ [117, 118] where it is referred to as a decrease in network "frustration" as the temperature is raised.

It is important to note that the SiO_2 FSDP actually *decreases* with temperature. This still, however, fits into the above analysis as silica has a very low thermal expansivity allowing the thermal vibration term to dominate [119].

Similarly, for the pressure behaviour [115]

$$\left(\frac{\partial I}{\partial p}\right)_T = \frac{\rho}{B}\left(\frac{\partial I}{\partial \rho}\right)_T , \tag{6.4}$$

where B is the bulk modulus. Again, it is the negative sign of the partial derivative on the right-hand side of this equation, due to the network relaxation with decreasing density, that results in the anomalous FSDP intensity behaviour.

It is important to note that this definition of the FSDP will separate *network forming* systems from non-network formers.

If one considers the FSDP to be pseudo-Bragg-like then the real space structure should contain structural features on a length scale [120]

$$R \simeq \frac{2\pi}{k_1}, \tag{6.5}$$

where k_1 is the position of the FSDP and R is the effective periodicity. The height and shape of the FSDP effects the nature of these real space oscillations

- An intense FSDP corresponds to *large amplitude* real-space oscillations.
- A sharp peak corresponds to a slow decay of these oscillations. A typical FSDP width corresponds to a correlation length of 15-25Å [121].

In section 5.5 it was shown that it is the intermediate-ranged oscillations in the *cation* density that gives rise to the FSDP in $ZnCl_2$. Similar arguments apply to other systems with this stoichiometry.

As mentioned in the previous section Iyetomi and Vashishta [114] have shown how an FSDP emerges as the anion-cation size ratio, R, is decreases from within a simple charged hard sphere model (CHS). However, this occurs between R=0.25 and 0.35 whereas R=0.41 for $ZnCl_2$. Indeed, the R=0.35 partial structure factors in the CHS model (figure 4 in reference [114]) appear very similar to those obtained from MD simulation using the RIM (figure 5.5). This is fully consistent with the earlier discussion that the short-range ordering of the ions is not the dominant factor in the observed MX_2 FSDP's. It is the manner in which the short-range units are linked that is crucial.

6.6.1 Modelling the FSDP.

Several models have been suggested in order to explain an appearance of the FSDP. Arguments based on the persistence of layered microcrystallites (with a low k Bragg peak) [122] are unlikely in the molten state as, for example, the intensity of the FSDP remains at worst undiminished with increasing temperature in $ZnCl_2$ [67]. Such a model would predict the structure to disappear with increasing temperature in accordance with the further breakup of the crystal structure. Models based upon the aggregation of particles clearly *do* apply to systems such as As and AsS_4 [123, 124].

A more general appreciation [125, 126, 115, 120] of the origin of the FSDP can be gained by decomposing the total scattering function in the Bhatia and Thornton [127] formalism. It has been the norm, over the last 20 years, to decompose the total scattering intensities obtained from experiment into partial structure factors that give information on the structural correlation between each species (the Faber-Ziman formalism [128]). However, this is by no means the only possible decomposition. In the Bhatia and Thornton [127] representation the total function is decomposed into the number-number, concentration-concentration and number-concentration partials (S_{NN}, S_{CC} and S_{NC} respectively). In this formalism the total scattering intensity is given by [124]

$$\begin{aligned} I(k) &= N\Big\{(c_A b_A + c_B b_B)^2 S_{NN}(k) \\ &+ 2(c_A b_A + c_B b_B)(b_A - b_B) S_{NC}(k) + (b_A - b_B)^2 S_{CC}(k)\Big\}, \end{aligned} \quad (6.6)$$

where N is the number of atoms, b_i is the coherent neutron scattering length of i and c_i the corresponding mole fraction.

The physical significance of each term is as follows [124, 120]

- $S_{NN}(k)$: Fourier transformation gives information regarding the *global structure* not concerned with the actual nature of each site.

- $S_{CC}(k)$: Fourier transformation yields information concerning the *chemical* ordering. For an ideal alloy AB $S_{CC}(k) = c_A c_B$. $S_{CC} > c_A c_B$ indicates preferential clustering whilst $S_{CC} < c_A c_B$ demonstrates *charge-ordering.*

- $S_{NC}(k)$: Fourier transformation gives the correlation between sites and their occupancy by A or B. In an ideal solution $S_{NC}(k) = 0$.

Note:

- For an ideal solution *all* the information is in $S_{NN}(k)$.

- If the scattering lengths of the two species are similar then the second and third terms in equation 6.6 become small. Thus, $S_{NN}(k)$ is measured *directly* in such systems. Examples include $FeCl_3$ [129] and $GeSe_2$ [130].

- For a "zero-alloy", that is, one in which $(c_A b_A + c_B b_B) = 0$ $S_{CC}(k)$ is measured directly.

Salmon [120] has surveyed nine MX_2 systems investigated by neutron scattering using the BT formalism. Seven of the systems studied possess an FSDP in $S_{MM}(k)$. Of these seven all possess a low-k feature in $S_{NN}(k)$ with a corresponding smaller feature in $S_{NC}(k)$. Three of the systems ($ZnCl_2$, $MgCl_2$ and $GeSe_2$) show a strong feature in $S_{CC}(k)$ whilst the other four (the three nickel halides and $CaCl_2$) show a shoulder. Salmon points out that $S_{CC}(k) = c_M c_X S_{ZZ}(k)$, where $S_{ZZ}(k)$ in the *charge-charge* correlation function. A low-k feature in $S_{CC}(k)$, therefore, corresponds to intermediate-ranged *charge fluctuations*. This is consistent with the interpretation of the origin of the FSDP in $ZnCl_2$ [93] (section 5.5).

Elliott [125, 131, 126] has used a different approach to explain the formation of an FSDP in the network liquids based on studying the correlations between cation centres and *voids* in the anion sublattice. Cervinka *et al* [132] have demonstrated how a prepeak can be produced in 2D. Blétry [133] and Dixmier [134] have shown how the three-dimensional feature can be generated by the systematic removal of atoms from the first and second coordination spheres about a given atom in a dense-random packed structure. These atoms are equivalent to the cation-centred clusters in the MX_2 systems and hence the prepeak in these systems can be considered as a result of the chemical ordering of voids around cation-centred clusters [115].

Uhlherr and Elliott [135, 136] have used this void-based model to look at the correlation length of the intermediate-range density fluctuations. As these lengths are predicted to be of the order of 15-25Å [121] ultra-large simulation cells have to be used. For amorphous Si the 13824 atom model from [137] was analysed and atomic density fluctuations were found out to at least 35Å.

Additionally, the void-based model can be used to consider the effect of adding different modifiers. The total scattering intensity, again within the BT formalism, is still given by equation 6.6 but now the subscripts A and B refer to the cation-centred clusters and voids respectively. (Indeed, it is worth stressing that the Elliott $S_{CC}(k)$ is different to that of Salmon as the former represents the correlation of cation-centred clusters and voids whilst the latter represents the correlation between the anions and cations themselves [115]).

To model the network-modified systems the modifier is considered to partially fill the voids. This will change the total scattering intensity by introducing a

new scattering length. For a modifier with a negative scattering length (for example, lithium) the FSDP will be *increased* in intensity with respect to the pure system via the enhancement of the $(b_A - b_B)$ term in equation 6.6. A modifier with a positive scattering length has the opposite effect. Experimental evidence supporting this analysis comes from alkali-modified silicates [138] and silver-modified $GeSe_2$ [139].

As Elliott himself comments [140] this model is not the full story. It is clear from the earlier work in this chapter, on the modified $ZnCl_2$ systems, that the Li^+ cation *can* fit into the network whist the larger K^+ and Rb^+ cations cannot. The larger modifiers more effectively depolymerize the network resulting in the formation of polyanions. It is then the correlations between these polyanions that causes the prepeak rather than the nature of any network.

Finally in this section it is of interest to speculate as to the more subtle aspects of FSDP structure. Consider all the MX_2 systems for which neutron scattering data is available and that form an FSDP (see, for example, [120]). There are subtle differences worthy of attention.

- NiX_2 FSDP's appear less sharp and high with respect to the ZnX_2 analogues.
- SiO_2 and $GeSe_2$ anomalously show an FSDP in *all three* partials. The usual behaviour is to show a main feature in S_{MM} and a lesser feature in S_{MX}.

Both of these differences may be attributed to the timescale over which the short-range structural units are stable.

Considering the first difference, it is known that Ni^{2+} cations have a relatively high mobility. This leads to a less viscous system with respect to the zinc analogues with a corresponding smaller timescale over which the local structural units are stable. This is associated with the less intense, broader FSDP's in the Ni systems. The enhanced mobility of the Ni^{2+} can be linked to the open-shell nature of the d^8 cation. It is known [141], for example, that simple shell models can predict the cation mobility energy for the *closed-shell* oxides MnO and MgO but predict too high an energy (i.e too small a mobility) for open shell systems such as NiO and CoO. The NiX_2 and ZnX_2 observations appear analogous to this. Note that this would also lead to the lower intensity low-k S_{CC} feature

observed by Salmon [120].

The second difference can also be related to a fundamental difference in these systems. As was discussed in chapter 3 *formal* ionic charges have been insisted upon throughout this thesis. Again, if this line is followed through then a fundamental difference is that SiO_2 and $GeSe_2$ have charges {+4,-2} whilst the others are {+2,-1}. The formal charges in the system has important implications for the nature of the network. The {+4,-2} systems have a deeper, sharper anion-cation potential well resulting in more tightly bound short-range structural units with respect to the {+2,-1} systems. Thus, these units are stable on a longer timescale and so small low-k features are observed in both S_{MX} and S_{XX} in contrast to the lower charge systems where the instability of the short-range units averages to zero the X-X correlations.

6.6.2 Summary: A Possible Classification of Prepeaks.

Three mechanisms can be identified although it should be stressed that it is largely impossible to assign a single FSDP mechanism to a particular system. The aim is to identify the *dominant* mechanisms.

- **Induction**(I): For the $ZnCl_2$-type systems the most important physical property causing the FSDP is the formation of dipoles on the anions causing intermediate-ranged cation density fluctuations. Without the induction effects *no* FSDP is observed.

- **Size-ratio**: These can be divided into two sub-classes:

  - *Ionic systems*(S_1): In Rb_2ZnCl_4 the FSDP arises due to the presence of a large anion (see section 6.5) Other examples include systems with polyanions such as BO_4^{5-} [142]. It also includes so called "Zintl" phases such as systems with the Pb_4^{4-} anion (i.e Rb_4Pb_4) [143].

  - *Molecular systems*(S_2): A similar argument applies to systems such as X_4 and X_2 [144, 145]. In these systems the total structure factor can be split into these two contributions

$$S(k) = \underbrace{f_m(k)}_{intra-} + \underbrace{D_m(k)}_{inter-}. \tag{6.7}$$

An FSDP feature appears when the characteristic *inter*-molecular length scale is greater than the corresponding *intra*-molecular scale [145]. This occurs in systems such as P_4 and CCl_4 but not in VCl_4 where these two length scales are very similar. An analogous argument applies to the liquid halogens [144, 146].

- **Coulombic ordering**(C): In systems with highly charged species the large coulombic repulsion between these species may lead to spatial correlations on an intermediate length scale. Typical of these systems are the MX_3 salts in which the +3 cation charge leads to a prominent low k feature in the total structure factor [129]. This means that these systems can be *relatively* successfully simulated with a RIM (see, for example [147]) although it is worth noting that the simulations still produce an FSDP at too high a k with respect to experiment implying that there is an additional *induction* mechanism contribution. The discrepancy between the RIM simulations and the experiment is much less than in the MX_2 where the induction mechanism is dominant.

The "reduced" scale to study is $k_1 r_1$ [131], where k_1 is the position of the FSDP and r_1 is the nearest-neighbour first radial distribution function peak position. Table 6.9 shows a range of systems possessing an FSDP in order of this reduced scale. Note that the r_1 distance for the systems with polyions is that between the centre of the polyion and its nearest neighbour. This is different to some previous work [148].

At $k_1 r_1 \leq 2.7$ the mechanisms are purely induction and charge-ordered, or a mix of the two. Above this both size-ratio mechanisms predominate. In the Elliott classification of the prepeak and FSDP *all* of the systems with $k_1 r_1 > 2.7$ possess prepeaks whilst the majority of the MX_2 systems below this would be expected to have FSDPs. The MX_3 system low-k features would be expected to be prepeaks.

System	$k_1/\text{Å}^{-1}$	$r_1/\text{Å}$	$k_1 r_1$	Mechanism	Reference
$NiBr_2$	0.92	2.42	2.23	I	[73]
$MgCl_2$	0.93	2.42	2.25	I	[65]
$ZnBr_2$	0.94	2.41	2.27	I	[67]
$ZnCl_2$	1.00-1.09	2.29	2.29-2.50	I	[66, 67]
ZnI_2	0.88	2.60	2.29	I	[67]
NiI_2	0.88	2.60	2.29	I	[74]
$AlBr_3$	1.0	2.29	2.29	C	[129]
GaI_3	0.9	2.54	2.29	C	[129]
$NiCl_2$	0.98	2.36	2.31	I	[73]
$GeSe_2$	0.97-1.01	2.35	2.28-2.34	I	[130]
GeS_2	1.04	2.23	2.32	I	[149]
$GaBr_3$	1.0	2.34	2.34	C	[129]
SiO_2	1.52	1.62	2.46	C/I	[150]
BeF_2	1.63	1.54	2.51	C/I	[151]
$NiTe_2$	1.0	2.56	2.56	I	[152]
$CaCl_2$	0.95	2.78	2.64	I	[71]
GeO_2	1.55	1.74	2.70	C/I	[153]
F_2	2.06	1.36	2.80	S_2	[144]
P_4	1.36	2.2	3.00	S_2	[145]
Cl_2	1.64	1.95	3.20	S_2	[144]
Br_2	1.57	2.29	3.60	S_2	[144]
I_2	1.45	2.75	3.99	S_2	[144]
KTe	1.2	3.6	4.32	S_1	[154]
KPb	1.0	4.38	4.38	S_1	[143]
NaPb	1.3	3.42	4.45	S_1	[143]
RbPb	1.0	4.5	4.50	S_1	[143]
CsPb	1.0	4.5	4.50	S_1	[143]

TABLE 6.9: *The product of the position of the FSDP and the smallest characteristic length scale in a cross-section of systems possessing an FSDP-like feature.*

7

Cation Polarization and Induced Quadrupoles.

The central role of *anion* polarization effects in determining the structural properties of both the liquid and crystalline MX_2 systems has now been clearly demonstrated. The next development is to investigate the possible role of *cation* polarization at both a dipolar *and* quadrupolar level.

The target for this study is AgCl as this system, although isostructural in the solid-state with many alkali halides, shows "anomalous" properties, not accounted for by normal pair-potentials, attributed to the post-transitional nature of the cation.

In order to study the effect of a cation of this type, simulation models will be used in which each cation polarization term is added in turn. This will allow for the systematic study of the roles of cation *dipole* polarizability and also the induced *quadrupoles*.

In order to clearly focus on the anomalous behaviour comparison will be made throughout to analogous alkali halide simulations in which only the anion polarization effects are included.

7.1 Crystalline LiF.

To model LiF the induction parameters derived in chapter 3 are used in addition to the Born-Mayer terms from [10].

Figure 7.1 shows the optical modes of the phonon dispersion curves for LiF along the three main high-symmetry directions for both the RIM and PIM. The LO-TO splitting is greatly reduced by the inclusion of the induction effects as previously observed for the shell model (see section 1.3). The shape of these curves is consistent with the other alkali halides that crystallize with the NaCl structure, which are known to agree with experiment [13].

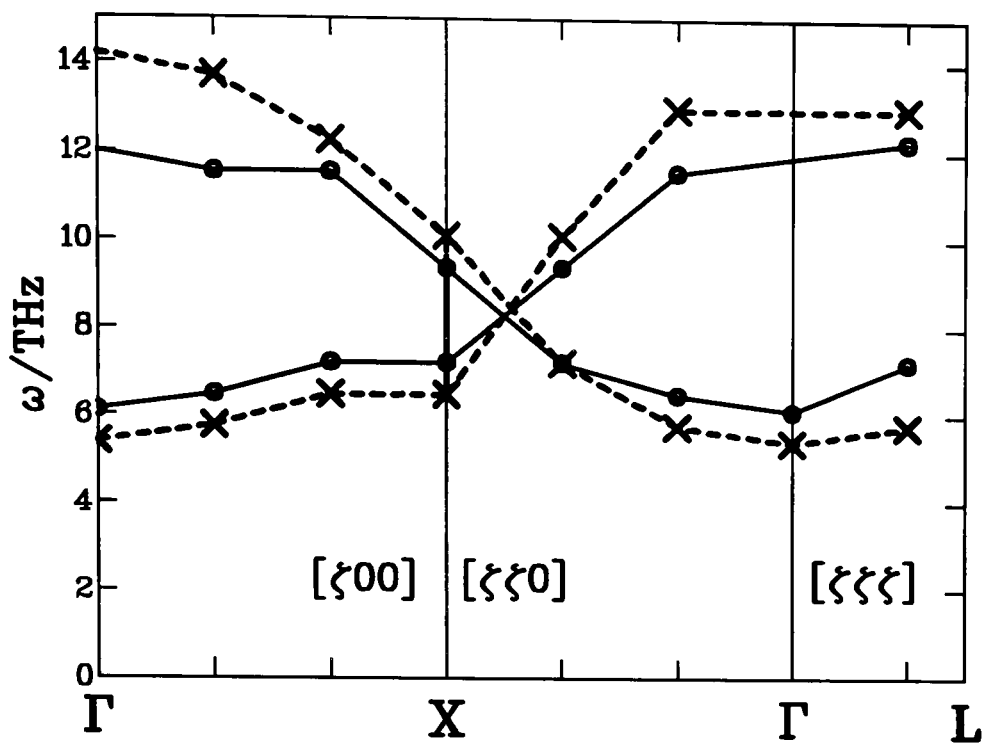


FIGURE 7.1: *Optic phonon dispersion curves for LiF at 100K. Key:* × *- RIM,* ○ *- PIM. Note that one TO mode in the [ζζ0] direction has been omitted for clarity. Also note that the lines are drawn as an aid to the eye.*

7.2 The "Anomalous" Behavior of AgCl.

7.2.1 Crystal.

In the crystalline phase AgCl adopts the NaCl structure and has been the subject of several experimental studies, covering four main areas:

- **Phonon dispersion curves**: Inelastic neutron scattering experiments [155] have shown these curves to be fundamentally different to the alkali halides [23], in particular, the shape of the optical modes differ with the TO(L)-point being particularly soft. The experimental curves for AgCl are shown in figure 7.3.

- **Elastic properties**: AgCl shows a pronounced Cauchy violation ([156] and references therein) attributed to the relative importance of many-body effects with respect to the alkali halides.

- **Diffusion**: AgCl exhibits a far greater rate of cation diffusion in the solid-state with respect to, say, KCl [157].

- **Defect formation**: The Frenkel defect formation energies have been found to be lower than those characteristic of the alkali halides [157].

The latter two properties have been combined to explain the higher conductivity of AgCl with respect to, say, KCl [157]. The lower defect formation energy leads to a larger number of defects at a given temperature which move more quickly with respect to analogous alkali halide defects.

7.2.2 Melt.

The most striking difference between liquid AgCl and the alkali halides lies in the melting point. Table 7.1 gives typical alkali halide melting points along with that of AgCl (all from [59]). The alkali halide temperatures are consistently higher than that of AgCl. Notice also that the ionic (crystal) radius of Ag^+ falls between that of Na^+ and K^+ [59]. It would appear that the silver cation prefers the less symmetrical coordination environments typical of the melt relative to the alkali cations.

System	T_m/K	σ_+/Å
LiCl	880	0.60
NaCl	1074	0.95
KCl	1040	1.33
RbCl	988	1.48
CsCl	918	1.69
AgCl	728	1.26

TABLE 7.1: *Experimental melting points for a selection of alkali halides and AgCl. Also shown are the crystal cation radii. All from [59].*

Derrien and Dupuy [158] performed neutron scattering experiments using isotopic Cl^- substitution to derive the three partial structure factors. Inui *et al* [159] later obtained the *total* structure factors for all three silver halides. Although the partial structure factors appear to contain too much structure for the liquid phase (i.e they appear noisy), several features are clear.

- There is a persistent oscillatory character in the structure factors that continues out to large momentum transfer.

- The position of the first peak in $g_{AgCl}(r)$ is on a much shorter length scale with respect to the crystal (2.6Å in the liquid but 2.97Å in the crystal). This is in contrast to typical alkali halide behaviour; for example, the same property in LiCl falls from 2.57Å in the crystal at atmospheric pressure [9] to 2.45Å in the liquid just above freezing [56].

- The Ag-Cl coordination number falls from 6 in the crystal to $\simeq$4 at 783K to $\simeq$3 at 1123K. NaCl, for example, remains six coordinated across the melting transition, though LiCl changes from six to four coordination on melting.

- The anion-anion and cation-cation partial structure factors are not similar, in direct contrast to alkali halide behavior.

These observations have been taken to indicate the existence of ill-defined "quasi-molecular" structures [158].

7.3 Previous Silver Halide Simulations.

Theoretical studies have shown that both the phonon dispersion curves and the Frenkel and Schottky defect energies are sensitive to the introduction of explicit three-body terms into the potential models [160, 161, 156]. A pronounced Cauchy violation is also observed supporting the importance of the many-body effects. Baetzold *et al* [156] have shown how agreement with experiment could be improved via the introduction of angle-bending (three-body) terms and triple-dipole interactions. However, although accounting for the Cauchy violation and improving the defect energetics, this model still produced alkali halide-like phonon dispersion curves (see fig 3 of ref. [156]). The authors attribute this to the omission of Ag^+ deformability from the model.

Quadrupolar deformations of the Ag^+ cation were included in the breathing-shell model of Fischer *et al* [23, 162] in lattice dynamics calculations on AgCl. They showed how such deformations could be manipulated to reproduce the experimental phonon dispersion curves [155]. These calculations demonstrated that it is the greater quadrupolar deformability of the Ag^+ cation that alters the characteristic lattice dynamics with respect to the alkali halides with the same (NaCl) crystal structure [163]. The ability of this model to reproduce key

phonon dispersion curve characteristics with *cation* induced quadrupoles makes clear the dominant role of these over any anion quadrupoles. Reasons for this will be discussed in section 7.4.2.

Theoretical studies [164, 165] on the crystal properties suggest that (in contrast to the alkali halides) pairwise additive models assuming spherically-symmetric ionic species are of limited validity. Simulations on molten AgCl are rare due to recognised inadequacies of such potentials.

Pair-potentials have been derived, notably by Mayer [166], Bücher [167] from quantum calculations modified to fit experimental properties, and by Baetzold *et al* [156] by fitting to defect energies. A comparison of these potentials is given by Margheritis & Sinistri [165] who perform MC simulations in the liquid state using a modified Mayer model in a RIM and the so-called soft-ion model (SIM) [168]. In the SIM the dipole polarization effect is included in a non-self-consistent way. (That is, the field on the ions is due to the permanent charges only). In the RIM the polarization energy is calculated as $-\frac{1}{2}\sum_{i=1}^{N_t}\alpha^i E^{i2}$.

Costa Cabral *et al* [169, 170] have performed both MC and MD simulations in both the NVT and NpT ensembles with various potential models within an RI approximation. Some of these results will be discussed in section 7.7 where they will be compared with PIM results. It is clear, however, that the RIM gives a poor account of the melting point with simulations initiated from liquid-like configurations remaining glassy up to and including 1123K (the experimental melting point at atmospheric pressure is 728K [59]). Although Margheritis and Sinistri performed MC simulations at 728K and 1000K it is unclear from the published results whether they find these systems to be liquid-like or glassy.

As was noted in section 1.3 the RVP [15] potential has succeeded in modelling the solid-state phase transitions in silver *iodide* using effective pair-potentials containing extra-soft repulsive walls, reduced ionic charges and additional r^{-4} terms in both the Ag-I and I-I functions, crudely mimicking anionic polarization effects. HNC calculations [171] on the liquid using the RVP potential indeed gives a set of partial structure factors in which the anion-anion and cation-cation distributions are distinct in clear parallel to the AgCl experiments. A bold conjecture which might be drawn from this survey is that it is the *dipolar* polarization effects that are important in the liquid state whereas the quadrupole deformability of the silver cation is crucial in determining the *solid-state* prop-

erties.

7.4 Parameterization of the AgCl model.

7.4.1 The Dipolar Model.

As was shown in section 3.3 the polarizability of a halide anion can be related to the lattice parameter [46] via equation 3.7. For AgCl R=2.7746Å [172] giving $\alpha_{Cl^-} = 20.83au$. The anion induction damping term is estimated from the MX_2 work giving $b = 1.50au$.

Unlike the previous simulations described in this thesis the polarizability of the cation cannot be neglected. For alkali metal cations it is known that the effect of the crystalline environment on the polarizability is negligible [5]. However, the filled d-orbitals in Ag^+ are split by the crystal field causing the "in-crystal" polarizability to be greater than that of the free ion [46] ($\alpha_{Ag^+}^{FREE} = 8.26au$, $\alpha_{Ag^+}^{CRYS} = 11.76au$ (in AgF) [46]). Fowler and Pyper [46] have traced this effect back to the V_4 term (see section 1.2) in the confining potential. Refractive index measurements confirm a polarizability of this magnitude, a value of 13.1au [172] being deduced for Ag^+ in AgCl.

The effect of overlap on the induced cation dipoles is neglected as there are no *ab initio* calculations on which to base an estimate. The discussion of section 1.4 tells us that the overlap effect on the cation dipoles would tend to *reinforce* that induced by the coulombic field, so the calculations might be expected to *underestimate* the cation induction effects.

7.4.2 Including the Induced Quadrupoles.

The model derived in section 2.1.2 requires the quadrupole polarizabilities (C), dipole-dipole-quadrupole hyperpolarizabilities (B) and, in addition, an assessment of the importance of overlap effects at the quadrupole level in the same way as in the dipolar model (see section 2.1.1).

Note that, from the outset, the quadrupole polarizability of the chloride anion is going to be neglected as it is known not to play a significant role in the alkali halide properties. A possible explanation for this will be discussed below.

Quadrupole Polarizabilities.

Quadrupole polarizabilities are available for the *free* Ag^+ ion from

- McEachran *et al* [173] present coupled Hartree-Fock (CHF) calculations on a range of $3d^{10}$ and $4d^{10}$ cations and find $C_{Ag^+} = 21.49au$.
- Mahan [4] gives values based on the Sternheimer method [174] using local density functional techniques to model exchange and correlation effects. This gives $C_{Ag^+} = 32.29au$. Fowler and Pyper [46] note that the Mahan method gives consistently higher *dipole* polarizabilities than the CHF methods for a variety of cations and inert gases. Indeed, Mahan gives $\alpha_{Ag^+} = 10.123au$ as opposed to $\alpha_{Ag^+} = 8.28au$ [173], and 8.26au [46], the latter two both from CHF calculations. It is possible that the increase is due to the inclusion of correlation effects in the density functional calculations.

Ab initio calculations to determine the crystal field effects on the quadrupole polarizability are not available. The dominant transition governing the magnitude of the *dipole* polarizability is 4d↔5p. For the quadrupole polarizability, it is 4d↔5s. The energy between the 4d and 5s states is much less than between the 4d and 5p. Hence, the effect of the crystal field in splitting the d-orbitals will influence the d↔s more than the d↔p. Thus, although it is impossible to determine the magnitude without detailed quantum calculations it is possible to speculate that the quadrupole polarizability will be affected *more* by crystal field effects than the dipole analogue.

Dipole-dipole-quadrupole Hyperpolarizabilities.

The value of B is not known and so an estimate must be sought. The *ab initio* data available is limited to the CHF work of Kelly and Fowler (KF) [175] for the anions in the five crystals LiH, LiF, NaF, MgO and MgS, and the free F^- anion plus the density-functional based techniques of Mahan [4, 176]. Table 7.2 lists the KF values along with some possible approximate relationships between α, B and C. Table 7.3 lists the Mahan values for the alkali chlorides. Two possible relationships between the polarizabilities can be identified:

- $B \simeq -6C$,

- $B \simeq 2.5\alpha\sqrt{C}$.

The latter expression contains the same combination of transition dipole and transition quadrupole matrix elements as the perturbation expression for B.

System	α/au	C/au	B/au	$-\frac{B}{C}$	$-\frac{B}{\alpha\sqrt{C}}$	$-\frac{B}{\alpha^2 C}$
LiF	6.18	9.7	-48.4	4.99	2.515	0.130
NaF	7.57	11.6	-71.5	6.16	2.773	0.108
MgO	11.18	26	-161	6.19	2.825	0.050
MgS	29.55	106	-657	6.19	2.160	0.007
LiH	11.54	18.6	-214.5	11.53	4.311	0.087
F^-	10.65	38.3	-560	14.61	4.475	0.129

TABLE 7.2: *CHF anion polarizabilities due to Kelly and Fowler [175] with possible approximate relationships between the three.*

System	α/au	C/au	B/au	$-\frac{B}{C}$	$-\frac{B}{\alpha\sqrt{C}}$	$-\frac{B}{\alpha^2 C}$
LiCl	23.214	91.093	-365.35	4.01	1.65	0.0074
NaCl	24.429	100.974	-551.30	5.46	2.25	0.0091
KCl	25.239	107.963	-682.56	6.32	2.60	0.0099
RbCl	25.576	111.095	-796.3	7.17	2.95	0.0110

TABLE 7.3: *Anion polarizabilities due to Mahan (B from [176], C and α from [4]) with possible approximate relationships between the three.*

Overlap Effects.

Information on the short-range damping of induced quadrupoles comes from the *ab initio* data of Fowler and Madden [16] for LiF. Table 7.4 gives a single component of the induced quadrupole on the anion for four different first shell distortions. Thus, the actual quadrupole moment induced is an order of magnitude *smaller* than that predicted by the asymptotic model and has the *opposite* sign. For the induced dipoles it has already been shown how the overlap-induced terms *oppose* those induced by the coulombic field but leave a term of the same sign as that induced by the coulombic field. It is apparent that this effect is even

Configuration	θ_{ZZ}^{ANI}	θ_{ZZ}^{SR}	θ_{ZZ}^{CLUS}
1	$1.857e^{-2}$	$-2.008e^{-2}$	$-1.515e^{-3}$
2	$9.17e^{-3}$	$-9.91e^{-3}$	$-7.42e^{-4}$
3	$3.620e^{-2}$	$-3.891e^{-2}$	$-2.709e^{-3}$
4	$1.762e^{-2}$	$-1.891e^{-2}$	$-1.294e^{-3}$

TABLE 7.4: *The calculated* ab initio *anion ZZ-component of the induced quadrupole moment for four different first cation shell distortions from reference [16].* θ^{ANI} *is the coulombic (asymptotic) moment,* θ^{SR} *is the short-range effect, and* θ^{CLUS} *is the sum of the two.*

greater for the induced quadrupoles, the short-range term effectively cancelling that induced by the coulombic field gradient.

In simulating AgCl the quadrupole on the anion will be neglected due to this effective cancellation and, on more pragmatic grounds, because it is the cation that is the difference between AgCl and the alkali chlorides.

In order to allow for the possible overlap effects on the induced cation quadrupole in the crystalline environment, several enhanced values for the quadrupole polarizability will be used.

7.5 Overview of the Simulations.

The objective is to demonstrate how the inclusion of the additional *cation* induced moments affects both the liquid and solid state properties with respect to the alkali halides.

In addition to the RIM the following models are considered:

- PIM1 - Cl^- only considered polarizable, in effect, the Ag^+ is treated as an alkali ion.
- PIM2 - both species are considered polarizable at a *dipolar* level.
- PIM-QA - both species are considered as dipolar polarizable with induced quadrupoles on Ag^+ also considered.

Generally, systems with 216 ions in total are used. However, limited additional calculations are performed on 512 ion systems in order to assess possible system-size effects and to generate more points on the phonon dispersion curves.

Table 7.5 lists typical runtimes per MD time step for the PIM-QA model. There is a 5.2 increase in time required in going from the 216 ion cell to the next possible size of 512 ions.

System Size	Runtime/s
216	3.97
512	20.58

TABLE 7.5: *System sizes and run times per MD time step for the PIM-QA model used in the AgCl crystal simulations.*

7.6 The Crystal.

7.6.1 Simulation Details.

The reference pair-potential model chosen is that due to Mayer [166]. Table 7.6 gives the potential parameters. Although by far the oldest data set, the Mayer

Ion-pair	a^{ij}/au	B^{ij}/aeu	C_6^{ij}/au
Ag-Ag	1.5346	20.6375	62.23
Ag-Cl	2.0373	309.6509	92.97
Cl-Cl	1.5346	102.9876	138.90

TABLE 7.6: *AgCl potential parameters from ref. [166].*

parameters were derived in line with the thinking in chapter 3, being fitted to perfect crystal properties. More recent fits [160, 167] have included properties such as defect energies and phonon frequencies. The unphysical dispersion parameters obtained seem to indicate that physics which becomes important in the distorted crystals is missing from these models and is somehow being represented by greatly enhanced dispersion effects. Table 7.7 lists the three dipole-dipole dispersion coefficients for the three potential models plus the *ab initio* value for C_6^{AgAg} [8] (in AgF). Comparison of the C_6^{AgAg} values and the C_6^{ClCl} with the typical alkali halide values of table 4.7 shows that only the Mayer terms seem physically reasonable for both C_6^{AgAg} and C_6^{ClCl}.

C_6^{ClCl}/au	C_6^{AgCl}/au	C_6^{AgAg}/au	Reference
138.90	92.97	62.23	[166]
810	412	210	[167]
125.35	367.68	375.00	[160]
-	-	73.85	[8]

TABLE 7.7: *AgCl C_6 dispersion coefficients for three potential models with an* ab initio *value for comparison.*

The phonon frequencies are calculated from peaks in the Fourier transforms of the longitudinal and transverse charge and mass current correlation functions corresponding to the optic and acoustic modes respectively. Thus, the optic modes are obtained from

$$C_{XX}^{LO}(\mathbf{k},t) = \left\langle \left(\sum_{j=1}^{N_t} -X^j(t) i\mathbf{k}.\mathbf{v}^j(t) e^{-i\mathbf{k}.\mathbf{r}^j(t)} \right) . \left(\sum_{l=1}^{N_t} X^l(t) i\mathbf{k}.\mathbf{v}^l(t) e^{i\mathbf{k}.\mathbf{r}^l(t)} \right) \right\rangle \tag{7.1}$$

$$C_{XX}^{TO}(\mathbf{k},t) = \left\langle \left(\sum_{j=1}^{N_t} -X^j(t) i\mathbf{k} \wedge \mathbf{v}^j(t) e^{-i\mathbf{k}.\mathbf{r}^j(t)} \right) . \left(\sum_{l=1}^{N_t} X^l(t) i\mathbf{k} \wedge \mathbf{v}^l(t) e^{i\mathbf{k}.\mathbf{r}^l(t)} \right) \right\rangle , \tag{7.2}$$

where v^j is the velocity of ion j and $X^j(t)$ represents the charge of species j. Equivalent expressions with X^j as the ion mass give the acoustic frequencies.

Table 7.8 lists the details of the phonon dispersion curve production runs for the PIM-QA runs. The quadrupole polarizability is varied from the value of

C/au	Run length/ps	Correlation function length/ps
21.49	7.26	0.73
42.98	12.09	0.73
60.0	12.09	0.97

TABLE 7.8: *Run lengths and correlation function lengths for the PIM-QA simulations.*

McEachran [173] (21.49au) to 60au (twice as big as Mahan's value for the free cation). Such an enhancement could be attributed to the crystal field and/or overlap effects, as discussed above. The B-term is scaled according to $B = -6C$. The simulation density in all cases is 5.69077gcm^{-3} [172] corresponding to an experimental temperature of 100K.

7.6.2 Results.

Optic Modes.

Tables 7.9 and 7.10 lists the phonon frequencies along three high symmetry directions in the Brillouin zone for the longitudinal and transverse waves respectively, along with the experimental values [155]. Figure 7.2 shows the LO and TO frequencies for the RIM, PIM1, PIM2 and experiment respectively. It is evident that each additional polarization term improves the agreement with experiment.

k	RIM	PIM1	PIM2	Experiment
100	7.44	6.89	5.24	5.3
200	7.03	6.61	5.79	5.7
300	7.03	6.61	5.51	5.9
220	6.20	5.24	5.79	5.2
110	7.44	5.59	6.06	5.7
111	7.44	6.89	6.34	6.1

TABLE 7.9: *Longitudinal optic mode frequencies for the RIM, PIM1 and PIM2 for 216 ion systems compared with experiment [155]. The k-vectors (mnp) are of moduli $\frac{2\pi}{L}$ where L is the simulation cell length.*

k	RIM	PIM1	PIM2	Experiment
100	4.96	4.69	4.13	3.8
200	5.37	4.69	4.69	4.4
300	5.37	5.24	4.69	4.7
220	6.20 / 2.48	6.61 / 2.48	4.41 / 2.20	5.3 / 3.3
110	4.96 / 2.07	4.69 / 2.20	4.41 / 1.65	4.7 / 1.8
111	4.54	4.68	4.41	3.2

TABLE 7.10: *As table 7.9 but for the transverse optic modes.*

- **RIM $\longrightarrow$ PIM1**: The observed behavior is analogous to that observed in the alkali halides [13, 14] (compare with figure 7.1). The frequencies of the modes are reduced as the chloride polarizability is added. However, the

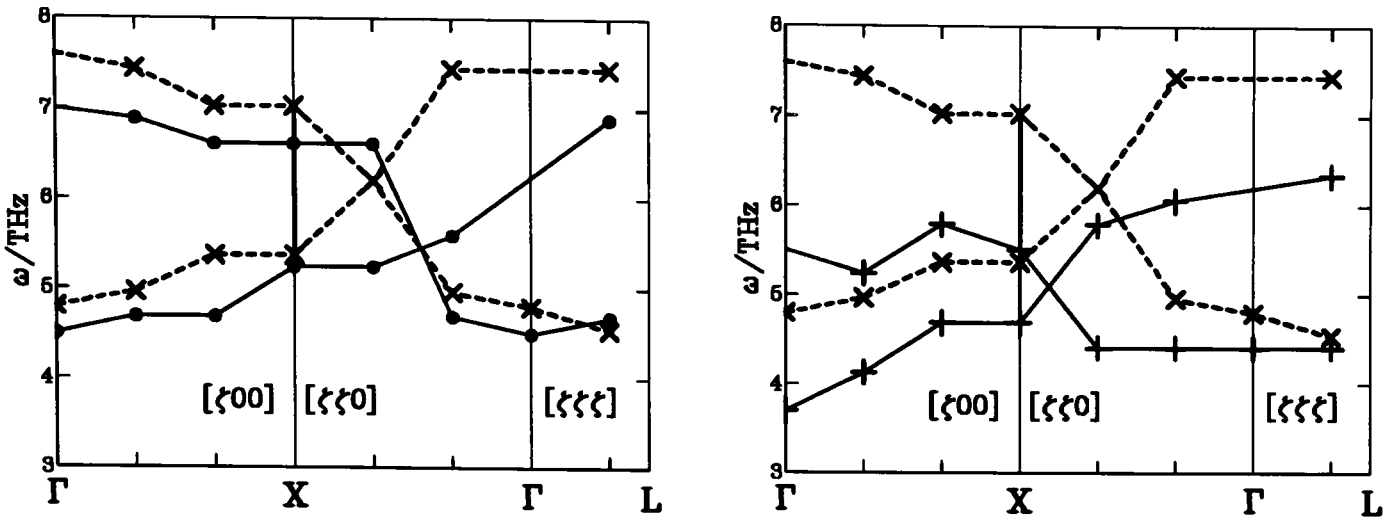


FIGURE 7.2: *Longitudinal and transverse optic phonon dispersion curves for AgCl. Left* - × - *RIM,* ○ - *PIM1, right* - × - *RIM,* + - *PIM2.*

shape of the curves is alkali halide-like and so is in poor agreement with experiment.

- **PIM1 ⟶ PIM2**: The addition of the cation *dipole* polarizability greatly improves the optic mode frequencies with respect to experiment. This reduction is consistent with the overall increase in the (optical) dielectric permittivity. Note, however, that the TO [111] phonon remains at too high a frequency, barely shifted from the RIM value.

- **PIM2 ⟶ PIM-QA**: Tables 7.11 and 7.12 lists the frequencies of the optical modes for the three quadrupole models studied. The best agreement with experiment is seen for C=60au.

Fischer *et al* [23, 162] have shown how the quadrupolar Ag^+ distortions affect the TO(L) mode in particular. Table 7.13 lists the frequencies of the [111] mode (i.e two thirds from the Σ- to L-point) along with the experimental value. The effect of increasing the quadrupole polarizability of the silver cation is to lower this frequency towards the experimental value.

Acoustic Modes.

The polarization effects do little to improve the agreement with experiment. Tables 7.14 and 7.15 list the acoustic mode frequencies for all the models. Again, as for the dipole polarizable systems, there is relatively little effect as

	PIM-QA			
k	22	43	60	Experiment
100	5.24	5.88	5.58	5.3
200	5.41	5.51	5.78	5.7
300	4.89	5.14	5.86	5.9
220	5.79	5.50	5.17	5.2
110	6.06	5.91	5.78	5.7
111	6.06	5.88	6.20	6.1

TABLE 7.11: *Longitudinal optic mode frequencies for the three PIM-QA models compared with experiment [155].*

	PIM-QA			
k	22	43	60	Experiment
100	4.41	4.41	3.93	3.8
200	4.69	4.41	4.30	4.4
300	4.69	4.78	4.96	4.7
220	4.41 / 2.20	4.78 / 2.76	4.96 / 3.10	5.3 / 3.3
110	4.13 / 1.10	4.41 / 1.65	3.93 / 1.86	4.3 / 1.8
111	4.13	3.67	3.31	3.2

TABLE 7.12: *As table 7.11 but for the transverse optic modes.*

Model	$\nu_{[111]}$/THz
RIM	4.54
PIM1	4.68
PIM2	4.41
PIM-QA22	4.13
PIM-QA43	3.67
PIM-QA60	3.31
Experiment	3.2

TABLE 7.13: *Frequency of the TO mode at the [111]-point in the 216-ion systems studied. The trend towards the experimental value as the quadrupole polarizability of the cation is increased is clear.*

the quadrupole is increased except that there is a *slight* improvement in the transverse mode for the PIM-QA with C=60au.

	RIM	PIM1	PIM2	PIM-QA			
k				22	43	60	Experiment
100	2.07	2.20	2.20	2.20	2.20	2.07	1.85
200	3.31	3.03	2.76	3.31	3.31	3.31	2.3
300	3.31	2.75	2.48	3.20	3.20	3.20	1.6
220	3.31	3.03	3.03	3.03	2.94	3.11	2.3
110	2.48	2.02	2.48	2.48	2.57	2.69	1.8
111	3.31	2.20	3.03	3.03	2.94	3.10	2.8

TABLE 7.14: *Longitudinal acoustic mode frequencies for all models studied compared with experiment [155].*

	RIM	PIM1	PIM2	PIM-QA			
k				22	43	60	Expt.
100	1.24	1.10	1.10	1.10	1.01	0.83	0.6
200	1.65	1.65	1.65	1.65	1.65	1.65	0.9
300	2.07	1.93	1.84	1.93	1.84	1.86	1.0
220	2.89	2.40	2.20	2.20	1.65	1.65	1.4
110	1.65	2.20	1.45	1.47	1.24	1.24	0.8
111	2.07	1.93	1.93	1.93	1.84	1.71	1.6

TABLE 7.15: *As table 7.14 but for the transverse acoustic modes.*

Larger System Simulations.

In addition to the series of 216 ion runs analogous simulations have been performed on 512-ion systems (the next size up allowed by the imposition of the cubic periodic boundary conditions) for the PIM2 and PIM-QA60 models only.

Tables 7.16 and 7.17 list the frequencies at each k value for these larger systems. The results are consistent with the smaller cell results. Note that the [222] value now corresponds directly to the L-point and confirms the softening effect of the increased cation quadrupole polarizability.

	LO		TO	
k	PIM2	PIM-QA	PIM2	PIM-QA
100	5.51	5.72	4.13	3.80
200	5.79	5.45	4.41	4.05
300	5.79	5.78	4.69	4.52
400	5.51	5.86	4.85	4.96
330	5.51	5.10	4.69	5.05
220	6.06	5.51	4.41	4.62
110	6.02	5.78	4.13	4.01
111	6.34	6.05	4.41	3.50
222	6.61	6.20	4.13	3.02

TABLE 7.16: *Optic mode frequencies for the 512-ion systems. Note here that the simulation cell size is greater than in the 216-ion systems and so, for example, the 100 modes are not equivalent in the two models.*

	LA		TA	
k	PIM2	PIM-QA	PIM2	PIM-QA
100	1.65	1.88	0.83	0.73
200	2.76	2.94	1.38	1.47
300	2.76	3.31	1.65	1.84
400	2.48	3.20	1.84	1.86
330	2.76	2.94	2.20	2.20
220	3.31	3.31	2.20	2.20
110	2.20	2.20	1.10	1.10
111	2.48	2.57	1.65	1.50
222	3.58	3.67	2.20	2.57

TABLE 7.17: *Acoustic mode frequencies for the 512-ion systems.*

7.6.3 Summary and Comments.

Figure 7.3 shows the optical phonon dispersion curves for the PIM-QA model with C=60 taken from both the 216 and 512 ion runs, along with the experimental curves [155] for comparison. For both the longitudinal and transverse

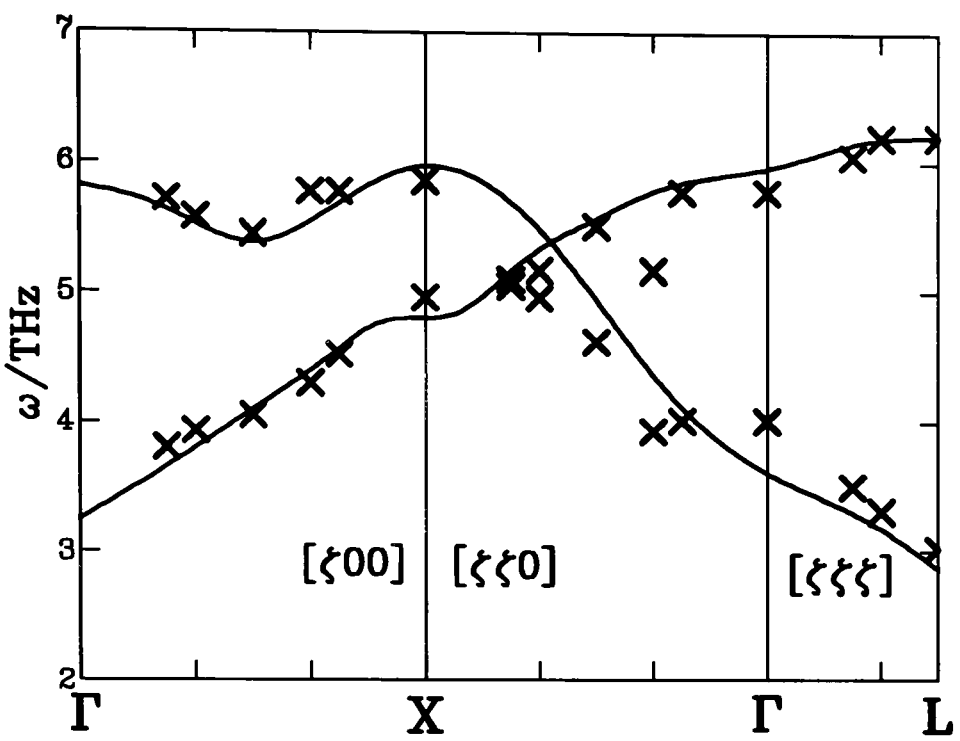


FIGURE 7.3: *LO and TO modes for AgCl using the PIM-QA60 model. The solid lines represent the experimental data from ref. [155].*

optical modes the effect of adding each polarization term is clear:

- The Cl^- dipole polarizability improves the LO-TO splitting, as in the LiF simulations, but does not reduce the mode frequencies enough.
- The Ag^+ dipole polarizability improves the LO-TO splitting yet further but fails to generate the experimentally observed soft TO(L)-branch.
- The Ag^+ quadrupole polarizability retains the good agreement of the fully dipole polarizable model *and* accounts for the soft TO(L)-mode [23, 162].

The acoustic modes are less satisfactory in every model studied, indicating a universal deficiency in the potential model. The exception is in the [111]-direction where the overall agreement is good. In addition to a reappraisal of the short-range pair-potential model, further many-body effects may be required in order to accurately model the acoustic modes.

7.7 The Molten State.

7.7.1 Simulation Details.

Table 7.18 gives the system densities and production runtimes at each temperature.

		Runtime/ps		
T/K	ρ/gcm^{-3}	PIM1	PIM2	PIM-QA
728	4.8749	10.88	-	-
783	4.7868	10.88	7.26	24.19
1000	4.6382	21.77	-	-
1123	4.4850	42.09	9.68	15.12
1500	4.2030	10.88	4.84	9.07
1700	3.9542	10.88	-	-

TABLE 7.18: *Experimental molten AgCl densities and run times for the simulations performed.*

The PIM-QA model uses a cation with a quadrupole polarizability of 43au, intermediate between the isolated ion (22au [173]) and the value which produces the best account of the optic phonons (60au).

The low temperature RI simulations were performed by starting from a higher temperature (liquid) system and reducing the temperature.

Energetics.

Table 7.19 shows the internal energy over the range of statepoints investigated in the PIM1, PIM2 and PIM-QA models along with the RIM of reference [165]. In general, the PIM energies are consistently more negative than the corresponding RIM values. This corresponds to a *lowering* of the melting point via a greater lowering of the liquid energies with respect to those of the crystal owing to the greater induction effects. This is consistent with previous alkali halide simulation work [14] but the effect in AgCl is larger due to the additional cation induced moments.

Tables 7.20 and 7.21 show the dipole polarization energies for the Cl^- and Ag^+ subsystems respectively. Table 7.22 gives the *total* dipole polarization energy (i.e the sum of the contributions from the two ionic subsystems) along with

the RIM and SIM results of Margheritis and Sinistri (MS) [165, 168]. At first glance it would appear that the different models produce similar polarization energies *despite* the clear criticism of the MS calculations. However, further consideration of the *individual* energies for the two subsystems tells a different story. At each of the three temperatures the polarization energy of each subsystem is comparable in the PIM simulations. This will not be the case in either the RIM or SIM where this energy is given by $-\frac{1}{2}\sum_{i=1}^{N_t}\alpha^i E^{i\,2}$. In these cases the fields acting on the anions and cations will be of comparable magnitudes as they are simply the effect of the topological disorder of a system of charges of equal magnitude; that is, they contain no dipole-induced-dipole (and higher order) terms. The MS model uses polarizabilities of 11.27au and 22.20au for the silver and chloride respectively and so the polarization energy of the anion subsystem will be around twice that of the cation. In the PIM the additional overlap effect on the anion dipoles acts to damp the coulombic effects thus making the anion polarization energy comparable with that of the cation subsystem. If this effect were in place in the MS RIM and SIM then the polarization energies would be *less* than that in the PIM.

Table 7.23 gives all the polarization energies from equation 2.26 for the PIM-QA model. Note that the *quadrupole* polarization energy of the Ag^+ subsystem is comparable to the *dipole* energy of the same subsystem. Thus, in energetic terms at least, the quadrupole polarization of the Ag^+ cation is as important as the dipole distortion. However, the total polarization energy is about the same. Also note that the dipole-quadrupole cross term (in k_2) and the higher order dipole term (in k_4) are small compared with the k_1 and k_3 terms.

T/K	RIM	PIM1	PIM2	PIM-QA
728	-776.1	-800.9	-	-
783	-	-794.0	-794.7	-791.3
1000	-755.6	-778.5	-	-
1123	-	-769.8	-780.0	-779.8
1500	-718.4	-746.2	-753.8	-740.4
1700	-	-732.5	-	-

TABLE 7.19: *Internal energies for the PIM1, PIM2 and PIM-QA models.*

T/K	PIM1	PIM2	PIM-QA
	$kJmol^{-1}$		
728	-3.40	-	-
783	-3.82	-6.64	-6.67
1000	-4.96	-	-
1123	-5.48	-7.81	-8.11
1500	-6.68	-12.66	-10.22
1700	-7.52	-	-

TABLE 7.20: *Dipole polarization energies for the Cl^- subsystem.*

T/K	PIM2	PIM-QA
	$kJmol^{-1}$	
783	-5.92	-5.12
1123	-6.89	-7.28
1500	-11.78	-9.39

TABLE 7.21: *Dipole polarization energies for the Ag^+ subsystem.*

T/K	PIM2	PIM-QA	SIM	RIM
	$kJmol^{-1}$			
728	-	-	-15.06	-13.39
783	-12.56	-11.79	-	-
1000	-	-	-17.58	-17.58
1123	-14.70	-15.39	-	-
1500	-24.44	-19.61	-22.59	-24.69

TABLE 7.22: Total *dipole polarization energies for the PIM2, PIM-QA, and the MS SIM and RIM.*

T/K	$\sum_{i=1}^{N_{Cl}} k_1\mu^{i2}$	$\sum_{i=1}^{N_{Ag}} k_1\mu^{i2}$	$\sum_{i=1}^{N_{Ag}} k_3\theta^{i2}$	$\sum_{i=1}^{N_{Ag}} k_2\mu^{i2}\theta^{i}$	$\sum_{i=1}^{N_{Cl}} k_4\mu^{i4}$	$\sum_{i=1}^{N_{Ag}} k_4\mu^{i4}$
	$kJmol^{-1}$					
783	5.12	6.67	5.60	-4.56×10^{-2}	1.30×10^{-2}	5.82×10^{-4}
1123	7.27	8.11	7.80	-8.22×10^{-2}	2.64×10^{-2}	1.41×10^{-3}
1500	9.39	10.22	11.31	-6.32×10^{-2}	2.20×10^{-2}	1.34×10^{-3}

TABLE 7.23: *Energies of each polarization term in equation 2.26 for the PIM-QA model.*

Diffusion Coefficients.

Figures 7.4a and 7.4b show the *mean square displacement* (MSD) for the Cl^- and Ag^+ respectively at three temperatures. The MSD is defined as

$$M^{\beta} = \frac{1}{N}\sum_{i=1}^{N^{\beta}} \left\langle \mid \mathbf{r}^i(t) - \mathbf{r}^i(0) \mid^2 \right\rangle, \tag{7.3}$$

where β represents the anion or cation. At long times, t, the *Einstein relation* can be used to give the diffusion coefficient,

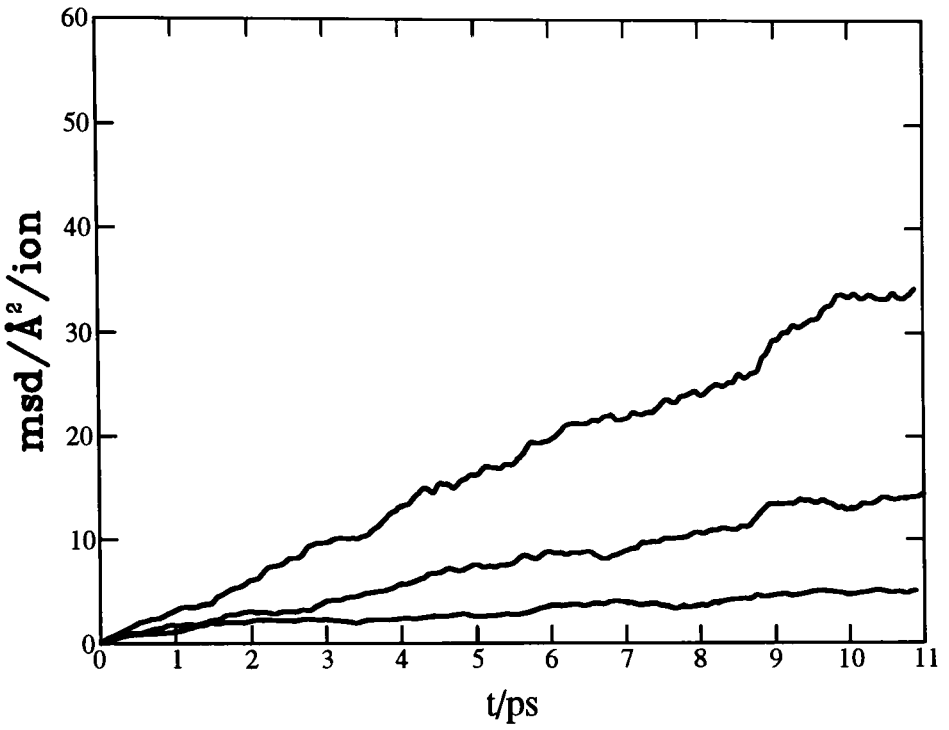
$$D^{\beta} = \frac{M^{\beta}}{6t}. \tag{7.4}$$

Table 7.24 gives the Cl^- and Ag^+ diffusion coefficients at five temperatures from 783K to 1700K for both the RIM and PIM1.

T/K	Cl^-		Ag^+	
	RIM	PIM1	RIM	PIM1
	$\times10^{-5}cm^2s^{-1}$			
783	0	0.86	0	1.03
1000	0	1.35	0	1.50
1123	0	2.49	0	3.62
1500	4.60	5.33	5.02	8.70
1700	6.06	8.50	7.29	11.78

TABLE 7.24: *Diffusion coefficients for the RIM and PIM1 for lq. AgCl.*

The outstanding features are



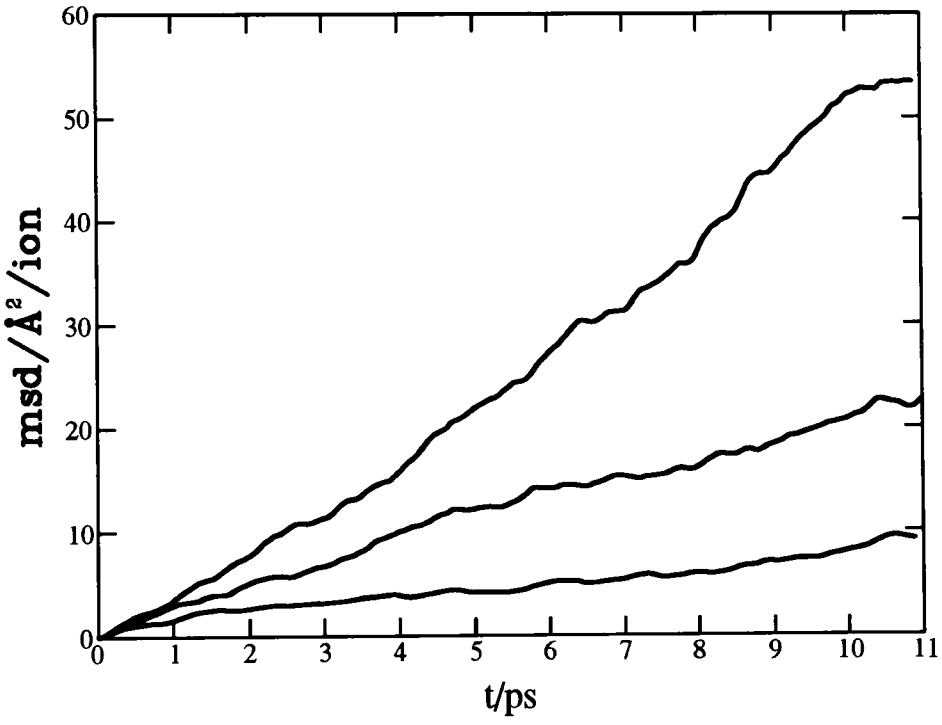


FIGURE 7.4: *Mean square displacements for, top - Cl^- and bottom - Ag^+ at three temperatures. From top to bottom in each figure 1500K, 1123K and 783K.*

- Both D_+ and D_- are zero at $\leq 1123K$ in the RIM simulations. The melting point of AgCl is 728K at atmospheric pressure. It would appear that all the RIM potentials produce arrested (glassy) states well above the normal melting point.

- Both D_+ and D_- are non-zero for the PIM1 model above the experimental melting point.

- D_+ is enhanced in the PIM with respect to the RIM at high temperature, where the latter gives a liquid. D_- is also enhanced but to a lesser extent.

Table 7.25 lists the diffusion coefficients for the PIM-QA model. There is very little difference between these and the PIM1 values indicating that it is the anion dipole polarization that is critical in allowing the liquid-like behaviour down to the melting point.

T/K	Cl^-	Ag^+
	$\times 10^{-5} cm^2 s^{-1}$	
783	0.87	0.97
1123	2.60	3.46
1500	6.22	8.75

TABLE 7.25: *Diffusion coefficients for PIM-QA for liquid AgCl.*

Again, the comparison with simulated alkali halide properties is of interest. Table 7.26 lists the two diffusion coefficients for LiF [14], LiCl [177] and AgCl at similar temperatures ΔT above the experimental melting point. Both the lithium salts show typically liquid-like values for the diffusion coefficients whilst the AgCl ions move more slowly, that is, the AgCl is *more viscous.*

The results at high temperature, where a direct comparison with the RIM can be made, suggest that the inclusion of the polarization effects substantially lowers the energy barrier to diffusion, especially for the cations. An approximate activation energy can be obtained from an Arrhenius analysis of the temperature dependence of the diffusion coefficient. These energies are given in table 7.27 (derived from figure 7.5).

This can be understood by considering the diffusion process itself, specifically a cation breaking out of a first coordination shell of anions. Figure 7.6 shows

System	ΔT/K	D_-	D_+
		$\times 10^{-5} cm^2 s^{-1}$	
LiF	30	6.3	8.2
LiCl	53	4.8	8.1
AgCl	55	0.9	1.0

TABLE 7.26: *Simulation diffusion coefficients at temperatures ΔT above the experimental melting point.*

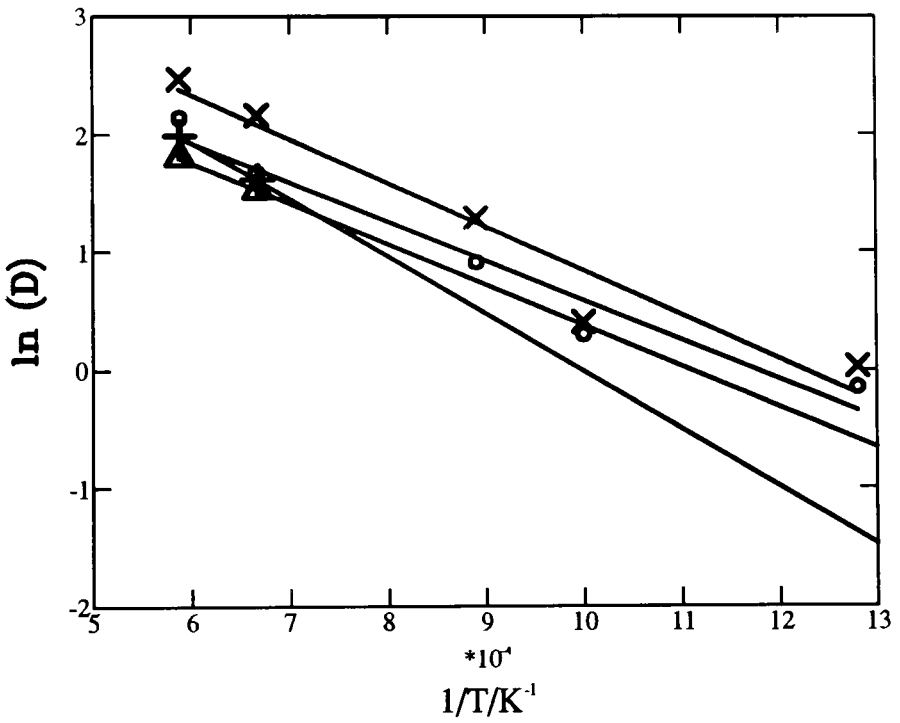


FIGURE 7.5: *Arrhenius plot of ln D v. 1/T. Key:* × - $D^{pim}_{Ag^+}$ ○ - $D^{pim}_{Cl^-}$ + - $D^{rim}_{Ag^+}$ △ - $D^{rim}_{Cl^-}$. *The lines are the least-squares fits.*

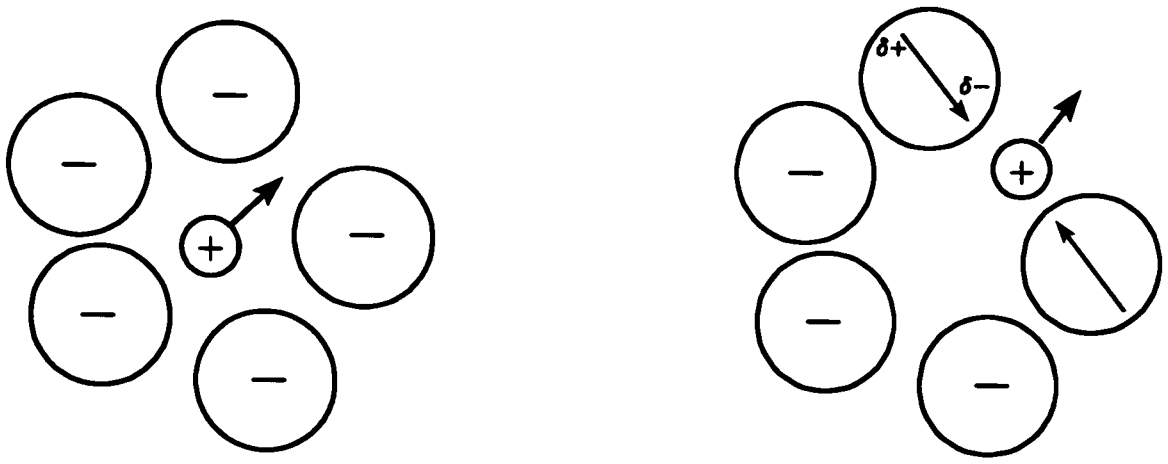


FIGURE 7.6: *Schematic representation of the role of induced anion dipoles in lowering the activation barrier associated with cation diffusion.*

such a diffusion process. The presence of the anion polarization has the effect of lowering the energy of the activation barrier by allowing the diffusing cation to induce dipoles on the nearest anions.

Model	E_+	E_-
	/kJmol^{-1}	
RIM	40.3	28.6
PIM1	29.6	28.2

TABLE 7.27: *Approximate activation energies for single species diffusion in the two models.*

Figure 7.5 leads to some interesting speculation. If one were to join the lowest two temperature points this would indicate a *lower* activation energy for the diffusion process in this temperature range with respect to the higher temperature behaviour. It is tempting to speculate, therefore, that there is an alternative mechanism that dominates the low-temperature diffusion process, possibly linked to the low Frenkel defect formation energy discussed earlier.

Structure.

Figure 7.7 shows the radial distribution functions for molten LiF at 1170K using the PIM. Again, these curves are typical of the alkali halides (see [10]), clearly demonstrating the charge-ordered nature of these systems in the anti-phased behaviour of g_{+-} with respect to the like-ion functions. Note that g_{++}

T/K	n_{AgCl}	n_{ClCl}	n_{AgAg}
783	4.55	11.32	11.15
1123	4.24	17.70	17.36
1500	4.39	15.26	17.76
1700	4.17	16.86	16.18

TABLE 7.28: *Coordination numbers for the PIM1, calculated by integration to the first minimum in the partial rdf.*

and g_{--} are very similar.

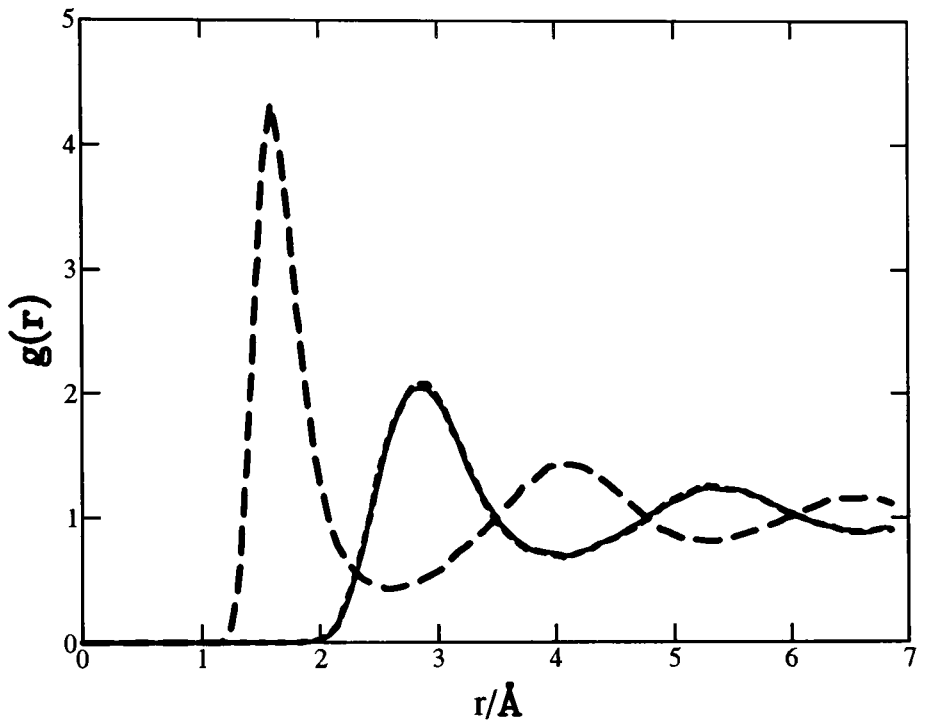


FIGURE 7.7: *Partial radial distribution functions for liquid LiF at 1170K. Key: solid line - g_{LiLi}, short-dashes - g_{FF}, long-dashes - g_{LiF}.*

Figures 7.8 to 7.10 shows three sets of rdfs for AgCl for three temperatures over the range of statepoints studied. Each rdf set contains three figures corresponding to results for the RIM, PIM1 and PIM-QA. Let us consider each temperature in turn:

- 1500K. All three curves in figure 7.8 are clearly liquid-like. The only substantial difference between the three models lies in $g_{AgAg}(r)$ which is broadened and the closest approach moves inwards as more polarization effects are included. With respect to LiF there is a pronounced shoulder in both g_{++} and g_{--} at ~ 5Å for all the models studied. No such feature

is apparent in the LiF curves. This is presumably a packing effect corresponding to the difference in radius ratios between the two systems. The principal peaks in g_{++} and g_{--} are of similar height to those in LiF but there is a greater difference between g_{++} and g_{--} in AgCl.

- 1123K. Both the PIM1 and PIM-QA curves are liquid-like with the 5Å shoulder even more prominent than in the higher temperature curves. The difference between the PIM1 and PIM-QA is again quite subtle; the $g_{AgAg}(r)$ peak *shape* is changed with a reduction in the distance of closest approach of the cations to each other when the quadrupoles are included.

  The RIM curves are clearly anomalous. Two particular features are apparent

  - *Peak heights.* The heights of both the g_{++} and g_{--} functions are around 50% higher than would be expected for a typical ionic liquid. This also applies to the longer ranged peaks. The extra height is a direct result of the arrest of diffusion processes.
  - *Fine structure.* The g_{+-} function shows fine structure that is not present in the liquid-like functions. This has the form of an additional peak at around 4.8Å. In the liquid systems this peak is "ironed-out" by the diffusion processes resulting in the classical two peak g_{+-} on the length scale of the figure.

- 783K. Again, both the PIM1 and PIM-QA curves are liquid-like with the 5Å shoulder even more prominent. The RIM curves are again "glassy" with the extra g_{+-} fine structure indicated by an arrow.

Table 7.28 gives the coordination numbers at each temperature. The number of chlorides around a silver cation remains at ~ 4 across the temperature range studied.

Figures 7.11 and 7.12 show the partial and total structure factors for the liquid at 1123K using the PIM-QA model. The partials are calculated directly from equation 4.13 and also from the Fourier transformation of the partial distribution functions (equation 5.1). The two curves are linked on the high-k side of the principal peak, with the direct calculations providing the low-k points, in order to produce a smooth function free of low-k truncation errors. The total

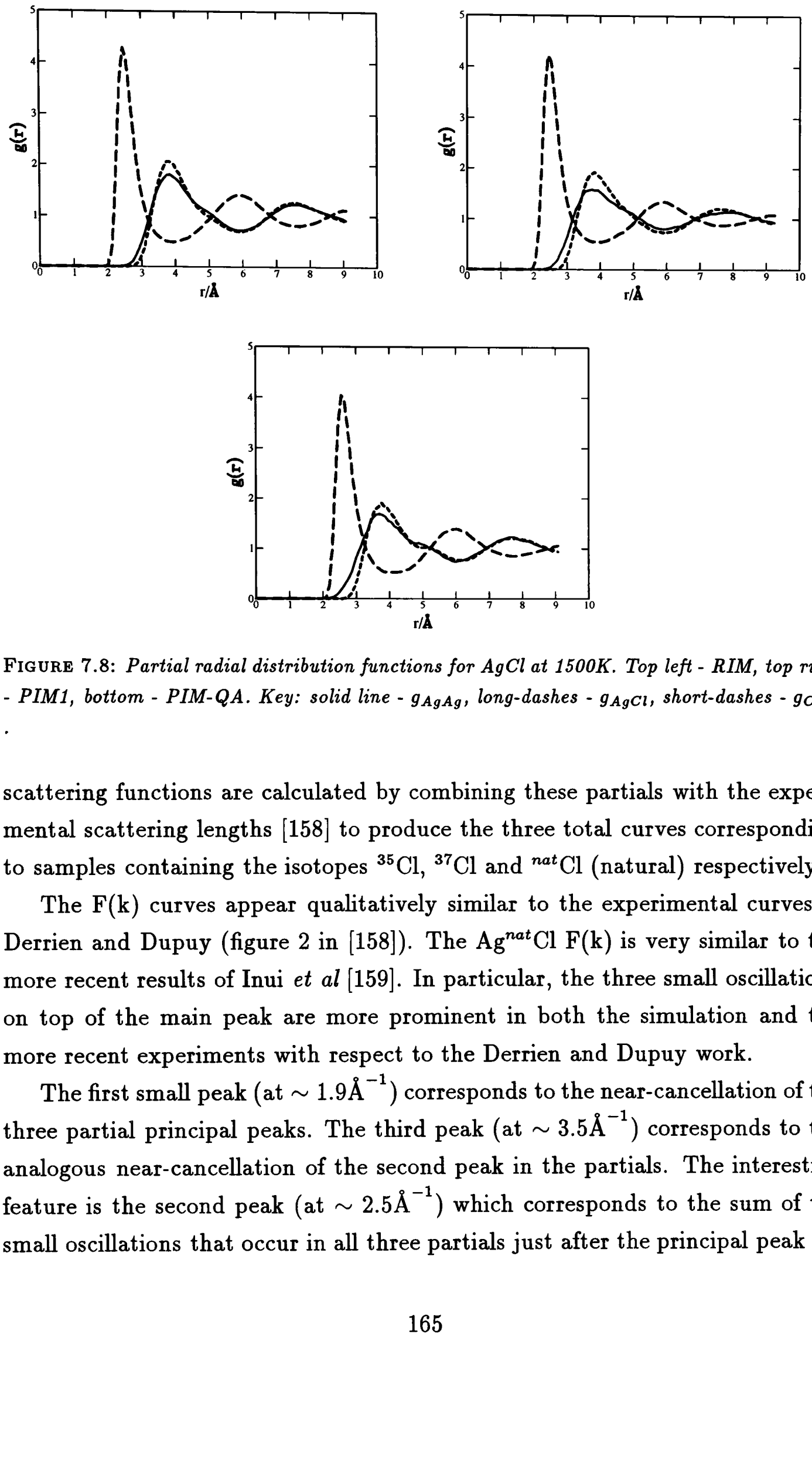


FIGURE 7.8: *Partial radial distribution functions for AgCl at 1500K. Top left - RIM, top right - PIM1, bottom - PIM-QA. Key: solid line - g_{AgAg}, long-dashes - g_{AgCl}, short-dashes - g_{ClCl}*

.

scattering functions are calculated by combining these partials with the experimental scattering lengths [158] to produce the three total curves corresponding to samples containing the isotopes ^{35}Cl, ^{37}Cl and ^{nat}Cl (natural) respectively.

The F(k) curves appear qualitatively similar to the experimental curves of Derrien and Dupuy (figure 2 in [158]). The Ag^{nat}Cl F(k) is very similar to the more recent results of Inui *et al* [159]. In particular, the three small oscillations on top of the main peak are more prominent in both the simulation and the more recent experiments with respect to the Derrien and Dupuy work.

The first small peak (at $\sim 1.9\text{Å}^{-1}$) corresponds to the near-cancellation of the three partial principal peaks. The third peak (at $\sim 3.5\text{Å}^{-1}$) corresponds to the analogous near-cancellation of the second peak in the partials. The interesting feature is the second peak (at $\sim 2.5\text{Å}^{-1}$) which corresponds to the sum of the small oscillations that occur in all three partials just after the principal peak (at

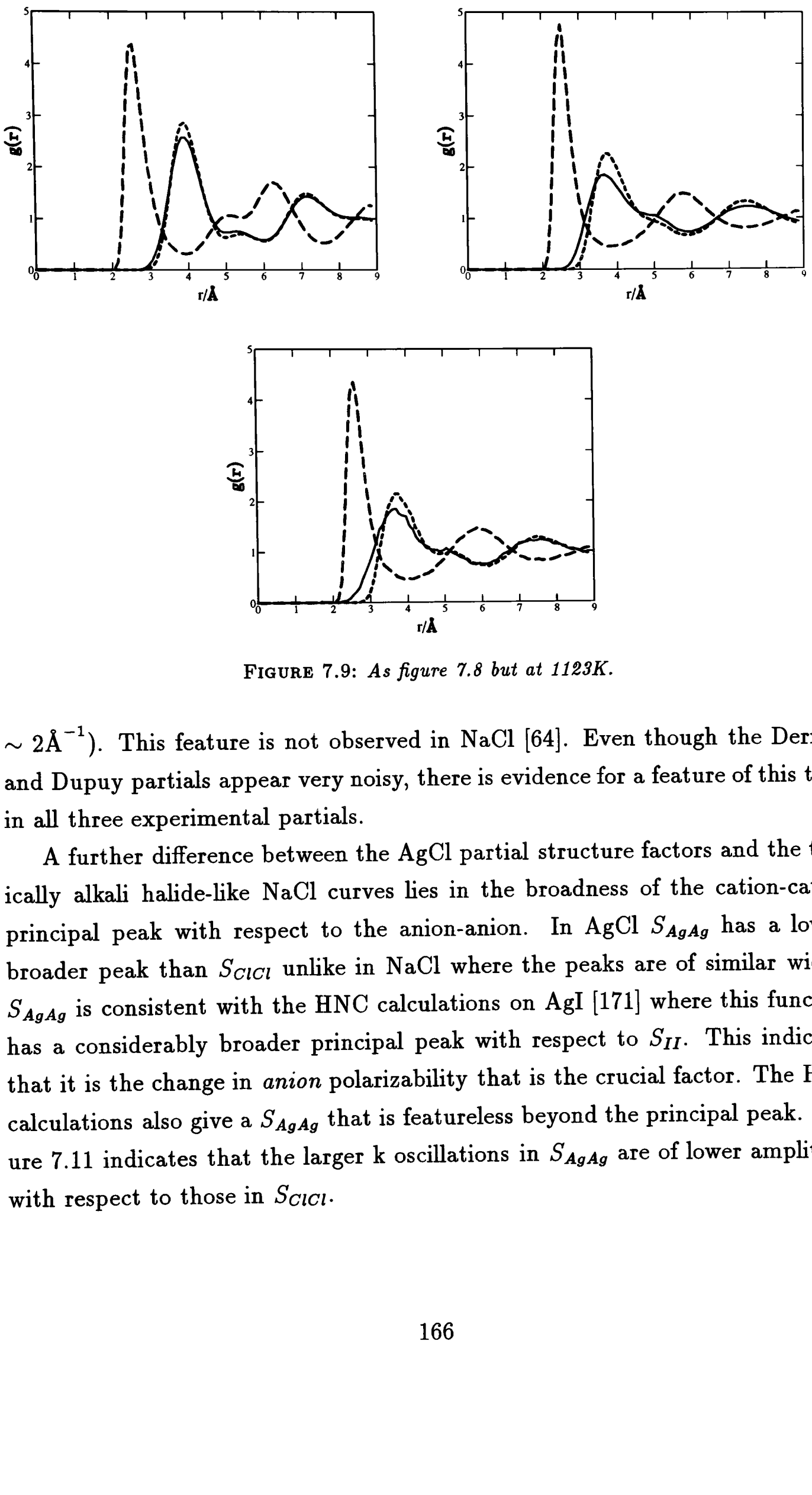


FIGURE 7.9: *As figure 7.8 but at 1123K.*

$\sim 2\text{Å}^{-1}$). This feature is not observed in NaCl [64]. Even though the Derrien and Dupuy partials appear very noisy, there is evidence for a feature of this type in all three experimental partials.

A further difference between the AgCl partial structure factors and the typically alkali halide-like NaCl curves lies in the broadness of the cation-cation principal peak with respect to the anion-anion. In AgCl S_{AgAg} has a lower, broader peak than S_{ClCl} unlike in NaCl where the peaks are of similar width. S_{AgAg} is consistent with the HNC calculations on AgI [171] where this function has a considerably broader principal peak with respect to S_{II}. This indicates that it is the change in *anion* polarizability that is the crucial factor. The HNC calculations also give a S_{AgAg} that is featureless beyond the principal peak. Figure 7.11 indicates that the larger k oscillations in S_{AgAg} are of lower amplitude with respect to those in S_{ClCl}.

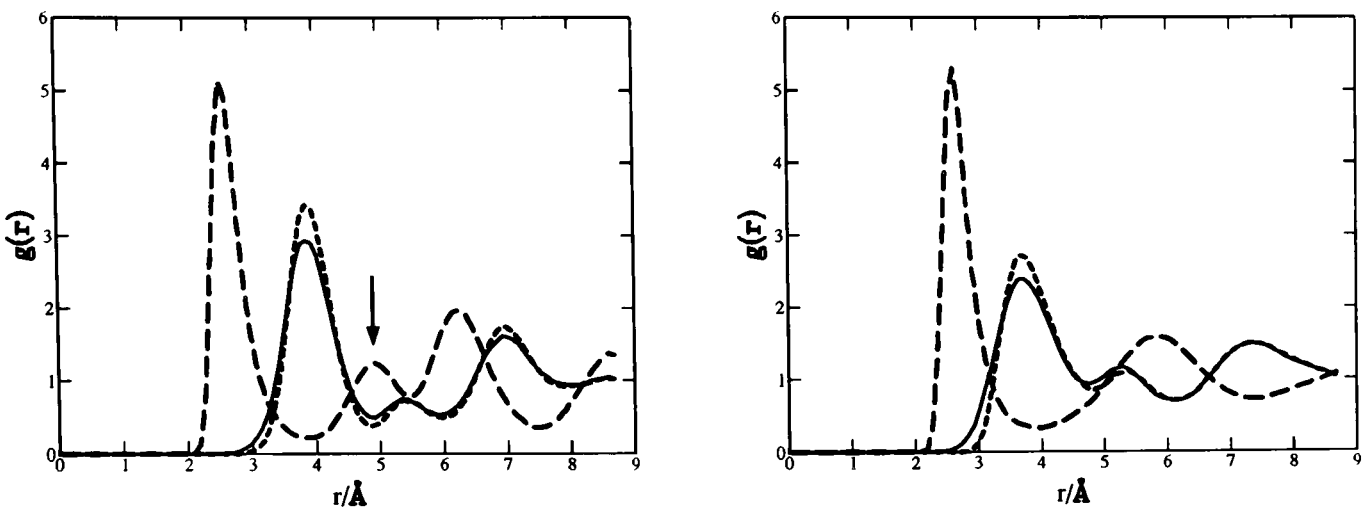


FIGURE 7.10: *As figure 7.8 but at 783K.*

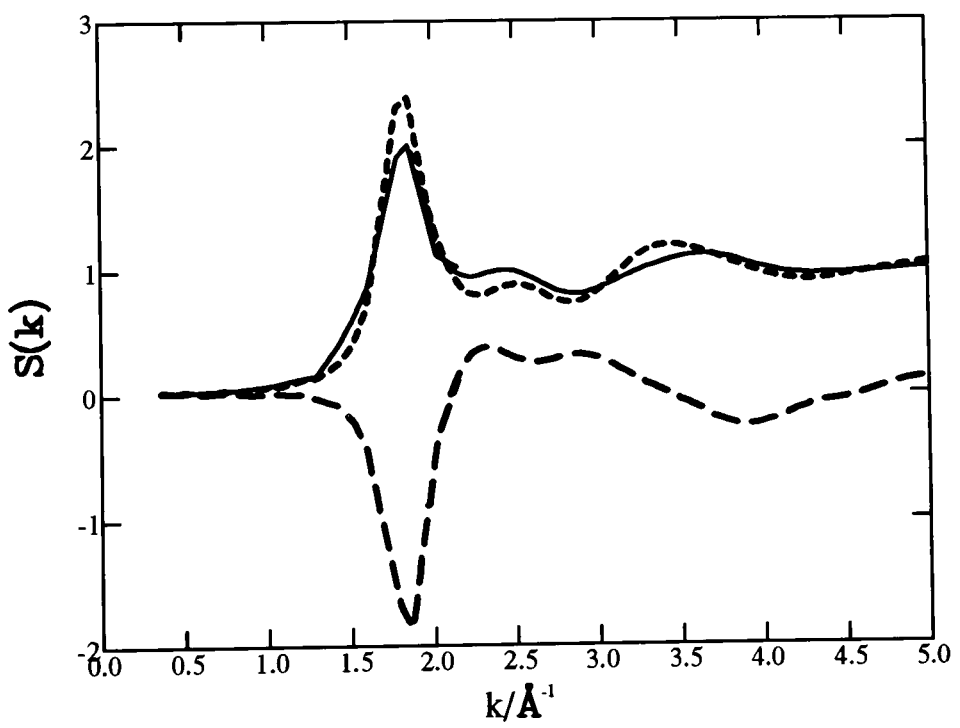


FIGURE 7.11: *Partial structure factors for AgCl at 1123K using the PIM-QA model. Key: solid-line - S_{AgAg}, long-dashes - S_{AgCl}, short-dashes - S_{ClCl}.*

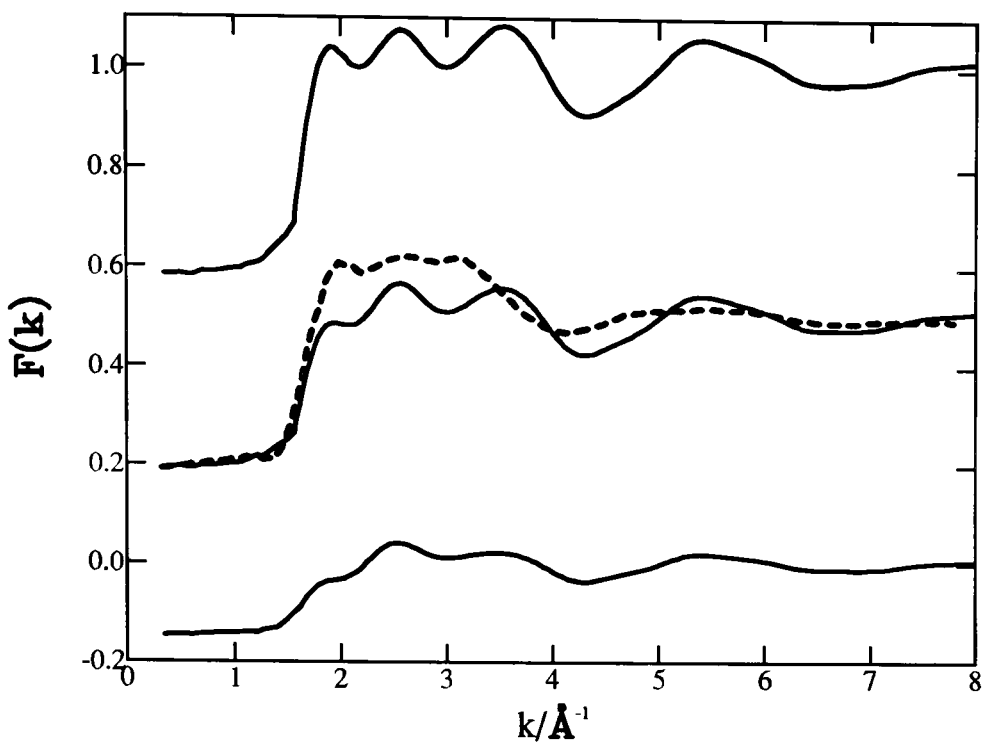


FIGURE 7.12: *Total structure factors for AgCl constructed from the partials in figure 7.11. Each successive curve is raised by 0.5 along the y-axis. The dashed line is the experimental data of Inui* et al *[159].*

7.8 The Role of Induced Quadrupoles in the Liquid.

It is clear that the role of the induced quadrupoles in the liquid phase is much more subtle than in the crystal.

In the molten state both the energetics and diffusion characteristics are virtually unaffected in going from a model which allows for anion polarization to one that allows for anion polarization and cation dipole and quadrupole effects. This conclusion is, perhaps, surprising considering the supposed importance of the cation quadrupolar deformations in explaining cation-diffusion phenomena in the solid. However, the inherent crystal symmetry allows for much smaller induced dipoles than in the liquid.

There is, however, a small but significant effect upon the inherent liquid structure. Across the temperature range studied the quadrupoles tend to slightly broaden $g_{AgAg}(r)$ *and* shift the closest approach, r_c, to lower r (table 7.29). Although the available experimental partial distribution functions are noisy it is clear that this close Ag-Ag approach *is* observed. HNC calculations on AgI using the RVP-potential [171] predict an even broader $g_{AgAg}(r)$ and a closer Ag-Ag approach than in AgCl. Since the RVP potential includes only a crude

	r_c/Å		
T/K	RIM	PIM	PIM-QA
783	2.50	2.40	2.22
1123	2.55	2.46	2.11
1500	2.40	2.28	1.98

TABLE 7.29: *Closest approach of a pair of silver cations in the three models studied.*

approximation to the anion dipole polarization effects it appears that it is these *anion* dipoles that dominate the structure in the liquid state.

In conclusion, therefore, liquid AgCl is broadly similar to the alkali halides but with a subtle differences in all three partials and, in particular, in the cation-cation correlations. Although there is no simulation evidence for the sheer number of weird peaks and troughs that arise in the partial structure factors in reference [158] in the liquid phase, there is evidence for a small peak at $\sim 2.5\text{Å}^{-1}$ which is observed experimentally.

8

Beyond the Polarizable-Ion Model.

8.1 Introduction: The Problems of Simulating Oxides.

As discussed in the introduction (section 1.2) it has long been appreciated [92] that the properties of oxides and chalcogenides are much more dependent upon the nature of the crystalline environment than, say, the halides. In order to effectively simulate the oxides it is necessary to perform the full energy partition discussed in chapter 3.

In the previous work in this thesis the anion has almost exclusively been a halide. As discussed in section 1.2 the volume of a halide anion can be considered as almost independent of the crystalline environment. Hence, the anion self energy is approximately constant and so can effectively be absorbed into the Born-Mayer short-range overlap repulsion parameters. The much greater dependence of the oxide anion upon the crystalline environment means that this approximation is no longer valid; the energy must be decomposed into an *overlap* term representing the anion-cation repulsions, and a *self* (rearrangement) energy representing the energy required to compress the anion to a given volume. Modelling oxides using this kind of energy division will be the subject of the final chapter of this thesis.

Previous work has identified the important role of many-body forces in the alkaline earth oxides. These include electron-gas [178, 179, 180, 181, 182] and density-functional calculations [183], as well as models based on the Watson sphere [184, 185, 186] parameterized from the electronic structure calculations.

8.2 Pressure-induced Phase Transitions.

All the alkaline-earth oxides have a B1 (NaCl, rocksalt) phase as the ground state. Only CaO and SrO have experimentally observed transitions to the B2 (CsCl) phase at 63 and 36GPa respectively. BaO transforms into a tetragonal

form at 9GPa whilst theoretical studies on MgO indicate a B1$\longrightarrow$B2 transition between 117GPa [187] and 1050GPa [183].

Additionally, it is expected that the B3 (zinc blende) structure will be energetically close to the B1 ground state.

The attractiveness of studying the interplay between these phases lies in the change in *coordination number* that occur. In the B1 phase each anion is surrounded by six nearest-neighbour cations compared with eight in the B2 and four in the B3. Hence, by studying the relative stability of these three (cubic) phases the effect of the energy subdivision should be made clear.

8.3 The Anion Compression Model (ACM).

What is required, therefore, is a simulation model, based on the same ionic model assumptions as before, that allows for the partition of the anion short-range energy between a rearrangement term and an overlap term.

An additional degree of freedom will be added which represents the size of the anion. A possible way to represent the effect of the change in ionic size on the short-range interactions is via a modification of the Born-Mayer repulsive term to

$$U^{SR}(r^{ij};\delta^i,\delta^j) = Ae^{-a^{ij}(r^{ij}-(\sigma^i+\delta^i)-(\sigma^j+\delta^j))}, \tag{8.1}$$

where σ^i is the ion radius in some reference environment. For a given r^{ij}, the value of U^{SR} will be reduced if the ion is compressed (δ^i negative). Counteracting this will be the self-energy necessary to bring about the compression of the ion which will be expressed simply as a function, F, of δ. Thus, for the interaction between a distortable anion and a non-distortable cation

$$U^{SR} + U^{self} = e^{a\delta^i}U^{BM} + F(\delta^i), \tag{8.2}$$

where U^{BM} is the Born-Mayer potential energy for the reference ionic radii.

δ is to be treated as a parameter to be variationally optimised for a given set of ionic positions, thus

$$\left(\frac{\partial U}{\partial \delta}\right)_r = ae^{a\delta}U^{BM} + \left(\frac{\partial F}{\partial \delta}\right)_r = 0, \tag{8.3}$$

determines the value of δ. The form of F(δ) may be chosen to be so as to fit the self-energy as a function of lattice parameter determined *ab initio*. A typical

function has the form

$$F(\delta) = C(e^{-\gamma\delta} + e^{\gamma\delta}), \tag{8.4}$$

leaving the parameters C and γ to be varied to fit to the data.

Consider the properties of F(δ). The derivative has the form

$$\frac{\partial F}{\partial \delta} = \gamma C(e^{\gamma\delta} - e^{-\gamma\delta}). \tag{8.5}$$

Thus, substituting into equation 8.3 gives

$$\frac{\partial U}{\partial \delta} = ae^{a\delta}U^{BM} - \gamma C(e^{-\gamma\delta} - e^{\gamma\delta}), \tag{8.6}$$

which will be zero at equilibrium at which point the size of the anion will contain the many-body interactions with surrounding cations. Thus,

$$ae^{a\delta}U^{BM} = \gamma C(e^{-\gamma\delta} - e^{\gamma\delta}). \tag{8.7}$$

Figure 8.1 shows how these terms vary.

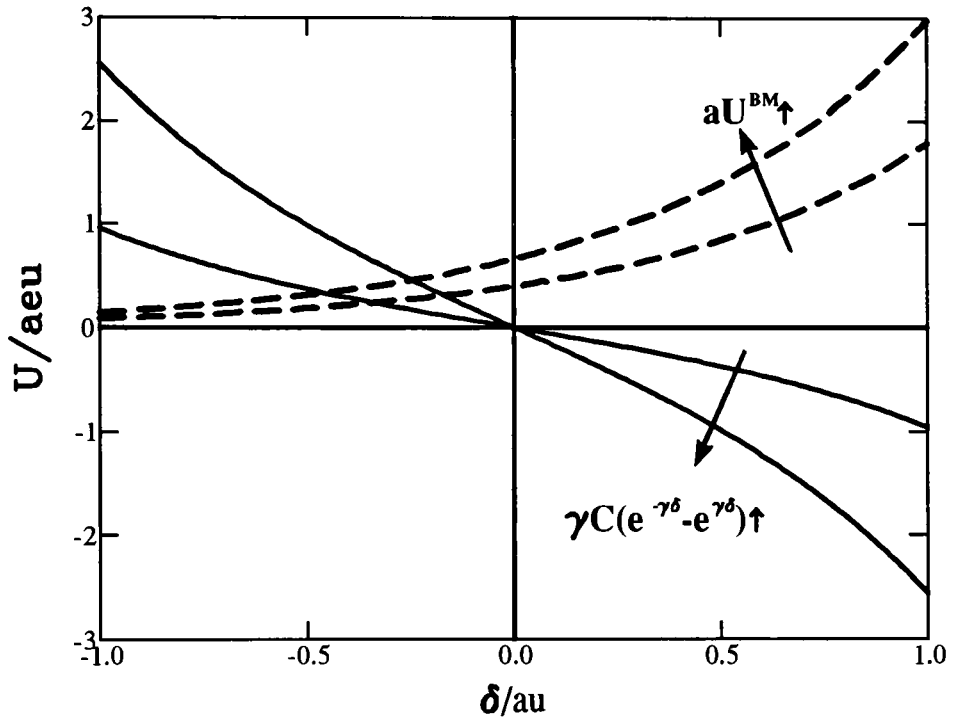


FIGURE 8.1: *Properties of the two terms in equation 8.7 as C and U^{BM} are varied.*

- δ becoming more negative corresponds to the anion becoming smaller. The $\gamma C(e^{-\gamma\delta} - e^{\gamma\delta})$ term becomes larger, that is, the self-energy of the anion becomes larger corresponding to more energy being required to compress the anion into a smaller volume. Correspondingly, the $ae^{a\delta}U^{BM}$ decreases in accordance with the smaller interaction between the anion and the first coordination shell of cations for a given lattice parameter.

- as U^{BM} increases δ becomes more negative. This corresponds to the repulsive interaction with the first cation shell becoming physically larger and so compressing the anion into a smaller volume via the increased overlap effects. Note that setting $U^{BM} = 0$ (corresponding to no neighbouring cations) gives $\delta = 0$ which correspond to an *idealized free ion.* However, as discussed in the introduction, O^{2-} is unstable with respect to electron loss as a free ion and so the meaning of the $\delta = 0$ configuration as corresponding to an *idealised* free ion must be kept clear.

To determine δ at each lattice parameter it is assumed that only the first coordination shell of cations contributes to the compression of the anion. This simplifies the fitting procedure and is justified as the interaction energy of the anion with the second shell of cations is only of the order of 5% of the first shell contribution. Thus, for a system such as MgO or CaO in the B1 phase this involves six cations but will consist of only four cations for a fluorite system such as ThO_2 or UO_2.

It is found that the shorter-ranged part of the normal Born-Mayer short-range term has to be "fortified" with an additional term in order to fit the *ab initio* data. Thus, the short-range overlap function now has the form

$$U^{BM}(r) = \underbrace{Be^{-ar}}_{Born-Mayer\ term} + \underbrace{B'e^{-\beta r^2}}_{Additional\ term}, \tag{8.8}$$

with

$$\frac{\partial U^{BM}}{\partial r} = -aBe^{-ar} - 2r\beta B'e^{-\beta r^2}. \tag{8.9}$$

For MgO and CaO equation 8.7 becomes

$$6ae^{a\delta}(Be^{-ar} + B'e^{-\beta r^2}) = \gamma C(e^{-\gamma\delta} - e^{\gamma\delta}), \tag{8.10}$$

where the six is the anion coordination number. This equation is then solved over the lattice parameter range of the *ab initio* data using the bisection method [41].

Additionally, an extra short-range term may be added to the short-range overlap potential that is *not* involved in the determination of δ. Thus,

$$U^{SR'}(r) = U^{SR}(r) + De^{-\epsilon r}. \tag{8.11}$$

This can greatly improve the fit to the *ab initio* data at the expense of increasing the parameter set. However, as this simply serves to allow a better fit to the *ab initio* data then this should not be a problem.

8.4 Electronic Structure Calculations.

Pyper [188] has performed electronic structure calculations on both MgO and CaO dividing the short-range energy into the overlap and self terms. These calculations will be used to parameterize the model.

The calculations to be used are based upon the two systems in their ground state (B1) structure. In addition, Pyper has calculated the same crystal properties in both the B2 (CsCl) and B3 (zinc blende) phases [189] in order to assess the *transferability* of the model parameterized on the B1 phase only. Properties based on the B1 phase only are termed *frozen* whilst those based on all three phases are *optimal*.

8.5 Parameterization of the ACM.

For a given system, MO, the following fits are required:

- **M-O interactions**. U^{self} and $U^{SR'}$ with parameters a, β, B, B', C, and γ.

- **O-O interactions**. Fit the *ab initio* O-O data to the standard Born-Mayer term.

- **Dispersion terms**. Pyper [188] also calculates dipole-dipole and dipole-quadrupole dispersion terms (C_6 and C_8 respectively) for the systems. Also given are the *dispersion damping* terms parameters modelling the effect of overlap on the dispersion energy. The parameters are derived for the dispersion energy for the case of non-negligible electron overlap derived by Jacobi and Csanak [45]. The damping functions derived from this approach are too complicated to be readily used in an MD simulation and so are fitted to the simpler Tang-Toennies function.

  Theoretically the order of the polynomial in this function is six for C_6 and eight for C_8 [30]. However, whilst this is found to be true for the dipole-dipole terms, a higher order polynomial is required for the dipole-quadrupole dispersion terms.

Consider each fit in turn:

System	U^{asymp}/kJmol^{-1}
MgO	761.4
CaO	656.6

TABLE 8.1: *Asymptotic oxide self-energies for MgO and CaO.*

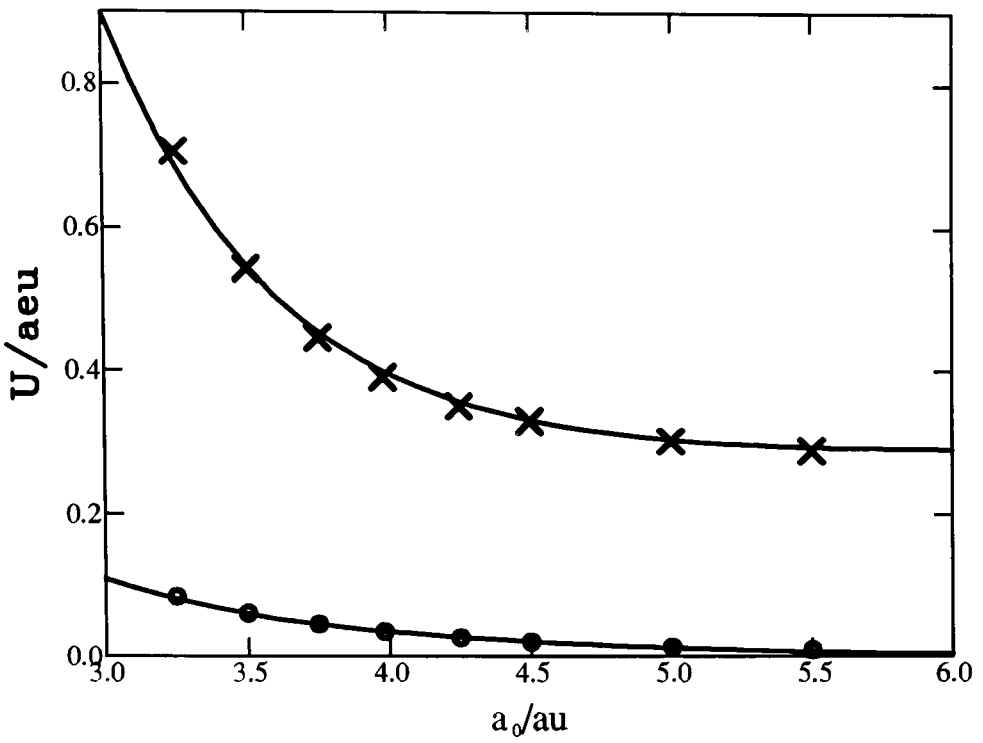
Parameter/au	MgO	CaO
a	1.60	1.75
B	55.0	300.1
β	0.60	0.50
B$\prime$	140.0	250.0
D	-	10000.0
ϵ	-	3.5
γ	1.25	1.15
C	0.1475	0.1350

TABLE 8.2: *Fitted ACM parameter sets for MgO and CaO.*

8.5.1 Magnesium Oxide.

- **Mg-O terms**. Figure 8.2a shows the best fit for U^{SR} and U^{self} with figure 8.2b showing the U^{SR} term alone for clarity. Note that the oxide self energy term tends to the *second electron affinity* for the ion *assuming* that the wavefunction used is correct. Hence, this does not correspond to a real physical state. Table 8.1 lists these values for MgO and CaO. The fit to U^{SR} is slightly problematic both at high and low r. However, the fit to the region probed over a wide pressure range is excellent. Table 8.2 lists the parameters in the potential fit. Note that the extra $De^{-\epsilon r}$ term is not required for a good fit in this case.

- **O-O terms**. Figure 8.3 shows the fit of the Born-Mayer short-range term to the *ab initio* data. Note that the potential curve goes negative as a result of the method of calculation of the correlation term [190]. Table 8.3 lists the fitting parameters.



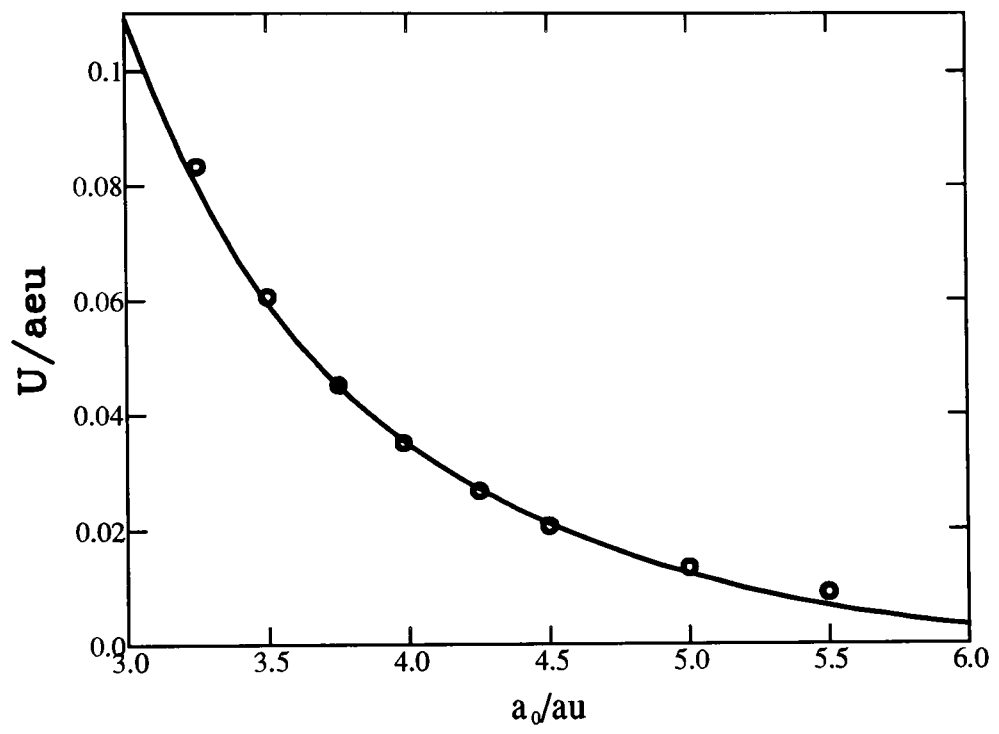


FIGURE 8.2: *Fits (solid lines) to the* ab initio *self-energy (crosses) and overlap energy (open circles) for MgO. Top - Self energy and overlap, bottom - Overlap energy only.*

System	a/au	B_{ij}/au
MgO	1.40	10.0
CaO	1.40	3.2

TABLE 8.3: *O-O potential parameters for MgO and CaO from the* ab initio *data of Pyper [188].*

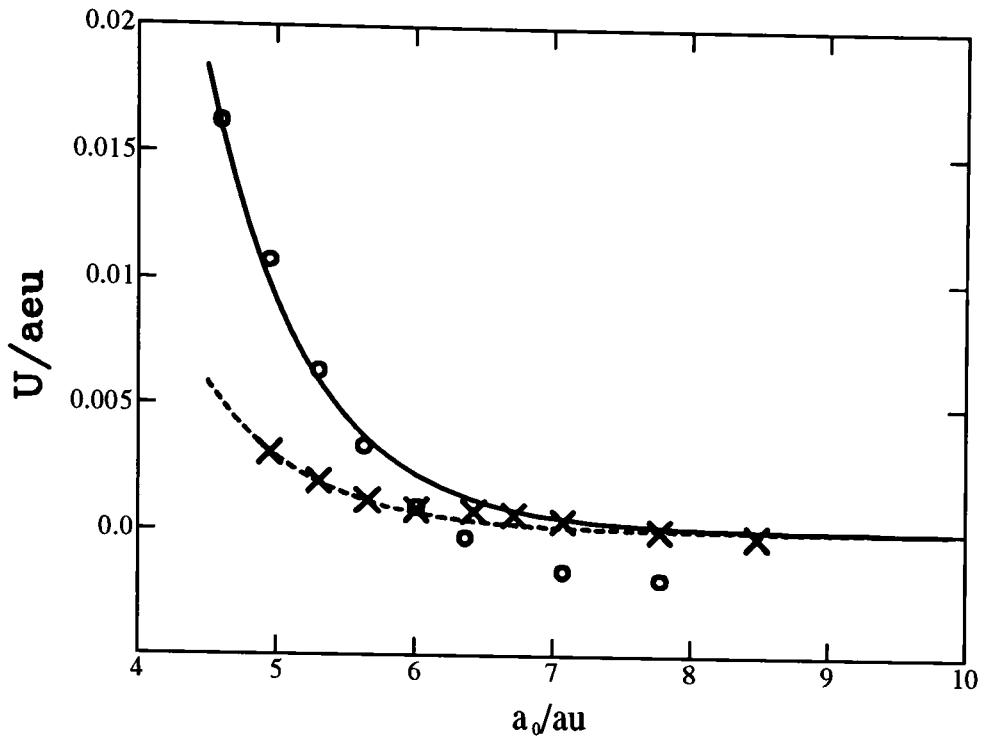


FIGURE 8.3: *Fits to the O-O potentials for MgO (fit - solid line,* ab initio - *open circles) and CaO (fit - dashed line,* ab initio - *crosses).*

- **Dispersion and damping terms.** Table 8.4 lists the *ab initio* dispersion terms along with the damping terms of Pyper and details of the Tang-Toennies fit. The order of the polynomial required to fit the C_8 term is found to be twelve, that is, the order eight polynomial does not appear to damp the interaction strongly enough at intermediate anion-cation separations.

Ion-pair	C_6/au	b^{sr}/au	C_8/au	b^{sr}/au
Mg-O	4.292	2.0443	{41.234,8.549}	2.1055
O-O (in MgO)	60.491	1.4385	1162.290	1.5140
Ca-O	29.380	2.1988	{251.827,141.051}	2.2501
O-O (in CaO)	102.226	1.8520	1752.438	1.9234

TABLE 8.4: Ab initio *dipole-dipole (C_6) and dipole-quadrupole (C_8) dispersion terms and the fitted Tang-Toennies coefficients. Where two C_8 terms are listed the first is the anion quadrupole-cation dipole term.*

System	a/au	B/aeu
MgO	1.45	17.2
CaO	1.50	41.9
MgO (Allan *et al*)	1.7734	49.4862

TABLE 8.5: *M-O RIM parameters for the* ab initio *potential for CaO and MgO with the parameters of Allan* et al *[191] for comparison.*

8.5.2 Calcium Oxide.

- **Ca-O terms**. Figure 8.4a shows the best fit for U^{SR} and U^{self} with figure 8.4b showing the U^{SR} term alone. Figure 8.4b also shows the effect of the additional $De^{-\epsilon r}$ term on the fit of the overlap energy. The fitting parameters are given in table 8.2.

- **O-O terms**. Figure 8.3 shows the fit of the Born-Mayer short-range term to the *ab initio* data. The fitting parameters are given in table 8.3.

- **Dispersion and damping terms**. Table 8.4 lists the *ab initio* dispersion terms along with the damping terms of Pyper and details of the Tang-Toennies fit. A polynomial of order eleven is required to fit the C_8 term.

8.6 Deriving RIM Potentials.

In order to assess the effect of splitting the energy into a self (rearrangement) and an overlap term RI potentials are also derived from the same *ab initio* data. These potentials can then be used to parallel the calculations performed with the ACM.

For an ion-pair in the B1 phase

$$U_{B1}^{RIM}(r) = \frac{U^{self}(r) + 6U^{SR}(r)}{6}. \tag{8.12}$$

Obviously the results using the ACM and the RIM should be identical in the B1 phase. It is away from the six-coordinated structures that the differences should be seen. Table 8.5 lists the short-range RI parameters.

It is instructive to compare this potential with that used by Allan *et al* [191] which was parameterized from known crystal properties. Figure 8.5 shows the

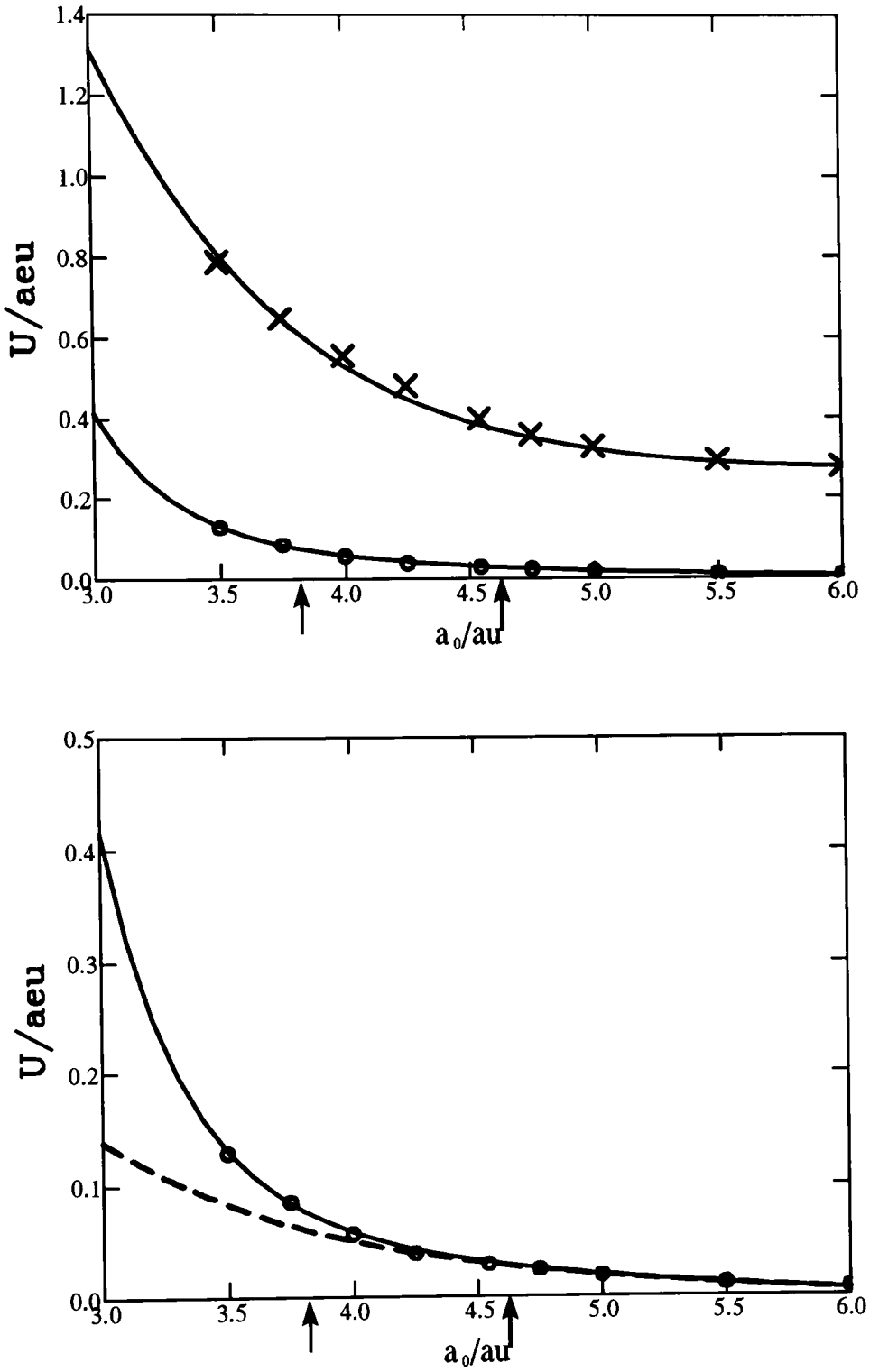


FIGURE 8.4: *As figure 8.2 but for CaO. In the bottom figure the dashed line represents* U^{SR} *without the* $De^{-\epsilon r}$ *term. The arrows on the x-axis indicate the lattice parameters probed by the pressure range 0-210GPa.*

two potentials and table 8.5 gives the parameters for comparison. The new potential appears less steep at smaller lattice parameters but, overall, is similar to the older model.

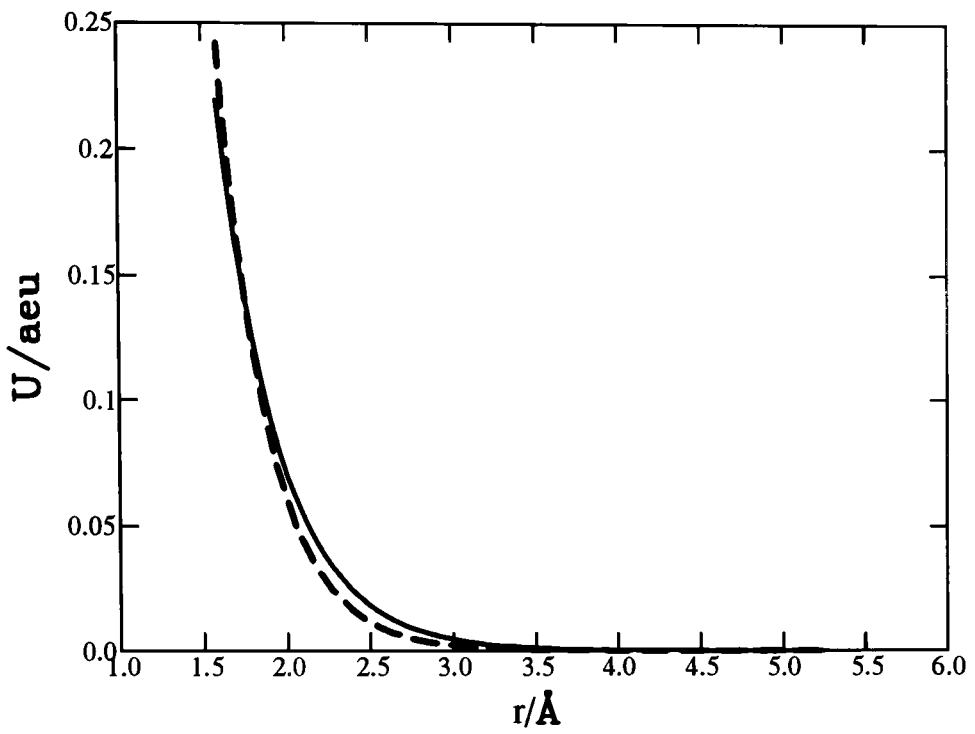


FIGURE 8.5: *Comparison of the* ab initio *RIM potential (solid line) with that due to Allan* et al *[191] (dashed line).*

8.7 Results.

8.7.1 Effect of Potential Terms.

Table 8.6 shows the equilibrium lattice parameter, a_0, and crystal energy, U^{crys}, for different modifications of the ACM for MgO. The effect of parts of the potential are as follows:

- **O-O repulsion:** The effect of adding this to the model is to increase the lattice parameter by 3.8%. The rise in crystal energy is of the order of 2.8%. This effect is, therefore, perhaps surprisingly significant.

- **Dispersion terms:** Adding both C_6 and C_8 with *no damping* reduces a_0 by 3.6%. Including the effects of dispersion damping sets the lattice parameter at 3.986au compared with the experimental value of 3.981au [192]. Hence, the inclusion of dispersion damping is *crucial* in obtaining a

O-O repulsion	C_6	C_8	Damping	a_0/au	U^{crys}/kJmol^{-1}
X	√	√	X	3.737	-3114.90
√	√	√	X	3.880	-3030.05
√	X	X	X	4.026	-2936.47
√	√	√	√	3.986	-3009.26
				3.981	-3038

TABLE 8.6: *The effect of various terms in the MgO ACM. The final row lists the experimental values.*

C_6	C_8	Damping	a_0/au	U^{crys}/kJmol^{-1}
√	√	X	4.340	-2596.40
√	√	√	4.522	-2643.52
			4.544	-2644

TABLE 8.7: *The effect of dispersion damping in the CaO ACM.*

good fit. This is worth stressing as this effect is often ignored in simulations of this type.

Overall, the agreement with experiment is excellent with the lattice parameter being only 0.1% too large. The lattice energy is around 1% too positive with respect to the experimental lattice energy [178] but is consistent with the *ab initio* data used to parameterize the model.

Table 8.7 shows the lattice parameters and crystal energies for CaO. The calculated lattice parameter is 0.5% smaller than experiment [192] and the crystal energy is almost spot on. Again, these are consistent with the *ab initio* data.

8.7.2 System Size Effects.

As ever in computer models of this type it is important to make sure that the simulation size is large enough to mimic the properties of the infinite system.

Table 8.8 lists the lattice parameters and energies for the full MgO model with C_6, C_8 and dispersion damping. Thus, a system size of 216 ions is acceptable.

N^t	a_0/au	U^{crys}/kJmol^{-1}
64	3.989	-3007.88
216	3.986	-3009.26
512	3.986	-3010.00

TABLE 8.8: *System size effects on the lattice parameter and energy for MgO using the ACM.*

8.7.3 Modelling Phase Transitions.

A phase transition occurs when the free energy of two phases is the same at a given pressure. At absolute zero the enthalpy H and Gibbs free energy G are equivalent. For example, for the B1-B2 phase transition in the MO systems the transition occurs when

$$G^{B1}(V,p) = G^{B2}(V,p). \tag{8.13}$$

To calculate G for each phase the start point is to note that at absolute zero

$$G(V,p) = U^{crys}(V) + pV, \tag{8.14}$$

where p is the system pressure and V the system volume. If the minimized free energy volume is denoted V_m then, at this minimum

$$\left(\frac{\partial G}{\partial V}\right)_{V=V_m} = 0. \tag{8.15}$$

Substituting this into equation 8.14 gives

$$p = -\left(\frac{\partial U^{crys}}{\partial V}\right)_{V=V_m}. \tag{8.16}$$

Thus, to determine the transition pressures the crystal energy versus volume is determined for each phase under study. The free energy is then evaluated from a knowledge of this energy and its gradient with respect to volume.

Crystal Energies.

Figures 8.6 and 8.7 show the crystal energies against volume for CaO and MgO respectively for the three phases of interest, B1 (NaCl), B2 (CsCl) and B3 (ZnS).

Both systems show some similarities:

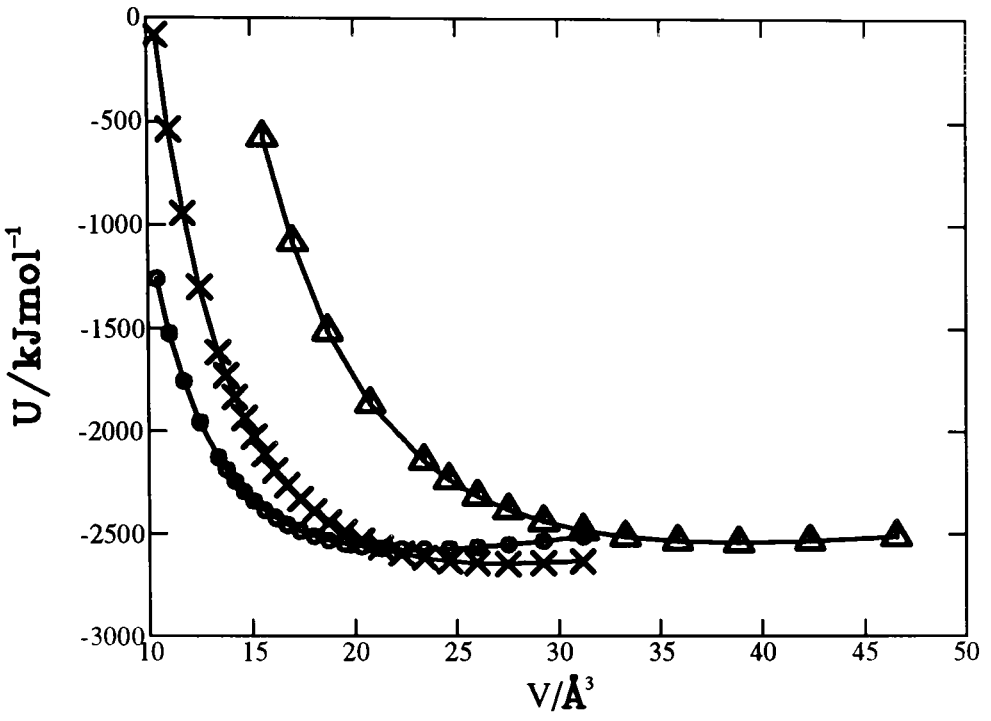
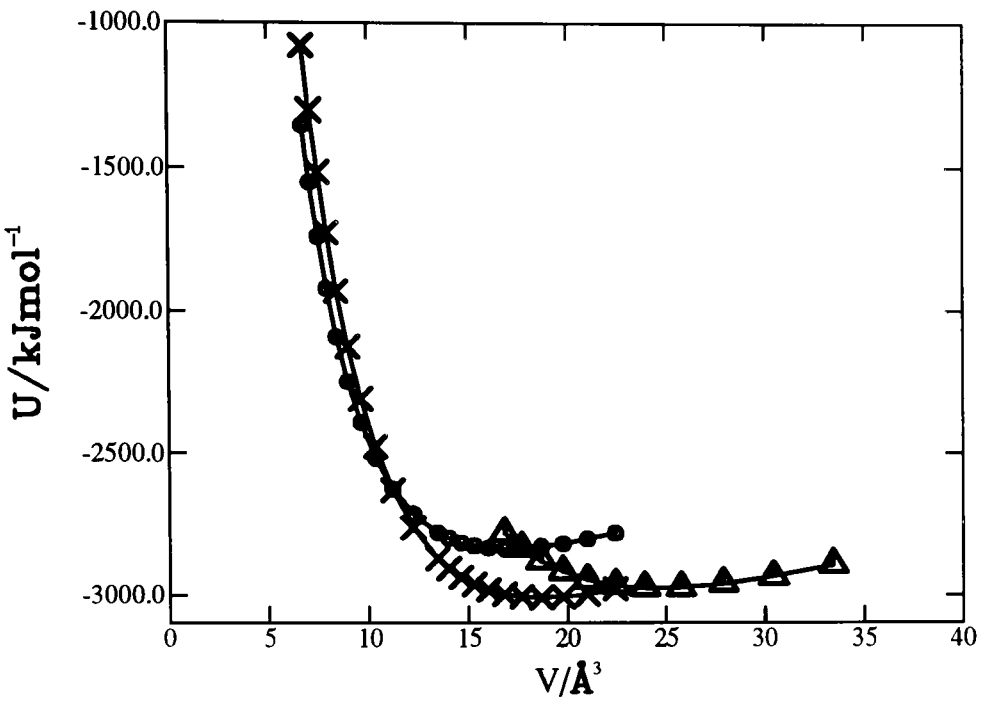


FIGURE 8.6: *Crystal energy as a function of volume for the CaO with the ACM. Top - Over the whole volume range studied, bottom - all points of energy lower than -2000kJmol^{-1}. Key:* × *- B1,* ○ *- B2,* △ *- B3.*



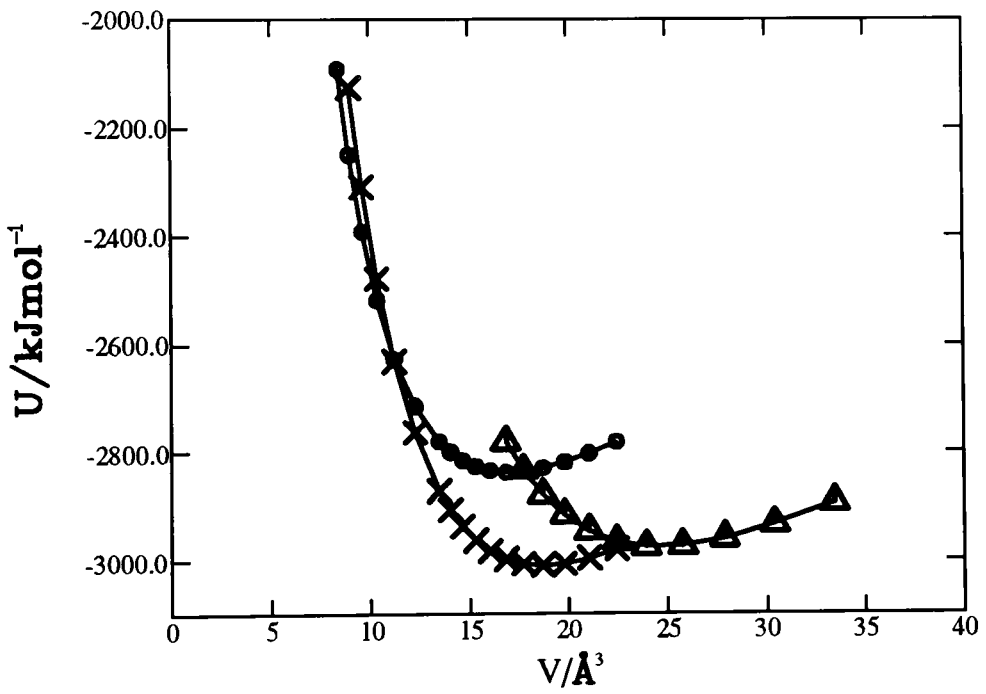


FIGURE 8.7: *As figure 8.6 but for MgO.*

- The B2 phase has a more positive energy at the minimum with respect to the B1. The B2 minimum is at a lower molar volume. This tells us that there will be a *positive* pressure phase transition at which point the B2 structure will become energetically favoured over B1.

- The B3 phase is at a more positive energy with respect to the B1 *and* the minimum occurs at a higher volume confirming no positive pressure phase transition to this structure.

Figures 8.8 and 8.9 show the crystal energy versus volume for the rigid-ion model. Tables 8.9 and 8.10 lists the energy differences between the three phases from the ACM, RIM and the electronic structure calculations of Pyper [189] derived from both the frozen and optimal potentials (see section 8.4). The effect of the ACM with respect to the RIM is to *stabilize* the B2 phase with respect to the B1 but *destabilize* the B3 with respect to the B1 for both MgO and CaO. This effect is even more dramatic with the B3 phase actually being of lower energy than the B1. This is *not* the experimentally observed structure and so is a failing of this RIM. The ACM correctly predicts the ground state crystal structure.

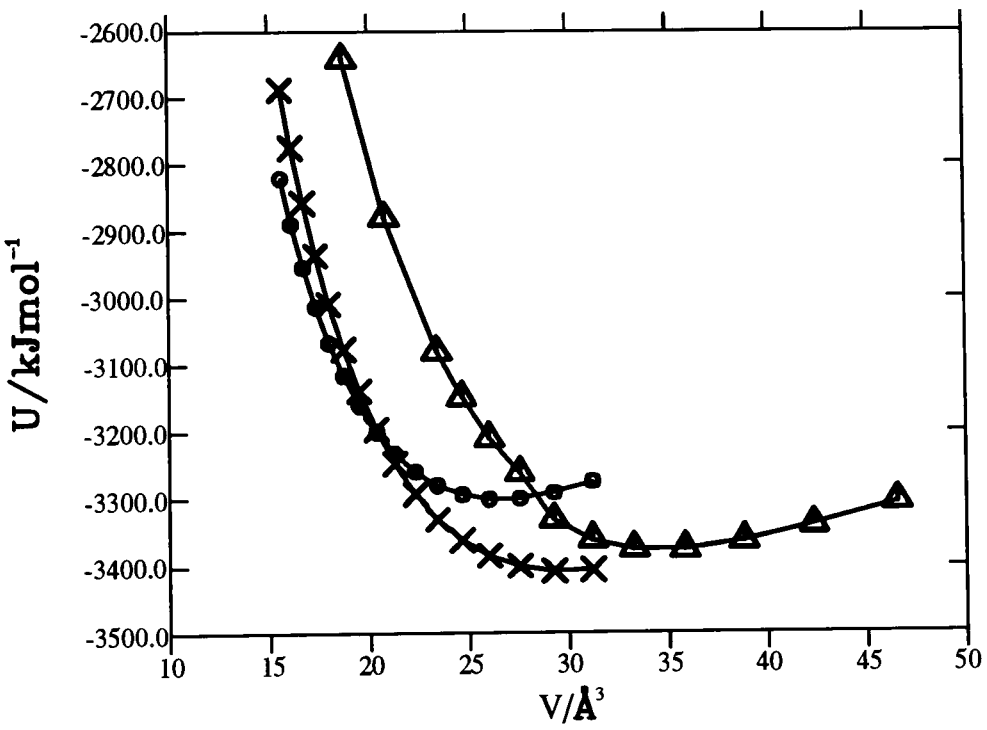


FIGURE 8.8: *As figure 8.6 but for the RIM. Note that the energy is more negative than the corresponding ACM calculation as the asymptotic energy has to be added back.*

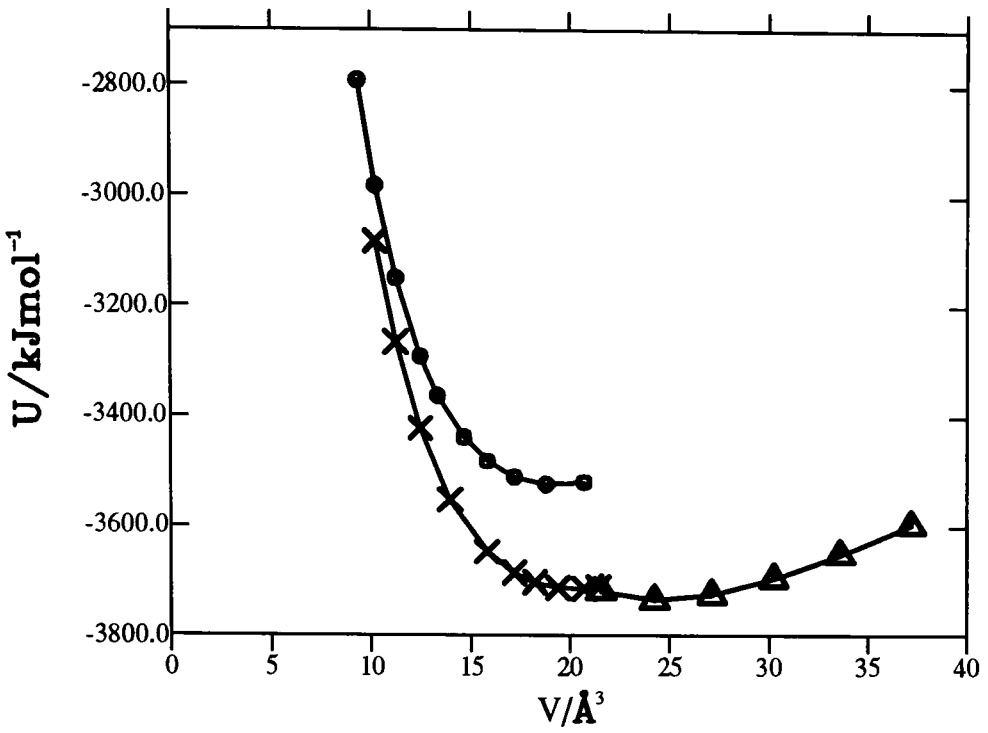


FIGURE 8.9: *As figure 8.7 but for the RIM. Note, again, that the energy is more negative than the corresponding ACM calculation as the asymptotic energy has to be added back.*

By considering the nature of the both the ACM and RIM potentials the reason for this behaviour becomes clear. The RI potential used here was derived from the B1 phase data using equation 8.12. Similarly, an alternative potential could be derived from the B2 phase giving

$$U_{B2}^{RIM}(r) = \frac{U^{self}(r) + 8U^{SR}(r)}{8}. \tag{8.17}$$

Thus, for an ion-pair the difference between the two potentials is given by

$$U_{B1}^{RIM}(r) - U_{B2}^{RIM}(r) = \frac{U^{self}(r)}{24}, \tag{8.18}$$

meaning that a crystal energy calculated with $U_{B2}^{RIM}(r)$ will be *more positive* than for the same structure using $U_{B1}^{RIM}(r)$. Similarly for the B3 phase

$$U_{B3}^{RIM}(r) = \frac{U^{self}(r) + 4U^{SR}(r)}{4}, \tag{8.19}$$

giving

$$U_{B1}^{RIM}(r) - U_{B3}^{RIM}(r) = -\frac{U^{self}(r)}{12}. \tag{8.20}$$

Thus, the destabilization of the B3 phase with respect to B1 is twice the energy of the stabilization of B2 with respect to B1.

Model	B2-B1/kJmol^{-1}	B3-B1/kJmol^{-1}
ACM	69.731	103.567
RIM	107.268	31.603
Pyper - Frozen	63.8	139.9
Pyper - Optimal	62.2	122.7

TABLE 8.9: *Energy differences between the three phases for CaO for the ACM, RIM, and the two models due to Pyper [189].*

Model	B2-B1/kJmol^{-1}	B3-B1/kJmol^{-1}
ACM	170.168	27.689
RIM	190.008	-20.977
Pyper - Frozen	176.8	55.9
Pyper - Optimal	86.9	63.4

TABLE 8.10: *As table 8.9 but for MgO.*

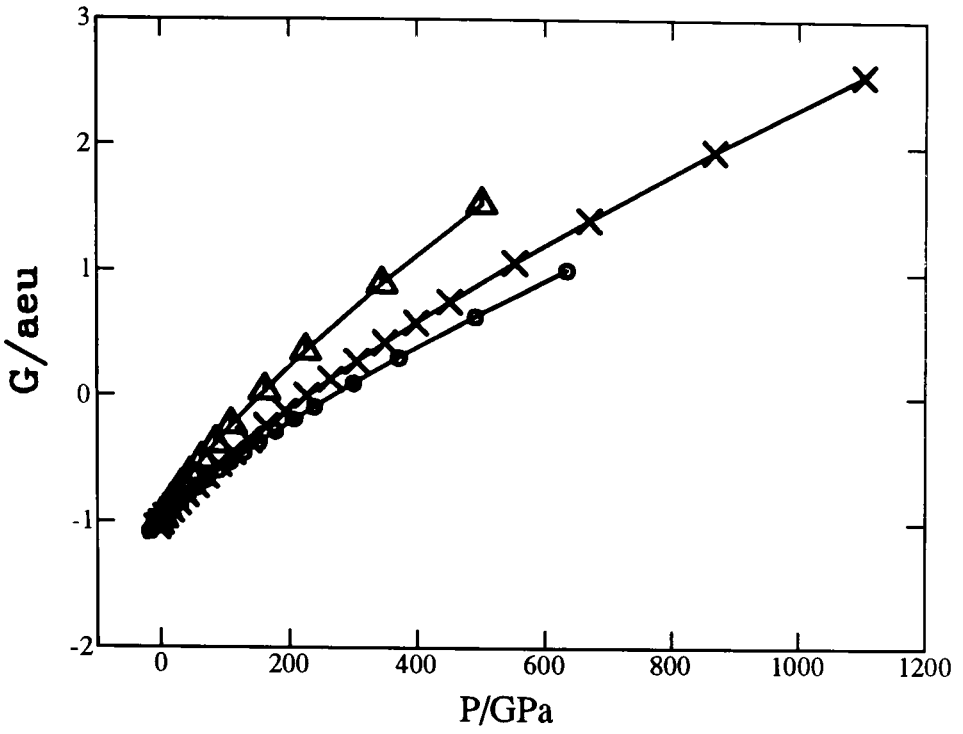
Free Energies.

Figures 8.10 and 8.11 show the variation in the free energy with pressure calculated from equation 8.14 for the two systems with the ACM. Figures 8.12 and 8.13 show the RIM analogues. It is clear that the phase transition from B1 to B2 occurs at a much higher pressure in MgO with respect to CaO.

Table 8.11 lists the transition pressures, P_t, for the RIM, ACM and experiment (for CaO only). The effect of stabilizing B2 with respect to B1 is to *lower* the transition pressure. In the case of CaO the RIM P_t is higher than that observed experimentally but the ACM result unfortunately lowers it by too much. Thus, although the RIM transition pressure is affected in the desired manner the magnitude of the change appears too great.

Equations of State.

Figures 8.14 and 8.15 show the molar volume (as V/V_0 where V_0 is the molar volume at zero pressure) for the two systems. Also shown are the empirical



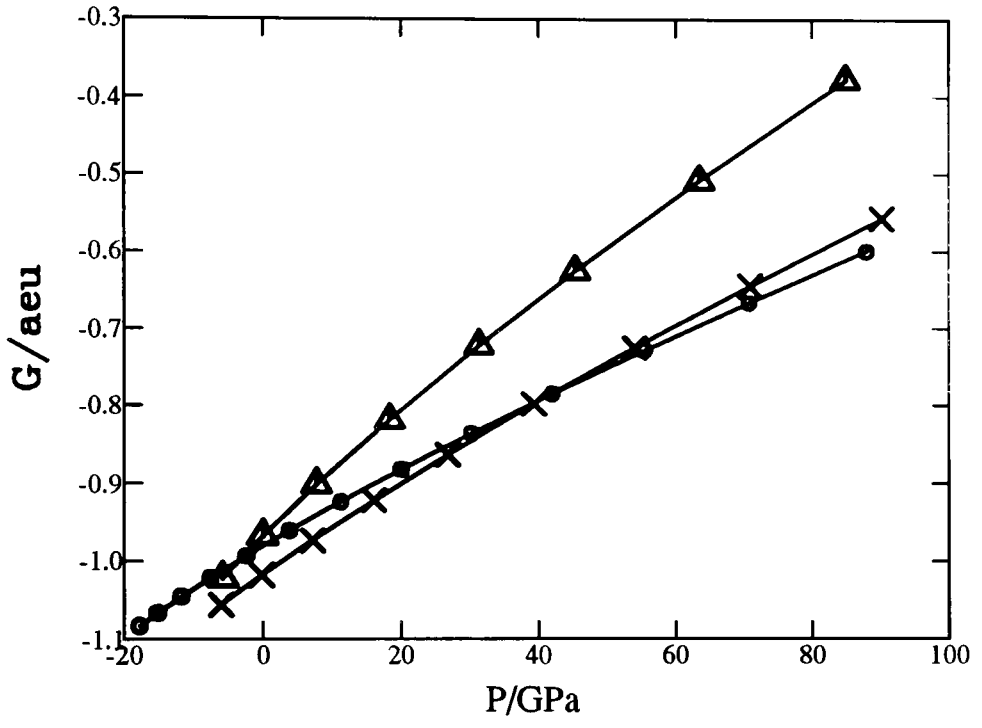


FIGURE 8.10: *Free energy versus pressure for CaO, top - over the whole pressure range studied, bottom - over a smaller range for clarity. Key as for figure 8.6.*

	P_t/GPa		
System	PIM	RIM	Experiment
CaO	42	82	63
MgO	220	1500	-

TABLE 8.11: *B1⟶B2 transition pressures from the RIM, ACM and experiment.*

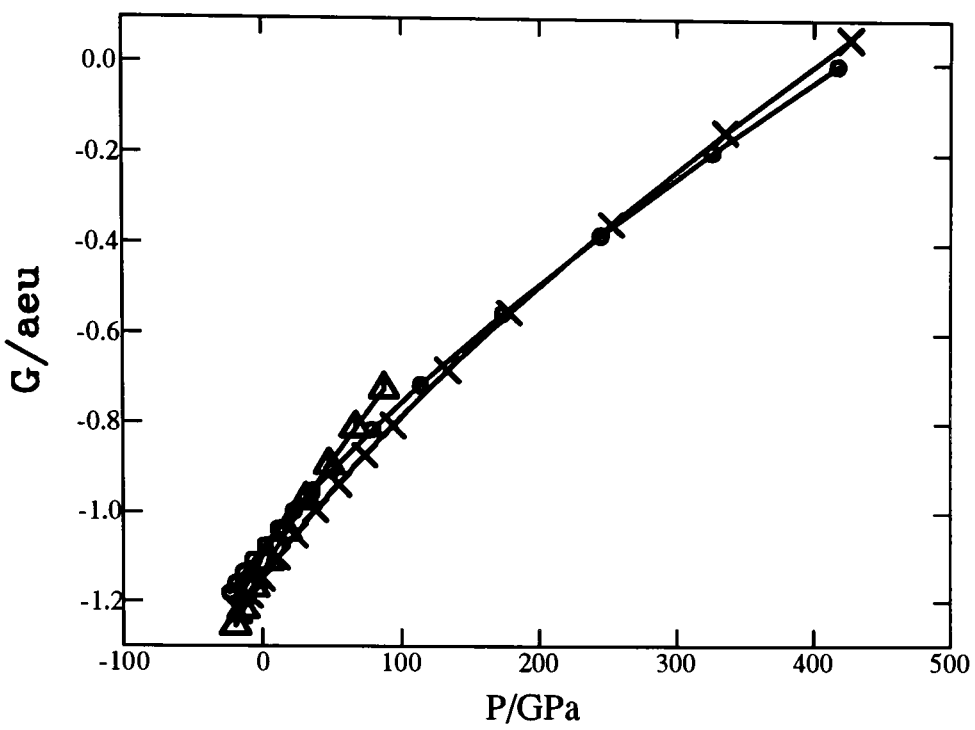


FIGURE 8.11: *As figure 8.10 but for MgO.*

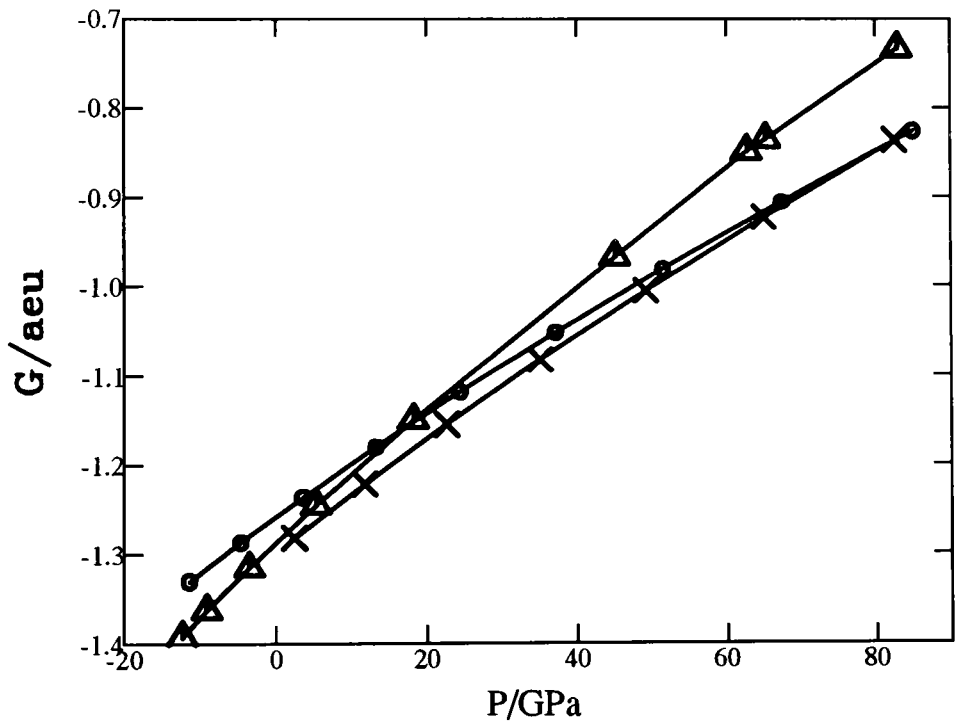


FIGURE 8.12: *As figure 8.10 but for the RIM.*

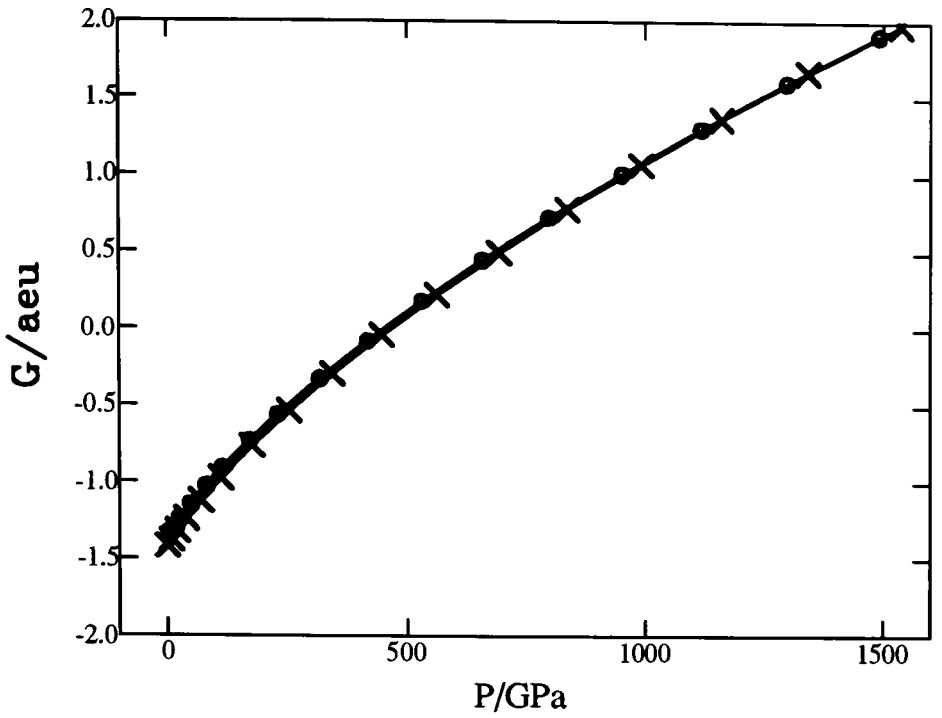


FIGURE 8.13: *As figure 8.11 but for the RIM.*

System	Phase	K_0	K_0'
MgO	B1	155±5	4.16±0.2
	B2	156±5	4.12±0.2
CaO	B1	109±5	4.62±0.2
	B2	123±5	4.4±0.2

TABLE 8.12: *Equation of state parameters.*

equations of state due to Burch and Murnaghan [193] truncated to third-order

$$p = \frac{3}{2}K_0\left\{\left(\frac{V_0}{V}\right)^{7/3} - \left(\frac{V_0}{V}\right)^{5/3}\right\}.\left\{1 + \frac{3}{4}(K_0' - 4)\left[\left(\frac{V_0}{V}\right)^{2/3} - 1\right]\right\}, \quad (8.21)$$

where K_0 and K_0' are the bulk modulus and its first pressure derivative respectively. These are given in table 8.12.

Overall, the agreement with the existing equations of state is excellent. Note that the MgO curves move away from the EOS at very high pressure ($> 1000GPa$). However, this is perhaps not too surprising given the large pressures involved. It may be that the contribution to the short-range energy at these pressures is significant from shells other than the first coordination shell.

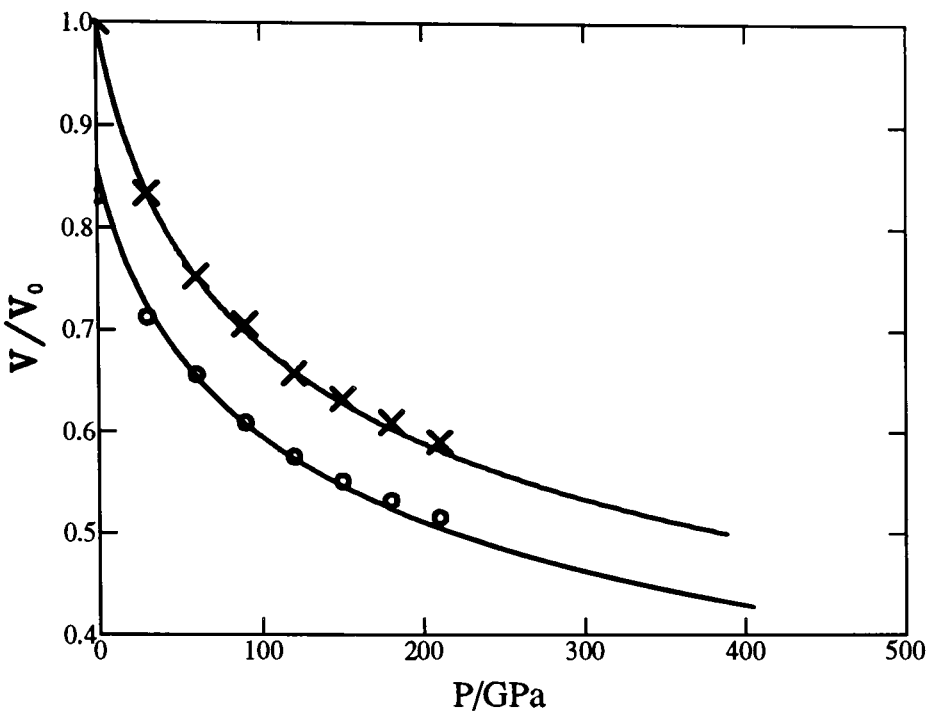


FIGURE 8.14: *Pressure-volume curves for CaO in the B1 and B2 phases. Key:* × - *B1,* ○ - *B2, solid lines - Burch and Murnaghan equation of state.*

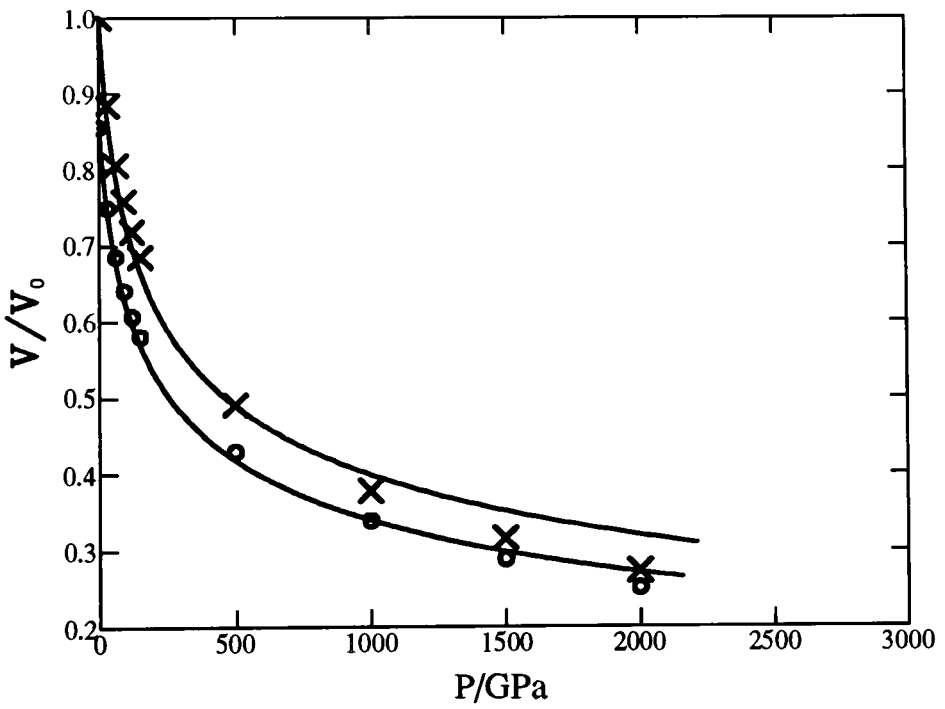


FIGURE 8.15: *As fig 8.14 but for MgO. Note the scale of the x-axis with respect to the previous figure*

	MgO		CaO	
p/GPa	B1	B2	B1	B2
0	-0.662	-0.623	-0.792	-0.786
30	-0.763	-0.722	-0.987	-0.972
60	-0.832	-0.788	-1.112	-1.080
90	-0.888	-0.842	-1.207	-1.164
120	-0.937	-0.886	-1.288	-1.235
150	-0.978	-0.925	-1.342	-1.288

TABLE 8.13: *Values of δ (in atomic units) for the MgO and CaO systems.*

8.8 Behaviour of the Model.

Let us consider the behaviour of the model in the B1→B2 phase transition. Table 8.13 shows the δ values in the ACM for both MgO and CaO in both phases over the pressure range 0-150GPa. In both cases δ is *less negative* in the B2 phase, that is, the ion is *more compressed* in the B1 phase with respect to the B2 phase. The two factors for pressure-induced phase transitions to consider are:

- As the pressure increases the coordination number wants to increase.
- As the coordination number increases the lattice parameter increases at a given pressure (the "pressure-distance paradox").

Thus, although the coordination number increases in going from B1→B2 the increased lattice parameter allows the anion to occupy a larger volume in the B2 phase with respect to the B1 at a given pressure.

8.9 Comparison with Other Oxides.

It is of interest to consider what is known about ZnO in order to compare with the present MgO work.

Jaffe and Hess [194] have studied the ZnO pressure transitions with Hartree-Fock electronic structure calculations. The central result of this work regards the relative stability of the B1 and B3 phases. ZnO crystallises into a wurtzite

(B4) structure with the Zn^{2+} cations occupying half the tetrahedral holes in the close-packed oxide sublattice. This differs from the B3 phase only in the relative packing of the anion sublattice and hence the energetics are very similar. ZnO forms this structure *despite* Mg^{2+} having a smaller cation radius than Zn^{2+}.

The B3→B1 transition is predicted at between 9.0 [195] and 9.5GPa (reference 1 in [194]) with the HF calculations giving 8.57GPa. The ZnO crystal energies versus volume curves are very similar to those of MgO (figure 8.7) with the zero pressure lattice parameter for the B1 phase being 4.058au in ZnO compared to 3.981au in MgO. Thus, MgO and ZnO appear very similar in the B1 phase, as would be expected using a sphere-packing analysis.

In the B3 phase the factor that differentiates between Mg^{2+} and Zn^{2+} is the induced *octupole* moment on the cation. In the B3 phase the cations sit in tetrahedral site allowing non-zero induced octupoles. Mahan [4] gives this energy as

$$U^{oct}(r) = \frac{-3.89Z^2(\Omega^+ + \Omega^-)}{r^8}, \tag{8.22}$$

for the B3 structure, where Z is the ion charge, $\Omega^{\pm}$ are the octupole polarizabilities, and r is the anion-cation separation. Following the discussion of section 7.4.2 the contribution of the anion will be neglected as it is suspected that the octupole induced by the coulombic field gradient gradient will be effectively cancelled by that induced by the overlap with the nearest-neighbour cations. Thus, for $r = 4.0au$,

$$U^{oct} = -0.6234\Omega^+, \tag{8.23}$$

in $kJmol^{-1}$.

The calculations in section 8.7.3 gives $U^{B1} - U^{B3}$ as $27.689kJmol^{-1}$ for MgO, whilst the HF calculations give -18.332$kJmol^{-1}$ for ZnO. Thus, it is possible to use equation 8.23 to estimate the octupole polarizability of the zinc cation necessary to stabilize the B3 phase by this amount. Taking $\Omega^{Mg^{2+}}$ as zero this gives

$$\Omega^{Zn^{2+}} \simeq 74.3au. \tag{8.24}$$

Mahan calculates this as 30.12au. However, it was shown in section 7.6.2 that a *quadrupole* polarizability of over twice the *ab initio* value was required to reproduce important features of the experimental phonon dispersion curves in AgCl. This was attributed to cooperative overlap effects along with possible

crystal-field effects. Similarly, in ZnO the overlap effect will cooperate with the coulombic effects to induce an octupole on the cation. This makes the value of 74.3au a realistic possibility for this system.

To summarize the different relative stability of the B3 phase with respect to the B1 in MgO and ZnO can be attributed to the larger induced octupoles that can be induced on the zinc cations with respect to those on the magnesium. However, it is clear that very large electronic structure calculations are required to confirm this theory.

8.10 Closing Remarks.

In this chapter it has been shown that important aspects of crystal energetics can be represented with a single degree of freedom. It is worth stressing that this can be used as a dynamical variable in a CP-like scheme analogous to the treatment of the induced multipoles in the earlier chapters.

Bibliography

[1] Car,R, & Parrinello,M, *Phys. Rev. Lett.*, **55**, 2471, 1985.

[2] Remler,D.K, & Madden,P.A, *Mol. Phys.*, **70**, 921-966, 1990.

[3] Enderby,J.E, & Barnes,A.C, *Rep. Prog. Phys.*, **53** , 85, 1990.

[4] Mahan,G.D, *Sol. State Ionics*, **1**, 29, 1980.

[5] Fowler,P.W, & Madden,P.A, *Phys. Rev. B*, **29**, 1035, 1984.

[6] Fowler,P.W, & Madden,P.A, *Mol. Phys.*, **49**, 913, 1983.

[7] Fowler,P.W, & Madden,P.A, *J. Phys. Chem.*, **89**, 2581, 1985.

[8] Pyper,N.C, *Adv. Sol. Stat. Chem.*, **2**, 223, 1991.

[9] Fumi,F.G, & Tosi,M.P, *J. Phys. Chem. Solids*, **25**, 31, 1964.

[10] Sangster,M.J.L, & Dixon,M, *Adv. Phys.*, **23**, 247, 1976.

[11] Lyddane,R.H, Sachs,R.G, & Teller,E, *Phys. Rev.*, **59**, 673, 1941.

[12] March,N.H, & Parrinello,M, "Collective Effects on Solids and Liquids", (Adam Hilger, Bristol, 1982).

[13] Jacucci,G, McDonald,I.R, & Rahman,A, *Phys. Rev. A*, **13**, 1581, 1976.

[14] Wilson,M, & Madden,P.A, *J. Phys.: Condens. Matter*, **5**, 2687, 1993.

[15] Parrinello,M, Rahman,A, & Vashishta,P, *Phys. Rev. Lett.*, **50**, 1073, 1983.

[16] Fowler,P.W, & Madden,P.A, *Phys. Rev. B*, **31**, 5443, 1985.

[17] Fowler,P.W, *Private communication.*

[18] Buckingham,A.D, *Adv. Chem. Phys.*, **12**, 107, 1967.

[19] Sprik,M, in "Computer Simulation in Chemical Physics", eds Allen,M.P, & Tildesley,D.J, (Kluwer, Berlin, 1993).

[20] Lindan,P.J.D, & Gillan,M.J, *J. Phys.: Condens. Matter*, **5**, 1019, 1993.

[21] Mitchell,P.J, & Fincham,D, *J. Phys.: Condens. Matter*, **5**, 1031, 1993.

[22] Schröder,U, *Sol. Stat. Commun.*, **4**, 347, 1966.

[23] Fischer,K, Bilz,H, Haberkorn,R, & Weber,W, *Phys. Stat. Sol. b*, **54**, 285, 1972.

[24] Sabounghi,M-L, Rahman,A, Halley,J.W, & Blander,M, *J. Chem. Phys.*, **88**, 5818, 1988.

[25] Sprik,M, & Klein,M.L, *J. Chem. Phys.*, **89**, 7556, 1988.

[26] Sprik,M, *J. Phys. Chem.*, **95**, 2283, 1991.

[27] Sprik,M, *J. Chem. Phys.*, **95**, 6762, 1991.

[28] Sprik,M, Klein,M.L, & Watanabe,K, *J. Phys. Chem.*, **94**, 6483, 1990.

[29] Böttcher,C.J.F, "Theory of Electric Polarization", Elsevier, London, 1973.

[30] Tang,K.T, & Toennies,J.P, *J. Chem. Phys.*, **80**, 3726, 1984.

[31] Allen,M.P, & Tildesley,D.J, "Computer Simulation of Liquids", Clarendon Press, 1987.

[32] Pastore,G, Smargiassi,E, & Buda,F, *Phys. Rev. A*, **44**, 6334, 1991.

[33] Fois,E.F, Madden,P.A, & Penman,J.I, *Advances in Biomolecular Simulation*, (Eds. Lavery,R., Rivail,J-L. & Smith,J.) American Institute of Physics, New York, 1991.

[34] Blöchl,P.E, & Parrinello,M, *Phys. Rev. B*, **45**, 9413, 1992.

[35] Bogoljubov,N.N, "Asymptotic Methods in the Theory of Nonlinear Oscillations" (Hindustan, Dehli, 1961).

[36] Arnold,V.I, "Geometrical Methods in the Theory of Ordinary Differential Equations" (Springer, Berlin, 1988).

[37] Pearson,M.N, M.Sc thesis, Oxford 1992 (unpublished).

[38] Nosé,S, *Mol. Phys.*, **52**, 255, 1984; *J. Chem. Phys.*, **81**, 511, 1984.

[39] Hoover,W.G, *Phys. Rev. A*, **31**, 1695, 1985.

[40] Toxvaerd,S, *Mol. Phys.*, **72**, 159, 1991.

[41] Press,W.H, Flannery,B.P, Teukolsky,S.A, & Vetterling,W.T, "Numerical Recipes", Cambridge University Press, 1986.

[42] Martyna,G.J, Klein,M.L, & Tuckerman,M, *J. Chem. Phys.*, **97**, 2635, 1992.

[43] Harding,J.H.H, *Mol. Sim.*, **4**, 255, 1990.

[44] Casimir,H.B.G, & Polder,D, *Phys. Rev.*, **73**, 366, 1948.

[45] Jacobi,N, & Csanak,G, *Chem. Phys. Lett.*, **30**, 367, 1975.

[46] Fowler,P.W, & Pyper,N.C, *Proc. R. Soc. Lond. A*, **398**, 377, 1985.

[47] Slater,J.C, & Kirkwood,J.G, *Phys. Rev.*, **37**, 382, 1931.

[48] Fowler,P.W, Knowles,P.J, & Pyper,N.C, *Mol. Phys.*, **56**, 83, 1985.

[49] Fowler,P.W, & Pyper,N.C, *Mol. Phys.*, **59**, 317, 1986.

[50] Busing,R.W, *Trans. Am. Cryst. Assoc.*, **6**, 57, 1970.

[51] de Leeuw, S.W, *Mol. Phys.*, **36**, 103, 1978.

[52] Wilson,M, *unpublished.*

[53] Wyckoff, R. W. G, "Crystal Structures", (Interscience, New York, 1965).

[54] Hutchings,M.T, Clausen,K, Dickens,M.H, Hayes,W, Kjems,J.K, Schnabel,P.G, & Smith,C, *J. Phys. C: Sol. Stat.*, **17**, 3903, 1984.

[55] D'Aguanno,B, Rovere,M, Tosi,M.P, & March,N.H, *Phys. Chem. Liq.*, **13**, 113, 1983.

[56] Rovere,M, & Tosi,M.P, *Sol. Stat. Commun.*, **55**, 1109, 1985.

[57] Desa,J.A.E, Wright,A.C, Wong,J, & Sinclair,R.N, *J. Non-Cryst. Solids*, **51**, 57, 1982.

[58] Wells,A.F, "Structural Inorganic Chemistry", 5^{th} ed., Clarendon, Oxford, 1984.

[59] Stark,J.G, & Wallace,H.G, "Chemistry Data Book", 2^{nd} edition, (John Murray, 1984.)

[60] Harrison,N.M, & Saunders,V.R, *J.Phys.: Condens. Matter*, **4**, 3873, 1992.

[61] Harrison,N.M, Saunders,V.R, Aprà,E, Causà,M, & Dovesi,R, *J.Phys.: Condens. Matter*, **4**, L261, 1992.

[62] Tosi,M.P, *J. Phys. Condens. Matter*, **6**, A13, 1994.

[63] Hullinger,F, *Structure and Bonding*, **4**, 83, 1968.

[64] Edwards,F.G, Enderby,J.E, Howe,R.A, & Page,D.I, *J. Phys C: Sol. Stat.*, **8**, 3483, 1975.

[65] Biggin,S, Gay,M, & Enderby,J.E, *J. Phys C: Sol. Stat.*, **17**, 977, 1984.

[66] Biggin,S, & Enderby,J.E, *J. Phys C: Sol. Stat.*, **14**, 3129, 1981.

[67] Allen,D.A, Howe,R.A, Wood,N.D, & Howells,W.S, *J. Chem. Phys.*, **94**, 5071, 1991.

[68] McGreevy,R.L, & Mitchell,E.W.J, *J. Phys C: Sol. Stat.*, **15**, 5537, 1982.

[69] Edwards,F.G, Howe,R.A, Enderby,J.E, & Page,D.I, *J. Phys C: Sol. Stat.*, **11**, 1053, 1978.

[70] Wood,N.D, Howe,R.A, Newport,R.J, & Faber,J.Jr, *J. Phys C: Sol. Stat.*, **21**, 669, 1988.

[71] Biggin,S, & Enderby,J.E, *J. Phys C: Sol. Stat.*, **14**, 3577, 1981.

[72] Day,S.E, & McGreevy,R.L, *Phys. Chem. Liq.*, **15**, 129, 1985.

[73] Wood,N.D, & Howe,R.A, *J. Phys C: Sol. Stat.*, **21**, 3177, 1988.

[74] Newport,R.J, Howe,R.A, & Wood,N.D, *J. Phys C: Sol. Stat.*, **18**, 5249, 1985.

[75] Takagi,Y, & Nakamura,T, *Phil. Mag. B*, **51**, L43, 1985.

[76] McGreevy,R.L, *Sol. State. Phys.*, **40**, 247, 1987.

[77] Bunten,R.A.J, McGreevy,R.L, Mitchell,E.W.J, Raptis,C, & Walker,P.J, *J. Phys. C: Sol. Stat.*, **17**, 4705, 1984.

[78] Huang,C.-H, & Brooker,M.H, *Chem. Phys. Lett.*, **43**, 180, 1976.

[79] Bunten,R.A.J, McGreevy,R.L, Mitchell,E.W.J, & Raptis,C, *J. Phys. C: Sol. Stat.*, **19**, 2925, 1986.

[80] Aliotta,F, Maisano,G, Migliardo,P, Vasi,F, Wanderlingh,F, Pedro Smith,G, & Trilo,R, *J. Chem. Phys.*, **75**, 613, 1981.

[81] Bues,W, & Brockner,W, *Z. für Physik. Chem. Neue Folge. Bd*, **88**, 290, 1974. (In German)

[82] de Leeuw, S.W, *Mol. Phys.*, **36**, 765, 1978.

[83] de Leeuw, S.W, *Mol. Phys.*, **37**, 489, 1979.

[84] Dixon,M, & Gillan,M.J, *J. Phys. C: Sol. Stat.*, **13**, 1901, 1980.

[85] Angell,C.A, *J. Phys. Chem. Solids*, **49**, 863 (1988).

[86] Woodcock,L.V, Angell,C.A, & Cheeseman,P, *J. Chem. Phys.*, **65**, 1565, 1976.

[87] Gardner,P.J, & Heyes,D.M, *Physica B*, **113**, 227, 1985.

[88] Kumta,P.N, Deymier,P.A, & Risbud,S.H, *Physica B*, **153**, 85, 1988.

[89] Pastore,G, Ballone,P, & Tosi,M.P, *J. Phys. C: Sol. Stat.*, **19**, 487, 1986.

[90] Ballone,P, Pastore,G, Thakur,J.S, & Tosi,M.P, *Physica B*, **142**, 294, 1986.

[91] Hansen,J.P & McDonald,I.R, "Theory of Simple Liquids", Academic press, London, 1986.

[92] Tessman,J.R, Kahn,A.H, & Shockley,W, *Phys. Rev.*, **92**, 890, 1953.

[93] Wilson,M, & Madden,P.A, *J. Phys.: Condens. Matter*, **5**, 6833, 1993.

[94] *Advanced Visualisation Software Ltd*, licensed through the University CHEST package.

[95] Andersen,H.C, *J. Chem. Phys.*, **72**, 2384, 1980.

[96] Parrinello,M, & Rahman,A, *Phys. Rev. Lett.*, **45**, 1196, 1980.

[97] Ray,J.R, & Rahman,A, *J. Chem. Phys.*, **82**, 443, 1985.

[98] Berendsen,H.J.C, Postma,J.P.M, van Gunsternen,W.F, DiNola,A, & Haak,J.R, *J. Chem. Phys.*, **81**, 3684, 1984.

[99] Marc,G, & McMillan,W.G, *Adv. Chem. Phys.*, **63**, 209, 1985.

[100] Rowlinson,J.S, & Swinton,F.L, "Liquids and Liquid Mixtures", (Butterworths, 1982.)

[101] Abraham,F, *Phys. Rep.*, **80**, 339, 1981.

[102] Metropolis,N, Rosenbluth,A.W, Rosenbluth,M.N, Teller,A.H, & Teller,E, *J. Chem. Phys.*, **21**, 1087, 1953.

[103] Lewis,G.V, & Catlow,C.R.A, *J. Phys. C: Sol. Stat.*, **18**, 1149, 1985.

[104] Mozzi,R.L, & Warren,B.E, *J. Appl. Crys.*, **2**, 164, 1969; Da Silva, J.R.G, Pinatti,D.G, Anderson,C.E, & Rudee,M.L, *Phil. Mag.*, **31**, 713, 1975.

[105] Dupree,R, & Pettifer,R.F, *Nature*, **308**, 523, 1984; Pettifer,R.F, Dupree,R, Farnan,I, & Sternberg,U, *J. Non. Cryst. Solids*, **106**, 408, 1988.

[106] Allen,D.A, Howe,R.A, Wood,N.D, & Howells,W.S, *J. Phys.: Condens. Matter*, **4**, 1407, 1992.

[107] Badyal,Y.S, & Howe,R.A, *J. Phys.: Condens. Matter*, **5**, 7189, 1993.

[108] McGreevy,R.L, & Howe,M.A, *J. Phys.: Condens. Matter*, **1**, 9957, 1989.

[109] Ellis,R.B, *J. Electrochem. Soc.*, **113**, 485, 1966.

[110] Janz,G.J, *et al*, *J. Phys. Chem. Ref. Data*, **4**, 1975.

[111] Derrien,J.Y, & Dupuy,J, *J. Physique*, **36**, 191, 1975.

[112] Biggin,S, & Enderby,J.E, *J. Phys. C: Sol. Stat.*, **15**, L305, 1982.

[113] Boulard,B, Kieffer,J, Phifer,C.C, & Angell,C.A, *J. Non. Cryst. Solids*, **140**, 350, 1992.

[114] Iyetomi,H, & Vashishta,P, *Phys. Rev. B*, **47**, 3063, (1993).

[115] Elliott,S.R, *Preprint.*

[116] Salmon,P.S, *Proc. R. Soc. Lond. A*, to be published.

[117] Vashishta,P, Kalia,R.K, Antonio,G.A, & Ebbsjö,I, *Phys. Rev. Lett.*, **62**, 1651, 1989.

[118] Vashishta,P, Kalia,R.K, & Ebbsjö,I, *Phys. Rev. B*, **39**, 6034, 1989.

[119] Susman,S, Volin,K.J, Montague,D.G, & Price,D.L, *Phys. Rev. B*, **43**, 11076, 1991.

[120] Salmon,P.S, *Proc. R. Soc. Lond. A*, **437**, 591, 1992.

[121] Sokolov,A.P, Kisliuk,A, Soltwisch,M, & Quitmann,D, *Phys. Rev. Lett.*, **69**, 1540, 1992.

[122] Busse, L.E, *Phys. Rev. B*, **29**, 3639, 1984.

[123] Philips,J.C, J. Non-Cryst. Solids, **43**, 37, 1981.

[124] Elliott,S.R, "The Physics of Amorphous Materials", 2^{nd} edition, (Longman, 1990.)

[125] Elliott,S.R, *Phys. Rev. Lett.*, **67**, 711, 1991.

[126] Elliott,S.R, *J. Phys.: Condens. Matter*, **4**, 7661, 1992.

[127] Bhatia,A.B, & Thornton,D.E, *Phys. Rev. B*, **2**, 3004, 1970.

[128] Faber,T.E, & Ziman,J.M, *Phil. Mag.*, **11**, 153, 1965.

[129] Saboungi,M-L, Howe,M.A, & Price,D.L, *Mol. Phys.*, **79**, 847, 1993.

[130] Susman,S, Volin,K.J, Montague,D.G, & Price,D.L, *J. Non-Cryst. Solids*, **125**, 168, 1990.

[131] Elliott,S.R, *Nature*, **354**, 451, 1991.

[132] Cervinka,L, Komrska,J, & Mikes,J, *J. Non-Cryst. Solids*, **75**, 69, 1985.

[133] Blétry,J, *Phil. Mag. B*, **62**, 469, 1990.

[134] Dixmier,J, *J. Phys. I France*, **2**, 1011, 1992.

[135] Uhlherr,A, & Elliott,S.R, *J. Phys: Condens. Matter*, **6**, L99, 1994.

[136] Uhlherr,A, & Elliott,S.R, *Phil. Mag. B*, in press.

[137] Holender,J.M, & Morgan,G.J, *J. Phys: Condens. Matter*, **3**, 7341, 1991.

[138] Misawa,M, Price,D.L & Suzuki,K, *J. Non-Cryst. Solids*, **37**, 85, 1980.

[139] Dejus,R.J, Susman,S, Volin,K.J, Price,D.L, & Montague,D.G, J. Non-Cryst. Solids, **106**, 34, 1988.

[140] Lee,J.H, & Elliott,S.R, *Phys. Rev. B*, submitted.

[141] Harding,J.H, *Private communication.*

[142] Börjesson,L, Hassan,A.K, Swenson,J, Torrell,L.M, & Fontana,A, *Phys. Rev. Lett.*, **70**, 1275, 1993.

[143] Reijers,H,T,J, Saboungi,M-L, Price,D.L, Richardson Jr,J.W, & Volin,K,J, *Phys. Rev. B*, **40**, 8018, 1989.

[144] M. Misawa, *J. Chem. Phys.*, **91**, 2575, 1989.

[145] M. Misawa, *J. Chem. Phys.*, **93**, 6774, 1990.

[146] Howe,M.A, *Mol. Phys.*, **69**, 161, 1990.

[147] Abramo,M.C, & Caccamo,C, *J. Phys.: Condens. Matter*, **6**, 4405, 1994.

[148] Price,D.L, Moss,S.C, Reijers,R, Sabounghi,M-L, & Susman,S, *J. Phys.: Condens. Matter*, **1**, 1005, 1989.

[149] Lin,C, Busse,L.E, Nagel,S.R, & Faber,J, *Phys. Rev. B*, **29**, 5060, 1984.

[150] Susman,S, Volin,K.J, Liebermann,R.C, Gwanmesia,G.D, & Wang,Y, *Phys. Chem. Glasses*, **31**, 144, 1990.

[151] Leadbetter,A.J, & Wright,A.C, *J. Non-Cryst. Solids* **7**, 156, 1972.

[152] Nguyen,V.T, Gay,M, Enderby,J.E, Newport,R.J, & Howe,R.A, *J. Phys. C: Sol. Stat.*, **15**, 4627, 1982.

[153] Leadbetter,A.J, & Wright,A.C, *J. Non-Cryst. Solids*, **7**, 37, 1972.

[154] Fortner,J, Saboungi,M-L, & Enderby,J.E, *Phys. Rev. Lett.*, **69**, 1415, 1992.

[155] Vijayaraghavan,P.R, Nicklow,R.M, Smith,H.G, & Wilkinson,M.K, *Phys. Rev. B*, **2**, 2098, 1970.

[156] Baetzold,R.C, Catlow,C.R.A, Corish,J, Healy,F.M, Jacobs,P.W.M, Leslie,M & Yan,Y.T, *J. Phys. Chem. Solids*, **50**, 791, 1989.

[157] Jacobs,P.W.M, Corish,J, & Catlow,C.R.A, *J. Phys. C: Sol. Stat.*, **13**, 1977, 1980.

[158] Derrien,J,Y, & Dupuy, J, *Phys. Chem. Liq.*, **5**, 71, 1976.

[159] Inui,M, Takeda,S, Shirakawa,Y, Tamaki,S, Waseda,Y, & Yamaguchi,Y, *J. Phys. Soc. Japan*, **60**, 3025, 1991.

[160] Catlow,C.R.A, Corish,J, & Jacobs,P.W.M, *J. Phys. C: Sol. Stat.*, **12**, 3433, 1979.

[161] Catlow,C.R.A, & Stoneham,A.M, *J. Phys. C: Sol. Stat.*, **16**, 4321, 1983.

[162] Fischer,K, *Phys. Stat. Sol. b*, **66**, 295, 1974.

[163] Kleppmann,W.G, & Weber,W, *Phys. Rev. B*, **20**, 1669, 1979.

[164] Greening,G.G.W, & Weil,K.G, *Z. Naturforsch*, **39a**, 764, 1984.

[165] Margheritis,C, & Sinistri,C, *Z. Naturforsch*, **43a**, 751, 1988.

[166] Mayer,J.E, *J. Chem. Phys.*, **1**, 327, 1933.

[167] Bücher,M, *Phys. Rev. B*, **27**, 5919, 1983; **30**, 947, 1984.

[168] Margheritis,C, & Sinistri,C, *Z. Naturforsch*, **43a**, 129, 1987.

[169] Costa-Cabral,B.J, *Private Communication.*

[170] Wilson,M, Costa-Cabral,B.J, & Madden,P.A, *in preparation.*

[171] Stafford,A.J, & Silbert,M, *Z. Phys. B*, **67**, 31, 1987.

[172] Lowndes,R.P, & Martin,D.H, *Proc. R. Soc. Lond. A*, **308**, 473, 1968.

[173] McEachran,R.P, Stauffer,A.D, & Brookfield,S, *J. Phys. B: At. Mol. Phys.*, **15**, 1581, 1982.

[174] Sternheimer,R.M, *Phys. Rev. A*, **1**, 321, 1970.

[175] Kelly,H.M, & Fowler,P.W, *Mol. Phys.*, **80**, 135, 1993.

[176] Mahan,G.D, & Subbaswamy,K.R, " Local Density Theory of Polarizability", (Plenum, London, 1990.)

[177] O'Sullivan,K.F, & Madden,P.A, *J. Phys.: Condens. Matter*, **3**, 8751, 1991.

[178] Cohen,A.J, & Gordon,R.G, *Phys. Rev. B*, **14**, 4593, 1976.

[179] Muhlhausen,C, & Gordon,R.G, *Phys. Rev. B*, **23**, 900, 1981.

[180] Wolf,G.H, & Bukowinski,M.S.T, *Phys. Chem. Min.*, **15**, 209, 1988.

[181] Causa,M, Dovesi,R, Pisani,C, & Roetti,C, *Phys. Rev. B*, **33**, 1308, 1986.

[182] D'Arco,P, Jolly,L-H, & Silvi,B, *Phys. Earth and Plan. Int.*, **72**, 286, 1992.

[183] Chang,K.J, & Cohen,M.L, *Phys. Rev. B*, **30**, 474, 1984.

[184] Mehl,M.J, Hemley,R.J, & Bayer,L.L, *Phys. Rev. B*, **33**, 8685, 1986.

[185] Jackson,M.D, & Gordon,R.G, *Phys. Rev. B*, **38**, 5654, 1988.

[186] Agnon,A, & Bukowinski,M.S.T, *Phys. Rev. B*, **41**, 7755, 1990.

[187] Singh,K.J, & Sanyal,S.D, *Phys. Stat. Sol. B*, **113**, K23, 1983.

[188] Pyper,N.C, *Proc. R. Soc. Lond. A*, to be published.

[189] Pyper,N.C, *Private communication.*

[190] Harding,J.H.H, *Private communication.*

[191] Allan,N.L, Braithwaite,M, Cooper,D.L, Mackrodt,W.C, & Wright,S.C, *J. Chem. Phys.*, **95**, 6792, 1991.

[192] Landolt-Börnstein, Series III, **7**, Berlin:Springer-Verlag, 1973.

[193] Birch,F, *J. Geophys. Res.*, **83**, 1257, 1978.

[194] Jaffe,J.E, & Hess,A.C, *Phys. Rev. B*, **48**, 7903, 1993.

[195] Jamieson,J.C, *Phys. Earth and Plan. Int.*, **3**, 201, 1970.

A

Multipole Interaction Tensors.

A.1 The Full Tensors.

The general expression for the components of the interaction tensor, **T**, are given by

$$T^{ij}_{\alpha\beta\gamma\delta....} = \nabla_\alpha \nabla_\beta \nabla_\gamma \nabla_\delta ... \frac{1}{r^{ij}}. \tag{A.1}$$

Thus, writing $r = r^{ij}$ for clarity

$$T^{ij} = \frac{1}{r} \tag{A.2}$$

$$T^{ij}_\alpha = \nabla_\alpha \frac{1}{r} = \frac{-r_\alpha}{r^3} \tag{A.3}$$

$$\begin{aligned} T^{ij}_{\alpha\beta} &= \nabla_\alpha \nabla_\beta \frac{1}{r} \\ &= \frac{1}{r^5}\left\{3r_\alpha r_\beta - r^2\delta_{\alpha\beta}\right\} \end{aligned} \tag{A.4}$$

$$\begin{aligned} T^{ij}_{\alpha\beta\gamma} &= \nabla_\alpha \nabla_\beta \nabla_\gamma \frac{1}{r} \\ &= \frac{1}{r^7}\left\{5r_\alpha r_\beta r_\gamma - r^2\left(r_\alpha\delta_{\beta\gamma} + r_\beta\delta_{\alpha\gamma} + r_\gamma\delta_{\alpha\beta}\right)\right\} \end{aligned} \tag{A.5}$$

$$T^{ij}_{\alpha\beta\gamma\delta} = \nabla_\alpha \nabla_\beta \nabla_\gamma \nabla_\delta \frac{1}{r} \tag{A.6}$$

$$\begin{aligned} &= \frac{1}{r^9}\{105r_\alpha r_\beta r_\gamma r\delta \\ &+ 3r^4\left(\delta_{\beta\gamma}\delta_{\alpha\delta} + \delta_{\gamma\alpha}\delta_{\beta\delta} + \delta_{\alpha\beta}\delta_{\gamma\delta}\right) \\ &- 15r^2\left(r_\alpha r_\beta \delta_{\gamma\delta} + r_\alpha r_\gamma \delta_{\beta\delta} + r_\alpha r_\delta \delta_{\beta\gamma}\right. \\ &+ \left. r_\beta r_\gamma \delta_{\alpha\delta} + r_\beta r_\delta \delta_{\alpha\gamma} + r_\gamma r_\delta \delta_{\alpha\beta}\right)\} \end{aligned} \tag{A.7}$$

$$T^{ij}_{\alpha\beta\gamma\delta\epsilon} = \nabla_\alpha\nabla_\beta\nabla_\gamma\nabla_\delta\nabla_\epsilon\frac{1}{r} \tag{A.8}$$

$$\begin{aligned}
&= \frac{1}{r^{11}}\{-945r_\alpha r_\beta r_\gamma r_\delta \\
&+ 105r^2\left(r_\alpha r_\beta r_\gamma \delta_{\delta\epsilon} + r_\alpha r_\beta r_\delta \delta_{\gamma\epsilon} + r_\alpha r_\gamma r_\delta \delta_{\beta\epsilon} + r_\beta r_\gamma r_\delta \delta_{\alpha\epsilon}\right. \\
&+ \left. r_\alpha r_\beta r_\epsilon \delta_{\gamma\delta} + r_\alpha r_\gamma r_\epsilon \delta_{\beta\delta} + r_\beta r_\gamma r_\epsilon \delta_{\alpha\delta} + r_\alpha r_\delta r_\epsilon \delta_{\beta\gamma} + r_\beta r_\delta r_\epsilon \delta_{\alpha\gamma} + r_\gamma r_\delta r_\epsilon \delta_{\alpha\beta}\right) \\
&- 15r^4\left(r_\epsilon \delta_{\beta\gamma}\delta_{\alpha\delta} + r_\epsilon \delta_{\gamma\alpha}\delta_{\beta\delta} + r_\epsilon \delta_{\alpha\beta}\delta_{\gamma\delta} + r_\alpha \delta_{\gamma\delta}\delta_{\beta\epsilon} + r_\alpha \delta_{\beta\delta}\delta_{\gamma\epsilon} + r_\alpha \delta_{\beta\gamma}\delta_{\delta\epsilon}\right. \\
&+ r_\beta \delta_{\gamma\delta}\delta_{\alpha\epsilon} + r_\beta \delta_{\alpha\delta}\delta_{\gamma\epsilon} + r_\beta \delta_{\alpha\gamma}\delta_{\delta\epsilon} + r_\gamma \delta_{\beta\delta}\delta_{\alpha\epsilon} + r_\gamma \delta_{\alpha\delta}\delta_{\beta\epsilon} + r_\gamma \delta_{\alpha\beta}\delta_{\delta\epsilon} \\
&+ \left. r_\delta \delta_{\beta\gamma}\delta_{\alpha\epsilon} + r_\delta \delta_{\gamma\alpha}\delta_{\beta\epsilon} + r_\delta \delta_{\alpha\beta}\delta_{\gamma\epsilon}\right)\}
\end{aligned} \tag{A.9}$$

A.2 The Interactions.

Tensor	Interaction
T^{ij}	charge-charge
T^{ij}_{α}	charge-dipole
$T^{ij}_{\alpha\beta}$	dipole-dipole,charge-quadrupole
$T^{ij}_{\alpha\beta\gamma}$	dipole-quadrupole
$T^{ij}_{\alpha\beta\gamma\delta}$	quadrupole-quadrupole

TABLE A.1: *Interaction tensor energy relationships.*

A.3 General.

For a given pair ij,

$$T^{ij}_{\alpha\beta\gamma.....} = (-1)^n T^{ji}_{\alpha\beta\gamma.....} \tag{A.10}$$

where n is the order of the tensor. Thus,

$$T^{ij}_{\alpha\beta} = T^{ji}_{\alpha\beta} \tag{A.11}$$

but

$$T^{ij}_{\alpha\beta\gamma} = -T^{ji}_{\alpha\beta\gamma}. \tag{A.12}$$

B

The Quadrupolar Model .

B.1 Derivation of the Dipole and Quadrupole Expressions.

Following equation 2.28 of section 2.1.1, at equilibrium $m^i_\mu \ddot{\mu}^i_\alpha = 0$. Thus

$$2k_1\mu^i_\alpha + 2k_2\mu^i_\beta\theta^i_{\alpha\beta} + 4k_4\mu^i_\alpha\mu^{i\,2} = E^i_\alpha. \tag{B.1}$$

A simple rearrangement gives

$$\mu^i_\alpha = \alpha E^i_\alpha + \frac{B\mu^i_\beta\theta^i_{\alpha\beta}}{3\alpha C} + \frac{B^2\mu^i_\alpha\mu^2}{9\alpha^4 C}. \tag{B.2}$$

Similarly from equation 2.29

$$k_2\mu^i_\alpha\mu^i_\beta + 2k_3\theta^i_{\alpha\beta} = -\frac{1}{3}E^i_{\alpha\beta} \tag{B.3}$$

giving

$$\theta^i_{\alpha\beta} = CE^i_{\alpha\beta} + \frac{B\mu^i_\alpha\mu^i_\beta}{2\alpha^2}. \tag{B.4}$$

Substituting equation B.4 into B.2 gives

$$\mu^i_\alpha = \alpha E^i_\alpha + \frac{B\mu^i_\beta}{3\alpha C}\left\{CE^i_{\alpha\beta} + \frac{B\mu^i_\alpha\mu^i_\beta}{2\alpha^2}\right\} + \frac{B^2\mu^i_\alpha\mu^2}{9\alpha^4 C}. \tag{B.5}$$

Neglecting the higher order terms (both E^3)

$$\mu^i_\alpha = \alpha E^i_\alpha + \frac{1}{3}B\frac{\mu^i_\beta}{\alpha}E^i_{\alpha\beta}. \tag{B.6}$$

Substituting in

$$\mu^i_\beta = \alpha E^i_\beta + \frac{1}{3}BE^i_{\beta\gamma}E^i_\gamma \tag{B.7}$$

yields

$$\mu^i_\alpha = \alpha E^i_\alpha + \frac{BE^i_{\alpha\beta}}{3\alpha}\left\{\alpha E^i_\beta + \frac{1}{3}BE^i_{\beta\gamma}E^i_\delta\right\}. \tag{B.8}$$

Again, neglecting the higher order ($E\nabla E^2$) term the correct dipole expression to the order required is recovered, i.e

$$\mu^i_\alpha = \alpha E^i_\alpha + \frac{1}{3} B E^i_{\alpha\beta} E^i_\beta. \tag{B.9}$$

Substituting this expression into equation B.4

$$\theta^i_{\alpha\beta} = C E^i_{\alpha\beta} + \frac{B\mu^i_\beta}{2\alpha^2} \left\{ \alpha E^i_\alpha + \frac{1}{3} E^i_{\alpha\beta} E^i_\beta \right\}. \tag{B.10}$$

Again, neglecting the $\nabla E E^2$ term and substituting in equation B.7

$$\theta^i_{\alpha\beta} = C E^i_{\alpha\beta} + \frac{B E^i_\alpha}{2\alpha} \left\{ \alpha E^i_\beta + \frac{1}{3} B E^i_{\beta\gamma} E^i_\delta \right\}. \tag{B.11}$$

Finally, neglecting the $\nabla E E^2$ term the correct form of the induced quadrupole is recovered

$$\theta^i_{\alpha\beta} = C E^i_{\alpha\beta} + \frac{1}{2} B E^i_\alpha E^i_\beta. \tag{B.12}$$

B.2 Derivation of the Induction Energy.

The energy describing the interaction of an ion with an external field can be written as

$$\begin{aligned} \mathcal{U} &= k_1 \sum_{i=1}^{N_t} \mu_i^2 + k_2 \sum_{i=1}^{N_t} \mu^i_\alpha \theta^i_{\alpha\beta} \mu^i_\beta \\ &+ k_3 \sum_{i=1}^{N_t} \theta^i_{\alpha\beta} \theta^i_{\alpha\beta} + k_4 \sum_{i=1}^{N_t} \mu_i^4 \\ &- \sum_{i=1}^{N_t} \mu^i_\alpha E^i_\alpha - \frac{1}{3} \sum_{i=1}^{N_t} \theta^i_{\alpha\beta} E^i_{\alpha\beta}. \end{aligned} \tag{B.13}$$

Substituting the μ^i_α and $\theta^i_{\alpha\beta}$ expressions (equations B.9 and B.12 respectively) and neglecting all terms of higher order than $E^2_\alpha E_{\alpha\beta}$

$$\begin{aligned} \mathcal{U} &= k_1 \sum_{i=1}^{N_t} (\alpha^2 {E^i_\alpha}^2 + \frac{2}{3} \alpha B {E^i_\alpha}^2 E^i_{\alpha\beta}) \\ &+ k_2 \sum_{i=1}^{N_t} \alpha^2 C {E^i_\alpha}^2 E^i_{\alpha\beta} \\ &+ k_3 \sum_{i=1}^{N_t} (BC {E^i_\alpha}^2 E^i_{\alpha\beta} + C^2 {E^i_{\alpha\beta}}^2) \end{aligned}$$

$$
\begin{aligned}
&- \sum_{i=1}^{N_t}(\alpha E_\alpha^i + \frac{1}{3}BE_\alpha^i E_{\alpha\beta}^i)E_\alpha^i \\
&- \frac{1}{3}\sum_{i=1}^{N_t}(\frac{1}{2}BE_\alpha^{i\,2} + CE_{\alpha\beta}^i)E_{\alpha\beta}^i. \qquad \text{(B.14)}
\end{aligned}
$$

Substituting the equations for the force constants

$$
\begin{aligned}
\mathcal{U} &= \sum_{i=1}^{N_t}(\frac{1}{2}\alpha E_\alpha^{i\,2} + \frac{1}{3}BE_\alpha^{i\,2}E_{\alpha\beta}^i - \frac{1}{6}BE_\alpha^{i\,2}E_{\alpha\beta}^i \\
&+ \frac{1}{6}BE_\alpha^{i\,2}E_{\alpha\beta}^i + \frac{1}{6}CE_{\alpha\beta}^{i\,2} \\
&- \alpha E_\alpha^{i\,2} - \frac{1}{3}BE_\alpha^{i\,2}E_{\alpha\beta}^i \\
&- \frac{1}{6}BE_\alpha^{i\,2}E_{\alpha\beta}^i - \frac{1}{3}CE_{\alpha\beta}^{i\,2}) \qquad \text{(B.15)}
\end{aligned}
$$

finally giving

$$
\mathcal{U} = \sum_{i=1}^{N_t}(-\frac{1}{2}\alpha E_\alpha^{i\,2} - \frac{1}{6}BE_\alpha^{i\,2}E_{\alpha\beta}^i - \frac{1}{6}CE_{\alpha\beta}^{i\,2}) \qquad \text{(B.16)}
$$

which is the desired energy expression.